Study of the effects of spherical aberration and signal levels on a diffraction-based multiplane microscope and its application to evaluate the fluid shear stress around a cell

Michele Gabriele Raffaele Guastamacchia

Thesis submitted for the qualification of Doctor of Engineering

Heriot-Watt University
School of Engineering and Physical Sciences
September, 2019

Abstract

Multifocal/multiplane microscopy (MUM) is a technique to acquire simultaneously several planes at sample and obtain axially extended 4D imaging. This is an important characteristic that allows to track fast single molecules/particles three-dimensionally, in real time and over wide axial ranges (≈ 8 μm). MUM avoids possible ambiguous localisations due to the scanning of the imaged plane to acquire a 3D volume over time.

For this thesis, a diffraction multiplane system has been characterised to evaluate the impact of different levels of spherical aberration and signal and applied to measure velocity and shear stress fields due to the flow of a liquid around a cell. The spherical aberration has been quantified via the curves of sharpness that can measure the amount of aberrations in images. This has shown that the measured plane spacing grows as the spherical aberration increases. The influence of spherical aberration on image sharpness as a function of emitter axial position could potentially be used to generate correction factors and improve the accuracy on the recovered positions. In terms of performance, the axial range over which the expected axial positions can be calculated with accuracies of at least 100 nm has been shown to vary linearly with the signal level in the studied range. The signal to noise ratio (SNR) threshold below which the axial range goes to 0 μm has been calculated to be 1.23 ± 0.71. It has also been demonstrated that the axial range can be potentially raised by enlarging the plane spacing. Regarding the precision on the axial positions, this varies exponentially with the signal with a decay constant of 0.51 ± 0.10 per SNR unit. This work has generated two equations to predict the expected axial range and precision, given the system parameters are known. Concerning its applications, MUM has been tested to perform micro-particle image velocimetry (μPIV), a technique able to reconstruct the velocity and shear stress fields imposed by a liquid flowing around a cell. The system has been, first, tested in absence of cells, achieving, within 10 μm from the coverslip glass, an accuracy on the calculated velocity of (0.42 ± 0.32) μm/s. This value is slightly worse than that obtained by using a confocal microscope, which is (0.30 ± 0.13) μm/s. Above 10 μm, instead, MUM performance is considerably inferior than that reached with the confocal microscope. In presence of cells MUM has been used for the first time to capture the perturbations to the expected laminar flow, allowing to measure velocities of 30 μm/s and shear stresses of 3 Pa around the observed cell. The reconstructed fields show characteristics similar to those reported in the literature. However, the observation of unexpected velocity and shear stress values indicate a reduction in accuracy caused by false axial localisations.

To the women of my life,

Angela and Elisa.

Acknowledgements

To start with, I would like to thanks my supervisors, Dr Paul A. Dalgarno and Dr Stephen E. D. Webb, which, despite some misunderstandings, have patiently guided me through the EngD and helped my comprehension of the working principles of microscopes.

A special thanks goes also the science and technology facilities council (STFC) people at the research complex at Harwell (RCaH) and, in particular, to the OCTOPUS group, whose help to solve technical problems and constant scientific support have been critical to the project.

A huge thanks goes to Dr Valentina Lo Schiavo for having looked after me during my lab and data analysis work.

Thank you from the bottom of my heart Dr Kamel Madi for your mentoring and friendship. This will never be forgotten!

Many thanks to Dr W. T. Eric Pitkeathly for having allowed me to use a piece of software he designed.

A huge thank you must go to all people in the centre for doctoral training in applied photonics at Heriot-Watt University and, particularly, to Prof. Derryck T. Reid, whose kindness and readiness to help and support have always been fundamental.

Another big thanks is due to all friends met during the EngD and in Oxford as Diego, Donato, Valentina, Davide, Francesco, Maria, Feng, Kant, Dimmytar, Teodor, Laura, Kiran, Nick, Indran, Ilir, Sofia, Abdullah, Benji, Trang Luke, Luis, Giannis and so on...

Thank you, Elisa, for your unconditional love.

Thank you very much to all people in Archangel Aerospace Group for their friendship.

Finally, the biggest thank you goes to my mum and all my family, which have always strongly supported me during this journey.

ACADEMIC REGISTRY
Research Thesis Submission

Name*:*	Michele Guastamacchia		
School:	School of Engineering and Physical Sciences		
Version: *(i.e. First, Resubmission, Final)*	Final	Degree Sought:	Doctor of Engineering

Declaration

In accordance with the appropriate regulations I hereby submit my thesis and I declare that:

1) the thesis embodies the results of my own work and has been composed by myself
2) where appropriate, I have made acknowledgement of the work of others and have made reference to work carried out in collaboration with other persons
3) the thesis is the correct version of the thesis for submission and is the same version as any electronic versions submitted*.
4) my thesis for the award referred to, deposited in the Heriot-Watt University Library, should be made available for loan or photocopying and be available via the Institutional Repository, subject to such conditions as the Librarian may require
5) I understand that as a student of the University I am required to abide by the Regulations of the University and to conform to its discipline.
6) I confirm that the thesis has been verified against plagiarism via an approved plagiarism detection application e.g. Turnitin.

* *Please note that it is the responsibility of the candidate to ensure that the correct version of the thesis is submitted.*

Signature of Candidate*:*	Michele Guastamacchia	Date:	27/08/19

Submission

Submitted By *(name in capitals):*	
Signature of Individual Submitting:	
Date Submitted:	

For Completion in the Student Service Centre (SSC)

Received in the SSC by *(name in capitals):*			
Method of Submission *(Handed in to SSC; posted through internal/external mail):*			
*E-thesis Submitted (**mandatory for final theses)***			
Signature:		Date:	

Table of contents

List of tables

List of figures

List of equations

List of abbreviations

A	Generic aperture
AC	Aperture control
ADC	Analog to digital conversion factor
AF	Apparent focus
AK	Aperture knob
Amp	Generic amplitude
APD	Avalanche photodiode
a.u.	Arbitrary unit
BFP	Back focal plane
BG	Blazed grating
BG/pix, Bpix	Background per pixel
BS	Beam splitter
Cal	Generic calibration curve
CC	Camera connector
CCD	Charged coupled device
CCG	Chromatic correction grating
CCP	Custom cage plate
CL	Condenser lens
CMC	C-mount connector
CMOS	Complementary metal oxide semiconductor
C_{nF}	Circles of the distorted diffraction grating
Col	Collector lens
CoM	Centre of mass
CP	Cage plate
CS	Chip size
d	Grating period
d_B	Period of a blazed diffraction grading
DDG	Distorted diffraction grating
DoF	Depth of focus or depth of field
d_p	Pupil diameter
d_s	Real position of the object in the sample
d_{sa}	Apparent position of the object in the sample
dSTORM	Direct stochastic optical reconstruction microscopy

d_0	Central grating period
EFL	Effective focal length
em	Electron multiplying
emCCD	Electron multiplying charged coupled device
EP	Eyepiece
eq.	Equation
e_r	Emitter radius
ET	Exposure time
F	Filter
FALCON	Fast localisation algorithm based on a continuous-space formulation
f_{gm}	Focal length of the distorted diffraction grating in the m^{th} order
fig.	Figure
f_L	Focal length of a lens L
FLIM	Fluorescence lifetime imaging
f_o	Objective lens focal length
FOV	Field of view
FSR	Focal shift ratio
F_{tl}	Focal length of the tube length
$F_{\backslash\backslash}$	Generic force parallel to a surface
G	Camera gain
GH	Grating holder
G_{max}	Peak value of a generic Gaussian curve
G_N	Gaussian read noise
GNN	Global nearest neighbour algorithm
GR	Grism
GSDIM	Ground state depletion microscopy followed by individual molecule
HeLa	Henrietta Lacks cell
hMSC	Human mesenchymal stem cell
HyD	Hybrid detector
i	Image distance
I_{bal}	Intensity balance among the diffraction orders
IC, ic	Image count or internal conversion
ic_{pix}	Image count per pixel
I_m	Intensity in the m^{th} order
iPALM	Interferometric photoactivated localisation microscopy

ISC	Intersystem crossing
J_0	Zeroth order Bessel function of the first kind
J_1	First order Bessel function of the first kind
$k_{x/y/z}$	Spatial frequencies in the Fourier space
k_0	Frequency resolution
L	Generic lens or infinity space
L_e	Entrance Length
L_d	Distance between the doublet lenses in Dalgarno relay
L_f	Length to filter
LM	Lens mount
L_{max}	Peak value of a generic Lorentzian curve
LNN	Local nearest neighbour algorithm
LoG	Laplatian of Gaussian filter
M	Magnification
m	Diffraction order
MACS	Multifocus astigmatism compressed sensing
MBG	Multiblazed grating
MFG	Multifocus grating
MFP	Multifacet prism
Mir	Mirror
MLE	Maximum likelihood estimation
MUM	Multifocal/multiplane microscopy
n	Refractive index
N, N_p	Number of imaged planes
NA	Numerical aperture or not available
n_{cv}	Refractive index of the coverslip glass
ND	Neutral density filter
NF	Nominal focus
n_F	Loci of the diffraction grating circles
n_{grat}	Refractive index of the diffraction grating
n_i, n_{im}	Immersion medium refractive index
n_k	Value of the k^{th} pixel
N_{ph}	Number of photons emitted
N_{pix}	Number of pixels
n_{ph}	Number of photons collected

n_{ratio}	Ratio between refractive indices
n_s	Sample refractive index
n_λ	Extra number of waves added to the path length
o	Objective distance
o.a.	Optical axis
OD	Optical density
OL	Objective lens
OTF	Optical transfer function
PALM	Photoactivated localisation microscopy
P_a	Pre-aperture distance
P_c	Pre-camera distance
PDF	Probability density function
PDMS	Poly-dimethylsiloxane
pix	Pixel
PMT	Photomultiplier tube
P_n	Generic n^{th} plane
PPFC	Parallel plate flow chamber
PS, Δo, Δz	Plane spacing
PS_c	Central plane spacing
PSF	Point spread function
$P_{1/2}$	Principal planes
q	Camera quantum efficiency or number of pixels in the sharpness box
R	Diffraction grating radius
Re	Reynolds number
r_{nF}	Radii of the circles of the distorted diffraction grating
R_m	m^{th} ratiometric sharpness curve
ROI	Region of interest
RSP, S_{max}	Relative sharpness peak height
$R_{x/y}$	Lateral resolution
R_z	Axial resolution
R^2	Linear fit regression goodness
R_{adj}^2	Adjusted linear fit regression goodness
s	Separation between optical components
SA	Spherical aberration
SB	Sharpness baseline or sharpness box

S_B	Sharpness of the background
SBR	Signal to background ratio
SBR_{pix}	Signal to background ratio per pixel
sCMOS	Scientific complementary metal oxide semiconductor
sec.	Section
SIM	Structured illumination microscopy
S_m	m^{th} sharpness curve
S_w	Wall shear stress
SMLM	Single molecule localisation microscopy
S_n	Generic n^{th} singlet state or n^{th} sub-region of interest
SNR	Signal to noise ratio
SNR_{pix}	Signal to noise ratio per pixel
SNR_0	Signal to noise ratio threshold
SOFI	Super-resolution optical fluctuation imaging
$S_{o/i}$	Object/image side length
SP	Sharpness peak height
S_{pix}	Camera pixel size
SPP	Sharpness peak position
SSIM	Saturated structured illumination microscopy
STED	Stimulated emission depletion microscopy
STORM	Stochastic optical reconstruction microscopy
S_w	Wall shear stress
T	Transmission
TIR	Total internal reflection
TIRF	Total internal reflection florescence microscopy
TL	Tube lens
T_n	n^{th} triplet state
$T_{o/i}$	Tube length on the object/image side
T_{tot}	Total transmission
V_f	Flow velocity
V_m	m^{th} variance curve
V_{mag}	Velocity magnitude
W	Aberration term
$W_{x/y}$	Standard deviations of a Gaussian profile
W_{20}	Defocus coefficient

x_0	Centre of the circles of the distorted diffraction grating
ΔI	Space per image plane
Δi	Distance between formed images
ΔPS	Plane spacing variation
Δx	Distortion of the diffraction grating or off-set among wavelength beams
$\Delta\lambda$, BW	Bandwidth
ε_d	Etching depth
ε_{dbal}	Etching depth for the intensity balance
φ	Phase delay
φ_{bal}	Phase delay for the intensity balance
λ	Wavelength
λ_c	Central wavelength
λ_{bal}	Wavelength at which the diffraction grating is balanced
$\lambda_{i/f}$	Initial/final wavelength
μ	Viscosity
μPIV	Micro-particle image velocimetry
ρ	Density or pupil function
ϑ_B	Blaze angle
ϑ_c	Critical angle
θ_i	Incident angle
ϑ_m	Diffraction angle associated to the m^{th} order

List of attended conferences

- M. G. R. Guastamacchia, S. E. D. Webb, "Optimization of the illumination path of a super resolution microscope", poster presented at the EngD conference in Optics and Photonics Technologies, Heriot-Watt University, Edinburgh, UK, 17 July 2014.

- M. G. R. Guastamacchia, S. E. D. Webb, P. A. Dalgarno, "Diffraction multifocal microscopy for super-resolved 3D localisation of single particles", poster presented at the EngD conference of the Centre for Doctoral Training in Applied Photonics, Heriot-Watt University, Edinburgh, UK, 26th June 2015.

- M. G. R. Guastamacchia, "Axial super-resolution multifocal microscopy", poster presented at the "Student at Harwell poster competition" in the Medical Research Council, Harwell campus, Harwell, UK, 25th October 2015.

- M. G. R. Guastamacchia, W. T. E. Pitkeathly, B. C. Coles, V. Lo Schiavo, S. E. D. Webb, P. A. Dalgarno, "Multifocal microscopy for single molecule imaging in cells", talk given at TransMed student CDT conference, Edinburgh University, Edinburgh, UK, 31st May - 1st June 2016.

- M. G. R. Guastamacchia, S. E. D. Webb, P. A. Dalgarno, "Multifocal microscopy for single molecule imaging in cells", talk given at the EngD conference of the Centre for Doctoral Training in Applied Photonics, Heriot-Watt University, Edinburgh, UK, 24th June 2016.

- M. G. R. Guastamacchia, W. T. E. Pitkeathly, K. Madi, P. A. Dalgarno, S. E. D. Webb, "Multifocal microscopy applications to cell studies", talk given at the Scottish Microscopy Group Symposium 2016, Heriot-Watt University, Edinburgh, UK, 24th November 2016.

- M. G. R. Guastamacchia, W. T. E. Pitkeathly, K. Madi, P. A. Dalgarno, S. E. D. Webb, "Multifocal microscopy applied to the fluid shear stress on cells", talk given at the conference Focus on Microscopy 2017, Palais des Congrès, Bordeaux, France, 10th April 2017.

- M. G. R. Guastamacchia, W. T. E. Pitkeathly, K. Madi, P. A. Dalgarno, S. E. D. Webb, “Diffraction multifocal microscopy applied to evaluate the fluid shear stress at sub-cellular level”, poster presented to the “White Rose Students” at the Research Complex at Harwell, Harwell campus, Harwell, UK, 12th June 2017.

- M. G. R. Guastamacchia, R. Xue, W. T. E. Pitkeathly, K. Madi, S. Cartmell, P. Lee, P. A. Dalgarno, S. E. D. Webb, “Multifocal microscopy applied to measure the fluid shear stress on cells”, talk given at the EngD conference of the Centre for Doctoral Training in Applied Photonics, Heriot-Watt University, Edinburgh, UK, 23rd June 2017.

Chapter 1
Introduction

1.1 Chapter overview

This introductive chapter will present optical microscopy as a tool to investigate 3D structures and dynamics in live cells. Optical microscopes can be subdivided into non-fluorescence (fig. 1.2) [1] and fluorescence techniques [2] (fig. 1.3, sec. 1.3.2). The former uses the light scattered by the samples to generate images, while the latter exploits either the fluorescence emitted by specifically labelled molecules and structures or the natural autofluorescence emitted by the sample. Microscopes have a fundamental limit of resolution that cannot be violated [3] (eq. 1.8 and 1.9, fig. 1.5). However, resolution can be improved by using superresolution techniques [4] (sec. 1.3.10), which laterally and axially have achieved more than 20-fold and 50-fold resolution improvements [5], respectively. 3D imaging can be performed by acquiring different images at different axial positions over time (fig. 1.4, z-stack imaging [6]). Microscopes without optical sectioning abilities, however, will produce images whose contrast is reduced by the out of focus background light. This problem can be reduced by microscopies as confocal [6] (sec. 1.3.7, fig. 1.8) and light sheet [7] (sec. 1.3.8, fig. 1.9), which can discard some of the background light and increase the contrast. Confocal microscopy, however, is not a widefield technique and this limits its temporal resolution [6]. To achieve full 4D imaging (i.e. simultaneously in three dimensions and over time) and capture fast 3D dynamics over extended axial depths, instead, a technique called multifocal microscopy [8, 9, 10] (sec. 1.3.9, fig. 1.10), where several planes are acquired at the same time, can be exploited.

1.2 3D Structures and dynamics in cells and need for 4D imaging

Cells are three-dimensional complex and dynamic structures and can be considered the fundamental unit of life [11], since they are the building block of all known organisms. All types of cells are elaborate machines, within which many biomolecular reactions take place to metabolise nutrients, synthesise required molecules, replicate themselves, carry out specific cell type functions, etc. [12]. Cells are composed of many parts, each dedicated to a specific task [13]. This can be visualised, for example, by considering a generic animal cell [13] (fig. 1.1), whose size can range from around 10 μm to over 100 μm (not considering axons in neurons [14], which can be much longer). Cells are confined within the cell membrane, which separates and protects them from the external

environment, regulates the movement of substances that enter and exit from the cells and is involved in functions such as cell adhesion [12], cell signalling [15, 16], etc. Several structures are present within cells. In eukaryotic cells, for example, some of them are referred to as organelles [13] (mitochondrion, nucleus, lysosomes, etc., fig. 1.1), whose dimensions can reach several micrometres and behave as specialised subunits. The largest one is the nucleus, which governs the activity of the cell and where

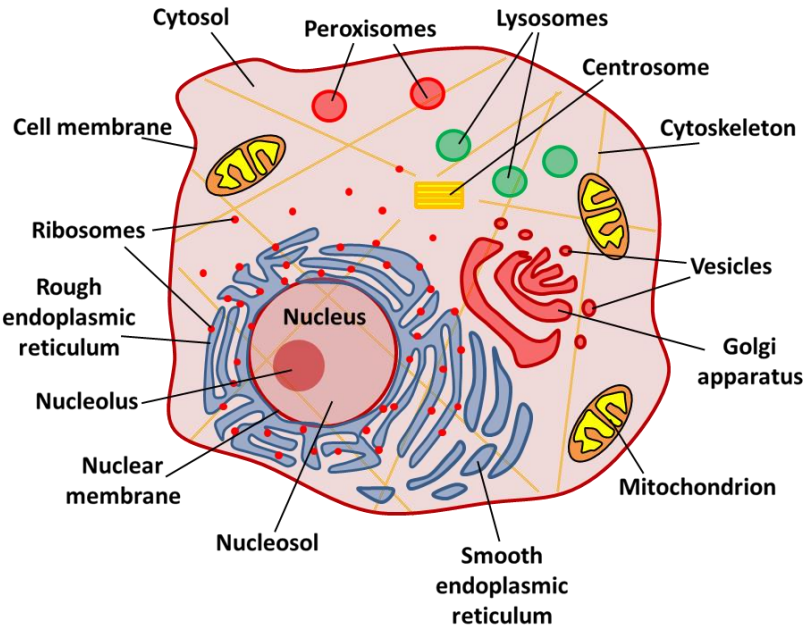

Figure 1.1 Schematic representation of an animal cell [13].

the genetic material, i.e. the deoxyribonucleic acid (DNA) [17], is stored and organized.

The complex cell structure and functioning described above are combined with similarly complex dynamics [11]. An example is provided by the endocytosis and endocytic pathway [18], which is used by cells to uptake macromolecules and large particles from the surrounding medium. Another example of complex dynamics in cells is given by signal transduction [15, 16], which is the process by which external signals (chemical or physical) carrying some information are transmitted inside a cell through a series of molecular events to stimulate a response (e.g. apoptosis, protein expression, cell differentiation, cell reproduction, etc.). These examples are only a small part of the vast universe of cellular processes [11]. However, they can provide an idea about the complexity of these phenomena. Their study is fundamental to better characterise cell behaviours and, for example, design specific therapies in case of disease [19, 20]. However, this might require instruments capable to provide access to the three-dimensional cellular structures and dynamics in real time [21] (4D). In the next section optical microscopy will be presented as a tools to conduct this task [22].

1.3 Optical light microscopy and 3D imaging

A fundamental instrument to investigate 3D live cell structures and dynamics is the optical microscope and the science related to its use and development is called microscopy [23, 24]. An optical microscope exploits the imaging power of lenses to capture the light scattered or emitted by the samples under study and generate magnified images that can provide information not normally accessible to the naked eye [25]. Even though the magnifying power of lenses has been known for centuries [26], the first compound microscopes (i.e. made by several lenses) appeared in Europe only around the 17th century [27]. In this period, the important work of Robert Hooke was published in his book Micrographia [28], where microscopic details of insects, leaves, minerals, etc., were shown and the term "cell" was coined. The quality of the lenses used in these early microscopes was poor and so were the generated images. A significant improvement in this sense was made by Antonie van Leeuwenhoek in the late 17th century, which developed superior methods of grinding and polishing lenses and, consequently, could build simple microscopes with higher image quality and hundred times magnification power [29]. This allowed him to discover the microorganisms. The increased magnifying ability of microscopes had permitted to resolve some of the micrometric and nanometric structures of the samples. However, in 1873 Ernst Abbe discovered that microscopes have a fundamental limit of resolution that is inversely proportional to their light collecting aperture and directly proportional to the wavelength of the used light [30]. Consequently, one way to lower this limit is, for example, by reducing the used wavelength, e.g. with electron [31] or x-ray microscopies [32]. Unfortunately, the former technique cannot be used with live specimens, while the latter one tends to destroy the samples due to the high photon energy. For these reasons, optical microscopy roughly in the visible – near infrared (NIR) range remains the only non-invasive imaging technique [9]. Despite the diffraction limit, the last decades have seen the advent of new microscopy techniques grouped under the name of superresolution [4], which can cleverly circumvent the diffraction limit (but not violate it) and improve the resolution (sec. 1.3.10).

The next sub-sections will present some of the most common optical microscopy techniques and how these can be conveniently exploited to achieve 3D imaging.

1.3.1 *Widefield microscopy*

In optical microscopes two light paths can be identified, i.e. the illumination and imaging paths [22]. The former is used to guide the light emitted by a source to illuminate a sample, while the latter to direct the light scattered or emitted by a sample to a detector.

Some examples of microscope setups are schematised in fig. 1.2. In these setups the illumination path is located to the left of the sample, while the imaging path to the right. The light emitted by a polychromatic non-coherent source (e.g. a halogen bulb [33]) is captured by a collector lens (Col) that focuses it to the back focal plane (BFP) of another lens denominated the condenser lens (CL), which, consequently, can uniformly illuminate the sample. This illumination scheme is called Köhler illumination [34] and avoids the formation of the image of the source at the sample and detector planes, which, in turn, could hide the image of the sample. Since the entire sample is illuminated at once, all points in the imaged planes are simultaneously captured on the detectors and these microscopes are termed widefield [23]. In fig. 1.2a the light scattered by the sample is collected by a lens or a system of lenses called the objective lens (OL) and directed toward the image plane, where the primary image of the sample will be formed. The position of the primary image can approximately be located by the lens equation [35] (eq. 1.1):

$$\frac{1}{o} + \frac{1}{i} = \frac{1}{f_o}, \qquad \text{(eq. 1.1)}$$

where o is the distance between the imaged plane and the OL, i that between OL and the primary image position and f_o is the OL focal length. The image will have a magnification (M) equal to (eq. 1.2):

$$M = -\frac{i}{o} = -\frac{f_o}{o - f_o}. \qquad \text{(eq. 1.2)}$$

The OLs shown in fig. 1.2 are just simplistic schematisations of real OLs. In reality OLs are very complicated lens groups designed to reduce the optical aberrations (sec. 1.5) and improve the image quality [36]. Consequently, the o and i distances should be considered from the principal planes of the OL [37]. The image formed by the OL can then be captured by a detector placed at the primary image position or further guided by another group of lenses termed the eyepiece (EP) [1] to the eyes of the microscope user.

The eyepiece is usually a binocular system, whose focal length can be varied not continuously and that applies a further magnification. The size of the imaged plane is denominated the field of view (FOV) and, in general, is smaller than the size of the illuminated area. The setup in fig. 1.2a can be further expanded by inserting another lens called tube lens (TL), as schematised in fig. 1.2b. In the setup of fig. 1.2b the imaged plane is placed at a distance equal to f_o from the OL. As a consequence, the light exiting the OL will be sent to infinity and intercepted by the TL, which will form an image at a distance equal to its focal length (f_{tl}). This design is called infinity corrected and is convenient in case there is the need to insert some optical components such as polarisers or filters after the OL [22]. Indeed, in case of a non-infinity corrected design (fig. 1.2a) these components would shift the image plane position (i.e. the distance i) and modify the aberration correction set by the OL. These problems are minimised with the infinity corrected design. The distance between OL and TL is called infinity space and does not affect the imaging, even though it affects the optical setup as, for example, the size of the tube lens. The M imposed by an infinity corrected design to the image at the primary image position is [38] (eq. 1.3):

$$M = -\frac{f_{tl}}{f_o}. \qquad \text{(eq. 1.3)}$$

The Ms described by eq. 1.2 and 1.3 act in the image plane and are termed lateral Ms. Microscopes provide also an axial M [39], which is equal to the lateral M squared. By axially scanning the sample (fig. 1.2a) or the OL (fig. 1.2b), different object planes can be observed. This axial scanning movement can be done within the working distance, which is the distance between the front lens of the OL and the bottom of the coverslip glass where the sample might sit or the surface of the sample. The microscopes schematised in fig. 1.2a and 1.3b are also called brightfield [40], since the image of the sample will appear darker with respect to the background. This is due to the fact that the sample back-reflects or absorbs part of the light, while this does not happen to the light that does not cross the sample. The microscopes shown in fig. 1.2 work in transmission, since the light from the source crosses the sample [38]. Particularly reflective or opaque samples can also be imaged in reflection [38], with the illumination and imaging paths on the same side with respect to the sample. Microscopes can also be divided into upright and inverted, based on the fact that the OL captures the light, respectively, from above or below the sample [38]. In brightfield microscopy, in situations where the refractive index (n) of the studied sample is close to

that of the surrounding environment, the contrast of the sample with respect to the bright background might be very low, making almost impossible its visualisation [22]. Microscopies such as darkfield and phase contrast could help to increase the contrast [41]. The former reduces the contribution of the light that has not been scattered by the sample, while the latter exploits the interference between scattered and non-scattered light. Stains such as hematoxylin and eosin (H&E) [42] are also commonly used to highlight specific structures in biological samples.

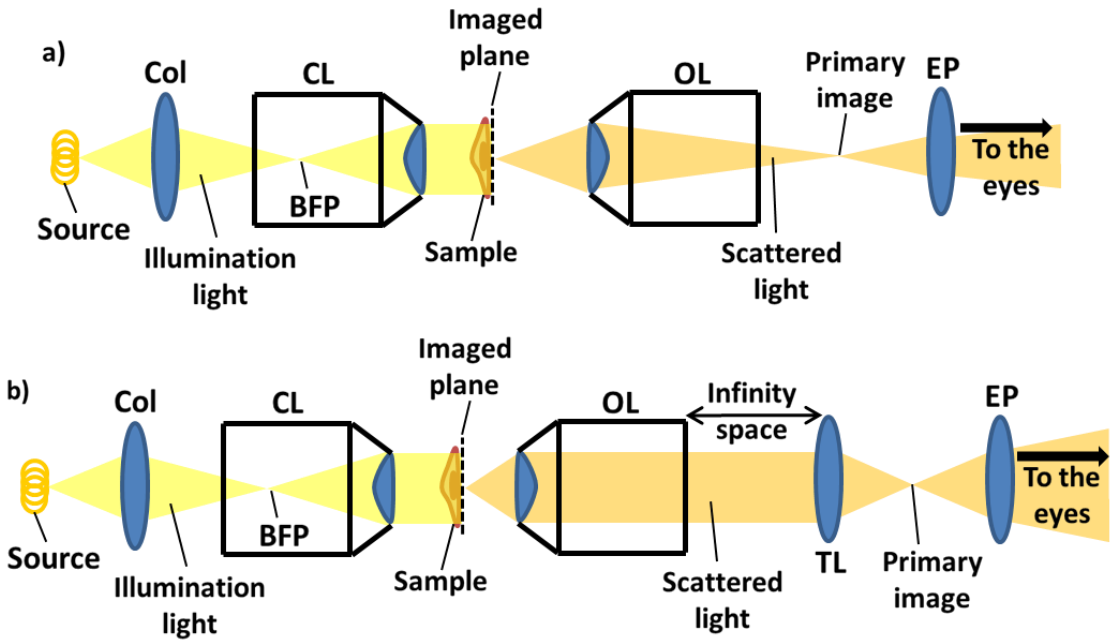

Figure 1.2 Schematic examples of non-fluorescence transmission microscopes. The schemes in a and b show, respectively, non-infinity and infinity corrected microscopes. Col is the collector lens, CL the condenser lens, BFP indicates the back focal planes, OL is the objective lens, TL the tube lens and EP the eyepiece.

1.3.2 *Fluorescence widefield microscopy*

The microscopies described in sec. 1.3.1 are non-fluorescence microscopies, since they exploit the light scattered by the samples to generate images, not the process of absorption and emission of the molecules (e.g. fluorescence [43]). In fluorescence microscopy, instead, the latter process is exploited [2]. With this technique molecules and/or structures of interest in samples (e.g. organelles) can be specifically labelled by fluorescent molecules and imaged to observe their behaviours or the natural fluorescence emitted by the samples (autofluorescence [44, 45]) can be directly observed [46]. A generic process of light absorption followed by the emission of fluorescence is schematised in the Jablonski diagram of fig. 1.3a [47]. Through the

absorption of photons (blue arrows), a fluorescent molecule can be excited from its singlet ground state (S_0) to its singlet excited states (S_1, S_2, etc.). This is immediately followed by ultra-fast relaxations (less than picoseconds [48]) called vibrational relaxations or internal conversion (IC) toward the ground level of the S_1 state (solid black arrows). Here the molecule can relax to the S_0 state through the emission of fluorescence (green arrows) or non-radiatively (black dotted arrow, fluorescence quenching [48]) via, for example, molecular collisions. When in the lowest S_1 level the molecule can also undergo a transition to the first triplet state (T_1) called intersystem crossing [49] (ISC, black dashed arrow). ISC is a forbidden and, hence, less probable transition than fluorescence and typically happens after several absorption – emission events. In addition, the transition from T_1 to S_0 is also forbidden and, thus, the T_1 state has a longer lifetime (even minutes [49]) than the S_1 one. This can cause the phenomenon of blinking [50], where the molecule intermittently moves between on singlet states, where fluorescence emission is allowed, and off long-lived triplet states. From the T_1 level the molecule can relax to the S_0 one via the emission of phosphorescence [51] or non-radiatively via the quenching of the triplet state [50]. Due to the presence of the non-radiative decays and the emission of phosphorescence, not all absorbed photons are re-emitted as fluorescence. This can be quantified through the fluorescence quantum yield [52], i.e. the ratio between the number of fluorescently emitted and absorbed photons. The range of wavelengths that can be absorbed by the fluorescent molecules constitutes the absorption band, while that that can be emitted the emission one [53, 54]. The wavelength associated to the emission peak is longer than that for the absorption one [55]. The process of fluorescence has been extensively studied during the 19^{th} century and this led to the development of the first fluorescence microscopes at the beginning of the 20^{th} century [56]. These early fluorescence microscopes were exploiting the natural autofluorescence [44, 45] of biological samples when using ultraviolet excitation sources. The subsequent development of techniques to selectively excite the desired fluorophores and the synthesis of a wide variety of fluorescent molecules emitting at several visible and NIR wavelengths (combined with the introduction of labelling protocols to tag the molecules of interest) have driven the large use of fluorescence microscopy in the second half of the 1900s. A schematisation of a widefield fluorescence microscope is shown in fig. 1.3b. The excitation light coming from a light source (e.g. a laser [57]) can be focused, through a system of lenses (L) and by using a dichroic beam splitter (BS) at the BFP of the OL, thus yielding a

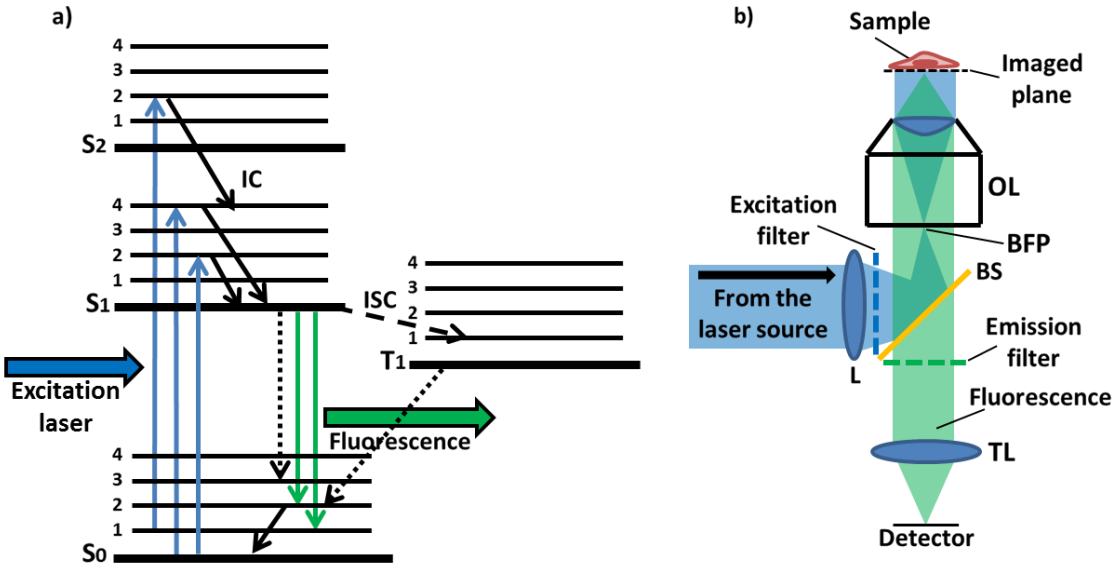

Figure 1.3 Schematisations of (**a**) a generic Jablonski diagram and (**b**) fluorescence microscope. OL is the objective lens, BFP the back focal plane, TL the tube lens, BS the beam splitter, L a lens, S_0, S_1 and S_2 are, respectively, the ground, first and second singlet states and T_1 is the first triplet state.

uniform illumination of the sample. The fluorescence emitted at every point of the imaged plane in the FOV is then collected by the OL, transmitted through the dichroic BS and focused on the detector by the TL, where the images are generated. The imaging and illumination paths might be equipped with, respectively, an emission and an excitation filter to excite only the desired fluorophores and to properly separate the emission and excitation wavelengths and avoid the excitation light and the unwanted fluorescence and autofluorescence to reach the detector. The latter might increase in fixed samples, since some fixation agents tend to be very autofluorescent [45]. To reduce this problem, solutions such as the use of particular buffers [58], the post-processing of images [59], the quenching of autofluorescence via pre-irradiation of the sample [60], etc. have been proposed. As said above, a wide range of different fluorescent emitters for fluorescence microscopy exists and these can be used to label molecules and structures in biological samples. There are three main classes of extrinsic fluorophores for fluorescence microscopy: organic dyes, quantum dots and fluorescent proteins [61]. Organic dyes (such as Alexa Fluor 488 [62]) are fluorescent molecules that can be chemically bound to molecules or structures of interest in the sample, in order to localise and/or track the behaviour of the latter. This is, for example, exploited in the study of the endocytic pathway of the epidermal growth factor receptor (EGFR) [63]. A ligand that binds its associated membrane receptor forms a complex that can be

internalised into vesicles and follow different fates inside a cell. By chemically binding a fluorescent molecule such as Alexa Fluor 488 to the EGF ligand this pathway can be studied. Other fluorescent molecules such as DiD [64] can, instead, be used to label phospholipids [65] and this, for example, can be used to study the cell membrane. Another class of fluorophores is that of quantum dots [66]. Quantum dots are inorganic semiconductor dyes, whose emission wavelength can be tuned by varying their size. They are usually surrounded by a biopolymer, in order to make them compatible with cellular environments and reduce their toxicity and are functionalised with biomolecule that allow them to bind the target molecules in samples. Quantum dots are several times brighter than organic fluorophores and this makes their use attractive. However, they also are generally bigger than organic emitters and this might modify the dynamics of the observed molecules [66]. Fluorescent proteins, instead, are proteins able to emit photons [61]. They have the advantage that they could directly be expressed by the cell during protein synthesis by attaching the gene that codifies for them directly to that that codifies for the protein of interest. This will produce a protein tagged with the fluorescent protein that can easily be imaged. However, fluorescent proteins are usually less bright than organic fluorophores [61]. Some of the most important fluorescent proteins are the green fluorescent protein (GFP) and its derivatives [67], which are very bright and photostable. Photostability is important, since a common issue of all fluorophores is photobleaching [68]. Photobleaching refers to the fact that fluorophores, after several absorption/emission cycles, permanently shelf themselves into a dark state, thus not allowing the study of the targeted molecules anymore. This is caused, for example, by the interactions of fluorophores with other substances such as oxygen, which modify their chemical structures. Consequently, a way to delay photobleaching is the introduction of oxygen scavengers (e.g. Trolox [50]), but these can have a cytotoxic effect [69]. The large availability of fluorophores emitting at several wavelengths allows also for multicolour fluorescence microscopy [21, 70], where different target molecules are labelled with different fluorophores and their behaviours are studied simultaneously. By combining a fluorescence microscope with a multicolour relay composed, for example, of mirrors, lenses, dichroic BS, filters, etc., the different emitted wavelength can be separated and imaged on different cameras or regions of the same camera. In multicolour fluorescence microscopy it is important to properly separate the different emission wavelengths among the dedicated detection channels and hence avoid their crosstalk [71], which would lead to a wrong interpretation of the observed behaviours.

1.3.3 *3D imaging*

As mentioned above, different planes at sample level could be imaged by either axially shifting the sample or the OL. This procedure could also be exploited to acquire different planes at different instants and stack them to reconstruct a 3D shape. The acquired spatial series of images is described as a z-stack [6] (fig. 1.4a). In a z-stack the

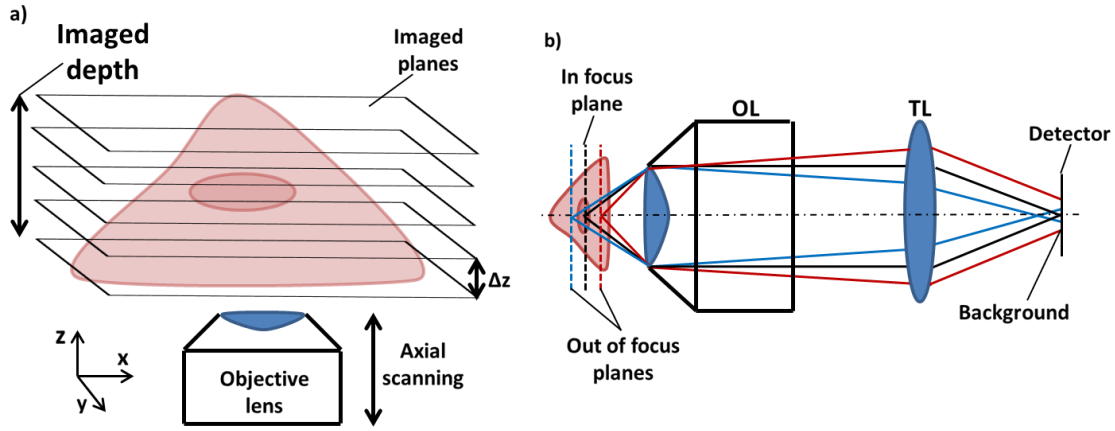

Figure 1.4 a) 3D image acquisition via z-stack imaging. **b)** Scheme showing the generation of background light on the detector due to the simultaneous acquisition of out of focus planes. OL is the objective lens, TL the tube lens and Δz the axial spacing between consecutive acquired planes.

images are acquired through a certain axial depth and are axially spaced by a defined Δz. Z-stacking is a standard approach to reconstruct 3D samples, but it has some drawbacks. During the acquisition of a z-stack the sample should be as static as possible to obtain a three-dimensional image at a set instant [72]. Another major problem arises from the fact that every time a plane is focused and imaged, the images on the detector will be formed by both the focused light coming from the imaged planes and the defocused light coming from the surrounding out of focus planes that have been simultaneously excited [6] (fig. 1.4b). The larger the number of out of focus emitters, the more this effect will be evident and the images will be degraded. Out of focus light can be one of the biggest components of the background signal [73].

1.3.4 *Microscope resolution*

As mentioned, microscopes have a fundamental limit of resolution that cannot be violated [3]. This concept can be explained by observing fig. 1.5a. Every time a point source is imaged through an optical system, it is diffracted by the circular apertures of the lenses and three-dimensionally spread over a pattern called point spread function

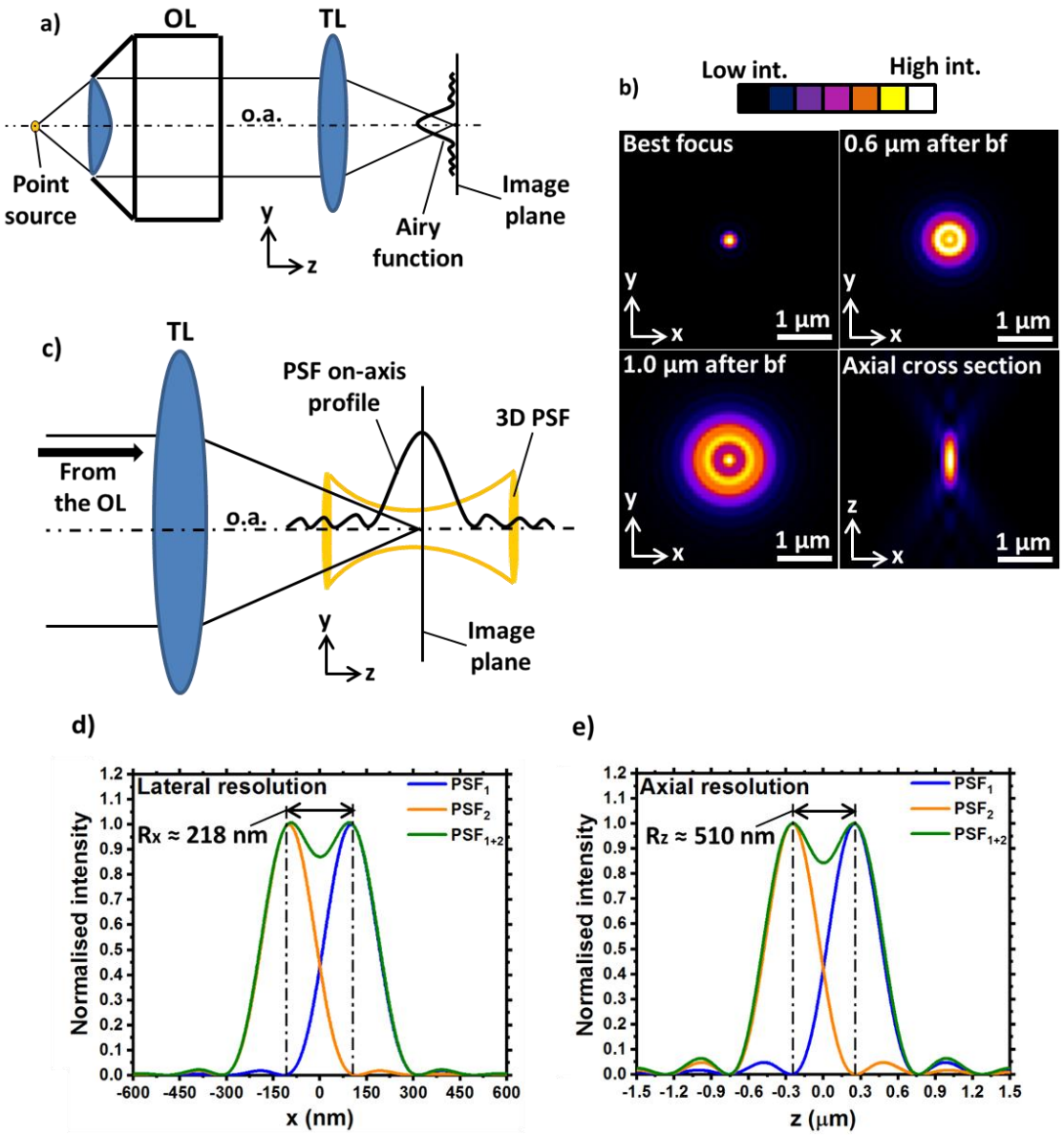

Figure 1.5 a) Scheme showing the lateral spreading of a point source into an Airy function [78] due to diffraction [75]. OL stands for objective lens, TL for tube lens and o.a. is the optical axis. **b)** Simulation of a 3D PSF by using the ImageJ [79] plugin PSF Generator [80] (Born and Wolf 3D optical model, λ = 500 nm, voxel = 40x40x40 nm^3, size = 100x100x100 pix^3, NA = 1.4 and n_{im} = 1.5). bf indicates the best focus. **c)** As in **a**, but axially. **d)** Plot showing the lateral Rayleigh diffraction limit R_x (eq. 1.8) by using a normalised version of eq. 1.5 with λ = 500 nm and NA = 1.4. **e)** Plot showing the axial Rayleigh diffraction limit R_z (eq. 1.9) by using a normalised version of eq. 1.7 with λ = 500 nm and NA = 1.4.

(PSF) [74]. Effectively, the PSF(x,y,z) is the impulse response function of an optical system. Mathematically, this can be expressed in terms of convolution [75] (eq. 1.4):

$$i(x,y,z) = o(x,y,z) * PSF(x,y,z), \qquad \text{(eq. 1.4)}$$

where o(x,y,z) is the real object intensity distribution and i(x,y,z) is the detected intensity distribution of the image. During the image formation process some noise from different sources is introduced [76]. Part of it is due, for example, to the inherent stochastic photon emission of emitters and is called Poisson noise [77]. Some other noise could be introduced by the reading process of the detector and is called read noise [77]. Since detectors are 2D sensors, they can only image a 2D cross section of the PSF. When a point source is focused, the 2D cross section of the PSF is an Airy function [78] and shows a central peak surrounded by a ring-like pattern of lower intensity. It can be described by the following equation (eq. 1.5) [81]:

$$PSF(x,y,0) = 4I_0 \left(\frac{J_1\left(\frac{2\pi}{\lambda} NA \sqrt{x^2+y^2}\right)}{\frac{2\pi}{\lambda} NA \sqrt{x^2+y^2}} \right)^2, \qquad \text{(eq. 1.5)}$$

where I_0 is the peak intensity of PSF(x,y,0), J_1 is the first order Bessel function of the first kind [82], λ is the emitted wavelength and NA is the numerical aperture of the OL [3]. The NA of an OL measures its light gathering ability and is equal to (eq. 1.6):

$$NA = n_{im} \sin\vartheta, \qquad \text{(eq. 1.6)}$$

where n_{im} is the refractive index of the medium (called the immersion medium) between the OL and the coverslip glass, while ϑ is the semi-angle at the vertex of cone of the light collected by the OL. As the point source is moved from the imaged plane, some defocus is introduced [78]. Because of this, the 2D PSF peak will decrease in intensity and the ring-like pattern will spread in space. This is shown in fig. 1.5b with the simulation of a 3D PSF. The 3D PSF has been simulated by using an ImageJ [79] plugin called PSF Generator [80] with the following parameters: Born and Wolf 3D optical model (based on scalar diffraction theory [83], it does not account for the sample – coverslip glass – immersion medium refractive index mismatch), λ = 500 nm, voxel size (i.e. volume unit [84]) = 40x40x40 nm^3, imaged volume size = 100x100x100 pix^3, NA = 1.4 and n_{im} = 1.5. As observable, the lateral cross section tends to increase in size moving from the best focal position (bf, top-left) to defocused ones (top-right and bottom-left) and the total energy is spread. The axially spreading due to the diffraction is larger than the lateral one, making the PSF elongated over the axial direction (bottom-

right and fig. 1.5c). The intensity distribution in the PSF over the optical axis (o.a.) can be described by eq. 1.7 [81]:

$$\mathrm{PSF}(0,0,z) = I_0 \left(\frac{\sin\left(\frac{\pi}{\lambda} NA^2 z\right)}{\frac{\pi}{\lambda} NA^2 z} \right)^2, \qquad \text{(eq. 1.7)}$$

which, similarly to eq. 1.5, presents a central maximum at z = 0 nm and several lateral peaks of lower intensity. Since point sources are spread into PSF, fluorophores such as the GFP that are few nanometres in size will appear much larger. This could be visualised by considering the widths of the central peaks of eq. 1.5 and 1.7. As said, these equations show a central peak surrounded by several minor peaks and these, in turn, are separated by intensity minima. The semi-width of the central peak, measured as the distance between the central peak and one of the two surrounding minima, is equal, for eq. 1.5, to ($R_{x/y}$ eq. 1.8) [3]:

$$R_{x/y} = 0.61 \frac{\lambda}{NA} \qquad \text{(eq. 1.8)}$$

and, for eq. 1.7, to (R_z eq. 1.9) [3]:

$$R_z = 2 \frac{\lambda n_{im}}{NA^2}. \qquad \text{(eq. 1.9)}$$

As observable from eq. 1.8 and 1.9, the size of the PSF will decrease as the wavelength decreases and the NA increases. The dependence from the NA is even more important for the axial width, where it appears squared. As an example, with λ = 500 nm and NA = 1.4, $R_{x/y} \approx 218$ nm and $R_z \approx 510$ nm. Clearly, the fact that the point sources are spread by the optical system and can be described by PSFs means that, below a certain distance, two point sources cannot be distinguished anymore. This is the resolution limit. There are several criteria to define the resolution limit, such as the Abbe, the Sparrow and the Rayleigh ones [85]. The latter is commonly used in microscopy and states that two PSFs are resolvable until each PSF peak sits on the first minimum of the adjacent PSF. In this case the lateral and axial resolution limits take the form of, respectively, eq. 1.8 and 1.9. This is shown in fig. 1.5d and 1.6e, where, respectively, eq. 1.5 (along x) and 1.7 (both normalised with respect to I_0) have been plotted for two

theoretical PSFs (λ = 500 nm and NA = 1.4) separated by the lateral and axial Rayleigh resolution limits. The resulting total signals have also been plotted.

Eq. 1.8 and 1.9 describe the importance of the NA: the higher this is, the better the resolution. The NA quantifies the amount of light (i.e. information) that can be collected by the OL. The concept of NA (eq. 1.6) is depicted in fig. 1.6: the larger the cone of collected light (i.e. ϑ), the higher the NA [3]. In an ideal situation where the refractive indices of sample (n_s) and immersion medium (n_{im}) perfectly match (e.g. water based samples and water immersion OLs) the light will travel toward the OL without undergoing any refraction (fig. 1.6a). However, in case $n_{im} < n_s$ (e.g. with dry OLs) the refraction and total internal reflection (TIR) at the sample – immersion medium interface will reduce the collection cone angle (fig. 1.6b). Instead, in a situation where $n_{im} \approx n_{cv} > n_s$, where n_{cv} is the refractive index of a coverslip glass where the sample might sit (e.g. with oil immersion OLs), the collection cone angle is increased thanks to the refraction at the sample – coverslip glass interface (fig. 1.6c). This indicates why increasing n_{im} increases the NA (eq. 1.6).

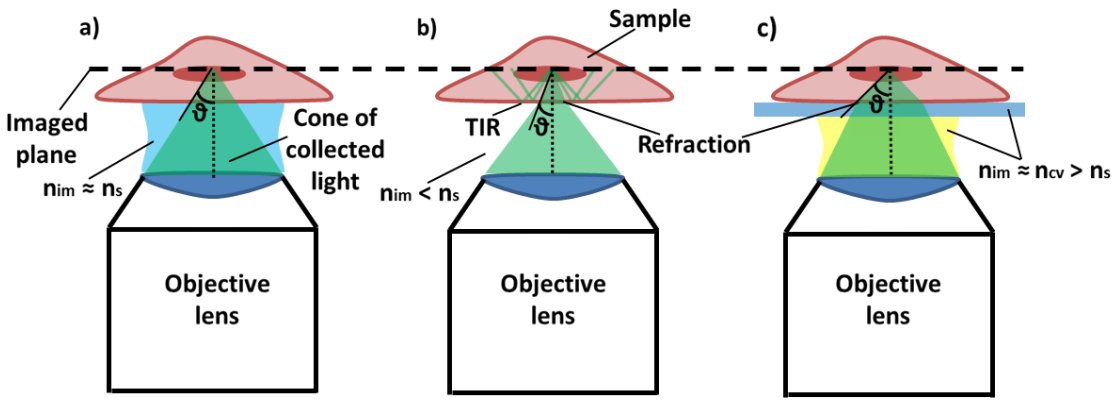

Figure 1.6 Schemes showing the NA (eq. 1.6) of an objective lens in case of (**a**) refractive index matching between sample (n_s) and immersion medium (n_{im}), in case (**b**) $n_s > n_{im}$ and total internal reflection (TIR) arises at the interface between sample and immersion medium and in case (**c**) $n_s < n_{im} \approx n_{cv}$, where n_{cv} is a coverslip glass where the sample is positioned.

In order to achieve the theoretical system resolution, some considerations on the detector should also be made. Detectors for widefield microscopy are composed of thousands of pixels [86], whose role is that of sampling the image formed by the microscope to capture it. To correctly sample the image and avoid loss of information, the Nyquist criterion [87] should be followed. This, basically, indicates that the sampling unit should be equal to half of the desired resolution. In the contest of

widefield microscopy this means that, given a resolution $R_{x/y}$ and a magnification M, the lateral size of each pixel should be equal to $MR_{x/y}/2$. Larger pixel sizes will cause undersampling and loss of resolution. Conversely, smaller pixels sizes (oversampling) will not had extra information and can increase the acquisition time and accelerate the photobleaching. The Nyquist criterion is also valid in the axial direction when acquiring a z-stack.

1.3.5 *Deconvolution microscopy*

Above, the problem of unwanted background light in widefield microscopy has been introduced (fig. 1.4) [6]. One possibility to tackle this problem comes from mathematically post-processing the acquired images by mean of deconvolution microscopy [88]. Essentially, the principle of deconvolution microscopy is that of deconvolving the PSF from the final image (eq. 1.4) to reassign the out of focus light to the right source, thus reducing the background and improving the contrast. Several algorithms for this technique have been developed and deconvolution microscopy has been proven to be a powerful tool. However, deconvolution microscopy has also some limitations. The deconvolution process, indeed, can introduce some artefacts such as the appearance of bright stripes and rings, brighter or blurred regions at the edges of the imaged FOV (edge artefact), the axial elongation of the imaged structures, etc. [89]. These could generate ambiguity in the subsequent interpretation of data. In addition, the PSF has to be experimentally measured or theoretically built (blind deconvolution), introducing other constraints.

1.3.6 *Total internal reflection fluorescence microscopy*

Another technique that allows a massive reduction in background light is total internal reflection fluorescence microscopy (TIRF) [90]. In TIRF, essentially, the evanescent wave [91] generated when light is totally internally reflected is exploited to excite only a thin layer of the sample. There are several setups for TIRF, one of them (through-the-objective) is schematised in fig. 1.7. In this setup, to achieve TIR and differently from the scheme shown in fig. 1.3b (epifluorescence microscopy [68]) the excitation laser is laterally shifted with respect to the o.a., for example, by using mirror or lens systems in the illumination path [90]. In this way, the laser will be bent toward the o.a. upon exiting the OL, making a certain angle ϑ against it. Assuming $n_{im} = n_{cv}$ for simplicity, when the laser light reaches the interface sample - coverslip glass, due to the fact that, usually, the refractive index of biological samples (n_s) is smaller than that of glasses

[92], it will experience TIR and be back-reflected if $\vartheta > \vartheta_c$. This will produce an evanescent wave at that interface with intensity I_0, which will be reduced to I_0/e after a certain penetration depth d. The parameter d, which grows with the wavelength and decreases with ϑ, is typically around 50 nm – 200 nm [92]. This permits TIRF to only excite the sample layers close to the coverslip glass (e.g. the cell membrane [92]) with much lower background and improved contrast. However, this characteristic clearly does not allow TIRF to study samples in 3D. In theory, TIRF microscopy requires objective lens NAs larger than n_s to work, i.e. over around 1.33 in case of water based samples [92]. However, in practise NA $\geq$ 1.45 are necessary [92], in order increase the surface over which TIR is achieved and due to the fact that biological systems can have $n_s \geq 1.33$.

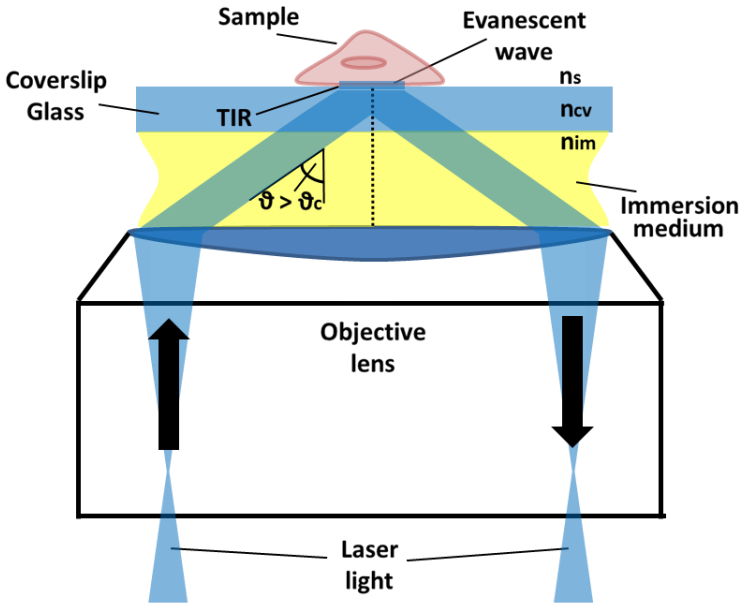

Figure 1.7 Illumination scheme in TIRF microscopy. TIR indicates the total internal reflection, ϑ is the illumination angle and ϑ_c the critical one, n_s, n_{cv} and n_{im} are, respectively, the sample, coverslip glass and immersion medium refractive indices.

1.3.7 *Confocal microscopy*

A very powerful technique to discard the out of focus light and achieve 3D optical sectioning is confocal microscopy [93]. A schematic diagram of a confocal microscope, which was introduced by Marvin Minsky in 1957, is shown in fig. 1.8. Confocal microscopy is not a widefield technique. In a confocal microscope the excitation laser light is not focused at the BFP of the OL, but, instead, it fills the back aperture of the latter. As a consequence, the OL will not produce a uniform illumination of the sample, but, instead, it will focus the laser light at its focal point, from which the fluorescence

will be collected. To acquire an entire image at a desired plane it is then necessary to scan the laser spot or move the sample (again, by following the Nyquist sampling criterion [87]). When this is done by using a fast steering mirror it takes the name of confocal laser scanning microscopy [94]. The fluorescence coming from the OL is then focused by the TL on a non-pixelated detector, since in confocal microscopy it is just needed to record the fluorescence coming from a single point at each time. Examples of detectors for confocal microscopy are photomultiplier tubes (PMTs), avalanche photodiodes (APDs), hybrid combinations of these two (HyDs), etc. [95, 96], in front of which a pinhole aperture is positioned. In comparison to pixelated detectors as charged coupled devices (CCDs) [97] or complementary metal oxide semiconductors (CMOSs) [98], non-pixelated detectors are much faster in acquiring the signals (even less than 1 μs [95]), thus allowing for the fast movements of the steering mirror. In addition, these detectors can also be very sensitive and can be used for single photon detection experiments as in fluorescence lifetime imaging (FLIM) [99]. The pinhole in front of the detector is used to discard the light coming from the out of focus planes (fig. 1.8b), whose fluorophores are excited by the light cone generated by the focused laser. Thanks to the pinhole (whose size can be varied) the sectioning ability of a confocal microscope is much higher than that of a non-TIRF widefield one, thus allowing for higher contrast

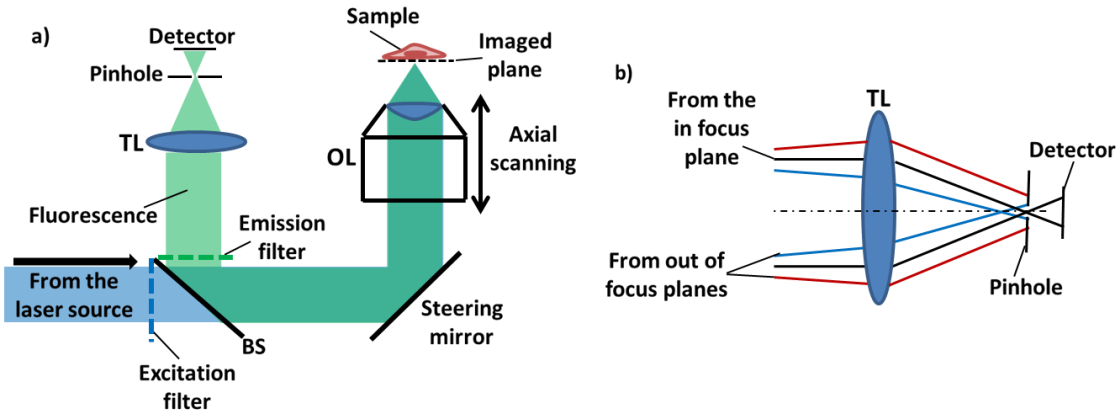

Figure 1.8 Generic schemes describing (**a**) a confocal microscope and (**b**) its background discarding ability due to the presence of the pinhole. OL is the objective lens, TL the tube lens and BS the beam splitter.

3D imaging. In confocal microscopy the overall lateral and axial resolutions are also slightly improved [100], since the system PSF results partially laterally and axially reduced in sizes. In confocal microscopy and according to the Rayleigh criterion in case of an infinity small pinhole the lateral resolution can be defined as (eq. 1.10):

$$R_{x/y} = 0.44\frac{\lambda}{NA}, \qquad \text{(eq. 1.10)}$$

while the axial one as (eq. 1.11):

$$R_z = 1.5\frac{\lambda\, n_{im}}{NA^2}. \qquad \text{(eq. 1.11)}$$

A reduction in the pinhole size can improve the resolution, but at the expenses of the signal level [101]. The major drawback of confocal microscopy is the image acquisition time, i.e. the temporal resolution [102], since, differently from widefield microscopies, images are not acquired at once, but point by point. Consequently, this poses problems when imaging fast dynamic systems, where the temporal resolution is essential.

To improve the acquisition speed a spinning disk confocal microscope could be preferred to a laser scanning one [103]. In the Yokogawa Electric spinning disk confocal microscope [104], for example, the steering mirror is substituted by two disks rotating simultaneously. One disk contains microlenses and is positioned before the dichroic BS used to separate the laser light from the fluorescence, while the other one is located after the dichroic BS and has several pinholes distributed with the same spatial patter as the microlenses on the other disk. The laser light, after crossing the microlens and the pinhole disks, illuminates simultaneously several points in the sample. As the disks rotate, different sets of points are illuminated. The generated fluorescence passes through the pinhole disk, where the out of focus light is blocked, and is then deviated toward the detector, which in spinning disk confocal microscopy is pixelated, since several points are imaged together. In spinning disk confocal microscopy the acquisition speed is massively increased by the fact that several points are imaged simultaneously. However, with this technique there are some drawbacks as the fact that more out of focus light could reach the detector through the multiple pinholes, thus reducing the optical sectioning ability, or the fact that the illumination FOV might not be uniform [103, 105].

A confocal microscope can be exploited also for multi-photon microscopy [106]. In multi-photon microscopy the fluorophores are excited by using two or more lower energy photons simultaneously (multi-photon absorption [106]), rather than a single higher energy one. This condition requires a high photon density and can be reached only in close proximity of the focal point, thus reducing the excited area. For this reason, multi-photon microscopy has a superior optical sectioning ability in comparison

to single-photon confocal microscopy and does not require a pinhole. In addition, the use of lower energy photons, i.e. with longer wavelengths, increases the penetration depth and permits the study of thicker samples [106]. However, this has the effect of worsening the resolution in comparison to single-photon confocal microscopy.

Finally, by using two opposite OLs rather than a single one to excite the sample and collect the fluorescence, it is possible to improve the axial resolution by around five times [107]. Such a setup takes the name of 4Pi microscopy. In a 4Pi microscope, essentially, the interference between the laser beams coming from the two OLs and that between the two collected fluorescence signals at the detector allow to axially reduce the size of the PSF and, thus, improve the axial resolution. However, despite this great advantage, this setup is not massively employed and has not had commercial success, due to its complexity and the lack of flexibility when mounting and accessing samples.

1.3.8 *Light sheet microscopy*

A different technique to selectively excite only a planar portion of the sample and achieve optical sectioning is light sheet microscopy [108]. In light sheet microscopy, two OLs positioned at, for example, 90° with respect to each other are used, one to excite the sample and the other to collect the fluorescence (fig. 1.9). By coupling the illumination OL with, e.g., a cylindrical lens to introduce astigmatism [109] (sec. 1.5), a light sheet to only excite a nearly flat section within the sample can be generated. To reconstruct 3D objects then, the sample can be positioned on a translation stage to image different planes or the light sheet can be scanned through it.

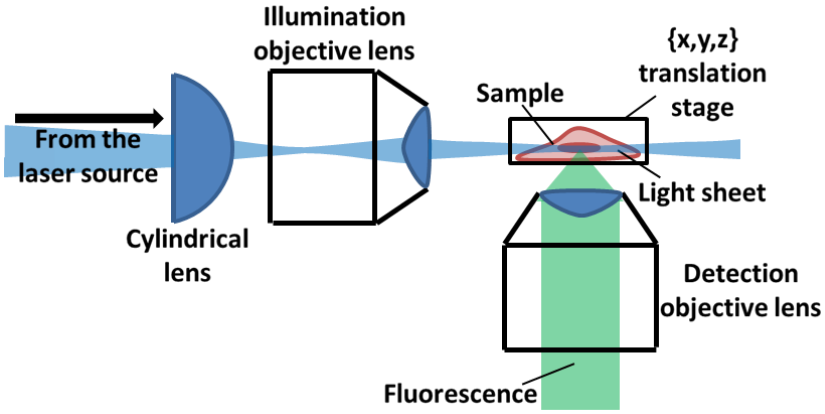

Figure 1.9 Generic scheme describing a light sheet microscope.

Light-sheet microscopy has some of the advantages of confocal microscopy and some of the widefield one. As a confocal microscope, a light sheet microscope has optical sectioning properties. However, as a widefield microscope, a light sheet one can

acquire an entire image simultaneously, making this system much faster than a confocal microscope and, consequently, able to quickly image large samples [110] and reduce the photobleaching and photodamage (phototoxicity [111]) imparted.

Light sheets generated as in the diagram of fig. 1.9 have not a uniform thickness through the sample [108]. Essentially, their thicknesses will decrease and then increase again after reaching a minimum, i.e. the beam waist [57]. The smaller the beam waist, the faster the change in thickness and, hence, the less uniform the light sheet will be. To keep a certain uniformity in the thickness, light sheets are usually made not smaller than 1 μm [112]. To improve the sectioning and, consequently, reduce the light scattered by the sample that deteriorates the images, light sheet and multi-photon microscopies can be combined [113], thus improving the penetration depth as well. Another way to reduce the thickness of the light sheet comes from the use of multi-photon Bessel beams [114] and Airy beams [115], which are quickly laterally scanned to generate virtual light sheets. These beams are propagation-invariant [116], i.e. they propagate uniformly in the sample.

1.3.9 *Multifocal microscopy*

The techniques presented above can be used to either image a single plane several times to capture the sample dynamics in 2D (x,y,t imaging) or to image a 3D static or quasi-static object by using a z-stack (x,y,z imaging). Unfortunately, these techniques cannot be used to simultaneously capture 3D sample dynamics over time (4D imaging), unless the temporal scale over which a sample evolves is much larger than the time to acquire a z-stack. This problem can be avoided by using multiplane or multifocal microscopy (MUM) [8, 9, 10], through which the simultaneous acquisition of multiple planes over time is possible. Essentially, a MUM setup (fig. 1.10) can be obtained by extending a widefield microscope via a multiplane system, which, by using, e.g., mirrors, BSs, lenses and distorted diffraction gratings, can acquire multiple planes simultaneously and image them on one or more detectors. MUM systems are generally designed to work with out of focus images and, due to this, are able to provide information over axial depths much larger than the distance between the first and last imaged planes. With MUM it is possible to achieve extended and instantaneous volumetric imaging [117] and capture long range axial dynamics of single molecules [10].

For this thesis, MUM is the core argument, since a MUM setup [9] has been

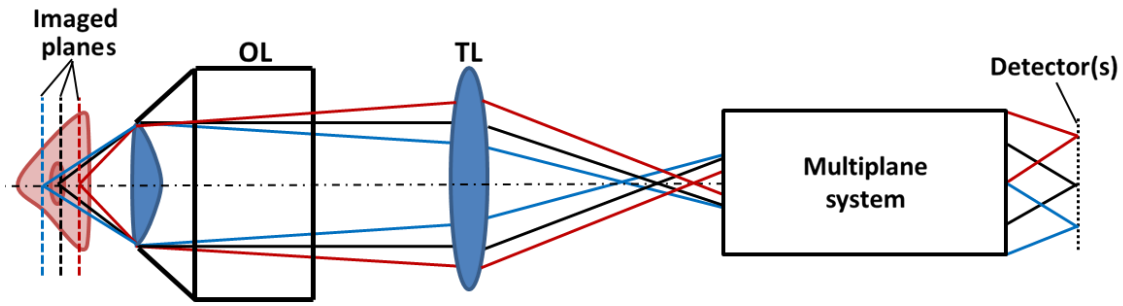

Figure 1.10 Scheme describing the principle behind multifocus microscopy. OL is the objective lens and TL the tube lens.

characterised (chapter 3 and 4) and used (chapter 5) to study a biological sample. For this reason, next chapter (chapter 2) will be entirely dedicated to it and will provide a literature review of the technique.

1.3.10 *Superresolution fluorescence microscopy*

In sec. 1.3.4 the fundamental limit of resolution of fluorescence microscopy has been described [3] (eq. 1.8 and 1.9 and fig. 1.5). This poses substantial limits to the study of molecular biology, due to the impossibility to resolve and observe the interaction among molecules closer than $R_{x/y}$ and R_z. For this reason, in the last 20 years the efforts to develop microscopy techniques able to overcome the resolution problem have been enormous [118]. These have led to the 2014 Nobel Prize in chemistry for the contribution to the development of superresolution fluorescence microscopy [119] to the scientists Eric Betzig, Stephan W. Hell and William E. Moerner.

Some of these techniques are grouped under the family of single molecule localisation microscopies (SMLMs) [120] and include techniques such as photoactivated localisation microscopy (PALM) [121], stochastic optical reconstruction microscopy (STORM) [122], direct stochastic optical reconstruction microscopy (dSTORM) [123], ground state depletion microscopy followed by individual molecule return (GSDIM) [124], etc. The working principle behind SMLMs is explained in fig. 1.11. As described above (sec. 1.3.4), when two emitters are closer than the diffraction limit, their PSFs will overlap and their distinction will be impossible (fig. 1.11a, I). However, if one of the emitters is temporarily switched off, it is possible to collect the fluorescence only from the remaining one, which can then be localised before it photobleaches or turns off (fig. 1.11a, II). By switching on the remaining emitter and repeating this step, also the other fluorophore can be localised (fig. 1.11a, III), taking to a final superresolved image, where only the localisation positions are shown (fig. 1.11a,

IV). Therefore, to perform SMLM it is necessary that not all fluorophores in the sample are in an active state simultaneously, but only a small subset of them, so to avoid PSFs overlapping. This can be done, for example, by using photoswitchable fluorescent proteins [125], which can be activated with an activation laser and subsequently excited with another one [121]. It can also be achieved by exploiting the natural blinking of fluorophores [50], which stochastically enter and exit from dark states. By tuning the excitation laser and selecting the right buffer [123, 124], the majority of fluorophores can be set to their off state, allowing for SMLM.

In SMLM, essentially, an image is built by acquiring several frames, even thousands [120], each one containing a different subset of sparse active fluorophores that are localised (fig. 1.11b). Then, by merging all the localisations in the acquired frames (which should be registered with respect to each other to remove the sample drift [126]), the superresolved image can be obtained. For this reason these techniques are also referred to pointillism [127, 128]. According to [129, 130], single fluorophores can be localised with a maximum theoretical precision proportional to $1/\sqrt{N_{ph}}$, where N_{ph} is the number of emitted photons. The higher N_{ph}, the better the precision and the final resolution. SMLMs have reported lateral resolutions smaller than 10 nm [131], i.e. a 20-fold improvement.

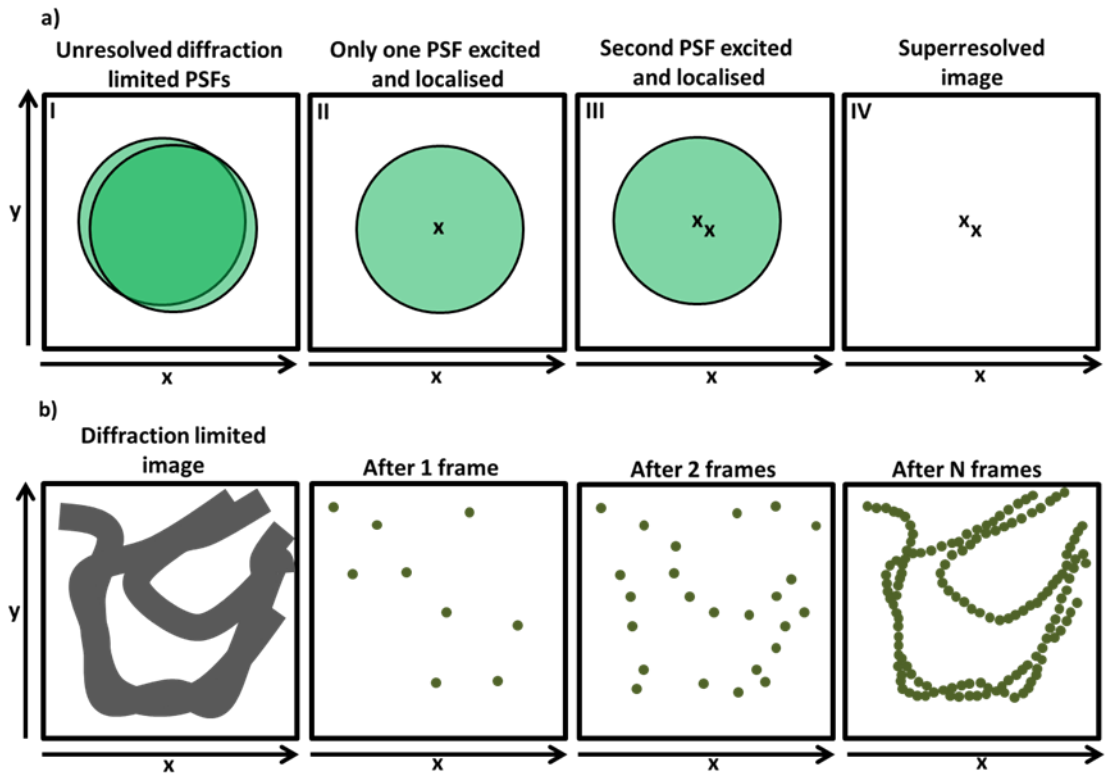

Figure 1.11 Principle behind SMLM (**a**) and scheme showing its application to obtain a superresolved image (**b**).

The fact that with SMLM several frames need to be acquired imposes a limitation on the temporal resolution of these techniques [4]. Essentially, the higher the required resolution, the higher the number of frames needed and the slower the imaging, which could last from seconds to minutes.

SMLMs have also been expanded to provide axial superresolution. For example, this has been done by combining these techniques with PSF engineering [109, 132, 133], where the axial positions of the emitters are encoded in the shapes and orientations of the PSFs. Two examples are shown in fig. 1.12. In [133], this has been obtained by inserting a spatial light modulator in the imaging path, in order to generate a PSF presenting two aligned lobes and called double-helix (fig. 1.12a). If the observed emitter is on the image plane, the double-helix will assume a certain orientation. If, instead, the emitter is above or below it, the double-helix will appear rotated and the

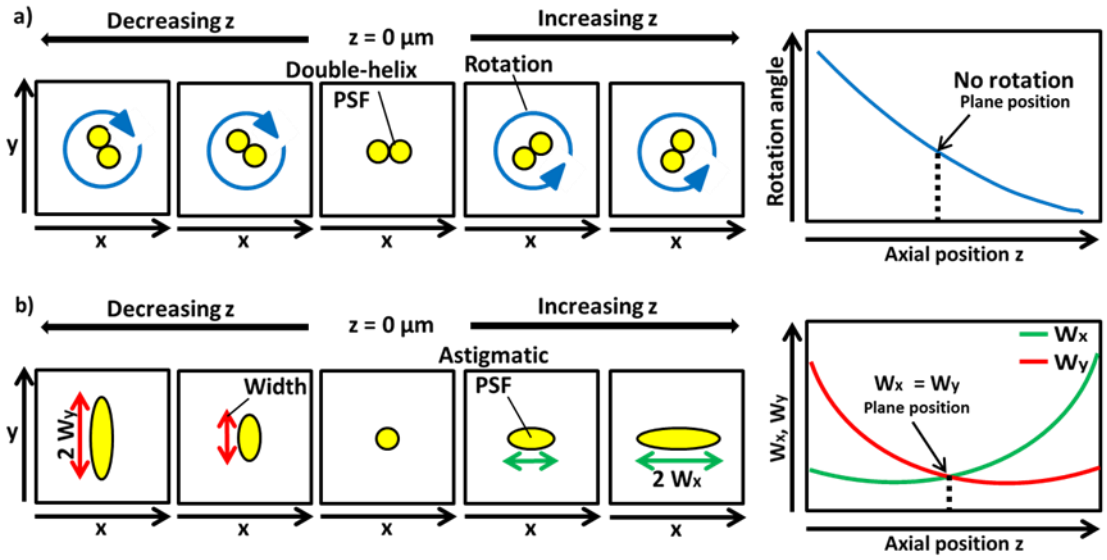

Figure 1.12 Schemes showing how double-helix [133] (**a**) and astigmatic [109] (**b**) PSF can be exploited to achieve 3D SMLM superresolution imaging. W_x and W_y are, respectively, the semi-FWHMs over x and y directions of the astigmatic PSFs.

amount and direction of the rotation will indicate the axial position and can be used to build a calibration curve. With this technique an axial resolution of 20 nm over 2 µm has been achieved. In [109], instead, the axial encoding has been done by inserting a cylindrical lens in the imaging path to introduce astigmatism [134] (sec. 1.5) and generate an elongated PSF. In this case, when the emitter is in the focal plane, the PSF on the detector plane will appear circular (fig. 1.12b). If, instead, the emitter is located above or below it, the PSF will be elliptical and its size and orientation can be used to

build a pair of calibration curves and calculate the axial position. In this case an axial resolution of 50 nm over a range of 1 μm has been obtained. Both these solutions for axial superresolution are commercially available [135, 136].

A higher axial resolution has been reported by combining PALM and interferometric imaging in a technique called iPALM [137]. With iPALM the photon emission is collected by means of two opposite OLs and imaged on three detectors, where interference patterns are generated. The analysis of the images then gives the axial localisation of the emitter. iPALM has reached an axial resolution of 10 nm. The observable axial range is limited to around 250 nm with this method, due to the periodic aspect of the interference pattern [138]. However, by using hyperbolic mirrors in the setup and introducing astigmatism, the axial range of iPALM has been increased to around 750 nm [139]. This SMLMs have also been combined with MUM [140, 141, 142, 143, 144, 145] (sec. 1.3.9). This will be described more in detail in the 2nd chapter (sec. 2.3 and 2.4.5).

Another important technique that differs from SMLMs and can achieve superresolution is structured illumination microscopy (SIM) [146]. SIM exploits the fact that when a sample is illuminated with patterned illumination, it is possible to extract frequency information that is not normally accessible with a uniform illumination. In SIM the 2D illumination pattern is stripe-like (fig. 1.13a) and is generated by the interference of two laser beams produced by a diffraction grid [147]. In the Fourier domain, the set of spatial frequencies of an illuminated sample results from the convolution between the spatial frequencies in the sample (i.e. the Fourier transform of the PSF, also called optical transfer function, OTF [148, 149]) and in the illumination pattern. In the 2D Fourier space (k_x - k_y plane) the OTF is a circle, whose radius (k_0) is the reciprocal of $R_{x/y}$ (eq. 1.8) and is the highest frequency that can be observed in case of uniform illumination. The stripe-like pattern, instead, will present three spots, as the number of frequencies it contains, and those different from zero will lie at k_0. The convolution between these two patterns will extend the accessible frequencies, which are present in the interference pattern (i.e. the Moiré fringes [146]) due to the interference between sample and illumination frequencies. Then, by repeating this process for different orientations of the illumination pattern, the final frequency domain can be expanded in all directions to a maximum of $2k_0$, thus doubling the lateral resolution after a post-acquisition processing of the data. This technique can also be extended to the axial dimension with 3D-SIM, where three rather than two interfering beams are used to create a stripe-like illumination pattern over the volume of the sample

and a z-stack is needed (fig. 1.13b). SIM has reported lateral and axial resolutions of around 100 nm and 300 nm, respectively [131].

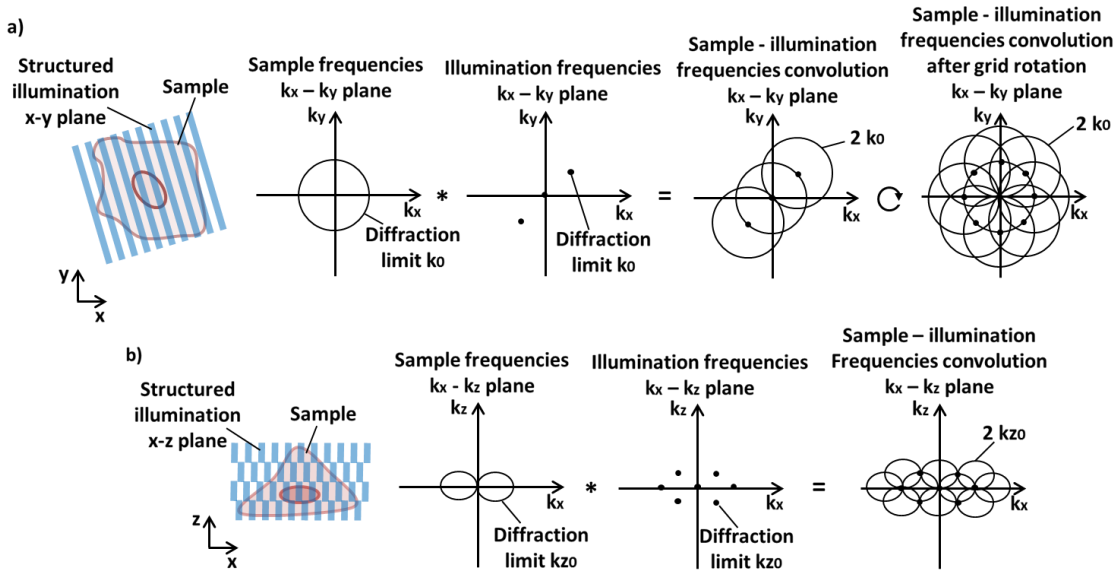

Figure 1.13 Lateral (**a**) an axial (**b**) SIM and its effect on the frequency domain.

Compared to SMLMs, SIM is faster in terms of data acquisition and processing [4], but it can at best only double the resolution limit. Laterally, the resolution can be improved with saturated SIM [150] (SSIM), which can reach a lateral resolution of 50 nm. In SSIM the laser power is increased to generate higher harmonics in the light source pattern and saturate the fluorophores to make them respond nonlinearly. This results in an increase in lateral resolution that, however, comes at the expenses of a higher photobleaching rate and longer data acquisition time. As for SMLMs, SIM has also been combined with MUM [151] (sec. 2.3.9).

Another important method to achieve superresolution is by exploiting a confocal microscope through a technique called stimulated emission depletion (STED) microscopy [152]. In STED a diffraction limited laser spot is used to excite the sample, while another doughnut-shaped laser, generated with a phase plate [153], is applied to reshape the excited area (fig. 1.14a). The reshaping is due to the fact that the doughnut-shaped laser, which presents a hole in the centre, de-excites the fluorophores located at the borders of the excited region, via stimulated emission depletion, hence the name of the technique. This can be done thanks to the fact that, by increasing the laser power of

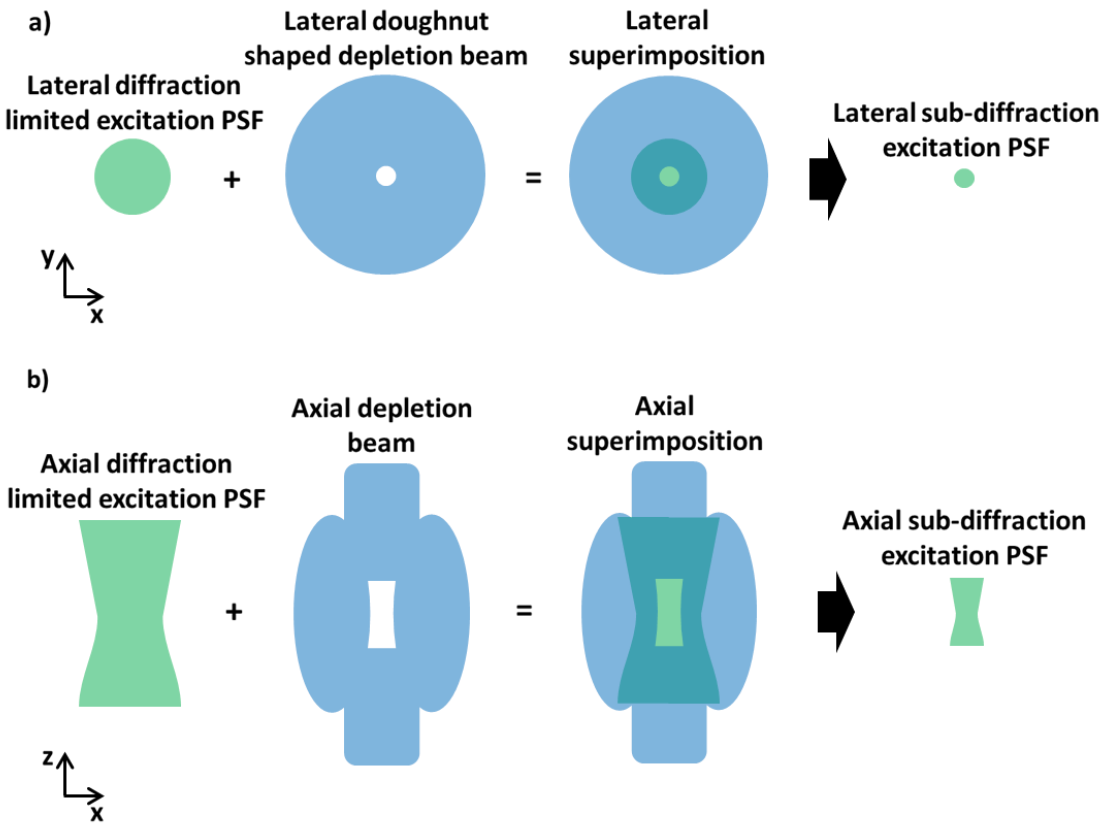

Figure 1.14 Lateral (**a**) an axial (**b**) excitation schemes in STED microscopy.

the depletion beam, the fluorophore stimulated emission will saturate and respond nonlinearly, thus leaving an undepleted spot that is smaller than the diffraction limit. With this approach (as with SSIM [150]), in theory, it is possible to get a resolution of few nanometres [152]. However, due to problems as fluorophore photostability and fluorescence signal intensity, in practice, it is limited in 2D to between 10 nm and 70 nm [5, 154]. By further engineering the depletion beam axially by combining STED with 4Pi microscopy (isoSTED [155]) or with other phase plates [156], the excited volume can be reduced also in the z direction, reaching axial resolutions around 30 nm [157] (fig. 1.14b).

1.4 Particle localisation and tracking

The images acquired with the different fluorescence microscopy techniques can be processed to reveal the spatio-temporal organisation of the fluorescently labelled molecules in the samples. In order to do this, it is first necessary to localise them. The process that takes to the localisation of the particles can be broken into some steps (fig. 1.15). The spots in the acquired images are not always easily detectable, due to the noise and the simultaneous presence of background structures (fig. 1.15a). Consequently,

many procedures [158] have a pre-filtering and thresholding stage that is applied to reduce the noise, remove the background and enhance the spot features (fig. 1.15b). Example of filters are Gaussian smoothing [159] and the Laplacian of Gaussian [160]. After this step, the images will be composed by clusters of bright pixels, which need to be grouped into individual spots. This is the classification/segmentation step [161, 162] (fig. 1.15c). Clusters of pixels whose sizes are different from the expected ones can be discarded during this stage. Finally, once the different spots have been found, these can be laterally localised (fig. 1.15d) by using, for example, algorithms as the centre of mass [163], curve fitting methods involving Gaussian [164] or Lorentzian [165] curves, etc. The described procedure can be expanded to z-stack data to obtain 3D localisations. Another method, instead [166], exploits Bayesian inference [167] to detect and localise spot features. In this algorithm, essentially, the probability of having a spot rather than a background or noise feature in the data is calculated, given two models to describe the spots and the background/noise structures present. This allows to segment the image

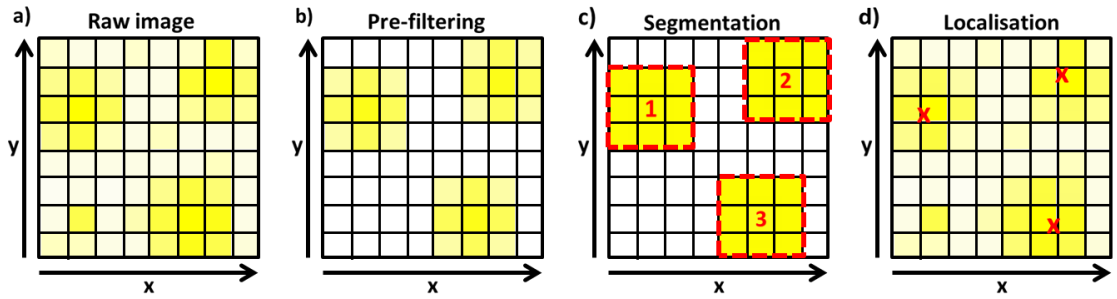

Figure 1.15 Scheme showing how single particle spots present in a raw acquired image (**a**), after the steps of filtering (**b**) and segmentation (**c**), can be localised (**d**).

and detect the spots. Then, by re-exploiting the Bayesian inference, the spots are localised by finding the most probable fitting parameters to perform Gaussian fitting.

Every time an emitter is localised, this is done with a certain degree of precision [168], which can be estimated by repeating the measurements a certain number of times. However, regardless of the type of unbiased algorithm (i.e. one that can reach the true values over a high number of measurements [168]) used to calculate the emitter positions, the best achievable precision with it is theoretically limited and, as mentioned in sec. 1.3.10, scales with the reciprocal of the square root of the number of collected photons [129, 130]. When this limit is derived from the Fisher information [169], which is a measure of the amount of information in a set of data on a certain parameter used to statistically describe the data themselves, it takes the name of Cramér-Rao lower bound (CRLB) [170]. Both lateral and axial CRLBs vary with the axial positions of the

emitters with respect to the imaged planes [171, 172, 173]. In [172], this has been studied for various 3D microscopy techniques, assuming as localisation algorithm a PSF fitting one [174] with the PSF based on the scalar diffraction theory [83]. In particular, for the simulations the pixelation effect [168] on the PSF and the Poisson noise [77] coming from both the emitter and the background were taken into account. In addition, as objective lens an oil immersion (n_{im} = 1.515) 1.45 NA one with magnification of 100x was assumed, together with a total number of collected photons of 4,000 per localisation and a background of 10 photons per pixel. The wavelength, instead, was set on 650 nm. To simulate the PSF geometry obtained with the different 3D microscopy techniques the simulation was also taking into account the use of the required phase masks [153]. The results in terms of axial range over which it is possible to obtain an axial precision within 10 nm obtained for 3D techniques as biplane (i.e. multiplane) microscopy [140], astigmatic [109] and double-helix PSF [133] are summarised in table 1.1, together with that achieved with single plane widefield microscopy [23]. As observable and expected, the single plane wide-field microscope is not capable of providing any axial range, due to the so called depth discrimination problem [175, 176]. Indeed, because of the axial symmetry of the PSF with respect to the imaged plane (in case of negligible aberrations [177, 178]), it is not possible to discriminate between images acquired below or above the latter. By moving to PSF

3D microscopy technique	**Axial range with axial precision ≤ 10 nm (μm)**
Single plane widefield microscopy	NA
Astigmatic PSF	1.6
Biplane microscopy	1.8
Double-helix PSF	2.1

Table 1.1 Axial range results with localisation precision ≤ 10 nm based on the CRLB criterion of the simulations presented in [172] in case of single plane widefield and biplane microscopies and astigmatic and double-helix PSF engineering techniques. Scalar diffraction model based PSF [83], M = 100x, NA = 1.45, n_{im} = 1.515, λ = 650 nm, 4,000 photons per localisation, 10 background photons per pixel. Plane spacing for biplane microscopy = 500 nm. Sagittal to tangential focal plane distance for astigmatic PSF = 800 nm.

engineering techniques as astigmatic [109] or double-helix [133] PSFs, this symmetry can be broken, leading to axial ranges of, respectively, 1.6 µm (setting a distance of 800 nm between the sagittal and the tangential planes) and 2.1 µm. Clearly and as anticipated in sec. 1.3.10 for the experimental data reported in [133], the double-helix PSF can achieve larger axial ranges than the astigmatic one, even though it is limited by a PSF rotation of 180° before it takes to ambiguous axial localisations [172]. Also the biplane technique, thanks to the fact the PSF is acquired with two planes simultaneously, can remove the axial ambiguity and provide a useful axial range of 1.8 µm (setting the plane spacing to 500 nm, with half of the total photons per each plane). The latter result, however, is highly depended on the particular MUM setup considered (chap. 2). The theoretical studies presented in [175, 176], indeed, indicates how the achievable axial range with a multifocal system also varies with the number of used planes as well as the spacing among them.

Once particles have been localised, there might be the necessity to track them. This could be useful, for example, to reconstruct trajectories and interactions among different molecules, reveal pathways or evaluate how the objects studied diffuse, etc. [163]. Tracking algorithms can generally be subdivided into deterministic and probabilistic approaches (fig. 1.16). The deterministic approach (fig. 1.16a), essentially, aims to link the different measured temporal positions of a particle (which do not correspond to the real positions due to the measurement errors [179]) to obtain a track, given a set expected displacement. Examples of deterministic methods are the local and the global nearest neighbour algorithms (LNN and GNN, respectively) [180, 181]. The deterministic approach is relatively simple and, hence, fast. However, it does not accounts for false localisations, which can be included in the tracks and reduce their accuracy [182]. The probabilistic approach, instead (fig. 1.16b), does not simply

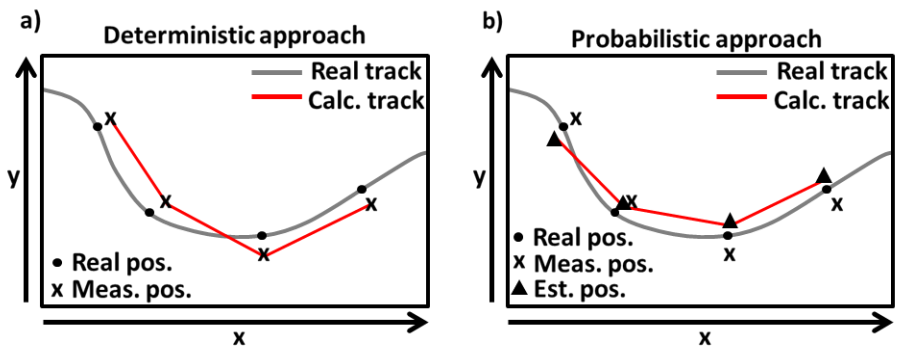

Figure 1.16 Representation of (**a**) the deterministic and (**b**) probabilistic approach in single particle tracking.

connect different temporal localisations. It attempts to estimate the true positions of the particle to build a track by making use of a set mathematical model for the motion and of the calculated localisations. This method, differently from the deterministic one, is able to limit the impact of false localisations, but it is also more computationally intense [183]. In addition, its tracking accuracy depends on the selection of the correct motion model. Example of probabilistic methods are the Kalman [184] and the bootstrap filters [185].

1.5 Aberrations in optical microscopy

In a perfect optical system the image of a point source would be a symmetric PSF such as that simulated in fig. 1.5b. From the point of view of ray optics, in such a situation all rays coming, for example, from infinity would be focused at the same point (fig. 1.17a) and the system would be defined as diffraction limited [186]. However, in real optical systems as microscopes there are deviations from this perfect behaviour and these are generally referred as aberrations [187]. Optical aberrations distort the PSF and, when not generated on purpose as explained in sec. 1.3.10, reduce resolution and contrast in acquired images, thus lowering, in turn, the accuracy on localisation and tracking of particles [188]. Consequently, optical microscopes (especially objective lenses [36]) are designed to counterbalance and minimise them under certain constrains (e.g. when the emitters are located within a certain distance from the coverslip glass) to produce nearly diffraction limited images. Some of the most common aberrations have been schematised in fig. 1.17. Defocus [189] (fig. 1.17a) is an aberration generated by the fact that the image is not formed in the imaged plane, since, for example, the object or the detector are not at the expected axial positions. In this case the image would appear blurred and broader than expected. Spherical aberration [190] (fig. 1.17b), instead, is due to the fact that not all light rays coming from a point source are imaged at the same point. This is caused, for example, by the fact that spherical surfaces do not have a single focal point, which, instead, varies with the distance from the o.a. of the incoming rays. Another important source, especially in microscopy, of spherical aberration is the presence of refractive index mismatches in the imaging path [78, 191, 192] (e.g. among sample, immersion medium and coverslip glass). Consequently, this could be reduced, for example, by matching the refractive index between sample and immersion medium (e.g. by using water immersion OLs with water based samples [36]) or between the coverslip glass and the immersion medium (e.g. with oil immersion OLs in TIRF

microscopy [91, 193]). If the observed object is not positioned on the o.a., another aberration termed coma might be introduced [194] (fig. 1.17c). With coma rays are not all focused at the same distance from the o.a., but, again, this varies with the distance from the o.a. of the incoming rays. Coma is an off-axis aberration and generates

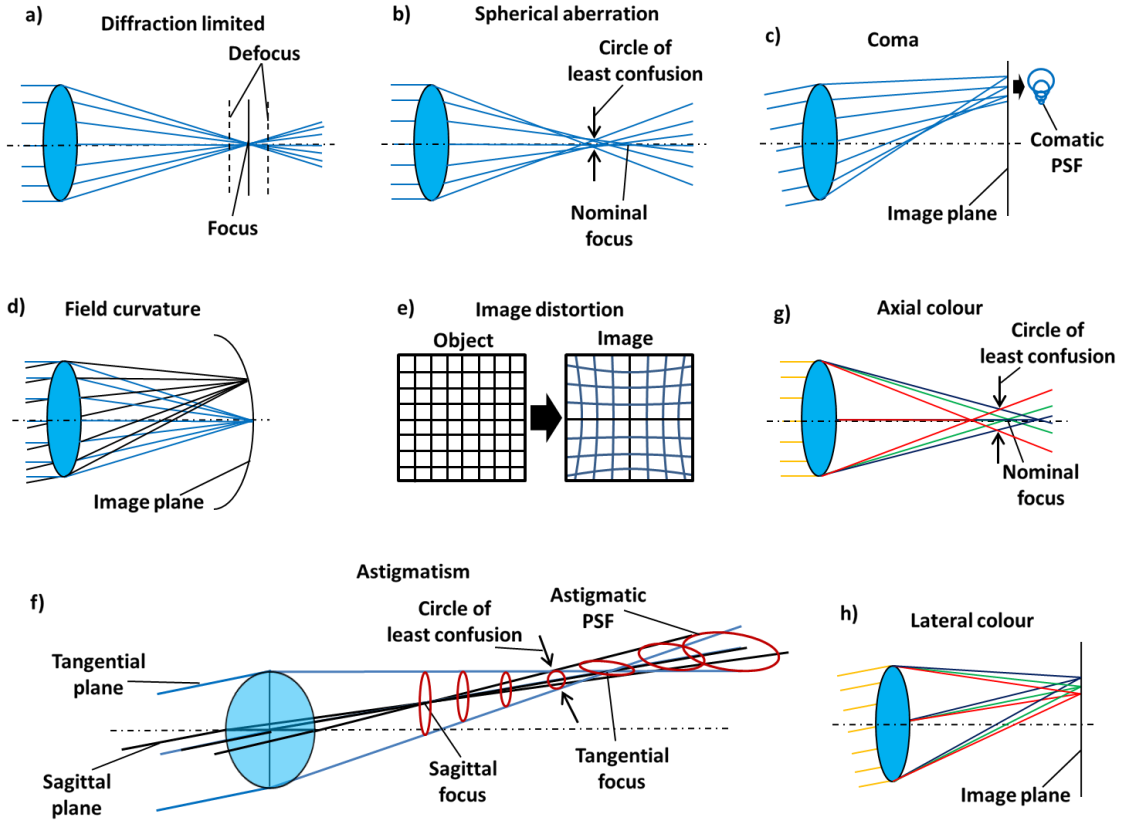

Figure 1.17 Schematic representation of some common aberrations in optical microscopy [187]. **a)** Diffraction limited imaging and defocus. **b)** Positive spherical aberration. **c)** Positive coma. **d)** Field curvature. **e)** Image distortion. **f)** Astigmatism. **g)** Axial colour. **h)** Lateral colour.

elongated comatic PSFs that are similar to comets, hence the name of the aberration. Other off-axis aberrations are the field curvature (fig. 1.17d) and image distortion [195] (fig. 1.17e). With field curvature the off-axis sources are focused at different focal distances than the on-axis one, thus the image plane is curved. With image distortion, instead, the magnification of the system varies from on-axis to off-axis positions, hence causing the distortion of the final image. Another important off-axis aberration is astigmatism [196] (fig. 1.17f). In presence of astigmatism the ray fan in the tangential plane (i.e. the plane that contains the o.a. and the central or chief ray of the system) is focused at a different position than the that in the sagittal plane (i.e. the plane perpendicular to the tangential one and that contains the chief ray). This deforms the PSF into elliptical and the size and orientation of the latter varies with its distance from

the best focal position, where the PSF is more circular. As explained in sec. 1.3.10 (fig. 1.12b), astigmatism can be introduced on purpose in microscope systems (by using cylindrical lenses [134]) to encode the axial positions of the emitters in the ellipticity of the PSF [109]. Aberrations in optical systems are also caused by the fact that the refractive index of materials varies with the wavelength of light [197], thus introducing chromatic smearing. Axial colour [198] (fig. 1.17g) is due to the fact that the focal length of the optical systems is a function of the refractive index [199], while, off-axis, lateral colour [198] (fig. 1.17h) causes the light of different wavelengths to be focused at different distances from the o.a. position. The best focal point that can be observed in presence of aberrations is the circle of least confusion [200], which represents the position where aberrations are minimised.

Apart from the aberration sources mentioned above, another important one in microscopy is the inhomogeneity of the refractive indices in the studied samples [201]. This can severely reduce the quality of images by introducing several aberrations and its effect increases by imaging deeper into specimens [201], thus reducing the 3D imaging abilities of microscopy techniques. To try to tackle this problem, during the last 20 years a technique called adaptive optics (AO) [202] (originally developed for applications in telescopy [201]) has been developed. Essentially, AO systems are designed to counterbalance the distortions in wavefronts caused by the aberrations via the application of equal and opposite distortions to them through, for example, deformable mirrors [203].

1.6 Summary and considerations

This chapter has presented light microscopy as a tool to investigate 3D biological samples and their dynamics [23, 24]. 3D imaging can be achieved via the acquisition of a z-stack [6] (fig. 1.4). However, in microscopes without optical sectioning abilities the images are degraded by the of out of focus light that reaches the detector and introduces background. This problem could be reduced by post-processing the acquired images via deconvolution microscopy [88] (sec. 1.3.5), even though some artefacts might be introduced [89]. Two important techniques able to reduce the out of focus background light and provide optical sectioning are confocal [93] (sec. 1.3.7) and light sheet [108] (sec. 1.3.8) microscopies. Confocal microscopy, however, is not a widefield technique and this limits its temporal resolution [6].

Apart from PSF engineering methods that are limited to short axial ranges [109, 132, 133] (fig. 1.12), the other 3D microscopy techniques presented cannot achieve full

4D imaging, since they can either image a single plane over time or acquire several planes at different axial positions and temporal instants. A technique that can achieve 4D imaging over extended axial ranges is multifocal/multiplane microscopy [8, 9, 10] (MUM, sec. 1.3.9), where several planes at different axial positions can be imaged simultaneously (fig. 1.10). MUM allows for instantaneous volumetric imaging over long axial ranges and, hence, provides access to fast and extended 3D dynamics [10]. MUM is central in this thesis. A particular MUM system developed by Dalgarno et al. [9] has been characterised from the point of view of its response to spherical aberration (chap. 3) and different levels of the signal (chap. 4) and has been applied to investigate the forces imposed by a fluid around a cell (chap. 5). Next chapter (chap. 2) will provide a description of the principal MUM setups and algorithms present in the literature.

1.7 References

[1] D. B. Murphy, "Fundamentals of light microscopy," in Fundamentals of light microscopy and electronic imaging, Wiley - Liss, 2001, pp. 1-16.

[2] D. B. Murphy, "Fluorescence microscopy," in Fundamentals of light microscopy and electronic imaging, Wiley - Liss, 2001, pp. 177-204.

[3] D. B. Murphy, "Diffraction and spatial resolution," in Fundamentals of light microscopy and electronic imaging, Wiley - Liss, 2001, pp. 85-96.

[4] A. G. Godin, B. Lounis and L. Cognet, "Super-resolution microscopy approaches for live cell imaging," Biophysical Journal, vol. 107, no. 8, pp. 1777-1784, 2014.

[5] M. Yamanaka, N. I. Smith and K. Fujita, "Introduction to super-resolution microscopy," Microscopy, vol. 63, no. 3, pp. 177-192, 2014.

[6] J. B. Pawley, "Comparison of widefield/deconvolution and confocal microscopy for three-dimensional imaging," in Handbook of Biological Confocal Microscopy, 3rd ed., Springer, 2006, pp. 453-467.

[7] O. E. Olarte, J. Andilla, E. J. Gualda and P. Loza-Alvarez, "Light-sheet microscopy: a tutorial," Advances in Optics and Photonics, vol. 10, no. 1, pp. 111-179, 2018.

[8] S. Abrahamsson, J. J. Chen, B. Hajj, S. Stallinga, A. Y. Katsov, J. Wisniewski, G. Mizuguchi, P. Soule, F. Mueller, C. D. Darzacq, X. Darzacq, C. Wu, C. I. Bargmann, D. A. Agard, M. Dahan and M. G. L. Gustafsson, "Fast multicolor 3D imaging using aberration-corrected multifocus microscopy," Nature Methods, vol.

10, no. 1, pp. 60-U80, 2013.

[9] P. A. Dalgarno, H. I. Dalgarno, A. Putoud, R. Lambert, L. Paterson, D. C. Logan, D. P. Towers, R. J. Warburton and A. H. Greenaway, "Multiplane imaging and three dimensional nanoscale particle tracking in biological microscopy," Optics express, vol. 18, no. 2, pp. 877-884, 2010.

[10] S. Ram, D. Kim, R. J. Ober and E. S. Ward, "3D single molecule tracking with multifocal plane microscopy reveals rapid intercellular transferrin transport at epithelial cell barriers," Biophysical Journal, vol. 103, no. 7, pp. 1594-1603, 2012.

[11] H. Lodish, A. Berk, C. A. Kaiser, M. Krieger, M. P. Scott, A. Bretscher, H. Ploegh and P. Matsudaira, Molecular cell biology, 6th ed., W. H. Freeman and Company, 2007.

[12] H. Lodish, A. Berk, C. A. Kaiser, M. Krieger, M. P. Scott, A. Bretscher, H. Ploegh and P. Matsudaira, "The work of cells," in Molecular cell biology, 6th ed., W. H. Freeman and Company, 2007, pp. 14-19.

[13] H. Lodish, A. Berk, C. A. Kaiser, M. Krieger, M. P. Scott, A. Bretscher, H. Ploegh and P. Matsudaira, "Organelles of the eukaryotic cell," in Molecular cell biology, 6th ed., W. H. Freeman and Company, 2007, pp. 372-379.

[14] H. Lodish, A. Berk, C. A. Kaiser, M. Krieger, M. P. Scott, A. Bretscher, H. Ploegh and P. Matsudaira, "Neurons and glia: Building blocks of the nervous system," in Molecular cell biology, 6th ed., W. H. Freeman and Company, 2007, pp. 1001-1005.

[15] H. Lodish, A. Berk, C. A. Kaiser, M. Krieger, M. P. Scott, A. Bretscher, H. Ploegh and P. Matsudaira, "Cell signaling I: Signal transduction and short-term cellular responses," in Molecular cell biology, 6th ed., W. H. Freeman and Company, 2007, pp. 623-664.

[16] H. Lodish, A. Berk, C. A. Kaiser, M. Krieger, M. P. Scott, A. Bretscher, H. Ploegh and P. Matsudaira, "Cell signalling II: Signaling pathways that control gene activity," in Molecular cell biology, 6th ed., W. H. Freeman and Company, 2007, pp. 665-712.

[17] H. Lodish, A. Berk, C. A. Kaiser, M. Krieger, M. P. Scott, A. Bretscher, H. Ploegh and P. Matsudaira, "Basic molecular genetic mechanisms," in Molecular cell biology, 6th ed., W. H. Freeman and Company, 2007, pp. 111-119.

[18] H. Lodish, A. Berk, C. A. Kaiser, M. Krieger, M. P. Scott, A. Bretscher, H.

Ploegh and P. Matsudaira, "Vesicular traffic, secretion and endocytosis," in Molecular cell biology, 6th ed., W. H. Freeman and Company, 2007, pp. 579-622.

[19] A. H. Futerman and G. v. Meer, "The cell biology of lysosomal storage disorders," Nature Reviews Molecular Cell Biology, vol. 5, no. 7, pp. 554-565, 2004.

[20] D. C. Rubinsztein, "The roles of intracellular protein-degradation pathways in neurodegeneration," Nature, vol. 443, no. 7113, pp. 780-786, 2006.

[21] Z. Gan, S. Ram, R. J. Ober and E. S. Ward, "Using multifocal plane microscopy to reveal novel trafficking processes in the recycling pathway," Journal of Cell Science, vol. 126, no. 5, pp. 1176-1188, 2013.

[22] D. B. Murphy, Fundamentals of light microscopy and electronic imaging, Wiley - Liss, 2001.

[23] D. J. Stephens and V. J. Allan, "Light microscopy techniques for live cell imaging," SCIENCE, vol. 300, no. 5616, pp. 82-86, 2003.

[24] M. Eisenstein, "Something to see," Nature, vol. 443, p. 1017–1021, 2006.

[25] D. B. Murphy, "Fundamentals of light microscopy," in Fundamentals of light microscopy and electronic imaging, Wiley - Liss, 2001, pp. 1-14.

[26] W. J. Croft, "Light and the ancient Greeks," in Under the Microscope: A brief history of microscopy, World Scientific, 2006, pp. 1-4.

[27] W. J. Croft, "Early microscopies," in Under the Microscope: A brief history of microscopy, World Scientific, 2006, pp. 5-10.

[28] R. Hooke, Micrographia: Or some physiological descriptions of minute bodies made by magnifying glasses. With observations and inquiries thereupon, Royal Society, 1665.

[29] W. J. Croft, "Early Microscopists," in Under the Microscope: A brief history of microscopy, World Scientific, 2006, pp. 11-14.

[30] E. Abbe, "Beiträge zur theorie des mikroskops und der mikroskopischen wahrnehmung," Archiv für Mikroskopische Anatomie, vol. 9, no. 1, p. 413–418, 1873.

[31] R. F. Egerton, Physical principles of electron microscopy: An introduction to TEM, SEM and AEM, Springer, 2008.

[32] P. C. Cheng and G. J. Jan, X-ray Microscopy: Instrumentation and biological applications, Springer -Verlag, 1987.

[33] D. Murphy, "Illuminators, filters, and isolation of specific wavelengths," in Fundamentals of light microscopy and electronic imaging, Wiley - Liss, 2001, pp. 29-42.

[34] D. B. Murphy, "Koehler illumination," in Fundamentals of light microscopy and electronic imaging, Wiley - Liss, 2001, pp. 6-11.

[35] D. B. Murphy, "Lenses and geometrical optics," in Fundamentals of light microscopy and electronic imaging, Wiley - Liss, 2001, pp. 43-60.

[36] M. Abramowitz, K. R. Spring, H. E. Keller and M. W. Davidson, "Basic principles of microscope objectives," Biotechniques, vol. 33, no. 4, pp. 772-+, 2002.

[37] F. A. Jenkins and H. E. White, "Focal points and principal points," in Fundamentals of optics, 4th ed., McGraw-Hill, 2001, pp. 81-82.

[38] M. W. Davidson and M. Abramowitz, "Optical microscopy," Encyclopedia of Imaging Science and Technology, 2002.

[39] J. E. Greivenkamp, "Longitudinal Magnification," in Field guide to geometrical optics, SPIE Press, 2004, p. 10.

[40] D. B. Murphy, Fundamentals of light microscopy and electronic imaging, Wiley-LISS, 2001.

[41] D. B. Murphy, "Phase contrast microscopy and dark-field microscopy," in Fundamentals of light microscopy and electronic imaging, Wley - Liss, 2001, pp. 97-116.

[42] J. A. Kiernan, Histological and histochemical methods: Theory and practice, 5th ed., Scion Publishing Limited, 2015.

[43] B. Valeur, Molecular Fluorescence: Principles and Applications, Wiley-VCH, 2001.

[44] H. Andersson, T. Baechi, M. Hoechl and C. Richter, "Autofluorescence of living cells," Journal of Microscopy - Oxford, vol. 191, p. 1–7, 1998.

[45] O. N. Shilova, E. S. Shilov and S. M. Deyev, "The effect of trypan blue treatment on autofluorescence of fixed cells," Cytometry Part A, vol. 91A, no. 9, pp. 917-925, 2017.

[46] M. Hasegawa, T. Shiina, M. Terazima and S. Kumazaki, "Selective Excitation of Photosystems in Chloroplasts Inside plant leaves observed by near-infrared laser-based fluorescence spectral microscopy," Plant and Cell Physiology, vol. 51, no.

2, pp. 225-238, 2010.

[47] B. Valeur, "Characteristics of fluorescence emission," in Molecular fluorescence: Principles and applications, Wiley-VCH, 2001, pp. 34-71.

[48] B. Valeur, "Internal conversion," in Molecular fluorescence: Principles and applications, Wiley-VCH, 2001, p. 37.

[49] B. Valeur, "Intersystem crossing," in Molecular Fluorescence: Principles and applications, Wiley-VCH, 2001, p. 41.

[50] T. Ha and P. Tinnefeld, "Photophysics of fluorescence probes for single molecule biophysics and super-resolution imaging," Annual Review of Physical Chemistry, vol. 63, p. 595–617, 2012.

[51] B. Valeur, "Phosphorescence versus non-radiative de-excitation," in Molecular fluorescence: Principles and applications, Wiley-VCH, 2001, p. 41.

[52] B. Valeur, "Quantum yields," in Molecular fluorescence: Principles and applications, Wiley-VCH, 2001, pp. 46-47.

[53] B. Valeur, "Emission spectra," in Molecular fluorescence: Principles and applications, Wiley-VCH, 2001, pp. 50-52.

[54] B. Valeur, "Excitation spectra," in Molecular fluorescence: Principles and applications, Wiley-VCH, 2001, pp. 53-54.

[55] B. Valeur, "Stokes shift," in Molecular fluorescence: Principles and applications, Wiley-VCH, 2001, p. 54.

[56] B. R. Masters, "The Development of fluorescence microscopy," Wiley Online Library, 2010.

[57] B. E. A. Saleh and M. C. Teich, "Beam optics," Wiley-Interscience, 2007, pp. 74-101.

[58] S. A. Schnell, W. A. Staines and M. W. Wessendorf, "Reduction of lipofuscin-like autofluorescence in fluorescently labeled tissue," Journal of Histochemistry & Cytochemistry, vol. 47, no. 6, pp. 719-730, 1999.

[59] C. H. A. Vandelest, E. M. M. Versteeg, J. H. Veerkamp and T. H. Vankuppevelt, "Elimination of autofluorescence in immunofluorescence microscopy with digital image-processing," Journal of Histochemistry & Cytochemistry, vol. 43, no. 7, pp. 727-730, 1995.

[60] M. Neumann and D. Gabel, "Simple method for reduction of autofluorescence in fluorescence microscopy," Journal of histochemistry & cytochemistry, vol. 50,

no. 3, pp. 437-439, 2002.

[61] H. Deschout, F. C. Zanacchi, M. Mlodzianoski, A. Diaspro, J. Bewersdorf, S. T. Hess and K. Braeckmans, "Precisely and accurately localizing single emitters in fluorescence microscopy," Nature Methods, vol. 11, no. 3, pp. 253-266, 2014.

[62] "ThermoFisher Scientific," [Online]. Available: https://www.thermofisher.com/it/en/home/life-science/cell-analysis/fluorophores/alexa-fluor-488.html. [Accessed September 2018].

[63] Y. Yarden and M. X. Sliwkowski, "Untangling the ErbB signalling network," Nature Reviews Molecular Cell Biology, vol. 2, no. 2, pp. 127-137, 2001.

[64] "ThermoFisher Scientific," [Online]. Available: https://www.thermofisher.com/order/catalog/product/V22887. [Accessed September 2018].

[65] T. Scientific, "Probes for Lipids and Membranes," in The molecular probes handbook, 11th ed., Invitrogen, 2010, pp. 547-587.

[66] W. J. Parak, T. Pellegrino and C. Plank, "Labelling of cells with quantum dots," Nanotechnology, vol. 16, no. 2, pp. R9-R25, 2005.

[67] J. D. Plautz, R. N. Day, G. M. Dailey, S. B. Welsh, J. C. Hall, S. Halpain and S. A. Kay, "Green fluorescent protein and its derivatives as versatile markers for gene expression in living Drosophila melanogaster, plant and mammalian cells," Gene, vol. 173, no. 1, pp. 83-87, 1996.

[68] D. J. Webb and C. M. Brown, "Epi-fluorescence microscopy," Methods in Molecular Biology, vol. 931, p. 29–59, 2013.

[69] J. Zheng, K. Payne, J. E. Taggart, H. C. Jiang, S. E. Lind and W. Q. Ding, "Trolox enhances curcumin's cytotoxicity through induction of oxidative stress," Cellular Physiology and Biochemistry, vol. 29, no. 3-4, pp. 353-360, 2012.

[70] D. Baddeley, D. Crossman, S. Rossberger, J. E. Cheyne, J. M. Montgomery, I. D. Jayasinghe, C. Cremer, M. B. Cannell and C. Soeller, "4D super-resolution microscopy with conventional fluorophores and single wavelength excitation in optically thick cells and tissues," Plos One, vol. 6, no. 5, 2011.

[71] S. C. Bhakdi and P. Thaicharoen, "Easy employment and crosstalk-free detection of seven fluorophores in a widefield fluorescence microscope," Methods and protocols, vol. 1, no. 2, 2018.

[72] K. W. Dunn, K. S. Lorenz, P. Salama and E. J. Delp, "IMART software for

correction of motion artifacts in images collected in intravital microscopy," IntraVital, vol. 3, no. 1, 2014.

[73] D. R. Sandison and W. W. Webb, "Background rejection and signal-to-noise optimization in confocal and alternative fluorescence microscopes," applied optics, vol. 33, no. 4, pp. 603-615, 1994.

[74] P. Mondal and A. Diaspro, "System point spread function and image formation," in Fundamentals of Fluorescence Microscopy: Exploring Life with Light, Springer, 2014, pp. 56-57.

[75] H. Köhler, "On Abbe's Theory of image formation," Optica Acta: International Journal of Optics, vol. 28, no. 12, pp. 1691-1701, 1981.

[76] M. Hirsch, R. J. Wareham, M. L. Martin-Fernandez, M. P. Hobson and D. J. Rolfe, "A stochastic model for electron multiplication charge-coupled devices - From theory to practice," Plos One, vol. 8, no. 1, p. e53671, 2013.

[77] D. Dussault and P. Hoess, "Noise performance comparison of ICCD with CCD and EMCCD cameras," Infrared Systems and Photelectronic Technology, vol. 5563, pp. 195-204, 2004.

[78] S. F. Gibson and F. Lanni, "Experimental test of an analytical model of aberration in an oil-immersion objective lens used in 3-dimensional light-microscopy," Journal Of The Optical Society Of America A - Optics Image Science and Vision, vol. 8, no. 10, pp. 1601-1613, 1991.

[79] ImageJ, [Online]. Available: https://imagej.nih.gov/ij/index.html. [Accessed September 2018].

[80] "PSF Generator," [Online]. Available: http://bigwww.epfl.ch/algorithms/psfgenerator/. [Accessed September 2018].

[81] M. Born and E. Wolf, "The distribution of intensity," in Principles of optics: Electromagnetic theory of propagation, interference and diffraction of light, 7th exp. ed., Cambridge University Press, 2003, pp. 489-492.

[82] B. G. Korenev, Bessel functions and their applications, Taylor & Francis, 2002.

[83] M. Born and E. Wolf, "Elements of the theory of diffraction," in Principles of optics: Electromagnetic theory of propagation, interference and diffraction of light, 7th exp. ed., Cambridge University Press, 2003, pp. 412-516.

[84] A. J. Lacey, "Numerical data extraction," in Light Microscopy in Biology: A Practical Approach, 2nd ed., Oxtord University Press, 1999, pp. 256-257.

[85] R. Heintzmann and G. Ficz, "Breaking the resolution limit in light microscopy," Briefings in functional genomics and proteomics, vol. 5, no. 4, pp. 289-301, 2006.

[86] H. Zimmermann, "Active-pixel sensors," in Integrated silicon optoelectronics, 2nd ed., Springer, 2010, pp. 104-114.

[87] J. B. Pawley, "Points, pixels, and gray levels: digitizing image data," in Handbook of biological confocal microscopy, 3rd ed., Springer, 2006, pp. 59-79.

[88] D. S. C. Biggs, "3D deconvolution microscopy," Current Protocols in Cytometry, vol. 52, no. 1, pp. 12.19.1-12.19.20, 2010.

[89] J. G. McNally, T. Karpova, J. Cooper and J. A. Conchello, "Three-dimensional imaging by deconvolution microscopy," Methods - A Companion to Methods in Enzymology, vol. 19, no. 3, pp. 373-385, 1999.

[90] D. Axelrod, "Total internal reflection fluorescence microscopy in cell biology," Traffic, vol. 2, no. 11, p. 764–774, 2001.

[91] K. N. Fish, "Total internal reflection fluorescence (TIRF) microscopy," Current Protocols in Cytometry, vol. 50, no. 1, pp. 12.18.1-12.18.13, 2009.

[92] M. Martin-Fernandez, C. Tynan And S. E. D. Webb, "A 'pocket guide' to total internal reflection fluorescence," Journal of Microscopy, vol. 252, no. 1, p. 16–22, 2013.

[93] J. B. Pawley, Handbook of biological confocal microscopy, Springer, 2006.

[94] J. B. Pawley, "Confocal laser-scanning microscope," in Handbook of biological confocal microscopy, 3rd ed., Springer, 2006, pp. 9-10.

[95] D. B. Pawley, "Photon detectors for confocal microscopy," in Handbook of biological confocal microscopy, 3rd ed., Springer, 2006, pp. 251-262.

[96] V. Foltánková, P. Matula, D. Sorokin and S. Kozubek, "Hybrid Detectors Improved Time-Lapse Confocal Microscopy of PML and 53BP1 nuclear body colocalization in DNA lesions," Microscopy and Microanalysis, vol. 19, no. 2, pp. 360-369, 2013.

[97] J. R. Janesick, Scientific charge-coupled devices, Spie Press, 2001.

[98] F. Long, S. Zeng and Z. L. Huang, "Localization-based super-resolution microscopy with an sCMOS camera Part II: Experimental methodology for comparing sCMOS with EMCCD cameras," Optics Express, vol. 20, no. 16, pp. 17741-17759, 2012.

[99] J. W. Borst and A. J. W. G. Visser, "Fluorescence lifetime imaging microscopy in

life sciences," Measurement Science and Technology, vol. 21, no. 10, 2010.

[100] D. B. Murphy, "Confocal laser scanning," in Fundamentals of light microscopy and electronic imaging, Wiley - Liss, 2001, pp. 205-232.

[101] T. WILSON, "Resolution and optical sectioning in the confocal microscope," Journal of Microscopy, vol. 244, no. 2, p. 113–121, 2011.

[102] J. B. Pawley, "A need for speed and less photobleaching," in Handbook of biological confocal microscopy, 3rd ed., Springer, 2006, p. 222.

[103] J. B. Pawley, "Disk-Scanning Confocal Microscopy," in Handbook of biological confocal microscopy, 3rd ed., Springer, 2006, pp. 221-238.

[104] "Yokogawa Electric," [Online]. Available: https://www.yokogawa.com/solutions/products-platforms/life-science/spinning-disk-confocal/. [Accessed September 2018].

[105] J. Jonkman and C. M. Brown, "Any Way You Slice It - A comparison of confocal microscopy techniques," Journal of Biomolecular Techniques, vol. 26, no. 2, pp. 54-65, 2015.

[106] E. E. Hoover and J. A. Squier, "Advances in multiphoton microscopy technology," Nature Photonics, vol. 7, no. 2, pp. 93-101, 2013.

[107] J. B. Pawley, "4Pi Microscopy," in Handbook of biological confocal microscopy, 3rd ed., Springer, 2006, pp. 561-570.

[108] P. A. Santi, "Light sheet fluorescence microscopy: A review," Journal of Histochemistry & Cytochemistry, vol. 59, no. 2, pp. 129-138, 2011.

[109] B. Huang, W. Wang, M. Bates and X. Zhuang, "Three-dimensional super-resolution imaging by stochastic optical reconstruction microscopy," Science, vol. 319, no. 5864, pp. 810-813, 2008.

[110] P. J. Verveer, J. Swoger, F. Pampaloni, K. G. M. Marcello and E. H. K. Stelzer, "High-resolution three-dimensional imaging of large specimens with light sheet-based microscopy," Nature Methods, vol. 4, no. 4, p. 311–313, 2007.

[111] J. Icha, M. Weber, J. C. Waters and C. Norden, "Phototoxicity in live fluorescence microscopy, and how to avoid it," BioEssays, vol. 39, no. 8, 2017.

[112] B. Berthet and A. Maizel, "Light sheet microscopy and live imaging of plants," Journal of Microscopy, vol. 263, no. 2, p. 158–164, 2016.

[113] Z. Lavagnino, F. C. Zanacchi, E. Ronzitti and A. Diaspro, "Two-photon excitation selective plane illumination microscopy (2PE-SPIM) of highly

scattering samples: characterization and application," Optics Express, vol. 21, no. 5, pp. 5998-6008, 2013.

[114] T. A. Planchon, L. Gao, D. E. Milkie, M. W. Davidson, J. A. Galbraith, C. G. Galbraith and E. Betzig, "Rapid three-dimensional isotropic imaging of living cells using bessel beam plane illumination," Nature methods, vol. 8, no. 5, pp. 417-423, 2011.

[115] T. Vettenburg, H. I. C. Dalgarno, J. Nylk, C. Coll-Llado, D. E. K. Ferrier, T. Cizmar, F. J. Gunn-Moore and K. Dholakia, "Light-sheet microscopy using an airy beam," Nature methods, vol. 11, no. 5, pp. 541-544, 2014.

[116] J. Durnin, J. J. Miceli and J. H. Eberly, "Diffraction-Free Beams," Physical Review Letters, vol. 58, no. 15, p. 1499–1501, 1987.

[117] S. Abrahamsson, M. McQuilken, S. B. Mehta, A. Verma, J. Larsch, R. H. R. Ilic, C. I. Bargmann, A. S. Gladfelter and R. Oldenbourg, "MultiFocus Polarization Microscope (MF-PolScope) for 3D polarization imaging of up to 25 focal planes simultaneously," Optics Express, vol. 23, no. 6, pp. 7734-7754, 2015.

[118] S. W. Hell, S. J. Sahl, M. Bates, X. Zhuang, R. Heintzmann, M. J. Booth, J. Bewersdorf, G. Shtengel, H. Hess, P. Tinnefeld, A. Honigmann, S. Jakobs, I. Testa, L. Cognet, B. Lounis, H. Ewers, S. J. Davis, C. Eggeling, D. Klenerman, K. I. Willig, G. Vicidomini, M. Castello, A. Diaspro and T. Cordes, "The 2015 super-resolution microscopy roadmap," Journal of Physics D: Applied Physics, vol. 48, no. 44, 2015.

[119] R. V. Noorden, "Insider view of cells scoops Nobel," Nature, vol. 514, no. 7522, pp. 286-286, 2014.

[120] J. R. Allen, S. T. Ross and M. W. Davidson, "Single molecule localization microscopy for superresolution," Journal of Optics, vol. 15, no. 9, 2013.

[121] E. Betzig, G. H. Patterson, R. Sougrat, W. Lindwasser, S. Olenych, J. S. Bonifacino, M. W. Davidson, J. Lippincott-Schwartz and H. F. Hess, "Imaging intracellular fluorescent proteins at nanometer resolution," Science, vol. 313, no. 5793, p. 1642–1645, 2006.

[122] M. Rust, M. Bates and X. Zhuang, "Sub-diffraction-limit imaging by stochastic optical reconstruction microscopy (STORM)," Nature Methods, vol. 3, no. 10, p. 793–796, 2006.

[123] M. Heilemann, S. v. d. Linde, M. Schüttpelz, R. Kasper, B. Seefeldt, A.

Mukherjee, P. Tinnefeld and M. Sauer, "Subdiffraction-resolution fluorescence imaging with conventional fluorescent probes," Angewandte Chemie International Edition in English, vol. 47, no. 33, p. 6172–6, 2008.

[124] J. Folling, M. Bossi, H. Bock, R. Medda, C. A. Wurm, B. Hein, S. Jakobs, C. Eggeling and S. W. Hell, "Fluorescence nanoscopy by ground-state depletion and single-molecule return," Nature Methods, vol. 5, no. 11, pp. 943-945, 2008.

[125] X. X. Zhou and M. Z. Lin, "Photoswitchable fluorescent proteins: Ten years of colorful chemistry and exciting applications," Current Opinion in Chemical Biology, vol. 17, no. 4, p. 682–690, 2013.

[126] M. J. Mlodzianoski, J. M. Schreiner, S. P. Callahan, K. Smolkova, A. Dlaskova, J. Santorova, P. Jezek and J. Bewersdorf, "Sample drift correction in 3D fluorescence photoactivation localization microscopy," Optics Express, vol. 19, no. 16, pp. 15009-15019, 2011.

[127] D. Toomre and J. Bewersdorf, "A new wave of cellular imaging," Annual Review of Cell and Developmental Biology, vol. 26, pp. 285-314, 2010.

[128] L. Schermelleh, R. Heintzmann and H. Leonhardt, "A guide to super-resolution fluorescence microscopy," Journal of Cell Biology, vol. 190, no. 2, 2010.

[129] S. T. Hess, T. P. Giriajan and M. D. Mason, "Ultra-high resolution imaging by fluorescence photoactivation localization microscopy," Biophysical Journal, vol. 91, no. 11, p. 4258–4272, 2006.

[130] R. E. Thompson, D. R. Larson and W. W. Webb, "Precise nanometer localization analysis for individual," Biophysical Journal, vol. 82, no. 5, p. 2775–2783, 2002.

[131] M. Yamanaka, N. I. Smith and K. Fujita, "Introduction to super-resolution microscopy," Microscopy, vol. 63, no. 3, p. 177–192, 2014.

[132] Y. Shechtman, L. E. Weiss, A. S. Backer, S. J. Sahl and W. E. Moemer, "Precise three-dimensional scan-free multiple-particle tracking over large axial ranges with tetrapod point spread functions," Nano Letters, vol. 15, no. 6, pp. 4194-4199, 2015.

[133] S. R. P. Pavani, M. A. Thompson, J. S. Biteen, S. J. Lord, N. Liu, R. J. Twieg, R. Piestun and W. E. Moerner, "Three-dimensional, single-molecule fluorescence imaging beyond the diffraction limit by using a double-helix point spread function," PNAS, vol. 106, no. 9, pp. 2995-2999, 2009.

[134] D. Malacara, "Testing of cylindrical surfaces," in Optical shop testing, 3rd ed.,

Wiley-Interscience, 2007, pp. 453-454.

[135] "Zeiss Elyra PS.1," [Online]. Available: https://www.zeiss.com/microscopy/int/products/superresolution-microscopy.html. [Accessed September 2018].

[136] "Leica SR GSD 3D," [Online]. Available: https://www.leica-microsystems.com/products/light-microscopes/inverted-microscopes/details/product/leica-sr-gsd-3d/. [Accessed September 2018].

[137] G. Shtengel, J. A. Galbraith, C. G. Galbraith, J. Lippincott-Schwartz, J. M. Gillette, S. Manley, R. Sougrat, C. M. Waterman, P. Kanchanawong, M. W. Davidson, R. D. Fetter and H. F. Hess, "Interferometric fluorescent super-resolution microscopy resolves 3D cellular ultrastructure," Proceedings of the National Academy of Sciences of the United States of America, vol. 106, no. 9, pp. 3125-3130, 2009.

[138] J. C. Waters and T. Wittmann, "Extending iPALM imaging depth with astigmatic," in Methods in Cell Biology - Quantitative Imaging in Cell Biology, Vol. 123, Elsevier, 2014, p. 290.

[139] T. A. Brown, A. N. Tkachuk, G, Shtengel, B. G. Kopek, D. F. Bogenhagen, H. F. Hess and D. A. Clayton, "Superresolution fluorescence imaging of mitochondrial nucleoids reveals their spatial range, limits, and membrane interaction," Molecular and Cellular Biology, vol. 31, no. 24, pp. 4994-5010, 2011.

[140] M. F. Juette, T. J. Gould, M. D. Lessard, M. J. Mlodzianoski, B. S. Nagpure, B. T. Bennett, S. T. Hess and J. Bewersdorf, "Three-dimensional sub-100 nm resolution fluorescence microscopy of thick samples," Nature Methods, vol. 5, no. 6, pp. 527-529, 2008.

[141] J. Huang, M. Sun, K. Gumpper, Y. Chi and J. Ma, "3D multifocus astigmatism and compressed sensing (3D MACS) based superresolution reconstruction," Biomedical Optics Express, vol. 6, no. 3, pp. 902-917, 2015.

[142] J. Min, S. J. Holden, L. Carlini, M. Unser, S. Manley and J. C. Ye, "3D high-density localization microscopy using hybrid astigmatic/biplane imaging and sparse image reconstruction," Biomedical Optics Express, vol. 5, no. 11, pp. 3935-3948, 2014.

[143] S. Geissbuehler, A. Sharipov, A. Godinat, N. L. Bocchio, P. A. Sandoz, A. Huss, N. A. Jensen, S. Jakobs, J. Enderlein, F. G. v. d. Goot, E. A. Dubikovskaya, T.

Lasser and M. Leutenegger, "Live-cell multiplane three-dimensional super-resolution optical fluctuation imaging," Nature Communications, vol. 5, no. 5830, 2014.

[144] B. Hajj, J. Wisniewski, M. E. Beheiry, J. Chen, A. Revyakin, C. Wu and M. Dahan, "Whole-cell, multicolor superresolution imaging using volumetric multifocus microscopy," Proceedings of the National Academy of Sciences of the United States of America, vol. 11, no. 49, pp. 17480-17485, 2014.

[145] L. Oudjedi, J. B. Fiche, S. Abrahamsson, L. Mazenq, A. Lecestre, P. F. Calmon, A. Cerf and M. Nöllmann, "Astigmatic multifocus microscopy enables deep 3D super-resolved imaging," Biomedical Optics Express, vol. 7, no. 6, pp. 2163-2173, 2016.

[146] M. G. L. Gustafsson, "Surpassing the lateral resolution limit by a factor of two using structured illumination microscopy," Journal of Microscopy, vol. 198, p. 82–87, 2000.

[147] C. Palmer and E. Loewen, Diffraction grating handbook, 6th ed., Newport Corporation, 2005.

[148] J. W. Goodman, "Frequency response for diffraction-limited incoherent imaging," in Introduction to Fourier Optics, 2nd ed., McGraw-Hill, 1996, pp. 137-144.

[149] M. R. Arnison and C. J. R. Sheppard, "A 3D vectorial optical transfer function suitable for arbitrary pupil functions," Optics Communications, vol. 211, no. 1-6, pp. 53-63, 2002.

[150] M. G. L. Gustafsson, "Nonlinear structured-illumination microscopy: Wide-field fluorescence imaging with theoretically unlimited resolution," Proceedings of the National Academy of Sciences of the United States of America, vol. 102, no. 37, pp. 13081-13086, 2005.

[151] S. Abrahamsson, H. Blom, A. Agostinho, D. C. Jans, A. Jost, M. Müller, L. Nilsson, K. Bernhem, T. J. Lambert, R. Heintzmann and H. Brismar, "Multifocus structured illumination microscopy for fast volumetric super-resolution imaging," Biomedical Optics Express, vol. 8, no. 9, pp. 4135-4140, 2017.

[152] S. W. Hell and J. Wichmann, "Breaking the diffraction resolution limit by stimulated-emission - stimulated-emission-depletion fluorescence microscopy," Optics Letters, vol. 19, no. 11, pp. 780-782, 1994.

[153] J. W. Goodman, Introduction to Fourier Optics, 2nd ed., McGraw-Hill, 1996.

[154] S. Arroyo-Camejo, M. P. Adam, M. Besbes, J. P. Hugonin, V. Jacques, J. J. Greffet, J. F. Roch, S. W. Hell and F. Treussart, "Stimulated emission depletion microscopy resolves individual nitrogen vacancy centers in diamond nanocrystals," ACS Nano, vol. 7, no. 12, pp. 10912-10919, 2013.

[155] R. Schmidt, C. A. Wurm, S. Jakobs, J. Engelhardt, A. Egner and S. W. Hell, "Spherical nanosized focal spot unravels the interior of cells," Nature Methods, vol. 5, no. 6, pp. 539-544, 2008.

[156] T. A. Klar, S. Jakobs, M. Dyba, A. Egner and S. W. Hell, "Fluorescence microscopy with diffraction resolution barrier broken by stimulated emission," Proceedings of the National Academy of Sciences of the United States of America, vol. 97, no. 15, pp. 8206-8210, 2000.

[157] M. Maglione and S. J. Sigrist, "Seeing the forest tree by tree: super-resolution light microscopy meets the neurosciences," Nature Neuroscience, vol. 16, no. 7, pp. 790-797, 2013.

[158] I. Smal, M. Loog, W. Niessen and E. Meijering, "Quantitative comparison of spot detection methods in fluorescence microscopy," IEEE Transactions on Medical Imaging, vol. 29, no. 2, pp. 282-301, 2010.

[159] D. Thomann, D. R. Rines, P. K. Sorger and G. Danuser, "Automatic fluorescent tag detection in 3D with super-resolution: Application to the analysis of chromosome movement," Journal of Microscopy - Oxford, vol. 208, no. 1, pp. 49-64, 2002.

[160] D. Sage, F. R. Neumann, F. Hediger, S. M. Gasser and M. Unser, "Automatic tracking of individual fluorescence particles: Application to the study of chromosome dynamics," IEEE Transactions on Image Processing, vol. 14, no. 9, pp. 1372-1383, 2005.

[161] A. Genovesio, T. Liedl, V. Emiliani, W. J. Parak, M. Coppey-Moisan and J. C. Olivo-Marin, "Multiple particle tracking in 3-D+t microscopy: Method and application to the tracking of endocytosed quantum dots," IEEE Transactions on Image Processing, vol. 15, no. 5, pp. 1062-1070, 2006.

[162] W. J. Godinez, M. Lampe, S. Worz, B. Muller, R. Eils and K. Rohr, "Deterministic and probabilistic approaches for tracking virus particles in time-lapse fluorescence microscopy image sequences," Medical Image Analysis, vol. 13, no. 2, pp. 325-342, 2009.

[163] M. K. Cheezum, W. F. Walker and W. H. Guilford, " Quantitative comparison of algorithms for tracking," Biophysical Journal, vol. 81, no. 4, p. 2378–2388, 2001.

[164] B. Zhang, J. Zerubia and J. C. Olivo-Marin, "Gaussian approximations of fluorescence microscope point-spread function models," Applied Optics, vol. 46, no. 10, pp. 1819-1829, 2007.

[165] S. Stallinga, "Single emitter localization analysis in the presence of background," Optical Systems Design 2015: Computational Optics, vol. 9630, 2015.

[166] D. J. Rolfe, C. I. McLachlan, M. Hirsch, S. R. Needham, C. J. Tynan, S. E. D. Webb, M. L. Martin-Fernandez and M. P. Hobson, "Automated multidimensional single molecule fluorescence microscopy feature detection and tracking," European Biophysics Journal with Biophysics Letters, vol. 40, no. 10, pp. 1167-1186, 2011.

[167] J. M. Marin and C. P. Robert, Bayesian core: A practical approach to computational Bayesian statistics, Springer, 2007.

[168] R. J. Ober, S. Ram and E. S. Wardyz, "Localization accuracy in single-molecule microscopy," Biophysical Journal, vol. 86, no. 2, pp. 1185-1200, 2004.

[169] E. L. Lehmann and G. Casella, "The information inequality," in Theory of Point Estimation, 2nd ed., Springer-Verlag, 1998, pp. 113-123.

[170] S. M. Kay, "Cramér-Rao Lower Bound," in Fundamentals of statistical signal processing: Estimation theory, Prentice Hall PTR, 1993, pp. 27-77.

[171] S. Ram, E. S. Ward and R. J. Ober, "How accurately can a single molecule be localized in three dimensions using a fluorescence microscope?," Proceedings of SPIE, vol. 5699, p. 426–435, 2005.

[172] Y. Zhou, M. Handley, G. Carles and A. R. Harvey, "Advances in 3D single particle localization microscopy," APL Photonics, vol. 4, no. 6, pp. 1-17, 2019.

[173] H. I. C. Dalgarno, P. A. Dalgarno, A. C. Dada, C. E. Towers, G. J. Gibson, R. M. Parton, I. Davis, R. J. Warburton and A. H. Greenaway, "Nanometric depth resolution from multi-focal images in microscopy," Journal of the Royal Society Interface, vol. 8, no. 60, pp. 942-951, 2011.

[174] J. Chao, E. S. Ward and R. J. Ober, "Fisher information theory for parameter estimation in single molecule microscopy: tutorial," Journal of the Optical Society of America A, vol. 33, no. 7, pp. B36-B57, 2016.

[175] A. Tahmasbi, S. Ram, J. Chao, A. V. Abraham, F. W. Tang, E. S. Ward and R.

Ober, "Designing the focal plane spacing for multifocal plane microscopy," Optics Express, vol. 22, no. 14, pp. 16706-16721, 2014.

[176] A. Tahmasbi, S. Ram, J. Chao, A. V. Abraham, E. S. Ward and R. Ober, "An information-theoretic approach to designing the plane spacing for multifocal plane microscopy," Three-Dimensional and Multidimensional Microscopy: Image Acquisition and Processing XXII, vol. 9330, no. 933011, 2015.

[177] D. G. Abdelsalam and M. Stanislas, "Spherical aberration measurement of a microscope objective by use of calibrated spherical particles," Applied Optics, vol. 56, no. 16, pp. 4766-4771, 2017.

[178] F. A. Jenkins and H. E. White, "Spherical aberration of a thin lens," in Fundamentals of optics, 4th ed., McGraw-Hill Higher Education, 2001, pp. 153-157.

[179] M. Reuss, F. Fördős, H. Blom, O. Öktem, B. Högberg and H. Brismar, "Measuring true localization accuracy in super resolution microscopy with DNA-origami nanostructures," New Journal of Physics, vol. 19, 2017.

[180] H. Qian, M. P. Sheetz and E. L. Elson, "Single particle tracking. Analysis of diffusion and flow in two-dimensional systems," Biophysical Journal, vol. 60, no. 4, p. 910–921, 1991.

[181] I. F. Sbalzarini and P. Koumoutsakos, "Feature point tracking and trajectory analysis for video imaging in cell biology," Journal of Structural Biology, vol. 151, no. 2, pp. 182-195, 2005.

[182] W. J. Godinez, M. Lampe, S. Worz, B. Muller, R. Eils and K. Rohr, "Deterministic and probabilistic approaches for tracking virus particles in time-lapse fluorescence microscopy image sequences," Medical Image Analysis, vol. 13, no. 2, pp. 325-342, 2009.

[183] I. Smal, W. Niessen and E. Meijering, "Advanced particle filtering for multiple object tracking in dynamic fluorescence microscopy images," 2007 4TH IEEE International Symposium on Biomedical Imaging: Macro to Nano, Vols. 1-3, pp. 1048-1051, 2007.

[184] R. E. Kalman and R. S. Bucy, "New results in linear filtering and prediction theory," Journal of Basic Engineering, vol. 83, no. 1, pp. 95-108, 1961.

[185] N. J. Gordon, D. J. Salmond and A. F. M. Smith, "Novel approach to nonlinear non-gaussian bayesian state estimation," IEE Proceedings of Radar and Signal

Processing, vol. 140, no. 2, pp. 107-113, 1993.

[186] J. M. Geary, Introduction to lens design, Willmann-Bell, Inc., 2002.

[187] J. M. Geary, "Aberrations in General," in Introduction to lens design, Willmann-Bell, Inc., 2002, pp. 65-84.

[188] B. C. Coles, S. E. D. Webb, N. Schwartz, D. J. Rolfe, M. Martin-Fernandez and V. L. Schiavo, "Characterisation of the effects of optical aberrations in single molecule techniques," Biomedical Optics Express, vol. 7, no. 5, pp. 1755-1767, 2016.

[189] J. M. Geary, "Defocus," in Introduction to lens design, Willmann-Bell, Inc., 2002, p. 68.

[190] J. M. Geary, "Spherical Aberration," in Introduction to lens design, Willmann-Bell, Inc., 2002, pp. 68-71.

[191] M. J. Booth and T. Wilson, "Refractive-index-mismatch induced aberrations in single-photon and two-photon microscopy and the use of aberration correction," Journal of Biomedical Optics, vol. 6, pp. 266-272, 2001.

[192] E. Wolf, "The diffraction theory of aberrations," Reports on Progress in Physics, vol. 14, p. 95, 1951.

[193] E. J. Botcherby, R. Juškaitis, M. J. Booth and T. Wilson, "Aberration-free optical refocusing in high numerical aperture microscopy," Optics Letters, vol. 32, no. 14, pp. 2007-2009, 2007.

[194] J. M. Geary, "Coma," in Introduction to lens design, Willmann-Bell, Inc., 2002, pp. 71-73.

[195] J. M. Geary, "Field Curvature and Distortion," in Introduction to lens design, Willmann-Bell, Inc., 2002, pp. 75-77.

[196] J. M. Geary, "Astigmatism," in Introduction to lens design, Willmann-Bell, 2002, pp. 73-75.

[197] B. E. A. Saleh and M. C. Teich, "The Sellmeier Equation," in Fundamentals of photonics, 2nd ed., Wiley-Interscience, 2007, pp. 179-181.

[198] J. E. Greivenkamp, "Chromatic aberration," in Field Guide to Geometrical Optics, SPIE Press, 2003, p. 68.

[199] B. E. A. Saleh and M. C. Teich, "Ray optics," in Fundamentals of photonics, 2nd ed., Wiley-Interscience, 2007, pp. 1-37.

[200] W. T. Welford, Aberrations of optical systems, Adam Hilger, 1991.

[201] M. J. Booth, "Adaptive Optics in Microscopy," Philosophical Transactions of the Royal Society A - Mathematical Physical And Engineering Sciences, vol. 365, no. 1861, pp. 2829-2843, 2007.

[202] N. Ji, "Adaptive optical fluorescence microscopy," nature methods, vol. 14, no. 4, pp. 374-380, 2017.

[203] O. Azucena, J. Crest, S. Kotadia, W. Sullivan, X. Tao, M. Reinig, D. Gavel, S. Olivier and J. Kubby, "Adaptive optics wide-field microscopy using direct wavefront sensing," Optics Letters, vol. 36, no. 6, pp. 825-827, 2011.

Chapter 2
Multifocal microscopy systems

2.1 Chapter overview

This chapter is entirely dedicated to describing the multiplane microscopy (MUM) systems present in the literature. Both diffractive and non-diffractive setups will be presented, together with the principal algorithms used to extract their axial information, which can roughly be subdivided into PSF fitting and calibration methods. In general, with respect to diffractive setups (sec. 2.4), non-diffractive systems (sec. 2.3) do not suffer from grating induced chromatic aberration [1] (eq. 2.3), but those currently in the literature do not provide the same magnification per imaged plane (i.e. they are not telecentric [2], eq. 2.21). Diffractive MUM systems can be optically corrected to remove their chromatic aberration (via chromatic aberration counterbalance [3]) or the emission bandwidth can simply be reduced [4]. In terms of axial localisation algorithms, both PSF fitting and calibration curve solutions have been reported to be able to recover the axial positions with high precision [5, 6] and over extended axial ranges [6, 7]. However, the calibration curve solution does not require a pre-axial alignment of the imaged planes [8], since the correct plane spacing is encoded into the shapes of the curves, and to model the PSF.

2.2 Simultaneous multiplane imaging

In sec. 1.3.2 fluorescence microscopy has been described has an important tool to study alive biological samples [9]. However, the inability of non-multiplane systems as single-plane widefield, confocal and light sheet microscopy to image different planes simultaneously imposes severe limitations to the study of live 3D biological samples [3, 7] (i.e. 4D imaging). With single plane techniques, indeed, a 3D volume could only be imaged by acquiring several 2D planes at different instants and depths and stacking them (z-stack acquisition, fig. 1.4), a procedure that is time consuming and, thus, limits the achievable temporal resolution. Due to this, z-stack imaging can lead to ambiguous spatio-temporal localisations, since the planes are not imaged simultaneously. To partially overcome these limitations, PSF engineering techniques that, for example, exploit astigmatic or double-helix PSFs (sec. 1.3.10) could be used [10, 11], since they can image entire volumes simultaneously. However, these methods are typically limited to axial depths around 1 µm – 2 µm, thus precluding the observation of some

phenomena (e.g. intercellular molecule transfer [7]) that can occur over longer axial ranges.

Multiplane microscopy (MUM, sec. 1.3.9), instead, can easily achieve instantaneous volumetric imaging over extended axial depths by imaging multiple planes simultaneously [3, 7], thus avoiding slow imaging and ambiguous spatio-temporal localisation. Its temporal resolution is only limited by the camera acquisition time or by the exposure time required to achieve the desired axial range and localisation precision [3]. MUM is designed to image over depths longer than the distance between the first and last imaged planes by making use of defocused images.

In this chapter various MUM setups and axial localisation techniques are presented. Non-diffractive MUM methods, which obtain multiplane imaging by axially displacing the detector [1], will be shown before the diffractive ones, which exploits the focusing power of distorted diffraction gratings [12]. Then, the principle algorithms used in literature to extract axial localisations will be described.

2.3 Non-diffractive multifocal microscopy systems

Multifocal/multiplane microscopy (MUM) indicates a series of techniques where different focal planes are imaged simultaneously via the use of multiple imaging paths. As anticipated in sec. 2.2, MUM can be subdivided into non-diffractive [1] and diffractive optical systems [3]. Some schematised examples of non-diffractive MUM systems are shown in fig. 2.1b [1], 2.2c [13] and 2.2d [14] (images reproduced for clarity). In general, non-diffractive MUM setups are made by inserting lenses (Ls), mirrors (Mirs), prisms, apertures (As), beam splitters (BSs), etc., in the imaging path of an infinity corrected optical widefield microscope. The principle behind the functioning of non-diffractive MUM systems is presented in fig. 2.1a. As explained in sec. 1.3.1, the imaging path of an infinity corrected optical microscope can be approximated (when paraxial conditions are sufficient and there is no need to model aberrations or the wave nature of light) as a two lens system, i.e. the objective lens (OL) with focal length f_o and the tube lens (TL) with focal length f_{tl}. If the object to image is positioned at a distance o equal to f_o, the image will be formed at a distance i equal to f_{tl}, with magnification (M, eq. 1.3):

$$M = -\frac{f_{tl}}{f_o}. \qquad \text{(eq. 1.3)}$$

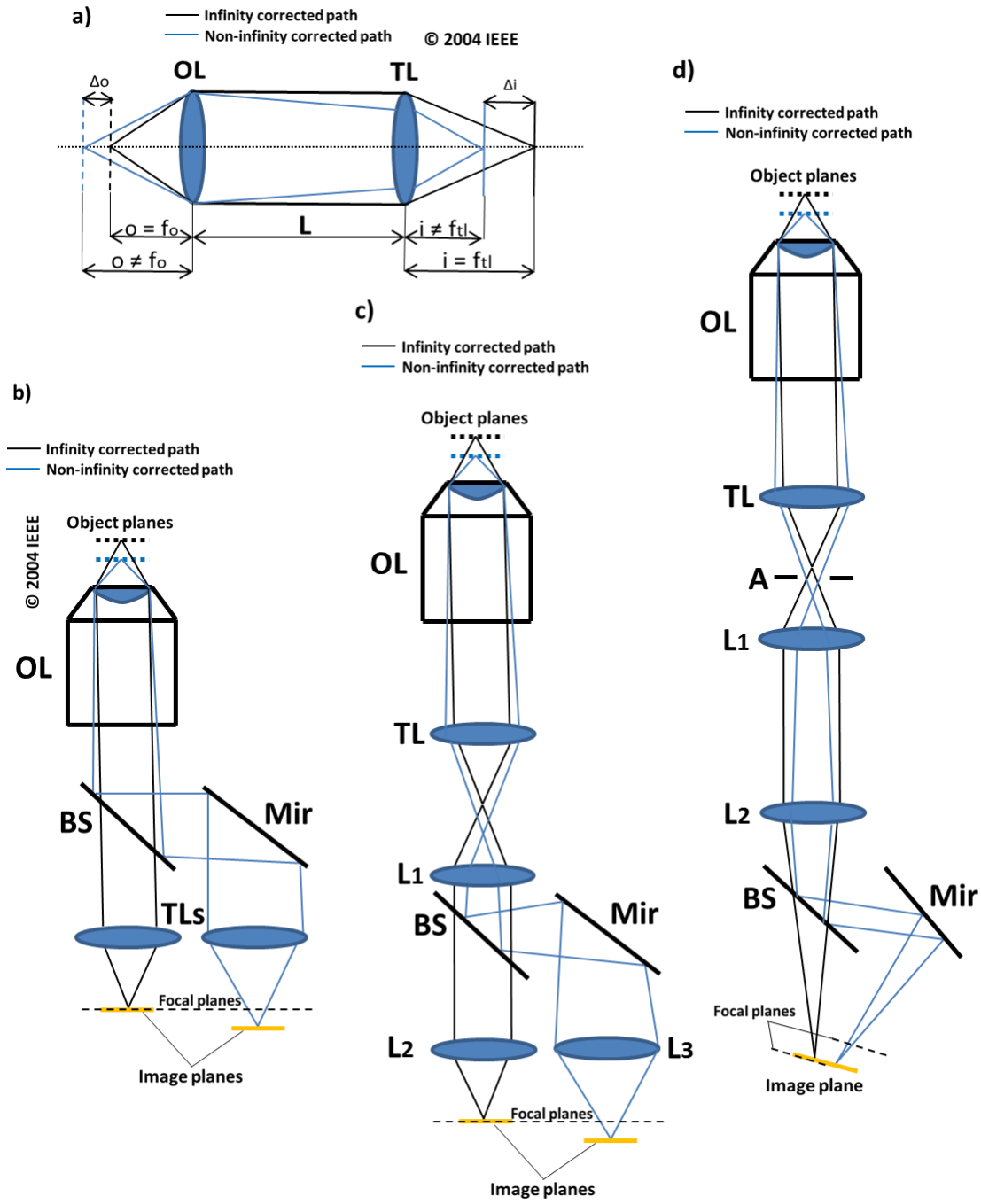

Figure 2.1 Schematic representation of some of the setups used to achieve non-diffractive multiplane microscopy. These setups have been used in (**b**) [1], (**c**) [13] and (**d**) [14] (images reproduced for clarity and adapted from [1], [13] and [14] with permission). In **a** a scheme showing the principle exploited by non-diffractive multiplane microscopy to achieve multiplane imaging is presented. OL = objective lens, TL = tube lens, BS = beam splitter, Mir = mirror, A = aperture, L_1, L_2 and L_3 = added lenses, o = object distance from OL, i = image distance from TL, L = distance between OL and TL, f_o = focal length of the OL, f_{tl} = focal length of the TL, Δo = plane spacing and Δi = distance between the formed imaged.

Consequently, in such a situation the detector should be placed a $i = f_{tl}$. This will allow to have only the plane at f_o in focus on the detector, while all the other planes on the object side will appear defocused and will contribute to the background light [3]. However, if the detector is moved to a distance i different from f_{tl}, also the imaged plane will be moved to a distance o different from f_o. By using the imaging equation ([15], eq. 1.1):

$$\frac{1}{o} + \frac{1}{i} = \frac{1}{f}, \qquad \text{(eq. 1.1)}$$

where o and i are, respectively, the object and image distances from a lens with focal length f, and by applying it in sequence to the OL and the TL, the distance $o \neq f_o$ can be demonstrated to be equal to (eq. 2.1):

$$o = \frac{f_o[L\,i - f_{tl}(L+i)]}{f_o(f_{tl}-i)+L\,i - f_{tl}(L+i)}, \qquad \text{(eq. 2.1)}$$

where L is the distance between OL and TL (fig. 2.1a). Eq. 2.1 shows that the image plane position o is a function of the detector position i, i.e. different depths can be imaged with different camera positions. Therefore, if the imaging path is modified in such a way to image simultaneously planes at $i = f_{tl}$ and at $i \neq f_{tl}$, multiplane imaging can be achieved (fig. 2.1b, 2.1c and 2.1d). This configuration, however, has the drawback of providing different magnifications (Ms) per imaged plane. Considering a single lens system, the M can be calculated as ([15], eq. 1.2):

$$M = -\frac{i}{o}. \qquad \text{(eq. 1.2)}$$

Also in this case, if eq. 1.2 is applied to, first, the OL and, then, the TL (fig. 2.1a), the total M in case $o \neq f_o$ (eq. 2.2) becomes equal to (eq. 2.2):

$$M = \frac{f_o\, f_{tl}}{f_o(f_{tl}-L)-o(f_o+ f_{tl}-L)}, \qquad \text{(eq. 2.2)}$$

which is a function of the object plane position o. Hence, non-diffractive MUM systems require a careful measurement of the M in each imaged plane, since this might be needed for rescaling and/or localisation operations [7]. The setups reproduced in fig.

2.1b, 2.1c and 2.1d apply the above describe principle. In fig. 2.1b MUM is achieved by inserting a 50:50 BS between OL and TL, to create a secondary path and image simultaneously another plane on another detector, which has been shifted with respect the focal length (f_{tl}) of the corresponding TL. This systems has also been expanded to image more than two planes by using additional BSs and mirrors [16]. In fig. 2.1c [13], instead, MUM is obtained by using an external relay attached to a widefield microscope. Also this setup has been demonstrated with more than two planes and has been successfully applied to perform multicolour multiplane microscopy [17]. The configurations in fig. 2.1b and 2.2c make use of more than one detector. This, in turn, introduces problems such as camera synchronisation [18]. In fig. 2.1d an example of non-diffractive multiplane setup designed to use a single detector is shown [14]. As observable, in fig. 2.1d both imaged planes are laterally shifted with respect to the centre of the detector. To avoid their overlap on the camera, an aperture (A) is positioned where the image is primarily formed by the microscope (fig. 2.1d), thus reducing the FOV to half of the sensor chip size. The configuration in fig. 2.1d requires the camera not to be perpendicular to the optical axis (the tilting angle is limited by the focal depth of the system), as, instead, it happens with the other two setups shown (fig. 2.1b and 2.1c), and this might introduce off axis aberrations such as coma [19]. This can be avoided as demonstrated with other non-diffractive MUM systems, which image even more than two planes on a single camera [20, 21, 22].

Non-diffractive MUM systems have been successfully applied to achieve 3D super-resolution imaging [23]. In particular, they have been implemented with photo-activated fluorescence microscopy [14] (PALM, sec. 1.3.10) and high emitter density 3D super-resolution algorithms as multifocus astigmatism compressed sensing [24] (3D-MACS), fast localization algorithm based on a continuous-space formulation [25] (3D-FALCON) and super-resolution optical fluctuation imaging [26] (3D-SOFI). For 3D super-resolution, multiplane imaging offers, differently from non-simultaneous plane acquisition, improved temporal resolution, since the different planes are acquired simultaneously and the samples are illuminated over shorter periods of time. With non-diffractive MUM, axial super-resolutions of 35 nm have been obtained [24].

Finally, from the point of view of some of the biological results achieved, non-diffractive MUM, in combination with 3D particle tracking (sec. 1.4), has been able to show the extended 3D movements of dynein proteins on microtubules [22] (involved in cell motility [27]), clarify some of the trafficking paths of the human immunodeficiency virus 1 ribonucleic acid (HIV-1 RNA) genome [21] (important to understand how HIV-

1 replicates [28]) and of the fragment crystallisable neonatal receptor [1, 17, 13, 16, 29] (FcRn, linked to the transport of antibodies [30, 31]) in cells and observe the rapid inter-cellular transfer of transferrin molecules [7] (connected to iron homeostasis [32, 33]), etc.

2.4 Diffractive multifocal microscopy systems

The other class of multiplane systems is represented by those that exploit diffraction to achieve MUM, i.e. the diffractive multiplane systems. Diffractive MUM uses distorted diffraction gratings that, when paired with a lens, can allow to image different axial planes at sample level [4, 3, 12]. The principle on which diffraction is based is described in fig. 2.2. A diffraction grating can be seen as a periodic optical device, where, for example, there is an alternation of vertical (or concentric, in case of a Fresnel

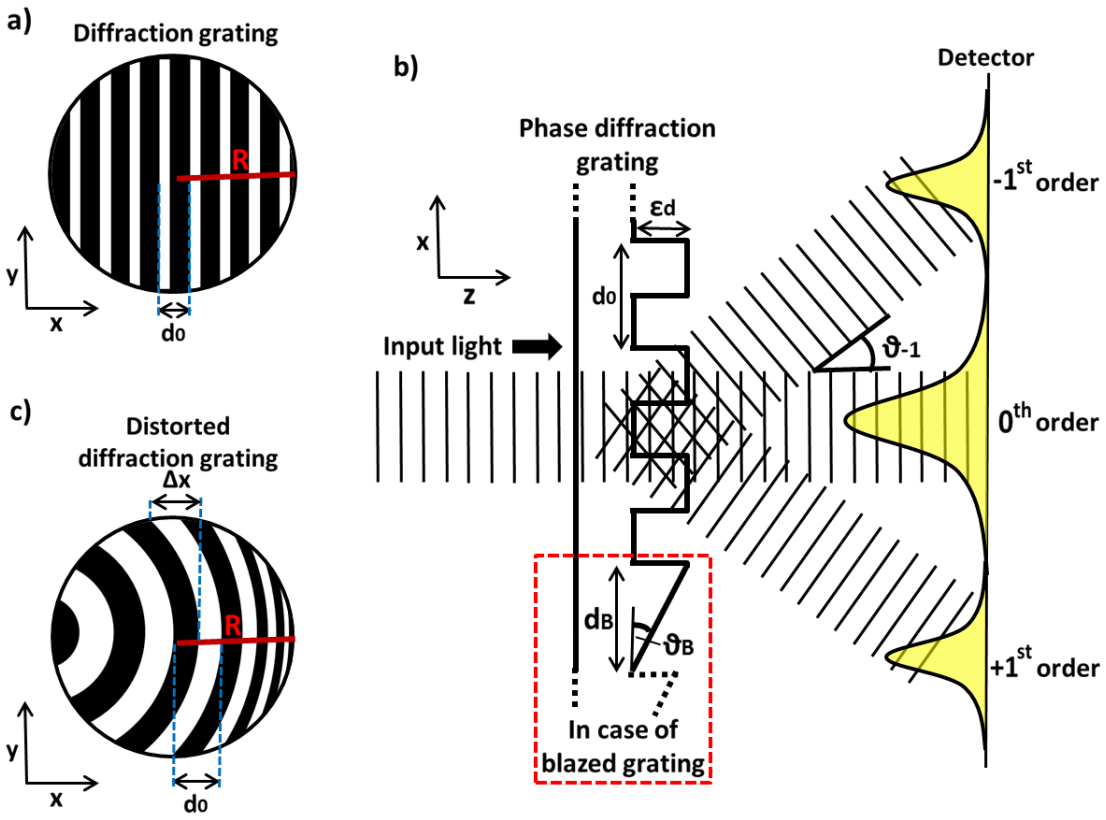

Figure 2.2 a) Schematic representation of a diffraction grating with ruling spacing d_0 and aperture radius R. **b)** Scheme showing the diffraction (0^{th} and $\pm1^{st}$ orders) generated by a phase diffraction grating, with ruling spacing d_0 and etching depth ε_d. The diffraction angle associated to the -1^{st} order (ϑ_{-1}) is shown. On the bottom, the geometry of a blazed diffraction grating is also shown. ϑ_B is the blaze angle and d_B the grating period. **c)** Schematic representation of a distorted diffraction grating with central ruling spacing d_0 and aperture radius R. A local distortion Δx is indicated.

zone plate [34]) opaque and transparent rulings, whose summed widths (d_0) is the grating period (fig. 2.2a). Such a device is referred as amplitude grating, since the wavefronts are modified by back reflecting parts of them on the opaque rulings, thus reducing the amplitude. The opaque rulings can be obtained via metal deposition [35]. Consequently, amplitude gratings are highly inefficient, since roughly 50% of light is lost [36]. This can be avoided by using phase gratings, where all rulings are transparent and present periodic thicknesses [37]. In phase gratings the wavefronts are modified by the fact that parts of them will travel over thicker, while others over thinner regions, thus introducing a delay between different parts of the wavefronts, known as phase delay [38]. The different thicknesses can be obtained via etching [39]. When light crosses a diffraction grating (either an amplitude or phase one), its wavefronts are broken into several spherical waves, whose constructive and destructive interference generates the diffraction orders. This is schematised in fig. 2.6b for a phase diffraction grating. The difference in thickness between the two levels of the grating is the etching depth ε_d. Diffraction, in case of normal incidence, follows the grating equation [37] (eq. 2.3):

$$d_0 \sin \vartheta_m = m \lambda, \qquad \text{(eq. 2.3)}$$

where m is the diffraction order, λ is the imaging wavelength, d_0 is the grating period and ϑ_m is the diffraction angle. The diffraction order m identifies the constructive interference peaks that occur with diffraction, while ϑ_m is the angle by which they are deviated from the optical axis. The central order is indicated as the 0^{th} one, while those at the sides as $\pm m^{th}$. The dependence on the wavelength is particularly important, since it gives rise to a grating-induced chromatic aberration, a major problem in diffractive MUM [3, 40, 41]. For simplicity, fig. 2.6b shows only the first three orders and the diffraction angle ϑ_{-1} for the -1^{st} order. Regarding the relative intensity distribution among diffraction orders (I_m), this, for a square binary phase gratings, is governed by eq. 2.4 [8]:

$$I_m = \left| \frac{4 \sin \frac{m\pi}{2}}{m} \cos\left(\frac{m\pi}{2} + \frac{\varphi}{2}\right) \right|^2, \qquad \text{(eq. 2.4)}$$

where the parameter φ is the phase delay introduced and is equal to (eq. 2.5):

$$\varphi = \frac{2\,\pi\,\varepsilon_d}{\lambda}\left(n_{grat} - 1\right), \qquad \text{(eq. 2.5)}$$

with n_{grat} the refractive index of the grating material. The fact eq. 2.5 depends on the ε_d indicates that the latter parameter can be modified to equalise the intensity distribution among the diffraction orders for the desired wavelength. In the 0^{th} and $\pm1^{st}$ orders eq. 2.4 can be reduced to (respectively, eq. 2.6 and 2.7):

$$I_0 = 4\pi^2\,\cos^2\left(\frac{\varphi}{2}\right) \qquad \text{(eq. 2.6)}$$

and

$$I_{\pm1} = 16\,\sin^2\left(\frac{\varphi}{2}\right). \qquad \text{(eq. 2.7)}$$

Eq. 2.6 and 2.7 have been plotted in fig. 2.3 after normalising both equations with respect to $4\pi^2$ and transforming them into percentages. Both I_0 and $I_{\pm1}$ are periodic functions. The phases at which $I_0 = I_{\pm1}$ (φ_{bal}) represent the phases needed to achieve the intensity balance between the 0^{th} and the $\pm1^{st}$ orders. The smallest φ_{bal}, to which the smallest etching depth ε_d correspond, can be found to be equal to 0.64π rad, i.e. around 2 rad (fig. 2.3). By substituting this value into either eq. 2.6 or 2.7, the percentage intensity (I_{bal}) into each of the first three orders can be found to be the 28.84% of the input one (fig. 2.3). Therefore, by using the first three orders, the DDG grating uses the 86.52% of the photons, while the remaining 13.48% is lost into higher orders. By inserting φ_{bal} into eq. 2.5 as well, the etching depth at which the intensity is balanced (ε_{dbal}) can be obtained (eq. 2.8):

$$\varepsilon_{dbal} = \frac{0.64\,\lambda_{bal}}{2\left(n_{grat}-1\right)}, \qquad \text{(eq. 2.8)}$$

where λ_{bal} is the wavelength at which the grating is designed to be intensity balanced in the first three orders. For example, in the case of a grating made by fused silica [42] ($n_{grat} \approx 1.46$ in the visible) and balanced for a fluorophore as Alexa Fluor 488 [43] (emission peak at $\lambda \approx 525$ nm) ε_{dbal} should be around 365 nm (eq. 2.8). As expectable, the grating manufacturing accuracy has an impact on ε_{dbal} and, in turn, on the energy balance. Typical etching accuracies can be around ±10 nm/±50 nm [44]. Assuming, as an example, an etching accuracy of ±10 nm on a grating made by fused silica for Alexa Fluor 488, φ would vary by around ±0.05 rad (eq. 2.5) with respect to φ_{bal} and,

consequently, I_0 by around ±2.53% (eq. 2.6) and $I_{\pm1}$ by around ±0.95% (eq. 2.7) with respect to I_{bal}.

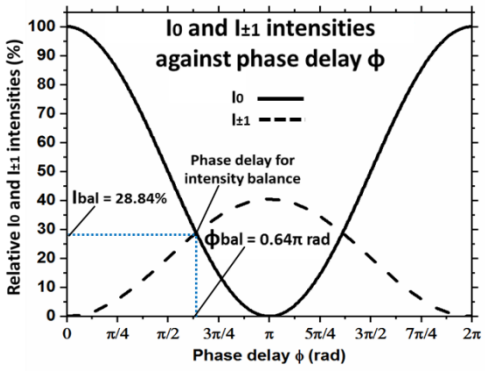

Figure 2.3 Plot showing the behaviour of the relative intensities in the 0^{th} (I_0, eq. 2.6) and $\pm1^{st}$ ($I_{\pm1}$, eq. 2.7) orders, as a function of the phase delay induced by the DDG φ (eq. 2.5). The parameter φ_{bal} is the smallest phase delay φ needed to obtain the balance of the intensities I_{bal} in the 0^{th} and $\pm1^{st}$ orders.

Another way to vary the intensity distribution among the diffraction orders is by radically modifying the phase grating structure from the binary one describe above (i.e. with only two thickness steps), to a blazed one [45]. In a blazed grating the thickness varies linearly within the grating period d_0 (called d_B in this case), as in the inset shown on the bottom of fig. 2.6b and the rulings make an angle called the blaze angle (ϑ_B) with respect to the plane of the grating. ϑ_B can be tuned in order to concentrate over 95% of the intensity hitting the grating at an incident angle ϑ_i in a single diffraction order m and for the needed wavelength, called the blaze wavelength (λ_B). This property of a blazed grating can be exploited, as it will be shown in sec. 2.4.4 and 2.4.5, to correct for grating-induced chromatic aberration [3, 40, 41].

2.4.1 *Distorted diffraction gratings*

Diffraction gratings such as that shown in fig. 2.2a with all the rulings parallel to each other do not have any focusing power. However, if a certain amount of quadratic distortion Δx is introduced on the grating rulings (fig. 2.2c), a further phase shift among the different parts of the wavefronts is added (detour phase effect [46]) and the wavefront curvatures in the non-zeroth orders can be modified. Effectively, the non-zeroth orders achieve focussing power. Hence, by coupling such distorted diffraction gratings with lenses into an external relay attached to a widefield microscope, it is possible to image multiple planes at sample level into the different diffraction orders, obtaining the multiplane effect. Usually, the grating period d is not constant in a

distorted grating, which varies across it. Thus, it is common to refer to the central one in this case, d_0. This the principle on which diffractive MUM is founded.

Distorted diffraction gratings (DDGs) have been used in the design proposed by Greenaway et al. [12] for a stand-alone multiplane imaging system. The latter is shown in fig. 2.4a (image reproduced for clarity). Greenaway's setup is composed of a DDG positioned just before (back-to-back) a lens (L), with the etched side not facing the L.

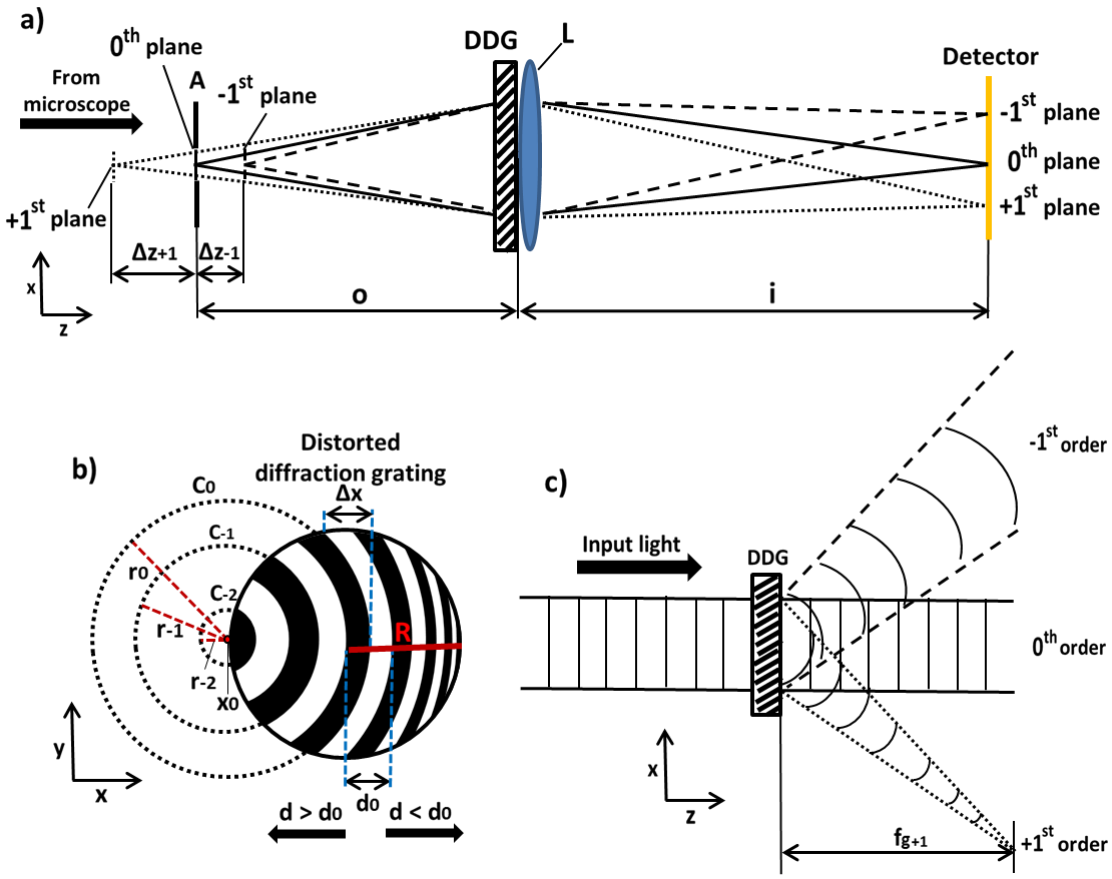

Figure 2.4 a) Diffractive multiplane relay presented by Greenaway et al. in [12] (image reproduced for clarity and adapted from [12] with permission). DDG is the distorted diffraction grating, L is a lens, Δz_{+1} and Δz_{-1} are, respectively, the distances between the $\pm 1^{st}$ planes and the 0^{th} one, o is the distance between the 0^{th} plane and the first principal plane of the optical system, while i is that between the second principal plane of the system and the detector. **b)** Schematic representation of the distorted diffraction grating used in **a**. The parameter d is the variable grating period given by eq. 2.11. The labels c_0, c_{-1} and c_{-2} indicate some of the Fresnel zone plate circles described by eq. 2.12, while r_0, r_{-1} and r_{-2} are the corresponding radii (eq. 2.14). **c)** Scheme showing the working principle of the DDG. The value f_{g+1} is the grating focal length in the $+1^{st}$ order (eq. 2.15).

As said, DDG, due to their ruling distortion (fig. 2.2c), modifies the phase of the light waves (i.e. the shape of the wavefronts [37]) in the non-zeroth orders, thus behaving as multiple lenses. Therefore, the system in fig. 2.4a behaves as a one lens system (L) in the 0^{th} order and as a two lens system (DDG + L) in the $\pm1^{st}$ ones. A schematic version (not to scale) of a DDG used in [12] is shown in fig. 2.4b. The phase shift imposed to the light in the non-zeroth orders φ(x,y) by the DDG (the detour phase), with respect to that in the 0^{th} order, can be described by eq. 2.9 [12]:

$$\varphi(x,y) = \frac{2\pi\, m\, \Delta x(x,y)}{d}. \qquad \text{(eq. 2.9)}$$

In eq. 2.9, d is the grating period and Δx(x,y) is the local ruling distortion imposed to the grating rulings in the x direction, which causes the phase shift. Clearly, φ(x,y) depends the diffraction order m. It will be equal and opposite in the $\pm1^{st}$ orders and zero in the zeroth one. Δx(x,y) varies across the grating and is equal to [12] (eq. 2.10):

$$\Delta x(x,y) = \frac{W_{20}\, d}{\lambda\, R^2}(x^2 + y^2), \qquad \text{(eq. 2.10)}$$

where R is the grating radial aperture, λ is the imaging wavelength, x and y are the spatial coordinates across the grating and W_{20} is the defocus coefficient, which determines the amount of wavefront curvature added in the non-zeroth orders. W_{20} represents the extra path length [47] added to the wave at the edge of the aperture in the $+1^{st}$ order and is the origin of the phase shift in eq. 2.6. W_{20} is a function of the wavelength and can be expressed as $n_\lambda\, \lambda$, where n_λ is the extra number of waves added to the path length. The grating period d varies across the grating by following the following equation [12] (eq. 2.11):

$$d = \frac{d_0\, \lambda\, R}{\lambda\, R + 2\, d_0\, W_{20} x}, \qquad \text{(eq. 2.11)}$$

with d_0 the central grating period. A DDG is essentially an off-axis Fresnel zone plate. The circles of a Fresnel zone plate can be described by the formula [12] (eq. 2.12):

$$\left(x + \frac{\lambda\, R^2}{2\, d_0\, W_{20}}\right)^2 + y^2 = \frac{n_F\, \lambda\, R^2}{W_{20}} + \left(\frac{\lambda\, R^2}{2\, d_0\, W_{20}}\right)^2, \qquad \text{(eq. 2.12)}$$

where n_F is the locus of each circle C_{nF} (it is an integer number) and identifies the latter. At $n_F = 0$ the circle passing through the centre of the grating is identified. The generic equation of a circle is $(x - x_0)^2 + (y - y_0)^2 = r^2$, where (x_0,y_0) is its centre and r its radius. By comparing this equation to eq. 2.12, it comes out that $y_0 = 0$ µm and that x_0 is equal to [12] (eq. 2.13):

$$x_0 = -\frac{\lambda R^2}{2 d_0 W_{20}}. \qquad \text{(eq. 2.13)}$$

The radius r, instead, varies with n_F (r_{nF}) and is equal to [12] (eq. 2.14):

$$r_{nF} = \sqrt{\frac{n_F \lambda R^2}{W_{20}} + \left(\frac{\lambda R^2}{2 d_0 W_{20}}\right)^2}. \qquad \text{(eq. 2.14)}$$

Acting as a multilens, the DDG has associated focal lengths. The latter (f_{gm}) can be expressed as follows [12] (eq. 2.15):

$$f_{gm} = \frac{R^2}{2 m W_{20}}. \qquad \text{(eq. 2.15)}$$

By observing eq. 2.15, it can be seen that f_{gm} will tend to $\pm\infty$ for m = 0 (i.e. no focal power), while f_{gm} will be equal and opposite between equal and opposite orders (fig. 2.4c). Consequently, a plane wave will be focused in the positive orders and defocused in the negative ones (fig. 2.4c). The effective focal length (EFL) provided by the combination of a lens L of focal length f_L and of the DDG can be expressed as (eq. 2.16):

$$EFL = \frac{f_L f_{gm}}{f_L + f_{gm} - s}, \qquad \text{(eq. 2.16)}$$

with s the separation between L and the DDG on the optical axis (o.a.). Effectively, the lens L and the DDG act as a compound lens system described by equation 2.16. By combining eq. 2.15 and 2.16 with s = 0 mm, the EFL of the system in fig. 2.4a can be shown to be [12] (eq. 2.17):

$$EFL = \frac{f_L R^2}{R^2 + 2 m f_L W_{20}}. \qquad \text{(eq. 2.17)}$$

Greenaway's relay is not telecentric [2], thus it provides different magnifications M per each diffraction order. In general, in a DDG – lens system with $s \neq 0$ mm the M can be expressed as (eq. 2.18):

$$M = -\frac{(f_L - s)(i - s)}{f_L f_{gm}} - \frac{(i - f_L)}{f_L}, \qquad \text{(eq. 2.18)}$$

where i is the fixed distance between the detector and the second principal plane of the system. From eq. 2.18 it is possible to see how M changes with f_{gm}, thus giving different Ms per plane. The absence of telecentricity makes also the plane spacing not constant between each pair of plane. Given a fixed i, the distance o between the imaged planes and the first principal plane of the system is (eq. 2.19):

$$o = \frac{f_L(s^2 + f_{gm}\, i - s\, i)}{f_{gm}(i - f_L) - (f_L - s)(s - i)}. \qquad \text{(eq. 2.19)}$$

By modifying f_{gm} for the different orders (eq. 2.15) and taking the differences between the associated o values (eq. 2.19), it can be seen that the absolute value of the distance between the $+1^{st}$ plane and the 0^{th} one (Δz_{+1}) is different from that between the latter and the -1^{st} one (Δz_{-1}). In particular, for the setup in fig. 2.4a Δz_m is (eq. 2.20):

$$\Delta z_m = -\frac{2\, m\, o^2\, W_{20}}{R^2 + 2\, m\, o\, W_{20}}. \qquad \text{(eq. 2.20)}$$

A grating as that shown in fig. 2.4b with defocus coefficient W_{20} can image a set of N planes aligned perpendicularly to the ruling direction. To image an array of NxN planes, instead, these rulings could be crossed by another set of perpendicular rulings, with defocus coefficient equal to $N\, W_{20}$, thus imaging NxN different planes disposed as an array on the detector [12]. The aperture A in fig. 2.4a placed at the 0^{th} plane position is necessary to reduce the FOV to $1/N_p^{th}$ of the detector size, with N_p the number of imaged planes, and avoid the planes to overlap. However, it should be pointed out that a proper image separation is achievable only if there are not entire circular periods on the DDG (re-entrant fringes), i.e. if the centre of the associated Fresnel zone plane is not present. Indeed, in such a situation the different imaged planes will always be overlapped [34].

2.4.2 *Telecentricity*

As mentioned above (sec. 2.4.1), the system in fig. 2.4a [12] is not telecentric, thus it provides different Ms per diffraction order (eq. 2.18) and the plane spacing varies between consecutive planes (eq. 2.20). However, by observing eq. 2.18 it can be seen that telecentricity from the object side can be achieved by setting s equal to f_L [2] (eq. 2.21):

$$M = -\frac{(i - f_L)}{f_L}. \qquad \text{(eq. 2.21)}$$

In eq. 2.21 the dependence from the grating focal length f_{gm}, and so from the diffraction order m, has disappeared. Therefore, by moving the DDG to a distance equal to the focal length of the coupled lens (L, fig. 2.4a), the system becomes telecentric from the object side and the same magnification is provided to all imaged planes. In this case, the DDG is said to be at the telecentric position. In such a telecentric system the distance o between the imaged planes and the first principal plane (eq. 2.20) becomes [2] (eq. 2.22):

$$o = \frac{i\, f_L}{i - f_L} - \frac{{f_L}^2}{f_{gm}}. \qquad \text{(eq. 2.22)}$$

By calculating o for the different f_{gm}s, the plane spacing between the $+1^{st}$ and the 0^{th} planes and that between the latter and the -1^{st} one can be shown to be the same and equal to [2] (eq. 2.23):

$$\Delta z = \frac{{f_L}^2}{f_{gm}}. \qquad \text{(eq. 2.23)}$$

2.4.3 *Dalgarno multifocal diffraction relay*

A modified version of the relay in fig. 2.4a that exploits telecentricity from the object side has been proposed by Dalgarno et al. in [4] to be coupled to a widefield microscope to achieve multifocal imaging. This is schematised in fig. 2.5a (image reproduced for clarity). Differently from Greenaway's relay, Dalgarno's one uses two achromatic doublets (L_1 and L_2) instead of one, separated by a distance L_d. L_1 and L_2 are positioned such that their thicker layers are facing each other, thus making negligible any

aberration introduced by the relay [48]. These lenses behave as a compound lens with EFL calculable via eq. 2.17. Consequently, the DDG (whose etched face is positioned in

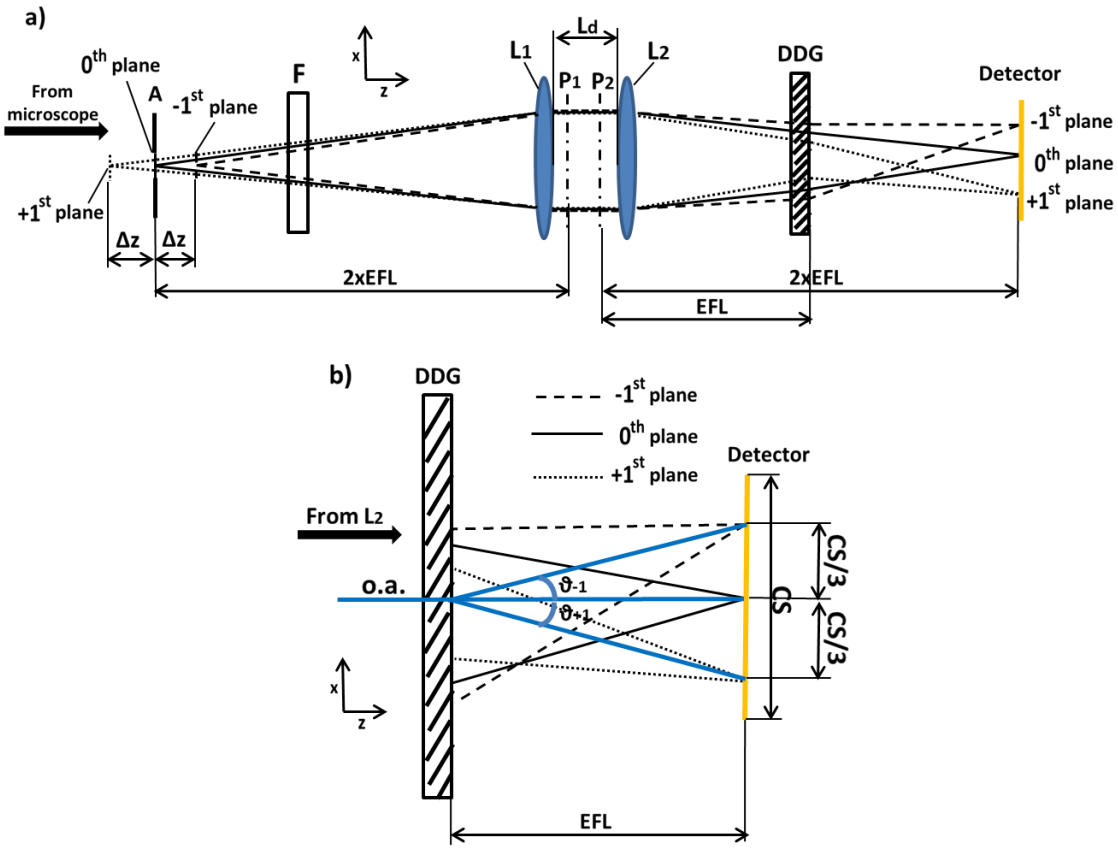

Figure 2.5 a) Diffraction MUM relay described by Dalgarno et al. in [4] (image reproduced for clarity and adapted from [4] with permission). L_1 and L_2 are two lenses and L_d is the distance between their vertices. Δz is the plane spacing. EFL is the effective focal length of the $L_1 - L_2$ system, while P_1 and P_2 are the associated principal planes. F is a narrow bandwidth filter. **b)** Scheme showing the diffraction in the 0^{th} and $\pm1^{st}$ orders due to the DDG. CS is the lateral detector chip size, $\vartheta_{\pm1}$ the diffraction angle in the $\pm1^{st}$ orders (eq. 2.3) and o.a. is the optical axis.

front of the detector) should be placed at a distance of EFL after the second principal plane (P_2) of the L_1 - L_2 system. The relay is designed to have a total distance o + i of 4f [49]. Consequently, the aperture A is placed at a distance of 2 EFL before the first principal plane (P_1) of the L_1 - L_2 system, while the detector 2 EFL after P_2 and unit magnification is provided (eq. 1.2). The plane spacing calculable via eq. 2.23 is at the aperture A level (fig. 2.4a and 2.5a). To obtain the plane spacing at the microscope sample level, instead, it is needed to take into account the axial magnification introduced by the microscope, which is equal to the lateral magnification squared M^2

(sec. 1.3.1). Therefore, by rescaling Δz in eq. 2.23 via M^2 the plane spacing at sample level becomes (eq. 2.24):

$$\Delta z = \frac{EFL^2}{M^2 f_{gm}}. \qquad \text{(eq. 2.24)}$$

Regarding the plane separation on the camera chip, this is illustrated in fig. 2.5b. Basically, the plane separation should be such that there is no overlap between the different planes, but simultaneously the detector chip is fully utilised. Secondly, it is also needed that each plane is centred on its own portion of the camera chip. This can be obtained if the EFL of the L_1 - L_2 system verifies the following relation (eq. 2.25):

$$EFL = \frac{CS}{N\, tg(\vartheta_m)}, \qquad \text{(eq. 2.25)}$$

where CS is the lateral chip size and N is the desired number of planes aligned on the chip. As a consequence, it can be concluded that the EFL, i.e. L_1, L_2 and L_d, should be chosen to satisfy the criteria expressed in eq. 2.24 and 2.25. The system in fig. 2.5a [4] is central in this thesis, since it has been selected to be characterised from the point of view of its responses to aberration (chap. 3) and signal levels (chap. 4) and has been applied to study a biological sample (chap. 5).

2.4.4 *Chromatically corrected diffraction multifocal relays*

As explained above, diffraction based MUM is affected by grating-induced chromatic aberration [3, 4, 40] (eq. 2.3). As a consequence, the Greenaway [12] (fig. 2.4a) and Dalgarno [4] (fig. 2.5a) setups should be used in presence of monochromatic light (e.g. by using a narrow bandwidth filter placed before the DDG, fig. 2.5a) to avoid the chromatic smearing, thus discarding the majority of the photons. A potential solution to this problem for the Greenaway relay is provided by Greenaway et al. in [40], where the use of a pair of twinned blazed gratings is suggested (fig. 2.6b, image reproduced for clarity). In general, to eliminate the chromatic aberration grating-induced all wavelength components of light should be diffracted at the same angle. This could be achieved by predispersing the incident polychromatic light and taking advantage of the fact the period of a DDG is not constant (eq. 2.11). By using eq. 2.3 it can be demonstrated that two λs are diffracted at the same angle in the $+1^{st}$ order if the following relation is satisfied (eq. 2.26):

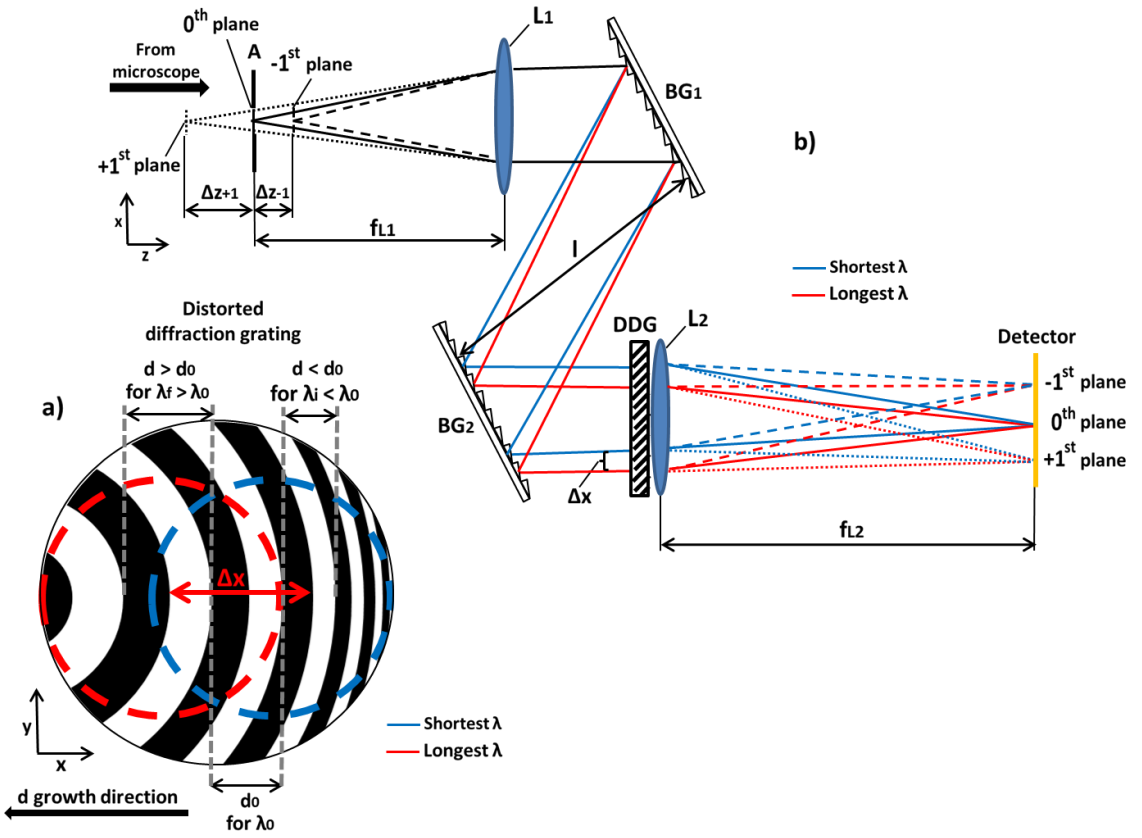

Figure 2.6 a) Scheme showing the relative illumination off-set Δx (eq. 2.36) on a DDG (balanced for a wavelength λ_0) needed between the two extreme wavelengths in the bandwidth (λ_i and λ_f) to have the same diffraction angles. **b)** Setup used in [40] (image reproduced for clarity and adapted from [40] with permission) to obtained the off-set Δx showed in **a** and correct for the grating-induced chromatic aberration. L_1 and L_2 are two lenses with focal lengths of, respectively, f_{L1} and f_{L2}. BG_1 and BG_2 are reflection blazed grating and l is the distance between them.

$$\frac{d_i}{\lambda_i} = \frac{d_f}{\lambda_f}, \qquad \text{(eq. 2.26)}$$

where λ_i and λ_f are, respectively, the initial and final wavelengths in the bandwidth Δλ and d_i and d_f are the respective grating periods that should be seen by λ_i and λ_f. Essentially, eq. 2.26 indicates the period d each wavelengths should see on the grating to keep the diffraction angle constant. In particular, d should grow with the wavelength. Therefore, by following eq. 2.6 and laterally pre-shifting the colour components of the incident light (fig. 2.6a), the chromatic smearing can be compensated. The relative shift $\Delta x = x_f - x_i$ between the centres of the two wavelength beams λ_f and λ_i (fig. 2.6a) can be calculated by combining eq. 2.11 and 2.26 (eq. 2.27):

$$\Delta x = \frac{R^2}{2\, d_0\, W_{20}}. \qquad \text{(eq. 2.27)}$$

To pre-disperse the light, the setup in fig. 2.6b [45] uses two reflective blazed gratings (BG_1 and BG_2), parallel to each other and separated by a distance l (for simplicity, the pre-dispersion effect is shown only on the light coming from the 0^{th} plane, but the principle is the same for all of them). These blazed gratings have the same blaze period d_B and angle ϑ_B. The latter is set to diffract around 95% of the desired wavelength (λ_B) in the -1^{st} order, in order to maximise the optical efficiency. BG_1 is employed to predisperse the light components, while BG_2 to recollimate them before they reach the DDG. The amount of lateral shift Δx obtained has to be equal to that calculated by eq. 2.27 and can be controlled by tuning the distance l and d_B.

Regarding the Dalgarno setup (fig. 2.5a), Dalgarno et al. [41] have proposed the design in fig. 2.7 (image reproduced for clarity) to correct for the chromatic aberration. This system makes use of two grisms [50] (GR_1 and GR_2). A grism is an optical device composed of a right angled triangular prism with a blazed grating attached on its wider side. The blaze angle of the grating and the wedge angle of the prism should be equal. In this way, the non-linearities in the chromatic dispersion introduced by the prism are reduced by those equal and opposite due to the blazed grating. As for the relay in fig. 2.6, also in this case the two blazed gratings have equal period d_B and blaze angle ϑ_B. The grisms are positioned between L_1 and L_2 and the centres of the gratings of the two grisms are separated by a distance GR_s. GR_1 and GR_2 have the same role of BG_1 and BG_2 in [40] (fig. 2.6b) and GR_s can be tuned to reach the desired Δx (eq. 2.27). Even though the relay in fig. 2.7 is telecentric from the object side and chromatically

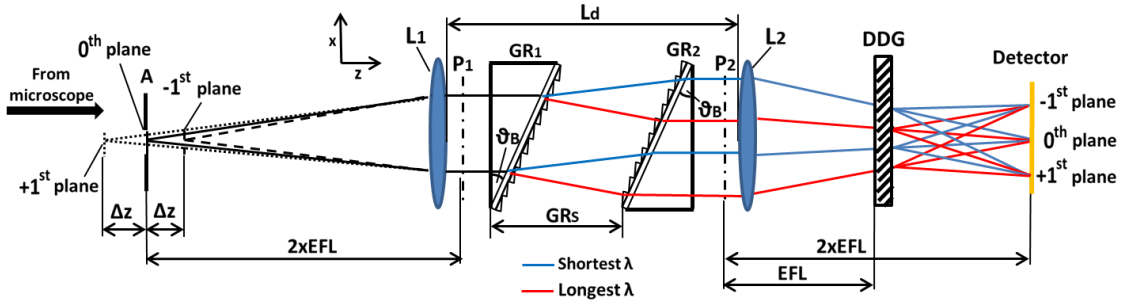

Figure 2.7 Diffraction MUM relay presented in [41] (image reproduced for clarity and adapted from [41] with permission). GR_1 and GR_2 are two grisms used to correct for the grating-induced chromatic aberration. GR_s is the distance between the grisms. ϑ_B is the grism wedge angle.

corrected, it can only work with relatively large EFL, since L_d (i.e. s) needs to allow the insertion of the grisms (eq. 2.16). This, in turn, raises the plane spacing to non-practical values (eq. 2.24). As an example, in [41] the system in fig. 2.7 has been reported to have a plane spacing of 97 mm at the aperture A level. This would mean that by using a 100x magnification objective lens the plane spacing at sample level would be around 9.7 µm (eq. 2.24), a value that could not allow the observation of typical emitters in several planes simultaneously, thus removing the advantage of multiplane systems.

The relay in fig. 2.7 corrects simultaneously for the grating-induced lateral chromatic aberration and for the magnification difference among imaged planes. However, it cannot remove the axial chromatic aberration arising from the increase in allowed $\Delta\lambda$ [51]. This is due to the fact that, since W_{20} is a function of the wavelength ($W_{20} = n_\lambda \lambda$), also f_{gm} (eq. 2.15) and, consequently, Δz (eq. 2.24) will be functions of the wavelength. The plane spacing Δz can be expressed as a function of the wavelength by the expression (eq. 2.28):

$$\Delta z = \frac{2\, m\, EFL^2\, n_\lambda\, \lambda}{M^2\, R^2}. \qquad \text{(eq. 2.28)}$$

From eq. 2.28 it is clear how the plane spacing increases with the wavelength, since the plane position is a function of f_{gm} (eq. 2.15) when $m \neq 0$. At $m = 0$, instead, the dependence from the wavelength disappears, making the 0^{th} plane the only one that does not move with the wavelength. Consequently, the variation in Δz will cause axial chromatic spreading in the non-zeroth orders. Redefining for convenience the variable for the plane spacing from Δz to PS and considering a variation in wavelength from λ_i to λ_f ($\Delta\lambda = \lambda_f - \lambda_i$), the associated variation in PS ($\Delta PS = PS_f - PS_i$) can be expressed as (eq. 2.29):

$$\frac{\Delta PS}{\Delta\lambda} = \frac{2\, m\, EFL^2\, n_\lambda}{M^2\, R^2}. \qquad \text{(eq. 2.29)}$$

By substituting into eq. 2.29 the plane spacing PS_c calculated at a specific wavelength λ_c (e.g. that at which the grating is balanced) and rearranging, the following relation can be obtained (eq. 2.30):

$$\frac{\Delta PS}{PS_c} = \frac{\Delta\lambda}{\lambda_c}, \qquad \text{(eq. 2.30)}$$

which states that the axial spreading introduced (ΔPS) is proportional to the imaging bandwidth (Δλ). To limit this problem, the use of a bandwidth filter should be considered.

2.4.5 *Abrahamsson diffractive multiplane system*

Another diffraction-based MUM system designed to be telecentric and chromatically

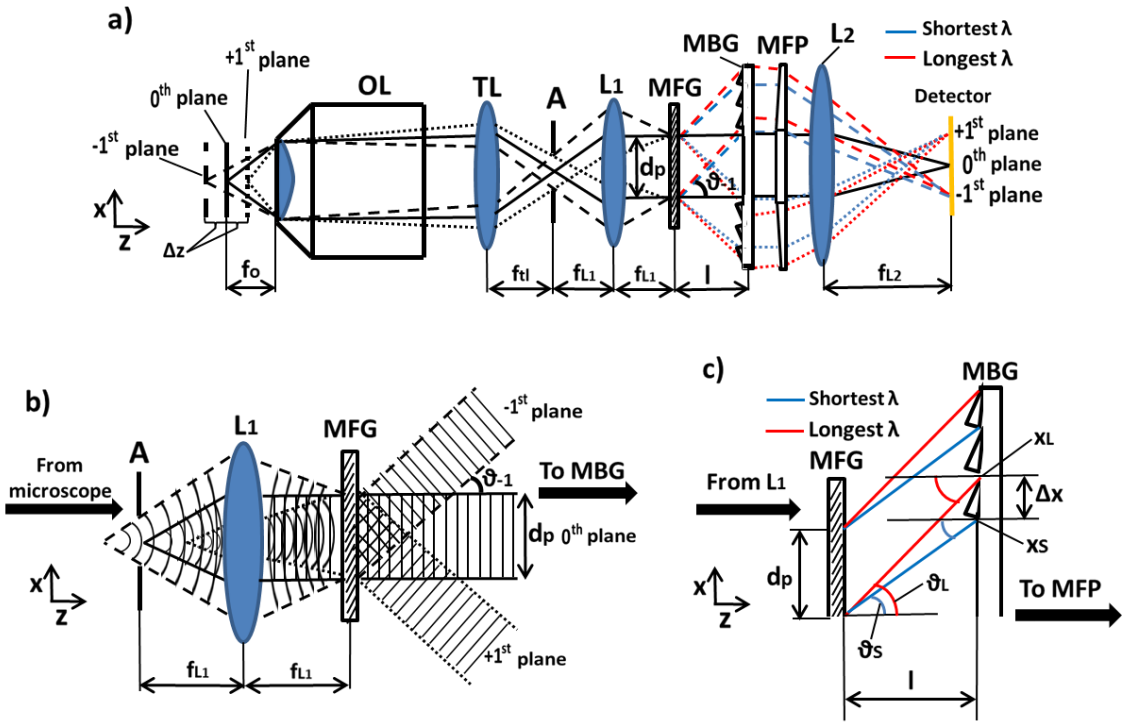

Figure 2.8 a) Schematic representation of the multifocal diffraction relay described in **[3]** (top view, image reproduced for clarity and adapted from [3] with permission). **b)** Scheme showing the wavefront distortion correction applied by the MFG element in **a** (eq. 2.12, [3], image reproduced for clarity and adapted from [3] with permission). **c)** Scheme showing the mechanism to correct the chromatic aberration induced by the MFG element in **a**. Δz = plane spacing, OL = objective lens, TL = tube lens, A = aperture, L_1 and L_2 = added lenses, MFG = multifocus grating, MBG = multiblazed grating, MFP = multifacet prism, λ = wavelength, f_o = OL focal length, f_{tl} = TL focal length, f_{L1} and f_{L2} = respectively, L_1 and L_2 focal lengths, l = MFG – MBG distance, ϑ_{-1} = diffraction angle associated to the -1st order, d_p = pupil diameter, ϑ_S and ϑ_L = diffraction angles associated to the -1st order with, respectively, the shortest and longest imaging wavelengths in the system, x_S and x_L = example arrival positions on the MBG of two rays having the shortest and longest imaging wavelengths in the system, after leaving the MGF from the same point and $\Delta x = x_L - x_S$.

corrected has been proposed by Abrahamsson et al. in [3]. This has been schematised in fig. 2.8a (image reproduced for clarity). This relay is composed of five optical elements. The first one is an achromatic doublet lens (L_1), positioned at a distance equal to its focal length (f_{L1}) from the primary image of the microscope. As a consequence, the Fourier/telecentric plane in the relay will be positioned at an equivalent distance f_{L1} after L_1. This is the position where the second optical element in the relay, the multifocus grating (MFG) [3], has to be positioned. This makes this system telecentric [2] and, hence, all planes have the same magnification.

The optical behaviour of the MFG is schematised in fig. 2.8b. The MFG element has two roles. It collects the incoming light from different planes at sample and separates it into the various diffraction orders, making sure the intensity is equally distributed among them, and corrects for the aberrations introduced by using the OL at non-design planes [52]. The latter aspect can be explained by considering the fact that OLs are designed to minimise the optical aberrations that arise when the imaged planes are positioned at their foci (f_os), i.e. at the designed object planes. Consequently, when OLs are used to image planes not located at f_o, as with MUM, non-corrected optical aberrations are introduced. This problem, which affects all multiplane systems, can distort the wavefronts in the non-zeroth orders from ideal, thus degrading the final images. To address this matter, the MFG is projected to counterbalance the wavefront error generated by these aberrations by imposing an equal and opposite phase shift to the wavefronts coming from the non-designed plane positions, thus obtaining flat wavefronts in all orders (fig. 2.8b). Consequently, all aberrations (defocus, spherical, etc.) are minimised to those expected for the used OL, allowing the imaging of several planes simultaneously. However, this implies the MFG has to be specifically designed and tailored to the optical system with which it will be used, otherwise the aberration correction will be lost. The MFG is a binary phase grating and has been reported to have a transmission efficiency around 65% [3]. The latter can, however, be increased (94% theoretically) by moving to multilevel etched gratings [53]. Regarding the grating-induced chromatic aberration issue, this is addressed in the setup in fig. 2.8a [3] by a multiblazed grating (MBG, which in [3] is called chromatic correction grating, CCG), the third element of the diffraction relay. The MBG (fig. 2.8c) is composed of several panels with the blazed grating facing the MFG, one per each used diffraction order. The central panel of the MBG element is flat, since the light in the 0^{th} order is not chromatically aberrated and no correction is needed. The couple MFG – MBG works

similarly to the blazed gratings/grisms pairs described in fig. 2.6b and 2.7 [40, 41]. The chromatic components of light are first dispersed by the MFG and then recollimated by the MBG. Once the chromatic aberration grating-induced has been completely reversed, light rays at all wavelengths will exit the MBG parallel to each other. Consequently, a lens positioned straight after the MBG will just focus all light coming from all panels of the MBG at the same point, totally removing the multifocal information. To avoid this, a multifacet prism (MFP) has been inserted into the relay (fig. 2.8a), thus constituting the 4^{th} optical element. The MFP is made of several prisms, one per used diffraction order, whose role is that of bending the light coming from the different panels of the MBG to different angles and direct it to the right positions on the camera chip, stopping the planes from overlapping. The central panel is flat, since the 0^{th} order should not be deviated from the central region of the detector. Prisms, however, are dispersive elements and introduce chromatic aberration [54]. Consequently, the MBG has to be designed to counterbalance the chromatic smearing due to the MFP as well. Finally, by placing another achromatic double lens (L_2) after the MFP, the different diffraction orders carrying the multifocal information can be imaged on different areas of a camera chip placed at the focal plane of L_2. The latter object constitutes the fifth element of the relay in fig. 2.8a. Also in this case the use of an aperture A is necessary to avoid the overlap among the imaged planes on the detector. The transmission of the MBG and MFP is around 95% in the lateral panels dedicated to the non-zeroth orders, while it is higher in the central flat one. Therefore, to re-establish an equal energy distribution in all orders, the MFG is also designed to slightly suppress the intensity in the 0^{th} order. Finally, as anticipated above, the MFG is designed to be used for a specific optical system and wavelength. When a different wavelength is used, one of the effects is the modification of the plane spacing Δz. Hence, a wide bandwidth $\Delta\lambda$ will introduce axial chromatic aberration [51] as in the cases with the DDG [41] and the use a filter to narrow it (e.g. to 30 nm [5]) can be required.

The Abrahamsson et al. setup [3] has successfully been tested for multicolour imaging by using a two colour relay similar to that in fig. 2.8a [53]. This relay has been built by positioning a dichroic beam splitter and a mirror after L_1, in order to direct two different bandwidths $\Delta\lambda$ to two sub-relays with MFGs, MBGs and MFPs tailored for distinct wavelengths. However, despite the loss in efficiency, the design in fig. 2.8a has also been used in a multicolour configuration by positioning a dichroic beam splitter before L_2 [3]. In addition, this relay has also been used with polarised light sources to achieve multifocal polarisation microscopy [55] and it has been shown that its

diffractive elements are able to preserve the polarisation information. In [56], instead, a simplified version of Abrahamsson setup without chromatic correction system (which was performed computationally) has been presented and tested to track moving bacteria.

This setup has also been used for super-resolution microscopy with techniques as structured illumination microscopy [57] (SIM), PALM and stochastic optical reconstruction microscopy (STORM) [5, 58, 59], achieving lateral and axial super-resolutions of, respectively, 20 nm and 50 nm. Combined with particle tracking, instead, the Abrahamsson setup has been able to track the nuclear multiprotein complex RNA polymerase II ([60], involved in DNA transcription) in osteosarcoma cells [61], over an axial range of 4 μm [3]. This has revealed its complex mobility by observing its transitions between bound and mobile states. In another study [62], the nuclear distribution and diffusion of the messenger RNA (mRNA [63], involved in the transmission of genetic information from the DNA to the ribosome) in fibroblast cells [64] has also been investigated.

2.5 Particle localisation algorithms used in multiplane microscopy

Multiplane microscopy, as introduced in previous sections, allows for the simultaneous imaging of emitters observed through several planes at sample level. Consequently, this means that the information available to localise three-dimensionally an object is also spread among several planes. This has mainly been done by exploiting the 3D point spread function (PSF) fitting [13, 14, 21] and by generating calibration curves for the axial localisation [6, 20, 22].

2.5.1 *Methods based on PSF fitting*

The concept behind 3D PSF fitting is shown in fig. 2.9. As introduced in sec. 1.3.4, when an emitter is observed on an imaging plane as, e.g., a detector, the PSF shows a 2D pattern called Airy function [65], with a characteristic ring-like pattern and a central peak. This is due to the diffraction through the circular apertures of lenses. As defocus is introduced and increases, the ring-like behaviour becomes more and more dominant and the intensity of the central peak decreases ([65], fig. 1.5). This can be visualised, for example, if a 3D PSF is imaged through different planes simultaneously (fig. 2.9a) and if it is observed three-dimensionally [65] (fig. 1.5 and fig. 2.9b). The intensity of a 3D PSF will be maximised around the emitter position and will decrease moving away from it. In order to calculate the position in space of an emitter (x_0, y_0 and z_0) imaged via MUM and by using PSF fitting, it is, basically, needed to register in space the

imaged planes and fit them by a 3D PSF ([14], fig. 2.9b). The registration step is required due to the fact that the different image planes are not necessarily aligned. In addition, if each imaged plane shows a different magnification, as it is the case with non-diffractive MUM ([14], eq. 2.2), the alignment procedure should also include a stretching/compressing step to correct for that. Usually, the alignment is performed by

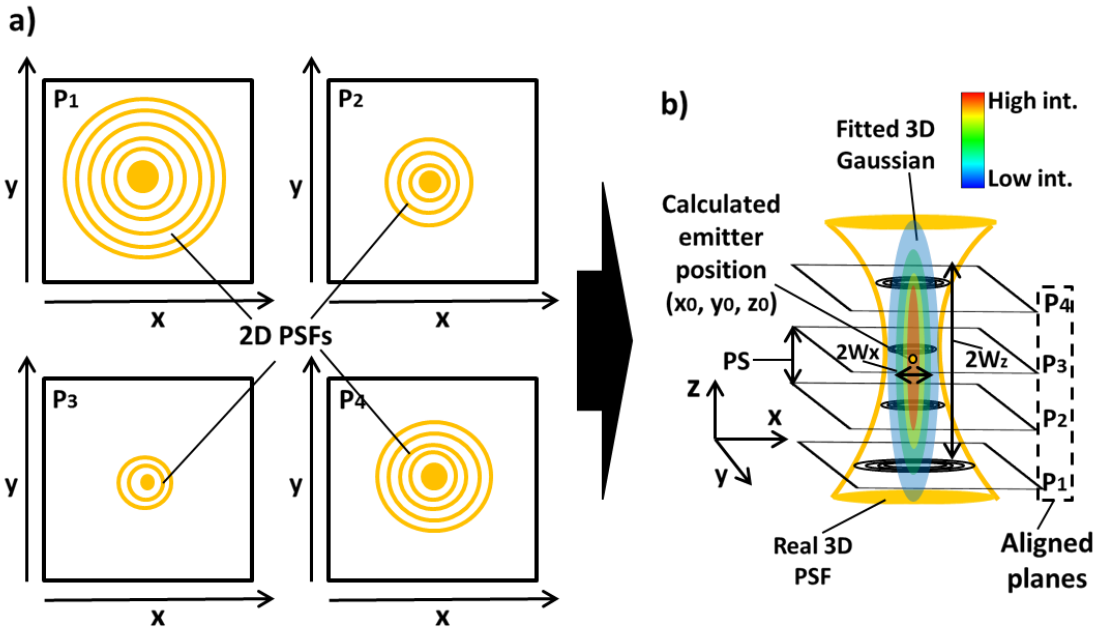

Figure 2.9 a) Schematic representation of a PSF imaged through a four planes (P_1, P_2, P_3 and P_4) multiplane system, showing 2D PSFs with different degrees of defocus. **b)** Scheme showing the imaged planes in **a** aligned and fitted by a 3D Gaussian PSF (which approximates the real 3D PSF), in order to obtained the 3D position (x_0, y_0 and z_0) of the corresponding emitter. PS is the plane spacing, int. the intensity of the Gaussian PSF and W_x and W_z are, respectively, the Gaussian curve standard deviations over x and z directions.

acquiring a z-stack (sec. 1.3.3) showing several fluorescent beads on a coverslip glass. By z-projecting (i.e. over the optical axis direction) these z-stacks into single images (e.g. by summing the images in the z-stacks), a z-projection per plane can be obtained. Each one of these will show the same fluorescent beads positioned in space, thus allowing for the lateral alignment [13, 21]. The latter has been done, for example, by fitting all the beads in the z-projections with 2D Gaussian curves or Airy functions and, subsequently, using the corresponding peaks, via designed software, to align the z-projections and, hence, the planes. This alignment procedure allows also for the creation of transformation matrices to deal with possible rotations and/or plane stretching/compression needed [21]. The acquired z-stacks can also be exploited to

calculate the plane spacing (PS) achieved and compare it with the theoretical one expected. This has been obtained by calculating the total intensity in every image of all the z-stacks (i.e. one per plane) acquired and plotting them against the nominal axial positions of the images in the z-stacks. This will produce a set of bell shaped curve, one per each z-stack, whose peaks can be used to estimate the PS [1]. In [62], instead, the axial alignment has been obtained by acquiring a series of z-stacks of a deoxyribonucleic acid (DNA) [66] sample and measuring the relative information entropy [67] as a function of the axial positions of the images in the z-stacks. When applied to a z-stack, information entropy will peak at the in focus position, i.e. where the focal plane is located and there is the highest information content.

Once all the planes are spatially aligned, the fitting procedure can be performed. Fitting the imaged planes by using analytical 3D PSFs would require the use of complex equations [65], which should also take into account the role of aberrations in the system and their impact on the PSF geometry (sec. 1.5). To avoid this, Airy functions are usually approximated by using Gaussian curves, which present similar characteristics in terms of central peak, decreasing intensity when moving away from the latter and circular symmetry [68]. Consequently, also 3D PSFs are approximated by using 3D Gaussian curves, as the form shown in eq. 2.31 [3, 5, 69, 70]:

$$\mathrm{PSF}_{\mathrm{Gauss}}[x,y,z] = I_0 e^{-\left[\frac{(x-x_0)^2}{2\,W_x{}^2}+\frac{(y-y_0)^2}{2\,W_y{}^2}+\frac{(z-z_0)^2}{2\,W_z{}^2}\right]}, \qquad \text{(eq. 2.31)}$$

where I_0 is the maximum PSF intensity and W_x, W_y and W_z are the standard deviations of the 3D Gaussian over, respectively, x, y and z directions and represent, also, the width of the curve when the intensity is reduced to I_0/e. I_0, W_x, W_y and W_z can either be theoretically or experimentally determined [14, 21]. The values x_0, y_0 and z_0 are the coordinates of the central position of the curve, where the emitter is supposed to be located, and are the values extrapolated by the 3D fit. Despite the fact Gaussian fitting is an easier method than exact PSF fitting [68], in the literature the latter solution has also been applied to extract the axial positions in non-diffractive MUM systems [13], since a Gaussian profile does not accurately represent a PSF. However, instead of fitting a 3D theoretical PSF to a z-stack of imaged planes, this is done by fitting 2D functions that take into account the aberration effects to each imaged plane simultaneously (after converting the image counts into photon counts [71]), by using the following equation (eq. 2.32):

$$\mathrm{PSF_{Airy}}[r, W] = \mathrm{Amp} \int_x \int_y \left| \int_0^1 \rho \, J_0 \left(\frac{2\pi \, \mathrm{NA} \, \rho}{\lambda \, M} \sqrt{r} \right) e^{i \, W} d\rho \right|^2 dx \, dy. \quad \text{(eq. 2.32)}$$

In eq. 2.4 Amp is the amplitude term, W is the aberration term, r is the radial distance from the centre of the function, ρ is the pupil function [72], which can vary between 0 and 1, NA is the numerical aperture of the objective lens, M is the magnification measured in the fitted plane, λ is the emission wavelength and J_0 is the 0^{th} order Bessel function of the first kind [73]. The amplitude, radial and aberration terms are functions of several parameters, such as the emitter position $\{x_0,y_0,z_0\}$, the PS and the M. The PS is calculated as explained above, while the magnification M in each plane is determined by acquiring fluorescent bead z-stacks and measuring the relative distances between bead pairs in each z-projection associated to the different planes. The difference in distances between the same bead pairs in different planes will determine the values of the relative M. In order to evaluate the axial position of the emitter z_0, each 2D PSF in each plane is first fitted by an Airy function [68] to extract the lateral positions x_0 and y_0 in all planes. This done, these values are then inserted into a set of equations equal to eq. 2.32 (i.e. one per plane), which will be solved simultaneously to extract the value of z_0. In general, with PSF fitting solutions, it is possible that not all the system planes are used, since this depends on the number of planes on with the PSFs are simultaneously visible [7]. As anticipated in sec. 1.3.9 and differently from non-simultaneous planes acquisition, MUM can allow to recover the axial positions of emitters over depths (i.e. axial ranges) longer than the distances between the first and last planes imaged. This is possible thanks to the ability of multiplane localisation algorithm to deal with defocused images. In addition, MUM can also avoid the depth discrimination problem present in single plane optical microscopy and caused by the axial symmetry of PSFs ([74, 75], fig. 2.9b), which does not allow to evaluate if an emitter is above or below the imaged plane. Usually, to estimate the axial range achievable with multifocal setups and algorithms, test emitters are repeatedly displaced over the optical axis by known steps, in order to recover their average axial positions and precisions and compare them to the nominal expected ones [7, 13, 14]. Generally, by using 3D fitting algorithms, axial ranges up to 8 μm [7] and precisions down to 5 nm [5] have been reached. However, it should be pointed out that these performance parameters, as for all imaging techniques, are strongly dependent on the signal level (signal to noise [71] and signal to background ratios [76]), In addition, in MUM they are also correlated to the number of used planes and to the plane spacing (PS) [13, 74, 75]. Theoretical and experimental studies have

shown that the axial range can be raised by increasing the PS and/or the number of planes. However, if the PS is too large and does not allow to image an emitter at least with two planes simultaneously, multifocal imaging abilities will be lost, since the system will fall into single plane imaging conditions and the axial depth discrimination will not be possible anymore. The same would happen in the opposite case, i.e. if the PS is too small. Regarding the number of planes, instead, this can have a strong impact on the lateral localisation precision, since it determines into how many channels the total amount of photons (i.e. the signal) is split, and so the signal to noise ratio (SNR) per plane.

2.5.2 *Methods based on the generation of calibration curves*

In parallel to PSF fitting, also calibration curve solutions have been applied to evaluate the axial positions of emitters imaged with MUM setups. For a biplane system [22] a calibration curve has been built by, first, acquiring a series of emitter z-stacks as described before. Than the PSFs in each plane and at each axial position of every z-stack have been fitted by 2D Gaussian curves to identify the average PSF centres. Finally, a calibration curve has been calculated by using the following equation (eq. 2.33):

$$\mathrm{Cal[z]} = \frac{\mathrm{Peak_1[z] - Peak_2[z]}}{\mathrm{Peak_1[z] + Peak_2[z]}}, \qquad \text{(eq. 2.33)}$$

where Cal[z] is the calibration curve, $Peak_1[z]$ is the pixel value at the 2D Gaussian peaks in plane 1 and $Peak_2[z]$ the equivalent one in plane 2. Eq. 2.33 is a discrete function, since it has values only corresponding to the axial positions of the images in the acquired z-stacks. Interpolating the latter will allow to have a continuous functions with unique values at each axial positions. This function can subsequently be inverted to obtain the unknown axial positions of emitters, given the values of Cal. Another calibration based algorithm is presented in fig. 2.10 [6]. As in the previous case [22], also with this one it is first necessary to acquire a series of emitter z-stacks and then fit the PSFs in each plane and at all axial positions by using 2D Gaussian curves. This allows to identify a series of concentric sub-regions of interest (sub-ROIs, fig. 2.10a) positioned on the PSFs. The first sub-ROI (S_1) will be the pixel containing the Gaussian peaks, the second one (S_2) the eight pixels surrounding it, the third one (S_3) the sixteen pixels around S_2 and so on, depending on the emitter size. The total intensity into each sub-ROI is then background subtracted and normalised with respect to the maximum

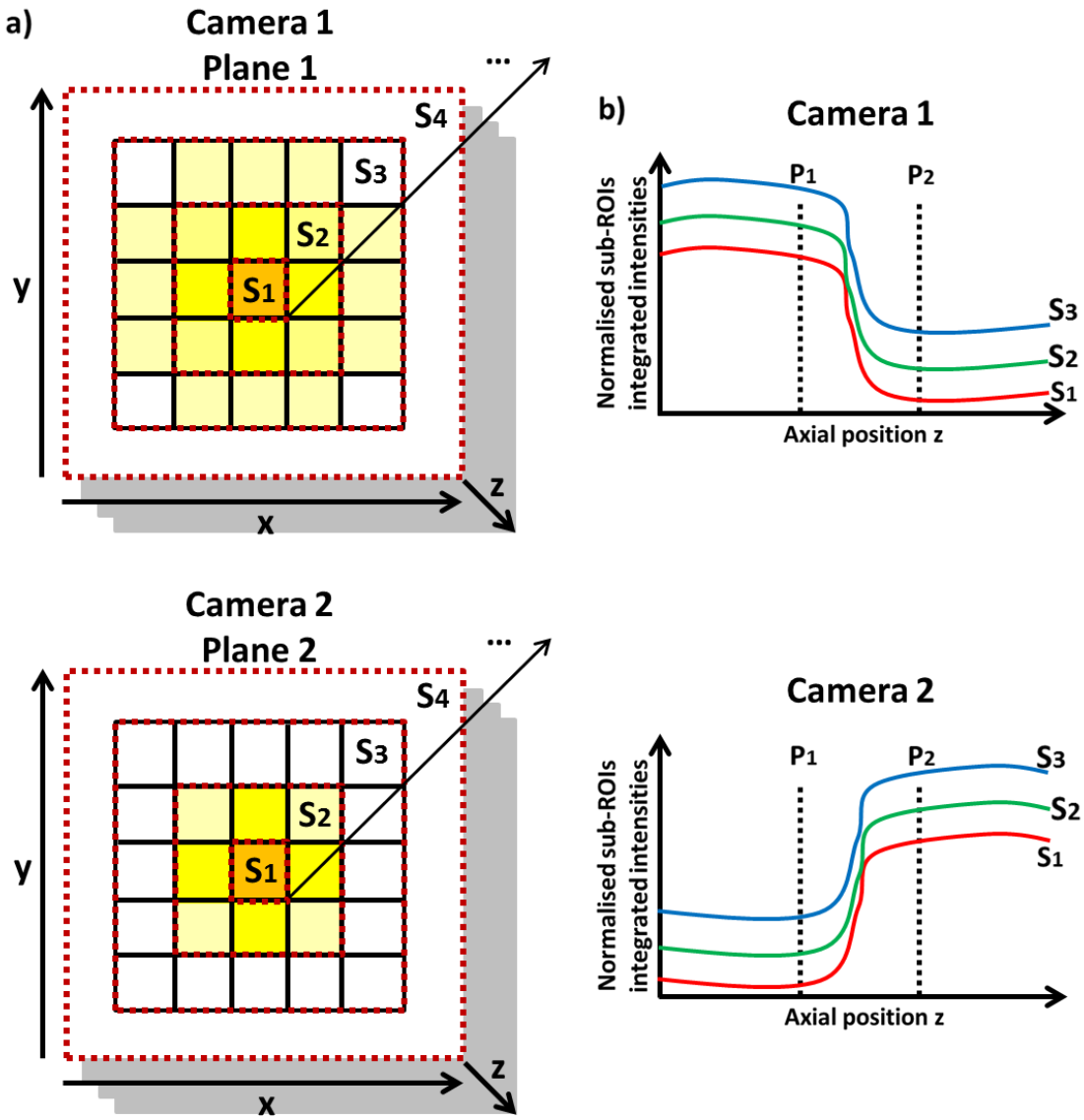

Figure 2.10 Schematic representation of how the calibration curves in **[6]** are calculated for a two plane system with two cameras (image reproduced for clarity and adapted from **[6]** with permission). The integrated intensities in the concentric sub-ROIs (**a**, S_1, S_2, S_3 and S_4) surrounding the PSF in all the imaged planes are calculated for all axial positions z and normalised with respect to the maximum value obtained among all those calculated. This allows for the calculation of a set of calibration curves (**b**, one per ROI and per plane), which can then be used to estimate unknown axial positions. P_1 and P_2 are, respectively, the axial positions of plane 1 and plane 2.

one among all those calculated. This permits the construction of a set of calibration curves, one per each sub-ROI and plane, which vary with the axial position z. For example, if the multiplane system consists of two planes (P_1 and P_2) and each PSF is identified by three sub-ROIs, six calibration curves will be obtained (fig. 2.10b). Also in

this case the calibration curves need to be interpolated to extend them continuously over the studied axial range. With this algorithm the axial positions of unknown emitters are calculated by comparing the various sub-ROI normalised values associated to each multiplane image to the calibration curves via a least squared method [77]. Calibration curves for the axial localisation in MUM have also been built by directly exploiting the increase in diameter of PSFs with defocus [20]. This has been done by using a biplane system, where one of the planes was positioned on the coverslip glass and the other one below it, in order to avoid the emitters from being focused in it. The plane on the coverslip glass has been used to recover the lateral positions of the PSFs by mean of 2D Gaussian fits, while the other one to calibrate the defocused PSF diameter against the emitter axial position (again, by using z-stacks as with the other calibration methods mentioned [1, 14]). This has generated a linear calibration curve, whose fit can be used to recover unknown axial positions. It is important to notice that this algorithm, even if it uses a single plane to infer the axial positions, is not affected by the depth discrimination problem. This is due to the fact that the plane used for the axial localisations is positioned below the coverslip glass, thus fixing the side of the plane on which the emitters can be observed. These calibration algorithms applied to MUM have been reported to have achieved axial ranges over 6.5 μm and axial precisions below 3 nm.

Calibration curves to infer the axial positions in MUM have also been obtained by exploiting PSF engineering techniques ([11], sec. 1.3.10). In [24] a setup similar to that in fig. 2.1c (non-diffractive MUM), but with three planes, has been modified by inserting a cylindrical lens before each one of the three cameras used to obtained z-dependent elliptical PSFs. In [58, 59], instead, a cylindrical lens has been added to Abrahamsson setup in fig. 2.8a (diffractive MUM) either after the first lens of the relay or just before the detector. This is possible since cylindrical lenses introduce depth dependant astigmatism [78, 79] (fig. 1.12). This, as explained in sec. 1.3.10, will make the PSF appear as elliptical when defocused and circular when in focus and the size and orientation of the ellipse can be used to recover the axial position. This PSF engineering technique, when applied to single plane optical microscopy, has been reported to have reached an axial range of around 1 μm [11]. The latter could be considerably expanded by combining this PSF engineering technique and MUM. In addition, these astigmatic setups have also shown advantages in situations where the emitters are visible in single rather than multiple planes and 3D PSF fitting cannot be implemented efficiently. Indeed, the asymmetry introduced in the astigmatic PSF can still allow for axial

localisation. To build these calibration curves, a series of z-stacks are acquired as described with the previous algorithms. The elliptical PSFs obtained in every plane and at all axial positions are then fitted, for example, by using anisotropic 2D Gaussian curves of the form [24] (eq. 2.34):

$$\mathrm{PSF}_{2D-\mathrm{Gauss}}[x,y] = \frac{\mathrm{const}}{2\pi\, w_x\, w_y} e^{-\left[\frac{(x-x_0)^2}{2\,W_x{}^2}+\frac{(y-y_0)^2}{2\,W_y{}^2}\right]} + b. \qquad \text{(eq. 2.34)}$$

where b is the average background and the value of const is linked to the intensity of the PSF. In fig. 2.11a an example of a 2D Gaussian curve obtained by plotting eq. 2.34 is shown, where b = 0, W_x = 425 nm, W_y = 850 nm and const = 6,800 nm^2. Clearly, due to the fact that $W_x \neq W_y$, the Gaussian curve in fig. 2.11a is anisotropic and presents an elliptical shape. By plotting the values of W_x and W_y against the axial positions of the Gaussian profiles they belong to, a couple of calibration curves as those schematised in fig. 2.11b can be obtained per each imaged plane. These have then been fitted by using 3rd degree polynomials [80] or an equation as [24] (eq. 2.35):

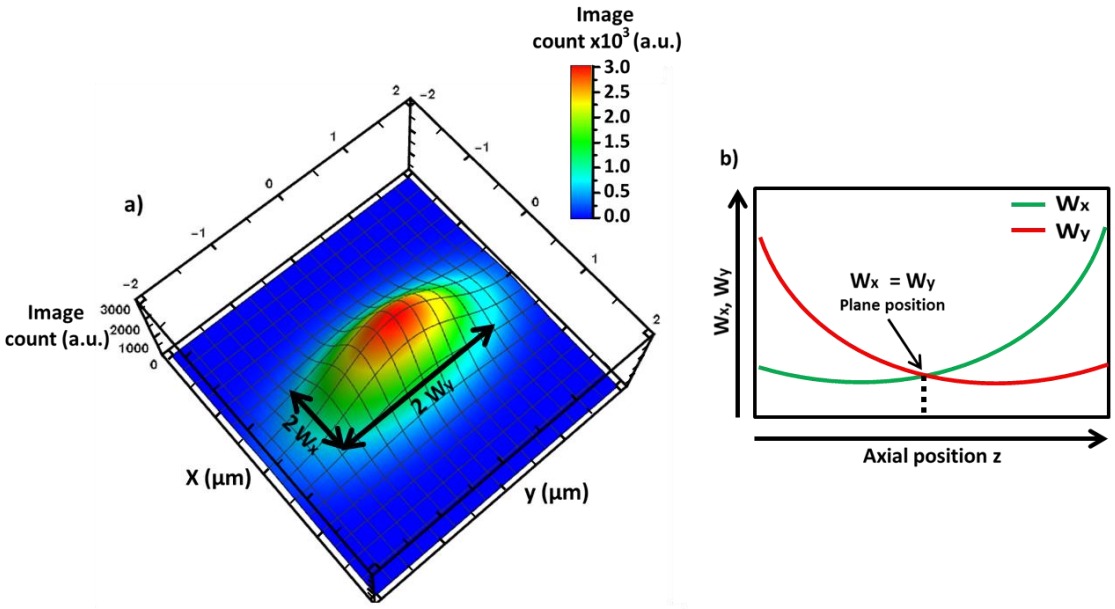

Figure 2.11 a) Example astigmatic 2D Gaussian curve plotted by using eq. 2.34 [24], with b = 0, const = 6,800 nm^2, W_x = 425 nm and W_y = 850 nm. b) Schematic representation of the variation of W_x and W_y with the axial distance z of the emitter from the imaged plane, where $W_x = W_y$. W_x and W_y are, respectively, the Gaussian curve standard deviations over x and y directions.

$$W_{x/y} = W_0 \sqrt{1 + \frac{(z_0 - P_{ref})^2}{DoF} + A\frac{(z_0 - P_{ref})^3}{DoF} + B\frac{(z_0 - P_{ref})^4}{DoF}}, \qquad \text{(eq. 2.35)}$$

where W_0 is the width at the focal position, DoF is the depth of focus [81], P_{ref} is the axial position of the reference plane and A and B are non-Gaussian coefficients to take into account possible non-linear behaviours of the optical system.

Alternatively to the fitting and calibration methods, in [58] the mathematical process of cross-correlation has also been exploited to achieve axial localisation [82]. Essentially, the various images of an emitter acquired with an Abrahamsson setup corrected with a cylindrical lens have been compared, via cross-correlation, to the corresponding z-stacks acquired in the different planes. This has generated a series of cross-correlation coefficient curves (up to one per plane), which vary with z and peak at the emitter axial position, localising it.

2.5.3 *Axial position localisation based on sharpness calibration curves and maximum likelihood estimation*

Dalgarno et al. [8] have presented an axial localisation method based on calibration curves. These curves rely on the calculation of the sharpness of an image [83] as a function of its axial position. As suggested by the name, the sharpness measures how sharp an image is. This is due to the fact that sharpness is a metric that defines the level of the aberration in the image and, consequently, is maximised at minimum aberration.

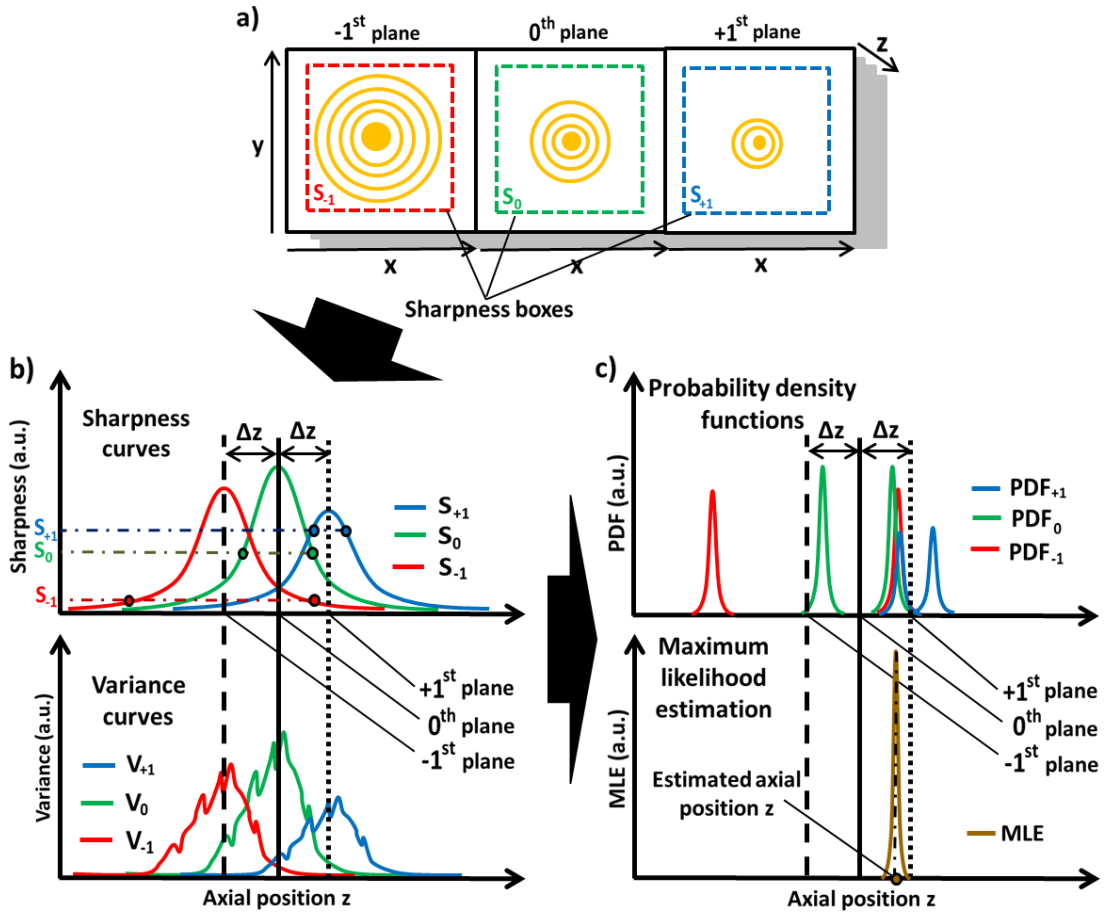

Figure 2.12 a) Scheme showing three PSFs from a single isolated with different degrees of defocus observed through three different planes and surrounded by their corresponding sharpness boxes, which allow to calculate the associated sharpness values of S_{-1}, S_0 and S_{+1} (eq. 2.36). **b)** Schematised sharpness (top) and variance curve (bottom) profiles associated with the series of PSF z-stacks acquired with a three plane system. Three example sharpness values (one per curve) and the plane positions are shown. **c)** Schematisation of PDFs (top, eq. 2.37) and MLE (bottom, eq. 2.38) curves associated with an axial localisation in a three plane system. The plane positions are shown by means of vertical lines.

As defocus is typically the dominating aberration as images are defocused, sharpness can be used to define how well focussed and, thus, sharp an image is. Examples of sharpness curves associated to a three plane system are shown in fig. 2.12.

The sharpness (S) of a 2D PSF can be calculated by using the following formula [8] (eq. 2.36):

$$S = \frac{\sum_{k=1}^{q}(n_k{}^2 - n_k)}{\left(\sum_{k=1}^{q} n_k\right)^2}, \qquad \text{(eq. 2.36)}$$

where n_k is the image count of the k^{th} pixel within a box (the sharpness box) of q pixels that contains a 2D PSF (fig. 2.12a). A depth dependant sharpness curve can be calculated by applying the formula in eq. 2.36 to all the images in a PSF z-stack. If this is done for a set of z-stacks acquired with the different planes of a MUM system, several sharpness curves (fig. 2.12b top) can be obtained. Sharpness curves are typically bell shaped for isolated PSFs. The peak position of each sharpness curve represents the best focal position of the PSF, where the related plane is located. Consequently, the distance between the positions of the peaks of adjacent sharpness curves can be used to approximate the system plane spacing (Δz). Image sharpness is also influenced by the total amount of background in the sharpness box. To take into account the variability due to the noise in the images [84] and the physical stability of the system, sharpness curves should be averaged over several z-stacks per imaged plane. This allows for the calculation of associated variance curves (i.e. the squares of the standard deviations [85]) as function of z (fig. 2.12b bottom), which are generally less smooth than the sharpness ones due to the non-perfect axial alignment among the PSFs. As with the other calibration methods introduced in previous section (sec. 2.5.2 [6, 22, 24, 58, 59]), also in this case the axial localisation is performed via comparison to the calibration curves. With the sharpness algorithm this is done by comparing the sharpness values associated to a multiplane image to the corresponding sharpness curves by exploiting Gaussian probability density functions [86] (PDFs). A PDF measures the relative probability for a system to stay in each one of the allowed states. Hence, given a sharpness value a PDF indicates the most likely associated axial positions. In [8] the PDF has the following form (eq. 2.37):

$$\mathrm{PDF_m}(z) = \frac{1}{\sqrt{2\pi\, V_m(z)}}\, e^{-\frac{(S_m - S_m(z))^2}{2\, V_m(z)}}, \qquad \text{(eq. 2.37)}$$

where $S_m(z)$ and $V_m(z)$ are, respectively, the sharpness and variance curves for the m^{th} plane and S_m is the sharpness value of a 2D PSF in the m^{th} plane and in an unknown axial position. In MUM each plane provides a sharpness value (e.g. S_{-1}, S_0 and S_{+1}, fig. 2.12a), which, due to the symmetricity of the sharpness curves, is related to two possible axial positions (fig. 2.12b top, the two points highlighted on each sharpness curve). This symmetricity is reflected in the PDF curves as well, which, unless the emitter is perfectly in focus, will also have two peaks (fig. 2.12c top). This is the depth

discrimination problem described in sec. 2.5.1 [74, 75], which is generated by the symmetry of the PSF and does not allow for the extraction of the axial positions by using single planes. However, since the particle position is unique, for each PDF curve only one of these peaks indicates the correct position and that is the axial position with a non-zero PDF value shared among all curves (fig. 2.12c top). Thus, by multiplying the PDFs associated to the various planes among them (eq. 2.38), it is possible to obtain the maximum likelihood estimation [87] (MLE, fig. 2.12c bottom) of the correct axial position:

$$\mathrm{MLE}(z) = \prod_{i=-m}^{+m} \mathrm{PDF}_m(z). \qquad \text{(eq. 2.38)}$$

The MLE function, which is an unbiased estimator [88], should provide a single peak around the correct axial position. To avoid incorrect axial localisations, each sharpness box should include a single PSF and its size should be kept equal (where possible) to that used to calculate the sharpness curves.

Dr Paul A. Dalgarno and Dr W. T. Eric Pitkeathly have also developed a ratiometric form of the sharpness curves (fig. 2.13). Ratiometric sharpness curves ($R_j(z)$) describe the aberration level in each plane in comparison to those in the others. The $R_j(z)$ curve associated to the j^{th} plane is calculated by using the following equation (eq. 2.39):

$$R_j(z) = \frac{S_j(z) - S_{Bj}}{\sum_{i=-m}^{+m}(S_i - S_{Bi})}, \qquad \text{(eq. 2.39)}$$

where S_{Bj} is the sharpness associated to the background in each plane and can be assumed to be equal to the smallest sharpness value of each sharpness curve, provided the PSF is very defocused at the corresponding axial positions. Eq. 2.39 states that the ratiometric sharpness curves ($R_j(z)$) can be calculated directly from the sharpness curves $S_j(z)$. The fact that the sharpness associated to the background is pre-subtracted can make the ratiometric sharpness curves suitable for those situations where a background subtraction might be needed (e.g. when a change in sharpness box size between sample and calibration data cannot be avoided). Differently from the sharpness curves (fig. 2.12b top), the ratiometric curves calculated for the different planes are less similar to each other and can vary from a value around 0 to one around 1 (fig. 2.13 top).

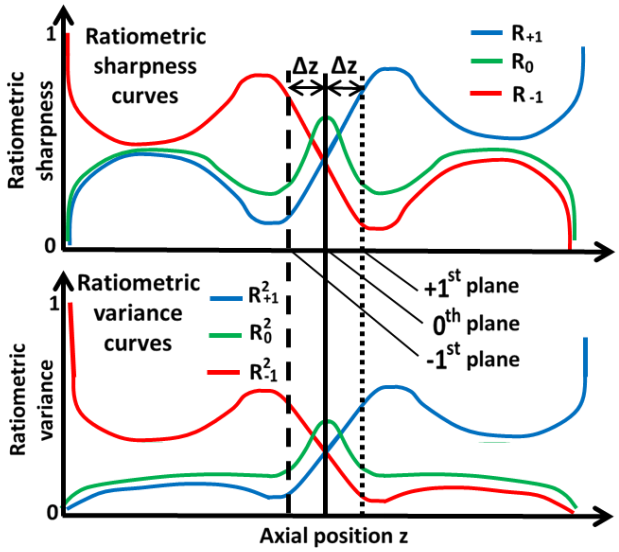

Figure 2.13 Schematised ratiometric sharpness (top, eq. 2.49) and variance curve (bottom) profiles associated to a series of PSF z-stacks acquired with a three plane system. The plane positions are shown by means of vertical lines.

Regarding the variance curves associated to the ratiometric ones, they are assumed to be equal to the square of the latter (fig. 2.13 bottom). Therefore, the PDF in eq. 2.37 becomes (eq. 2.40):

$$PDF_m(z) = \frac{1}{\sqrt{2\pi\, R_m{}^2(z)}}\, e^{-\frac{(R_m - R_m(z))^2}{2\, R_m{}^2(z)}}, \qquad \text{(eq. 2.40)}$$

where R_m and $R_m(z)$ are, respectively, the ratiometric sharpness values and curves associated to the different m^{th} planes. The MLE is then calculated by using eq. 2.38 to find the most likely axial position. The sharpness algorithm has been selected as tool for the studies (chap. 3 and 4) and application (chap. 5) of the Dalgarno multiplane system (fig. 2.5) presented in this thesis.

The sharpness and ratiometric algorithms described above have been inserted into an ImageJ [89] plugin created by Dr W. T. Eric Pitkeathly to process multifocal data (referred as independent and ratiometric methods, respectively). This MUM plugin has several features. One of them allows for the alignment of the different imaged planes with sub-pixel precision. Similarly to the techniques explained in sec. 2.5.1 and 2.5.2, this is done by using z-projected z-stacks (one per plane), where multiple bright emitters are present. The alignment feature of the plugin, first, processes the images by using a Laplacian of Gaussian (LoG) filter [90] to reduce the noise and enhance the spot

features and applies a threshold to detect bright features. Secondly, it segments the filtered/thresholded images to identify the spots and discard those made by a number of pixels below a certain threshold. Finally, the spots that have passed the segmentation step are 2D localised in each z-projection by calculating their centres of mass (CoMs). The 2D localisations associated to the non-zeroth orders are then laterally translated by the plugin to be aligned to the corresponding ones on the zeroth order. The alignment procedure is illustrated in fig. 2.14. It is performed by providing to the plugin a translation distance (fig. 2.14a), that roughly takes the corresponding spots on the different planes close to each other, and a pairing distance (fig. 2.14b), which is used to finely translate the images and find the best overlap between the CoMs within it. The lateral localisation is performed as described above, but with the difference that it is in

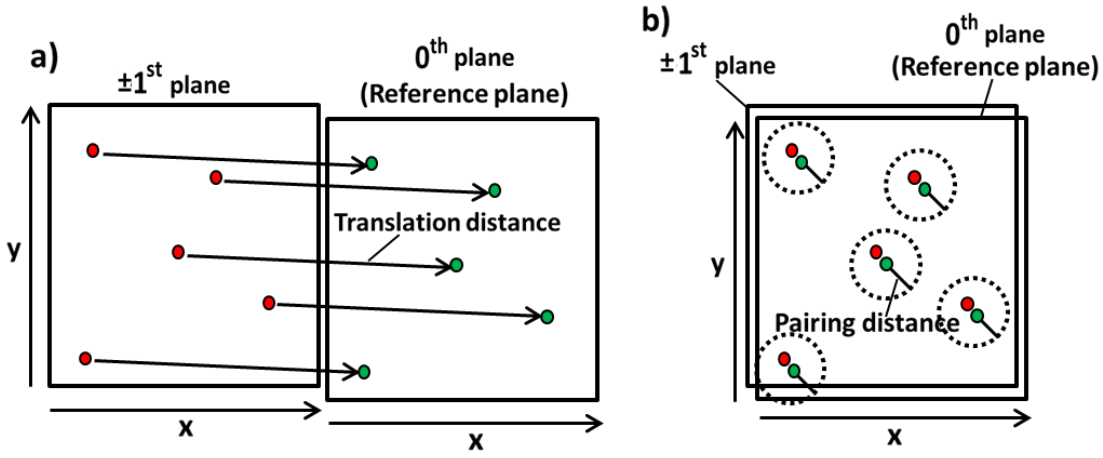

Figure 2.14 Schematisation of translation (**a**) and point matching (**b**) operations in Pitkeathly MUM plugin to achieve multiplane alignment.

3D on aligned multiplane data. The plugin performs axial localisation by exploiting all steps of the sharpness algorithm [8] discussed above. In addition, the sharpness curves are fitted by 3rd degree splines [91] to increase their number of points, while the variance curves by Lorentzian profiles [92] to make them smother. The curves obtained from the various z-stacks of the z-stack series can be axially aligned if required. The Pitkeathly plugin has also implemented a mixed deterministic-probabilistic tracking feature to work with moving emitters [93] (sec. 1.4). This has been designed to join single x-y localisations into multiple tracks (deterministic behaviour [94]), by predicting the future behaviour of the latter from the past (probabilistic behaviour [95]). Essentially, the algorithm combines x-y localisations that are within a specified spatial distance called the gate (d_G, fig. 2.15, deterministic behaviour) from positions predicted

by using an algorithm called the Kalman filter [95] (probabilistic behaviour). The latter takes

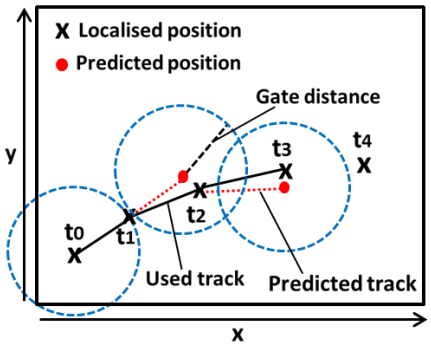

Figure 2.15 Scheme showing the tracking operation performed by Pitkeathly MUM plugin, which generates predicted positions to connect localisations at different instants (t_n) into tracks. Example predicted track and gate distance are shown.

into account the dynamic model of the motion selected. This process continues until no localisations are found within d_G and the track is terminated. To cope with the situation where one or more localisations are within the gates of several tracks simultaneously, the tracking system is also equipped with a global nearest neighbour (GNN) algorithm [94]. This is able to find the global optimal solution to assign each spot to the closest track via a cost function [96]. Once the tracks in the x-y plane have been formed, these are connected to the corresponding axial positions to obtain 3D tracks. The calculated localisation and track results can then be saved and exported to further process them. This MUM plugin has been extensively used for this thesis.

2.6 Summary and considerations

This chapter has presented the main characteristics of the diffractive (sec. 2.3) and non-diffractive (sec. 2.4) multiplane systems and the corresponding algorithms used to extract the axial localisations (sec. 2.5). As shown, non-diffractive MUM is based on the axial displacement of the detector positions with respect to the designed ones [1] (eq. 2.1), thus imaging different planes in the sample simultaneously (fig. 2.1). Conversely, diffractive MUM (fig. 2.5, 2.6, 2.7 and 2.8) exploits the focal power of distorted diffraction gratings [12], which provide an order dependent focal length and, consequently, can image several axial planes at the same time. Non-diffractive multifocal systems present in the literature suffer from non-telecentricity, thus having different magnifications per imaged planes [13] (eq. 2.2). Diffractive systems, instead, are heavily affected by lateral chromatic aberration grating-induced in the non-zeroth

planes (eq. 2.3). To avoid this problem, the emission bandwidth $\Delta\lambda$ could be strongly reduced by using narrow bandwidth filters [4] (fig. 2.5) or the chromatic aberration could be counterbalanced by using other dispersive elements [3, 40, 41] (fig. 2.6, 2.7 and 2.8). However, the first solution excludes the use of diffractive MUM from all those applications where capturing all possible photons is important (as with single molecule imaging in cells), while the second one increases the complexity of the system. Finally, it is important to underline that MUM systems induce an increase in aberrations in the non-zeroth orders, since the latter corresponds to planes imaged at position for which the objective lens has not been designed [52]. With diffractive MUM systems, however, this drawback could be counterbalanced by designing the grating element accordingly [3].

From the point of view of the axial localisation algorithms for MUM, the main solutions involve the use of either 3D Gaussian fitting [3, 13, 14, 21] or a calibration curve [6, 8, 22, 24]. In general, they have both shown to be able to localise with high precision and over extended axial ranges of emitter positions. However, 3D fitting solutions require the pre-axial alignment of the imaged planes, while this is not necessary with the use of calibration curves, since the axial plane positions are encoded in their shapes. In addition, 3D PSF fitting needs to model the PSF and this could reduce the localisation accuracy, be more computationally intense and require longer data analysis [6].

The next chapters are dedicated to the study and application of the Dalgarno setup in fig. 2.5 [4], in combination with the sharpness algorithm as the solution to recover the axial localisations [8] by using the Pitkeathly MUM plugin. The Dalgarno setup has been selected for several reasons. Differently from the non-diffractive systems in the literature, it is telecentric from the object side and, hence, presents the same magnification in all planes (eq. 2.21). It makes use of a single camera, thus avoiding problems such as camera synchronisations [18], even though this comes at the expenses of the FOV. In comparison to the Abrahamsson relay (fig. 2.8), it is simpler to design, build and align and its grating is not specifically tailored for a certain objective lens, thus making Dalgarno setup more versatile. However, the system proposed by Dalgarno et al. does not correct for the grating-induced chromatic aberration and requires the use of a narrow bandwidth filter, thus reducing the possibilities to apply this setup to single molecule imaging in cells. In addition the DDG element is not designed to eliminate the spherical aberration arising in the non-design planes. With respect to the grism design, instead [41] (fig. 2.7), the system in fig. 2.5 offers the possibility to have a plane

spacing more compatible to what might be needed by using typical emitters. Regarding the sharpness algorithm, this has been preferred to 3D PSF fitting to avoid the problems linked to the approximation of the PSF of the system and to the axial alignment of the planes. In comparison to the other calibration methods [6, 22], instead, it is easy to implement and can be used with more than two planes.

The next chapters will present the characterisation and application of the Dalgarno MUM system. In chapter 3 the impact of spherical aberration on Dalgarno MUM systems will be studied. In chapter 4 the limits on performances of MUM will be investigated in conditions of low photon fluxes, non-optimally corrected chromatic aberration and by using different objective lenses, which vary the signal sampling through their different numerical apertures and magnifications. Chapter 5, finally, will show how the Dalgarno MUM setup could be applied to perform high speed micro-particle imaging velocimetry [97] (μPIV) to reconstruct velocity and shear stress fields imposed by a fluid flowing around a cell.

2.7 References

[1] P. Prabhat, S. Ram, S. E. Ward and J. R. Ober, "Simultaneous imaging of different focal planes in fluorescence microscopy for the study of cellular dynamics in three dimensions," IEEE Transactions on Nanobioscience, vol. 3, no. 4, pp. 237-242, 2004.

[2] S. Djidel, K. J. Gansel, I. H. Campbell and H. A. Greenaway, "High-speed, 3-dimensional, telecentric imaging," Optics Express, vol. 14, no. 18, pp. 8269-8277, 2006.

[3] S. Abrahamsson, J. J. Chen, B. Hajj, S. Stallinga, A. Y. Katsov, J. Wisniewski, G. Mizuguchi, P. Soule, F. Mueller, C. D. Darzacq, X. Darzacq, C. Wu, C. I. Bargmann, D. A. Agard, M. Dahan and M. G. L. Gustafsson, "Fast multicolor 3D imaging using aberration-corrected multifocus microscopy," Nature Methods, vol. 10, no. 1, pp. 60-U80, 2013.

[4] P. A. Dalgarno, H. I. Dalgarno, A. Putoud, R. Lambert, L. Paterson, D. C. Logan, D. P. Towers, R. J. Warburton and A. H. Greenaway, "Multiplane imaging and three dimensional nanoscale particle tracking in biological microscopy," Optics express, vol. 18, no. 2, pp. 877-884, 2010.

[5] B. Hajj, J. Wisniewski, M. E. Beheiry, J. Chen, A. Revyakin, C. Wu and M.

Dahan, "Whole-cell, multicolor superresolution imaging using volumetric multifocus microscopy," Proceedings of the National Academy of Sciences of the United States of America, vol. 11, no. 49, pp. 17480-17485, 2014.

[6] R. Velmurugan, J. Chao, S. Ram, E. S. Ward and R. J. Ober, "Intensity-based axial localization approaches for multifocal plane microscopy," Optics Express, vol. 25, no. 4, pp. 3394-3410, 2017.

[7] S. Ram, D. Kim, R. J. Ober and E. S. Ward, "3D single molecule tracking with multifocal plane microscopy reveals rapid intercellular transferrin transport at epithelial cell barriers," Biophysical Journal, vol. 103, no. 7, pp. 1594-1603, 2012.

[8] H. I. C. Dalgarno, P. A. Dalgarno, A. C. Dada, C. E. Towers, G. J. Gibson, R. M. Parton, I. Davis, R. J. Warburton and A. H. Greenaway, "Nanometric depth resolution from multi-focal images in microscopy," Journal of the Royal Society Interface, vol. 8, no. 60, pp. 942-951, 2011.

[9] D. B. Murphy, Fundamentals of light microscopy and electronic imaging, Wiley-LISS, 2001.

[10] S. R. P. Pavani, M. A. Thompson, J. S. Biteen, S. J. Lord, N. Liu, R. J. Twieg, R. Piestun and W. E. Moerner, "Three-dimensional, single-molecule fluorescence imaging beyond the diffraction limit by using a double-helix point spread function," PNAS, vol. 106, no. 9, pp. 2995-2999, 2009.

[11] B. Huang, W. Wang, M. Bates and X. Zhuang, "Three-dimensional Super-resolution Imaging by Stochastic Optical Reconstruction Microscopy," SCIENCE, vol. 319, no. 5864, pp. 810-813, 2008.

[12] P. M. Blanchard and A. H. Greenaway, "Simultaneous multiplane imaging with a distorted diffraction grating," Applied Optics, vol. 38, no. 32, pp. 6692-6699, 1999.

[13] S. Ram, P. Prabhat, J. Chao, E. S. Ward and R. J.Ober, "High accuracy 3d quantum dot tracking with multifocal plane microscopy for the study of fast intracellular dynamics in live cells," Biophysical Journal, vol. 95, no. 12, pp. 6025-6043, 2008.

[14] M. F. Juette, T. J. Gould, M. D. Lessard, M. J. Mlodzianoski, B. S. Nagpure, B. T. Bennett, S. T. Hess and J. Bewersdorf, "Three-dimensional sub-100 nm resolution fluorescence microscopy of thick samples," Nature Methods, vol. 5, no. 6, pp. 527-529, 2008.

[15] D. B. Murphy, "Object - image math," in Fundamentals of light microscopy and electronic imaging, Wiley-Liss, 2001, pp. 46-50.

[16] P. Prabhat, S. Ram, E. S. Ward and R. J. Ober, "Simultaneous imaging of several focal planes in fluorescence microscopy for the study of cellular dynamics in 3D," Three-Dimensional and Multidimensional Microscopy: Image Acquisition and Processing XIII, vol. 6090, no. 60900L, 2006.

[17] Z. Gan, S. Ram, R. J. Ober and E. S. Ward, "Using multifocal plane microscopy to reveal novel trafficking processes in the recycling pathway," Journal of Cell Science, vol. 126, no. 5, pp. 1176-1188, 2013.

[18] A. D. Edelstein, M. A. Tsuchida, N. Amodaj, H. Pinkard, R. D. Vale and N. Stuurman, "Advanced methods of microscope control using μManager software," Journal of biological methods, vol. 1, no. 2, p. e10, 2014.

[19] Y. Feng, L. Scholz, D. Lee, H. Dalgarno, D. Foo and L. Yang, "Multi-mode microscopy using diffractive optical," Engineering Review, vol. 31, no. 2, pp. 133-139, 2011.

[20] E. Toprak, H. Balci, B. H. Blehm and P. R. Selvin, "Three-dimensional particle tracking via bifocal imaging," Nano Letters, vol. 7, no. 7, pp. 2043-2045, 2007.

[21] M. S. Itano, M. Bleck, D. S. Johnson and S. M. Simon, "Readily accessible multiplane microscopy: 3D tracking the HIV-1 genome in living cells," Traffic, vol. 17, no. 2, pp. 179-186, 2016.

[22] T. M. Watanabe, T. Sato, K. Gonda and H. Higuchi, "Three-dimensional nanometry of vesicle transport in living cells using dual-focus imaging optics," Biochemical and Biophysical Research Communications, vol. 359, no. 1, pp. 1-7, 2007.

[23] E. F. Fornasiero and S. O. Rizzoli, Super-Resolution Microscopy, Humana Press, 2014.

[24] J. Huang, M. Sun, K. Gumpper, Y. Chi and J. Ma, "3D multifocus astigmatism and compressed sensing (3D MACS) based superresolution reconstruction," Biomedical Optics Express, vol. 6, no. 3, pp. 902-917, 2015.

[25] J. Min, S. J. Holden, L. Carlini, M. Unser, S. Manley and J. C. Ye, "3D high-density localization microscopy using hybrid astigmatic/biplane imaging and sparse image reconstruction," Biomedical Optics Express, vol. 5, no. 11, pp. 3935-3948, 2014.

[26] S. Geissbuehler, A. Sharipov, A. Godinat, N. L. Bocchio, P. A. Sandoz, A. Huss, N. A. Jensen, S. Jakobs, J. Enderlein, F. G. v. d. Goot, E. A. Dubikovskaya, T.

Lasser and M. Leutenegger, "Live-cell multiplane three-dimensional super-resolution optical fluctuation imaging," Nature Communications, vol. 5, no. 5830, 2014.

[27] H. Lodish, A. Berk, P. Matsudaira, C. A. Kaiser, M. Krieger, M. P. Scott, L. Zipursky and J. Darnell, "Molecular motors and the mechanical work of cells," in Molecular cell biology, W. H. Freeman, 2008, pp. 79-82.

[28] D. L. Robertson, B. H. Hahn and P. M. Sharp, "Recombination in AIDS viruses," Journal Of Molecular Evolution, vol. 40, no. 3, pp. 249-259, 1995.

[29] P. Prabhat, Z. Gan, J. Chao, S. Ram, C. Vaccaro, S. Gibbons, R. J. Ober and E. S. Ward, "Elucidation of intracellular recycling pathways leading to exocytosis of the Fc receptor, FcRn, by using multifocal plane microscopy," Proceedings of the National Academy of Sciences of the United States of America, vol. 104, no. 14, pp. 5889-5894, 2007.

[30] C. M. Story, J. E. Mikulska and N. E. Simister, "A major histocompatibility complex class i-like fc receptor cloned from human placenta - possible role in transfer of immunoglobulin-g from mother to fetus," Journal of Experimental Medicine, vol. 180, no. 6, pp. 2377-2381, 1994.

[31] T. T. Kuo and V. G. Aveson, "Neonatal Fc receptor and IgG-based therapeutics," MABS, vol. 3, no. 5, pp. 422-430, 2011.

[32] M. F. Macedo and M. d. Sousa, "Transferrin and the transferrin receptor: of magic bullets and other concerns," Inflammation & Allergy-Drug Targets, vol. 7, no. 1, pp. 41-52, 2008.

[33] R. R. Crichton and M. Charloteaux-Wauters, "Iron transport and storage," European Journal of Biochemistry, vol. 164, no. 3, pp. 485-506, 1987.

[34] E. Hecht, "The fresnel zone plate," in Optics, 4th ed., Addison Wesley, 2002, pp. 495-497.

[35] C. Palmer and E. Loewen, "The replication process," in Diffraction grating, 6th ed., Newport Corporation, 2005, pp. 64-69.

[36] E. G. Loewen and E. Popov, "Introduction," in Diffraction gratings and applications, Marcel Dekker, Inc. , 1997, pp. 149-150.

[37] E. Hecht, "The Diffraction grating," in Optics, 4th ed., Addison Wesley, 2002, pp. 476-485.

[38] C. Palmer and C. Palmer, "Existence of diffraction orders," in Diffraction grating,

6th ed., Newport Corporation, 2005, pp. 25-26.

[39] E. G. Loewen and E. Popov, "Ruled, holographic and lithographic gratings," in Diffraction gratings and applications, Marcel Dekker, Inc., 1997, p. 61.

[40] P. Blanchard and A. Greenaway, "Broadband simultaneous multiplane imaging," Optics Communications, vol. 183, no. 1-4, p. 29–36, 2000.

[41] Y. Feng, P. A. Dalgarno, D. Lee, Y. Yang, R. R. Thomson and A. H. Greenaway, "Chromatically-corrected, high-efficiency, multi-colour, multi-plane 3D imaging," Optics Express, vol. 20, no. 18, pp. 20705-20714, 2012.

[42] I. H. Malitson, "Interspecimen Comparison of the refractive index of fused silica," Journal of the Optical Society of America, vol. 55, no. 10, pp. 1205-1209, 1965.

[43] "ThermoFisher Scientific," [Online]. Available: https://www.thermofisher.com/it/en/home/life-science/cell-analysis/fluorophores/alexa-fluor-488.html. [Accessed September 2018].

[44] K. Yamamura, M. Ueda, M. Shibahara and N. Zettsu, "Finishing of AT-cut quartz crystal wafer with nanometric thickness uniformity by pulse-modulated atmospheric pressure plasma etching," Journal of Nanoscience and Nanotechnology, vol. 11, no. 4, pp. 2922-2927, 2011.

[45] C. Palmer and E. Loewen, "Energy distribution (Grating efficiency)," in Diffraction grating handbook, 6th ed., Newport Corporation, 2005, pp. 38-41.

[46] B. R. Brown and A. W. Lohmann, "Complex spatial filtering with binary masks," Applied Optics, vol. 5, no. 6, pp. 967-&, 1966.

[47] C. A. Mack, "Defocus," in Field Guide to Optical Lithography, SPIE Press, 2006, p. 25.

[48] D. C. O'Shea, "Reducing aberrations," in Elements of modern optical design, John Wiley & Sons, 1985, pp. 204-219.

[49] T. Kurihara and Y. Takaki, "Improving viewing region of 4f optical system," Optics Express, vol. 19, no. 18, pp. 17621-17631, 2011.

[50] W. A. Traub, "Constant-dispersion grism spectrometer for channeled spectra," Journal of the Optical Society of America A - Optics Image Science and Vision, vol. 7, no. 9, pp. 1779-1791, 1990.

[51] D. C. O'Shea, "Chromatic aberration," in Elements of Modern Optical Design, John Wiley & Sons, Inc., 1985, pp. 162-169.

[52] E. J. Botcherby, R. Juškaitis, M. J. Booth and T. Wilson, "Aberration-free optical

refocusing in high numerical aperture microscopy," Optics Letters, vol. 32, no. 14, pp. 2007-2009, 2007.

[53] S. Abrahamsson, R. Ilic, J. Wisniewski, B. Mehl, L. Yu, L. Chen, M. Davanco, L. Oudjedi, J. B. Fiche, B. Hajj, X. Jin, J. Pulupa, C. Cho, M. Mir, M. E. Beheiry, X. Darzacq, M. Nollmann, M. Dahan, C. Wu, T. Lionnet, J. A. Liddle and C. Bargmann, "Multifocus microscopy with precise color multi-phase diffractive optics applied in functional neuronal imaging," Biomedical Optics Express, vol. 7, no. 3, pp. 855-869, 2013.

[54] B. E. A. Saleh and M. C. Teich, "Absorption and dispersion," in Fundamentals of photonics, 2nd ed., Wiley-Interscience, 2007, pp. 170-184.

[55] S. Abrahamsson, M. McQuilken, S. B. Mehta, A. Verma, J. Larsch, R. H. R. Ilic, C. I. Bargmann, A. S. Gladfelter and R. Oldenbourg, "MultiFocus Polarization Microscope (MF-PolScope) for 3D polarization imaging of up to 25 focal planes simultaneously," Optics Express, vol. 23, no. 6, pp. 7734-7754, 2015.

[56] K. He, Z. Wang, X. Huang, X. Wang, S. Yoo, P. Ruiz, I. Gdor, A. Selewa, N. J. Ferrier, N. Scherer, M. Hereld, A. K. Katsaggelos And O. Cossairt, "Computational multifocal microscopy," Biomedical Optics Express, vol. 9, no. 12, pp. 6477-6496, 2018.

[57] S. Abrahamsson, H. Blom, A. Agostinho, D. C. Jans, A. Jost, M. Müller, L. Nilsson, K. Bernhem, T. J. Lambert, R. Heintzmann and H. Brismar, "Multifocus structured illumination microscopy for fast volumetric super-resolution imaging," Biomedical Optics Express, vol. 8, no. 9, pp. 4135-4140, 2017.

[58] L. Oudjedi, J. B. Fiche, S. Abrahamsson, L. Mazenq, A. Lecestre, P. F. Calmon, A. Cerf and M. Nöllmann, "Astigmatic multifocus microscopy enables deep 3D super-resolved imaging," Biomedical Optics Express, vol. 7, no. 6, pp. 2163-2173, 2016.

[59] B. Hajj, M. E. Beheiry and M. Dahan, "PSF engineering in multifocus microscopy for increased depth volumetric imaging," Biomedical Optics Express, vol. 7, no. 3, pp. 726-731, 2016.

[60] R. A. Young, " RNA Polymerase II," Annual Review of Biochemistry, vol. 60, no. 1, p. 689–715, 2003.

[61] A. Luetke, P. A. Meyers, A. Lewis and H. Juergens, "Osteosarcoma treatment—where do we stand? A state of the art review," Cancer Treatment Reviews, vol. 40, no. 4, p. 523–532, 2014.

[62] C. S. Smith, S. Preibisch, A. Joseph, S. Abrahamsson, B. Rieger, E. Myers, R. H. Singer and D. Grunwald, "Nuclear accessibility of beta-actin mRNA is measured by 3D single-molecule real-time tracking," Journal of Cell Biology, vol. 209, no. 4, pp. 609-619, 2015.

[63] H. Lodish, A. Berk, P. Matsudaira, C. A. Kaiser, M. Krieger, M. P. Scott, L. Zipursky and J. Darnell, "The Three Roles of RNA," in Molecular cell biology, W. H. Freeman, 2008, pp. 119-125.

[64] M. M. Mueller and N. E. Fusening, Tumor-associated fibroblasts and their matrix, Springer, 2011.

[65] S. F. Gibson and F. Lanni, "Experimental test of an analytical model of aberration in an oil-immersion objective lens used in 3-dimensional light-microscopy," Journal of the Optical Society of America A-Optics Image Science And Vision, vol. 8, no. 10, pp. 1601-1613, 1991.

[66] H. Lodish, A. Berk, P. Matsudaira, C. A. Kaiser, M. Krieger, M. P. Scott, L. Zipursky and J. Darnell, "The Molecules of a Cell," in Molecular cell biology, W. H. Freeman, 2008, pp. 7-13.

[67] C. E. Shannon, "A Mathematical Theory of Communication," Bell System Technical Journal, vol. 27, no. 3, p. 379–423, 1948.

[68] S. Stallinga and B. Rieger, "Accuracy of the Gaussian Point Spread Function model in 2D localization microscopy," Optics Express, vol. 18, no. 24, pp. 24461-24476, 2010.

[69] B. Zhang, J. Zerubia and J. C. Olivo-Marin, "Gaussian approximations of fluorescence microscope point-spread function models," Applied Optics, vol. 46, no. 10, pp. 1819-1829, 2007.

[70] Y. L. Tong, The Multivariate Normal Distribution, Springer-Verlag, 1990.

[71] M. Hirsch, R. J. Wareham, M. L. Martin-Fernandez, M. P. Hobson and D. J. Rolfe, "A Stochastic Model for Electron Multiplication Charge-Coupled Devices - From Theory to Practice," Plos One, vol. 8, no. 1, p. e53671, 2013.

[72] D. Malacara and Z. Malacara, "Optical transfer function," in Handbook of optical design, 2nd ed., Marcel Dekker, Inc., 2004, pp. 257-261.

[73] B. G. Korenev, Bessel Functions and their Applications, Taylor & Francis, 2002.

[74] A. Tahmasbi, S. Ram, J. Chao, A. V. Abraham, F. W. Tang, E. S. Ward and R. Ober, "Designing the focal plane spacing for multifocal plane microscopy," Optics

Express, vol. 2, no. 14, pp. 16706-16721, 2014.

[75] "An information-theoretic approach to designing the plane spacing for multifocal plane microscopy," Three-Dimensional and Multidimensional Microscopy: Image Acquisition and Processing XXII, vol. 9330, no. 933011, 2015.

[76] D. R. Sandison and W. W. Webb, "Background rejection and signal-to-noise optimization in confocal and alternative fluorescence microscopes," Applied Optics, vol. 33, no. 4, pp. 603-615, 1994.

[77] J.Wolberg, Data Analysis Using the Method of Least Squares, Springer, 2006.

[78] R. Kingslake and R. B. Johnson, "Coma and Astigmatism," in Lens design fundamentals, 2nd ed., Elsevier, 2010, pp. 227-229.

[79] D. Malacara, "Testing of cylindrical surfaces," in Optical Shop Testing, 3rd ed., Wiley-Interscience, 2007, pp. 453-454.

[80] P. Borwein, Polynomials and polynomials inequalities, Springer, 1995.

[81] J. E. Greivenkamp, "Depth of focus and depth of field," in Field guide to geometrical optics, SPIE Press, 2003, p. 35.

[82] R. M. Gray and J. W. Goodman, "Convolution and correlation," in Fourier transforms: An introduction for engineers, Springer Science + Business Media, LLC, 2001, pp. 251-307.

[83] R. A. Muller and A. Buffington, "Real-time correction of atmospherically degraded telescope images through image sharpening," Journal of the Optical Society of America, vol. 64, no. 9, pp. 1200-1210, 1974.

[84] J. C. Waters, "Accuracy and precision in quantitative fluorescence microscopy," Journal Of Cell Biology, vol. 185, no. 7, pp. 1135-1148, 2009.

[85] J.Wolberg, "Statistical distributions," in Data analysis using the method of least squares, Springer, 2006, pp. 6-17.

[86] J. L. Devore and K. N. Berk, "Probability density functions," in Modern mathematical statistics with applications, 2nd ed., Springer Science + Business Media, LLC, 2018, pp. 159-171.

[87] J. L. Devore and K. N. Berk, "Methods of point estimation," in Modern mathematical statistics with applications, 2nd ed., Springer Science+Business Media LLC, 2018, pp. 350-361.

[88] R. J. Ober, S. Ram and E. S. Ward, "Localization accuracy in single-molecule microscopy," Biophysical Journal, vol. 86, no. 2, pp. 1185-1200, 2004.

[89] ImageJ, [Online]. Available: https://imagej.nih.gov/ij/index.html. [Accessed September 2018].

[90] D. Sage, F. R. Neumann, F. Hediger, S. M. Gasser and M. Unser, "Automatic tracking of individual fluorescence particles: Application to the study of chromosome dynamics," IEEE Transactions on Image Processing, vol. 14, no. 9, pp. 1372-1383, 2005.

[91] C. D. Boor, I. J. Schoenberg, K. Böhmer, G. Meinardus and W. Schempp, Spline Functions, Springer-Verlag, 1976.

[92] N. L. Johnson and N. B. S. Kotz, "Cauchy distribution," in Continuous univariate distributions volume 1, 2nd ed., John Wiley & Sons, Inc., 1994, pp. 298-336.

[93] K. S. Kaawaase and F. Chi, "A selective review on target tracking algorithms," Information Technology Journal, vol. 10, no. 4, pp. 691-702, 2011.

[94] K. Jaqaman, D. Loerke, M. Mettlen, H. Kuwata, S. Grinstein, S. L. Schmid and G. Danuser, "Robust single-particle tracking in live-cell time-lapse sequences," Nature Methods, vol. 5, no. 8, pp. 695-702, 2008.

[95] R. E. Kalman and R. S. Bucy, "New Results in Linear Filtering and Prediction Theory," Journal of Basic Engineering, vol. 83, no. 1, pp. 95-108, 1961.

[96] D. Rasch and D. Schott, "Statistical decision theory," in Mathematical statistics, Wiley, 2018, pp. 28-32.

[97] R. Lindken, M. Rossi, S. Große and J. Westerweel, "Micro-Particle Image Velocimetry (μPIV): Recent developments, applications, and guidelines," Lab on a Chip, vol. 9, no. 17, pp. 2551-2567, 2009.

Chapter 3

Impact of spherical aberration on diffraction multifocal microscopy

3.1 Chapter overview

After the theoretical description of multiplane microscopy provided in the previous chapter, here the impact of spherical aberration induced by refractive index mismatch at sample level [1], i.e. between the sample and immersion medium, for multifocal microscopy is addressed. This has been done by studying four experimental conditions: 1 μm and 100 nm beads in agarose and PDMS at several depths within the samples. Initially, the principles for the generation of mismatch-induced spherical aberration have been presented (sec. 3.2 and 3.3), showing how this affects the shape of the 3D PSFs distorting them [1] (fig. 3.5 and 3.6) and that this distortion grows with the refractive index mismatch. Then, the effect of the mismatch on the system plane spacing has been shown (sec. 3.5), indicating that the latter tends to grow as the mismatch increases (fig. 3.10). This result has also been verified through axial centre of mass calculations (fig. 3.13). Finally, the impact of mismatch-induced spherical aberration on the PSF has been quantified through the shape of the sharpness curves (sec. 3.6), showing how these get distorted as the level of spherical aberration gets higher (fig. 3.14 and 3.16). Characterising the impact of spherical aberration on multifocal imaging is important, since this can allow to generate correction factors to take it into account and help to evaluate more accurately the axial positions.

3.2 Spherical aberration induced by refractive index mismatch

Refractive index mismatch between sample and immersion medium is a well known source of spherical aberration [2, 3]. Some oil immersion microscope objectives (e.g. TIRF microscopy objectives [4]) can cancel this problem out, since they are designed to image objects located directly on the coverslip [5] and the oil refractive index maches that of the coverslip. On the other side, other kinds of objective lenses, such as long working distance, water immersion and dry objectives [6], are affected by this problem, caused by the multiple refractive index mismatches among sample, coverslip, immersion medium and objective glass. In particular, despite the high resolution achievable with oil immersion objectives [6], their imaging ability can quickly get degraded as the emitting sample is located deep into the sample, due to the spherical aberration introduced by the refractive index mismatch [1]. If the sample is water based, as it could be the case for biological speciments [6], and there is the need to acquire

images inside the sample, water immersion objective could be more appropriate, since the mismatch between sample and immersion medium is removed. In the case where there is the necessity to investigate a sample over some hundreds of micrometres axially, a dry objective might become more indicated, due to their generally long working distance [6]. However, it should be kept in mind that, every time an increasing refractive index mismatch is introduced at sample level and the distance of the emitting object from the coverslip grows within the sample, the spherical aberration becomes more severe [1]. In addition, as the refractive index of the immersion medium decreases, e.g. moving from oil to water or with air, also the numerical aperture is reduced [6], lowering the resolution laterally and axially (eq. 1.8 and 1.9).

Fig. 3.1a is a schematised representation of the optical path of a widefield microscope affected by spherical aberration induced by refractive index mismatch. In the presence of material mismatch, rays emitted from the same source located at the nominal objective focal plane, but at different angles or different distances from the coverslip, will all be imaged at positions different from the idealised one in absence of mismatch. In this case the idealised one would be the intersection between the nominal image plane (located at the tube lens focal distance) and the optical axis (o.a.), as represented by the dotted rays. The reason for the mismatch is, that from the point of view of the optical system, the rays are not coming from the nominal focus, but rather from the intersections between the projections of the refracted rays (dashed rays) and the o.a.. As already done for the excitation beam of a confocal microscope in [7], here the geometrical behaviour of an emitted light ray undergoing refraction at the mismatch between sample and immersion medium in a widefield microscope is presented in fig. 3.1b (as in [7], for the sake of simplicity the refraction at the coverslip glass has not been considered). A hypothetical ray emitted with angle theta$_s$ (θ_s) and at distance d_s from the interface between sample and immersion medium on the o.a. will be used. This ray will cross the boundary between the media at height h and will be refracted at an angle theta$_{sa}$ (θ_{sa}) by following Snell's law [8] (eq. 3.1):

$$n_s \sin\theta_s = n_i \sin\theta_{sa}, \qquad \text{(eq. 3.1)}$$

where n_s and n_i are, respectively, the refractive indices of sample and immersion medium. The incidence angle at the interface will be equal to θ_s because of Euclid's fifth postulate [9]. In a situation where $n_s < n_i$, i.e. with $\theta_{sa} < \theta_s$, the projection of the refracted ray will intersect the o.a. at a distance $d_{sa} > d_s$ from the boundary sample-

immersion medium and with an angle equal to θ_{sa} [10]. By using trigonometry it can be shown that (eq. 3.2):

$$h = d_s \tan\theta_s \qquad \text{(eq. 3.2)}$$

and (eq. 3.3):

$$d_{sa} = h \cot\theta_{sa}. \qquad \text{(eq. 3.3)}$$

The distance between the objective lens and the interface, d_i, is equal to the difference between nominal focus (NF) and d_s (eq. 3.4):

$$d_i = NF - d_s \qquad \text{(eq. 3.4)}$$

and, therefore, the apparent focus (AF) is equal to (eq. 3.5):

$$AF = d_{sa} + d_i. \qquad \text{(eq. 3.5)}$$

Combining eq. 3.1, 3.2, 3.3, 3.4 and 3.5 and dividing the result by NF, it is possible to obtain the equation for the focal shift ratio (FSR, eq. 3.6):

$$FSR = \frac{d_s \tan\theta_s \cot\left(\sin^{-1}(n_{ratio}\sin\theta_s)\right)+NF-d_s}{NF}, \qquad \text{(eq. 3.6)}$$

where $n_{ratio} = n_s/n_i$. The FSR expresses the ratio between apparent and nominal focuses (AF/NF) in terms of the conditions of the emitted light ray (d_s, θ_s), the mismatch (n_{ratio}) and the nominal objective focus (NF). It provides and understanding of the behaviour of emitted light rays in presence of sample-immersion medium refractive index mismatch, and of the associated spherical aberration, within the limits of ray optics [11].

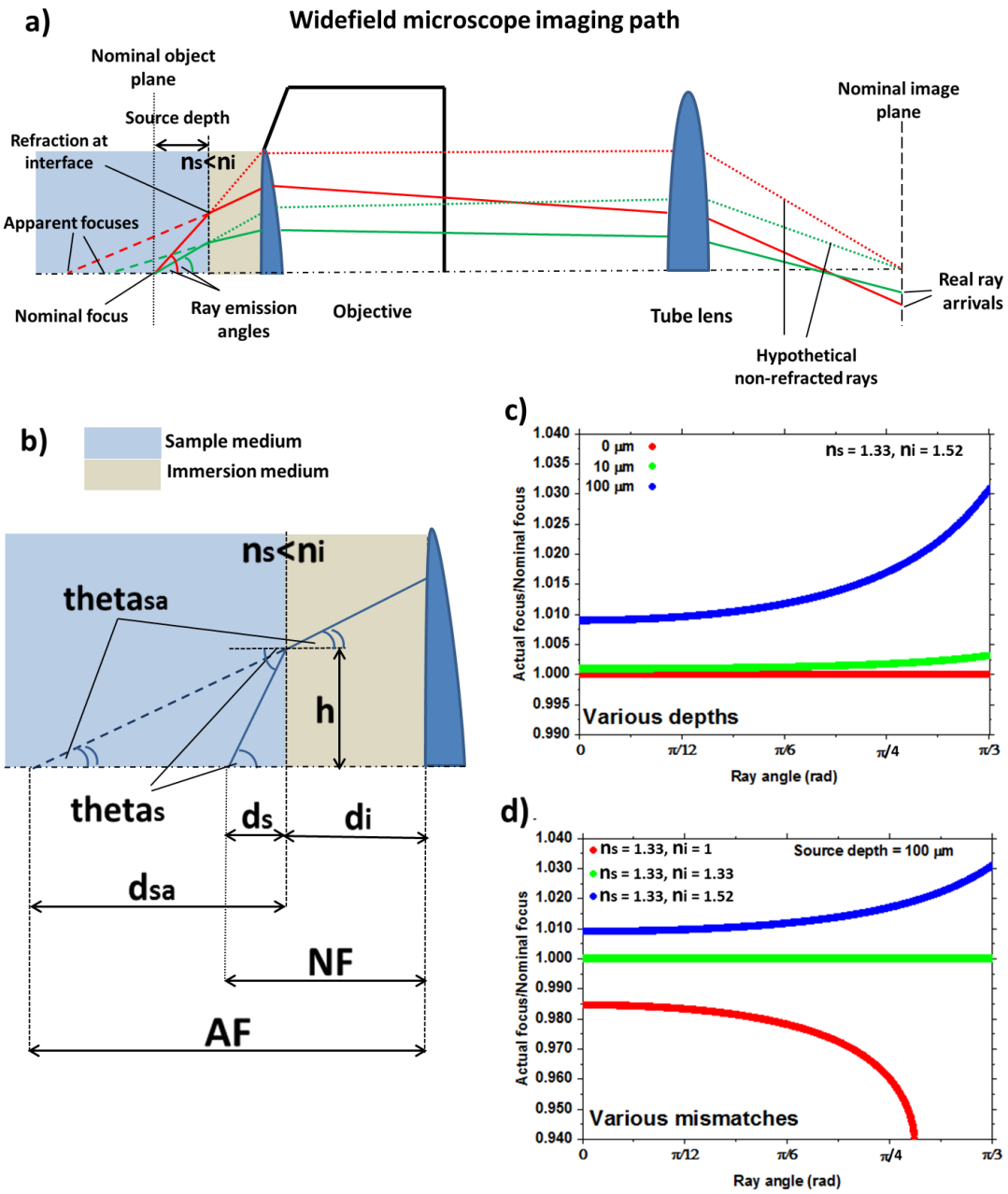

Figure 3.1 Impact of refractive index mismatch between sample and immersion medium on the generation of spherical aberration in the imaging path of a simplified widefield microscope. **a)** Scheme representing how rays emitted from the same position within the sample (the nominal focal position), but at different angles, are not imaged on the optical axis at the nominal image plane, due to the spherical aberration introduced by the refraction caused by the refractive index mismatch between sample and immersion medium refractive indices. The dashed rays are the propagated refracted ones to show the object positions (apparent focuses) perceived by the optical system, while the dotted rays represent the hypothetical non-refracted paths in absence of mismatch. **b)** Geometrical description of a ray undergoing refraction at the boundary between sample and immersion medium. The source is positioned at distance d_s from

the interface, which, in turn, is positioned at distance d_i from the objective. The apparent distance of the source from the interface is d_{sa}. The drawn ray is emitted with angle $theta_s$ (θ_s) and intersects the interface at height h. Its apparent emission angle is $theta_{sa}$ (θ_{sa}). NF is the nominal focal position and AF is the apparent one. **c)** Simulation showing how the ratio between apparent and nominal focuses changes by changing the ray emission angle, for rays emitted at different depths within the sample, but with the same refractive index mismatch (n_s = 1.33, n_i = 1.52), and **d)** same simulation as in **b**, but this time at a fixed depth within the sample (100 μm) and for different mismatches. A nominal focal distance of 1.65 mm was used for the simulation. The model does not take into account other sources of spherical aberrations, like spherical lens surfaces and refractive index mismatch at coverslip and other aberrations in general.

In fig. 3.1c and 3.1d FSR has been plotted with respect to the emission angle θ_s (which is varying from 0 rad to $\pi/3$ rad = 60°), for different source depths d_s and fixed mismatch n_{ratio} (fig. 3.1c) and for different mismatches and fixed source depth (fig. 3.1d), setting NF = 1.65 mm. In fig. 3.1c the mismatch n_{ratio} has been set equal to 0.875, i.e. sample and immersion medium refractive indices were set to, respectively, n_s = 1.33 and n_i = 1.52 (which is the case for water based sample and oil immersion lens), while the three different depths used as examples were 0 μm, 10 μm and 100 μm. As expected, the focal ratio is constantly equal to 1 for d_s = 0 μm, since in this case the ray source is positioned exactly at the interface and, therefore, no mismatch is present, making FSR independent from θ_s. The ray will cross the o.a. after the tube lens at the nominal image plane position. Increasing d_s to 10 μm, the curve deviates from unity. The ratio increases slightly at low angles, starting from a value close to 1 (≈ 1.001) at θ_s = 0 rad, and rises gradually over all simulated angles to a value of 1.003 at $\pi/3$ rad (60°). Further raising d_s to an imaging depth of 100 μm, the ratio now begins at a higher value of 1.009 for low angles and rises to 1.031 at an angle $\pi/3$ rad. Therefore, as the emitting source is moved into the sample and a refractive index mismatch is introduced, AF does not correspond to NF anymore and the emitted ray will not cross the o.a. at the nominal image plane, introducing spherical aberration. Furthermore, the latter will increase with the source depth within the sample d_s and the emission angle θ_s, indicating that, as the maximum allowed angle dictated by the objective lens numerical aperture (NA) increases, spherical aberration will increase too.

In fig. 3.1d the source depth has been fixed at 100 μm and the n_{ratio} has been varied among the values of 0.875, 1 and 1.33. As in fig. 3.1c, n_{ratio} = 0.875 represents

the mismatch between a water based sample (n_s = 1.33) and the immersion medium for an oil immersion objective lens (n_i = 1.52). Instead, n_{ratio}s equal to 1 and 1.33 are the cases for a water based sample and, respectively, the immersion medium for a water immersion objective lens (usually water, n_i = 1.33) and air (n_i = 1) for a dry objective. The blue curve in fig. 3.1d is equivalent to the blue one in fig. 3.1c, since it has been obtained at n_{ratio} = 0.875 and d_s = 100 μm. If now n_{ratio} is raised to 1, which would happen when sample and immersion medium share the same refractive indices, the FSR is equal to 1 at all used angles, since the mismatch has been removed and AF and NF are the same (this would not have happened if the refraction at the coverslip glass was included). Indeed, in absence of sample-immersion medium refractive index mismatch, no mismatch-induced spherical aberration is expected. Further increasing n_{ratio} over unity to 1.33, the FSR starts decreasing below the unity with the emission angle (i.e. AF < NF). It starts decreasing slowly from an initial value of 0.984 at θ_s = 0 rad, and then it goes down to a value of around 0.940 at $\theta_s = 10\pi/37$ rad, equivalent to 48.8°. Over this angle, the FSR assumes imaginary values, since there are no real ones. This is because this is the critical angle [12], over which total internal reflection begins and the refraction does not occur anymore (evanescent waves are not considered by this model [4]), since, with n_{ratio} = 1.33, $n_s > n_i$. Therefore, as n_{ratio} becomes different from 1, since a mismatch is introduced, the rays will deviate from their ideal behaviour and spherical aberration will be introduced. This later will increase with $|n_{ratio}-1|$ and, again, with the angle θ_s. If $n_{ratio} < 1$, then AF > NF, otherwise it will be the contrary and, over the critical angle, total internal reflection will start as well.

The focal shift ratio (FSR) equation (eq. 3.6) has the limitations of not including the refraction at the coverslip glass and not tending to a value exactly equal to 1 as θ_s tends to 0 rad (limitations also present in [7]). The latter one, in particular, is probably due to the fact that ray optics is too simple a theory to describe the behaviour of light and full optical modelling would be more appropriate to improve the accuracy of the results [13, 14] (e.g. by using Zemax [15], Code V [16] or other software). However, eq. 3.6 is still able to show that the refractive index mismatch at the interface sample-immersion medium can change the trajectory of rays from those ideal, not allowing them to be focused at the nominal image plane, hence introducing spherical aberration. This is what would happen in multiplane microscopy (MUM), where the objects under study are typically located within the sample medium [17, 18, 19], usually some micrometres from the coverslip glass, causing the appearance of spherical aberration mismatch-induced. In addition to that, in MUM, as explained in sec. 2.4.5 and unless

some corrections have been applied [5], other aberrations will arise due to the fact the objective lenses are used at non-design planes.

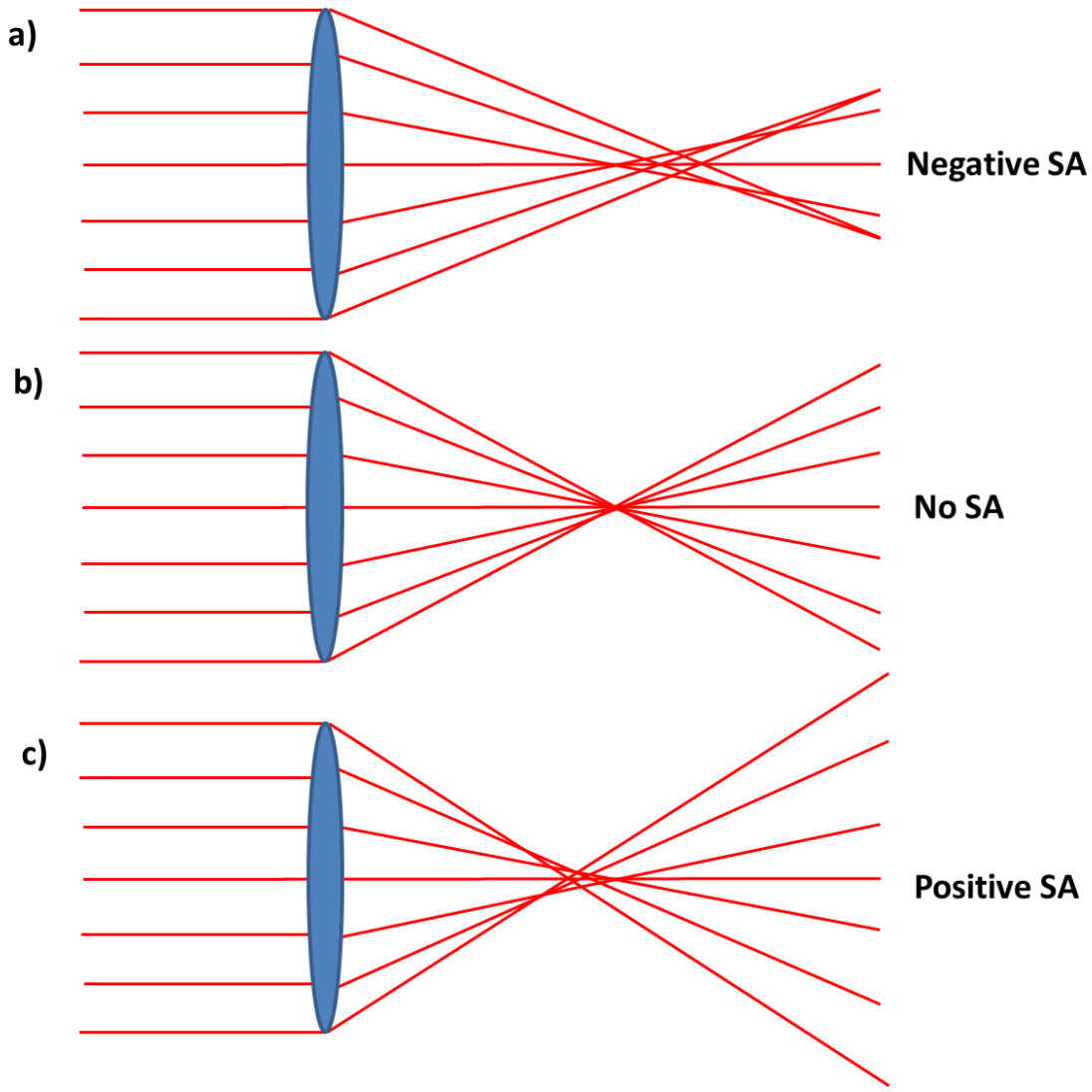

Figure 3.2 Schematic representation of the different kinds of spherical aberration (SA) by using ray optics. **a)** Negative spherical aberration, **b)** no spherical aberration and **c)** positive spherical aberration. Light is coming from the left.

Spherical aberration mismatch-induced at the interface sample-immersion medium is only one of the sources of spherical aberration. Other sources could be, for example, the refractive index mismatch among sample, coverslip glass and immersion medium (e.g. when dry or water immersion objectives are used) [6], the spherical aberration induced by the non-homogeneity of the refractive indices in the samples [20] and that induced by the sphericity of the lens curvatures in the optical system, since spherical lenses do not have a single focal point [21]. In particular, the latter source of spherical aberration can be reduced by tuning the lens radii or by using an aspherical

surface [22], but it cannot be eliminated. The combination of all the sources of spherical aberration produces the final spherical aberration pattern, which can be differentiated between positive and negative spherical aberration and distorts the final images. This has been schematised in fig. 3.2. In fig. 3.2b the case without spherical aberration shows that all the incoming parallel rays are focused at the same focal position. However, this is an ideal and unrealisable case, since, in general, those parallel light rays are focused at different distances from the lens, effectively depending on their initial distances from the optical axis. In particular, when rays travelling closer to the optical axis are focused closer to the lens (fig. 3.2a), the spherical aberration is said to be negative, vice versa (fig. 3.2c) it is called positive [23, 24].

In the following sections the impact of mismatch-induced spherical aberration on images acquired by the Dalgarno multifocal microscope [18] under study will be described. By exploiting the influence of spherical aberration on the shape of the sharpness curves, information relative to the amount of aberration has been extracted, together with the ability of the system to accommodate that. The experimental setup and method will be explained first.

3.3 Description of the experimental setup, materials and method used to evaluate the amount of spherical aberration in the Dalgarno multifocal microscope

To achieve multiplane imaging, the Dalgarno multifocal relay under study [18] presented in fig. 2.5 was used to convert a single plane widefield Zeiss Axio Observer microscope (Axio Observer.Z1) into a multiplane one. In this work a three-plane system was used. In fig. 3.3a the exact specifications used are shown on a scheme of the studied multiplane system (the image of the distorted diffraction grating has been extracted from [25]). Starting from the optical components, two 150 mm achromatic doublet lenses (Thorlabs, AC254-150-A), placed within two lens mounts (LM) and, thereby, spaced 8.49 mm (L_d) apart, were used. These lenses were positioned with the two thicker elements of the doublets facing each other, in order to minimise the off axis aberrations [26]. Knowing the focal lengths of the two lenses in the visible range and that the spatial separation between their closest principal planes [27] (whose positions were evaluated via the software Zemax [15]) was 11.06 mm, it was possible to calculate through eq. 2.16 the effective focal length (EFL) of the two lens system, which was 77.87 mm. This value is very important, since it allowed to establish the exact positions of object, Fourier [28] and image planes of the diffraction relay. Indeed, the relay being a system that has to provide a 1x magnification (i.e. no magnification), the object plane

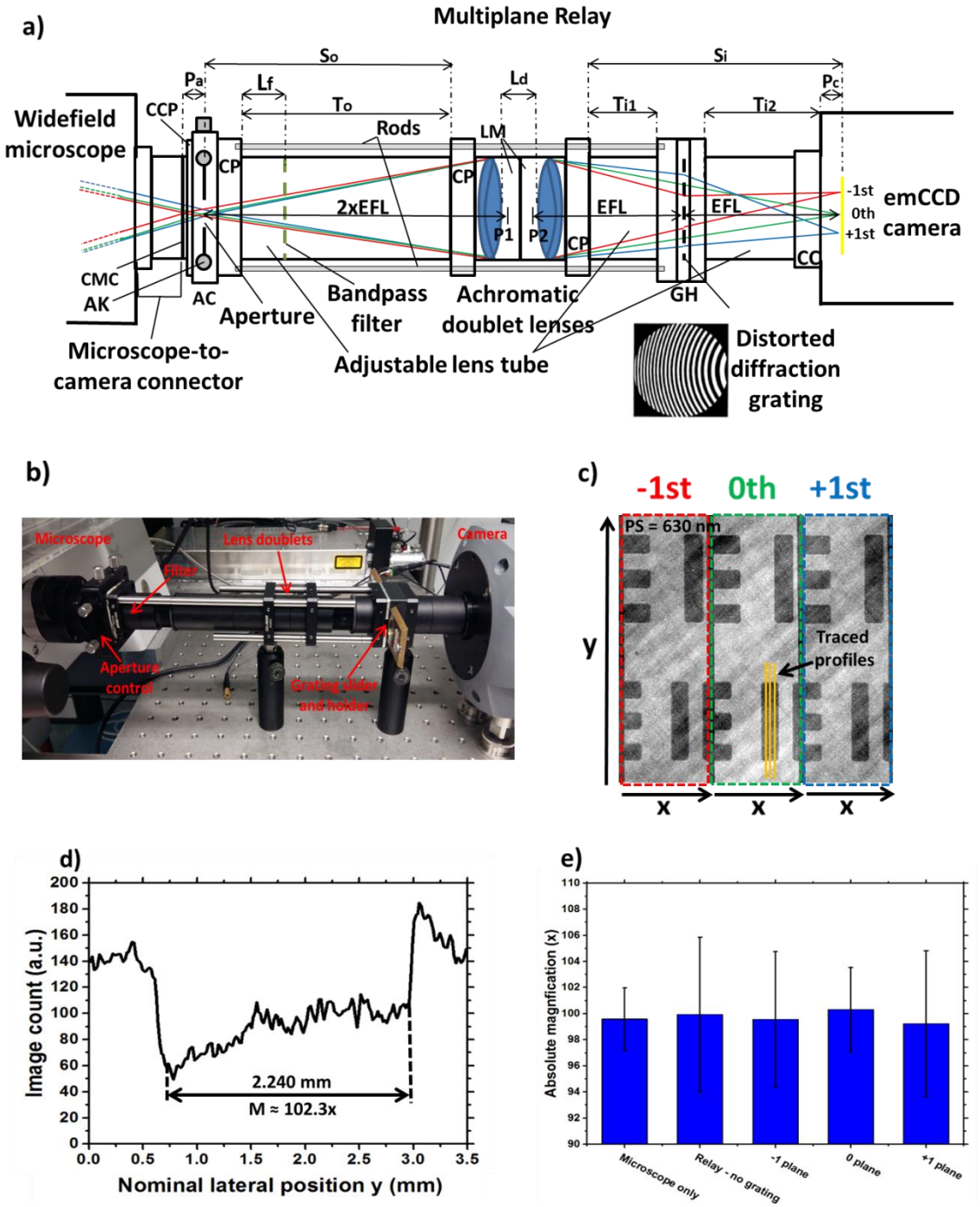

Figure 3.3 a) Specifications of the exact diffraction multifocal relay used (top view). CMC = C-mount connector, CCP = custom cage plate, AC = aperture control, AK = aperture knob, CP = cage plate, LM = lens mount, GH = grating holder, CC = camera connector, EFL = effective focal length, P1 = first principal plane of the compound lens, P2 = second principal plane of the compound lens, P_a = pre-aperture distance, P_c = pre-camera distance, L_f = length to filter, L_d = inter-lens distance, T_o = tube length on the object side, T_{i1} = first tube length on the image side, T_{i2} = second tube length on the image side, S_o = object side length and S_i = image side length. The schematisation of the distorted diffraction grating has been extracted from

[25]. **b)** Picture showing the diffraction multifocal relay used for the experiments. The grating is inserted. **c)** Image of the 1951 USAF resolution test acquired with the relay and the used grating in place. Some of the profiles traced to evaluate the magnification are show (yellow lines). Exposure time = 100 ms, em gain = 3,000. **d)** Lateral profile and magnification obtained by averaging the three example traces in **c** (yellow lines). **e)** Magnification test realised to verify that the built diffraction relay had a magnification of 1x. The bar chart compares the absolute values of the magnifications obtained without the relay, with the relay in absence of the grating and with the grating in the diffraction orders. Error bars are provided and represent the calculated standard deviations.

had to be placed two focal length before the first principal plane of the compound lens system (P1), while the image plane had to be located two focal length after the second principal plane of the relay (P2). P1 and P2 positions were also evaluated via Zemax to be in the space between the two doublet lenses, respectively, at 1.74 mm and 6.76 mm from the vertex of the lens on the left in fig. 3.3a. The system had also to be telecentric from the object side [27], in order to achieve the same 1x magnification for all the three planes imaged. Therefore, the diffraction grating [25] had to be placed at the Fourier plane, which for this system is at one EFL from both P2 and from the image plane on the camera chip.

The grating was placed into a slider, with its etched face in front of the camera (to protect it from damage), and inserted in the grating holder (GH). It was oriented with its distorted rulings positioned vertically and with the ruling density decreasing from the left to the right hand side, in order to obtain three horizontally oriented images on the camera chip, with the image associated to the lowest plane on the left hand side and that associated to the highest one on the right hand side. The used grating was a binary phase grating (designed at Heriot-Watt University in MATLAB and manufactured by Photronics), with diameter 20 mm, thickness 2.5 mm and refractive index 1.46 (fused silica [29]). Since several common fluorophores emit around the green wavelengths of the visible spectrum (Alexa Fluor 488 Dye, Qdot 525 Probe, Green Fluorescent Protein, etc. [30]), it was decided to use a grating balanced at 520 nm, so to provide an equal division of the diffracted light among the first three orders (i.e. 0^{th} and $\pm1^{st}$ orders), where the majority of energy was concentrate (around 86.5%). Thereby, the etching depth (ε_d) of the used grating had to be equal to 361 nm (eq. 2.8). Considering the need to use a 520 nm wavelength (λ) to balance the energy among the orders and remove the

grating-induced chromatic aberration [31], a 10 nm bandpass filter (Semrock, FF01-520/5-25) was placed after the cage plate (CP, Thorlabs, CP06/M) that was following the relay aperture control (AC) at 12.7 mm from it (L_f).

Another characteristic involving the grating properties is the desired plane spacing. This, indeed, is controlled by the EFL of the optical relay, the magnification of the objective used (M) and the grating focal length (f_g) through eq. 2.24. The latter, in turn, depends on the grating aperture radius (R), the diffraction order (m) and the defocus coefficient (W_{20}) [25] (eq. 2.15). W_{20}, effectively, controls the curvature of the grating rulings (quadratic for this defocusing purpose), which is responsible for the degree of defocus introduced in the $\pm1^{st}$ orders and so for the plane spacing. However, as eq. 2.15 shows, f_g is controlled by a combination of factors that have to be considered as a whole to achieve the desired plane spacing (PS). In order to collect the maximum number of photons, a high numerical aperture (NA) objective was selected. This was a 100x M, 1.46 NA oil immersion objective (Zeiss, 440782-9800-000), while the immersion oil refractive index was 1.518 (Zeiss, 444960-0000-000). To get an axial range extended over several micrometres [32, 33], it was decided to set the PS around 600 nm. Therefore, the grating to select had to have, together with an ε_d of 361 nm to be balanced for a λ = 520 nm, $W_{20} = 100\lambda$ (i.e. 52 µm) and R = 10 mm, so to provide an $f_{g\pm1}$ = ±962.50 mm (eq. 2.15). This, combined with an EFL = 77.87 mm, gave a PS = 630 nm (eq. 2.24) and so it was one of the reasons why 150 mm focal length lenses were used.

The other reason to use an EFL of 77.87 mm was linked to the selected camera. The choice fell on an electron multiplying charged coupled device (emCCD) camera (Andor, iXon Ultra 897, controlled via the software µManager [34]), due to factors as its ability to reduce the read noise [35], its chip size (512x512 pixels and pixel size of 16 µm, for a chip of 8.19x8.19 mm) that, together with the used objective, allowed for a field of view (FOV) of 81.9x81.9 µm at sample level, and its reading speed (up to 26.32 frame/s using the full chip size). The space per image plane (i.e. the separation among the centres of the diffraction orders ΔI) on the camera chip had to be roughly equal to one third of the chip size, i.e. 2.73 mm, over the horizontal direction, while it had to match the full chip size over the vertical one (this dimensions correspond to those needed by the aperture in front of the relay, since there in no additional magnification provided). By taking this into consideration and that the only available grating with ε_d = 361 nm, R = 10 mm and $W_{20} = 100\lambda$ had a central ruling spacing (d_0) equal to

15 μm and, as a consequence, was producing a diffraction angle of around 35.07 mrad (≈ 2°, eq. 2.3), the best EFL to get the wanted ΔI was the one used (eq. 2.25).

Having established the optical component specifications, it was necessary to consider the opto-mechanical parts to assemble the diffraction relay. In terms of entrance aperture (AC), this had to be variable, in order to match it to one third of the camera chip size. So it was decided to use an adjustable double slit system (OWIS, SP 60), where the four lamellas could be controlled separately by four knobs (AK). To connect this AC to the microscope and the relay, it was glued to two cage plates (CP, Thorlabs, CP06/M), one per side. To attach the CP on the microscope side to the microscope-to-camera connector, a further adapter c-mount to industry-standard thread (CMC) (Thorlabs, SM1A10) had to be used, since the microscope-to-camera connector, usually attached directly to the camera, mounts on c-mount threads. At this point it is needed to consider the pre-aperture distance (P_a) in fig. 3.3a, which is the distance between the beginning of the relay at CMC and the entrance aperture position, in the middle of the AC. The entrance aperture position is the position where the microscope image should be initially formed to then be transmitted through the relay. However, this can only happen if P_a is equal to the pre-camera distance (P_c), which is the distance between the camera entrance aperture and the camera detector chip and has a value of 17.5 mm. Indeed, since, as said, the microscope-to-camera connector is generally attached directly to the camera, it has been designed with a length that was also taking into account P_c, in order to get the image formed exactly on the detector. Therefore, since the sum of the thicknesses of CMC (5 mm), CP (8.9 mm) and half of AC (7.5 mm) was 21.4 mm and so greater than the 17.5 mm needed, the CP thickness was cut down to 5 mm (becoming custom cage plate, CCP), so to allow P_a to match P_c.

Regarding the central part of the relay, it consists of two lens mounts (LM, Thorlabs, SM1L05), with two retaining rings (Thorlabs, SM1RR) screwed inside them to fix the lenses on their positions. These LM were positioned one in front the other and screwed in two CP.

The grating was positioned within a grating holder (GH), which was custom made (Heriot-Watt University) by using two CP and a custom built assembly to hold the grating slider between them. The GH has a thickness of 33.25 mm. To connect the relay to the camera, it was used a camera connector (CC) custom made (Cairn [36]), with a c-mount thread to be screwed into the camera. On the other side, the CC could allow a lens tube [37] to slide inside itself and be fixed to it.

In order to keep the relay a telecentric from the object side and 1x magnification system, the distance between the object plane and the left central CP (S_o) and the image plane and the right central CP (S_i) had to be equal to 136.64 mm, while the distance between the right central CP and GH had to allow the grating to be in the Fourier plane. To achieve that, optical tubes [37] with different lengths were combined together, giving in fig. 3.3a T_o = 120.24 mm, T_{i1} = 45.43 mm and T_{i2} = 40.47 mm. Therefore, the total length of the diffraction relay was 316.49 mm, from the CMC to the camera. Finally, some rods [38] have been used to interconnect the various components among them and provide more mechanical stability and a black cloth was put on top of the relay to avoid scattered light from the environment to get into the optical path. A picture of the diffraction multiplane relay used for the experiments is presented in fig. 3.3b.

3.3.1 *Test of the magnification provided by the distorted diffraction relay*

Once the relay was built, it was tested in order to verify that it was providing no additional magnification to the that of the microscope and that this was true also with the diffraction grating in place, since the latter indicates that the grating is positioned in the telecentric position [27]. This test was done by using a 1951 USAF resolution test target (Thorlabs, R3L1S4P). This test target is characterised by several black bars oriented vertically and horizontally, whose dimensions (lengths and widths) have precise values. These bars are divided into groups and each group into elements. The bars in each element are the same. It was decided to image the bars in the 5^{th} and 6^{th} elements of the 6^{th} group. Those in the 5^{th} element have a length of 24.6 μm and a width of 4.92 μm, while those in the 6^{th} one have a length equal to 21.9 μm and a width equal to 4.38 μm [39]. The test target was positioned on the microscope sample holder, with its pattern facing the immersion oil. To establish the relay magnification performance, several transmission images were acquired (exp. time = 100 ms, em gain = 3,000): one without the relay, with the camera directly attached to the microscope, one with the relay inserted between microscope and camera and one with the diffraction grating positioned in the relay (fig. 3.3c). These images were then compared among them to evaluate if there were differences in the calculated magnifications. By using the software ImageJ [40], three profiles have been traced along the lengths and widths of each bar (fig. 3.3c), in order to average them and estimate the correct bar sizes (fig. 3.3d). The latter was measured as the distance between the first and last relative minima in the region where the intensity drops due to the opacity of the bars. Since the obtained values were in pixel units, they have been multiplied by the pixel size (16 μm) before

dividing them by the known lengths and widths of the bars to evaluate the magnifications (fig. 3.3d). Finally, from all the magnifications obtained in each single image and order the average magnification and the standard deviation values were calculated. The results are presented in fig. 3.3e as absolute values, since the magnification provided by the microscope without relay is negative. In general, all the magnification values are very close to each other and around 100x, with the standard deviations overlapped. With the relay without diffraction grating, the measured magnification is around (99.9 ± 5.9)x, while that calculated for the microscope without the relay is (99.6 ± 2.4)x. This indicates that the relay itself does not add any extra magnification to that already provided by the microscope. In addition, when the grating is inserted, the magnifications in all three planes are very similar to each other and to those for the microscope without relay and for the relay in place without grating and have an average value of (99.7 ± 1.0)x. This means that the grating is positioned in the telecentric plane as wanted.

3.3.2 *Preparation of the agarose and PDMS samples to study the influence of spherical aberration on the diffraction relay*

After setting up the multiplane system, ad hoc samples had to be created to study the its optical properties. In order to do that, it was decided to use some transparent materials as substrate into which three-dimensionally distributed fluorescent beads where set. The latter was then used to study the shape of the associated sharpness curves [41] and extract useful information about the system as the influence of spherical aberration (3^{rd} chapter) and photon flux (4^{th} chapter), or simply to create calibration curves for tracking applications (5^{th} chapter).

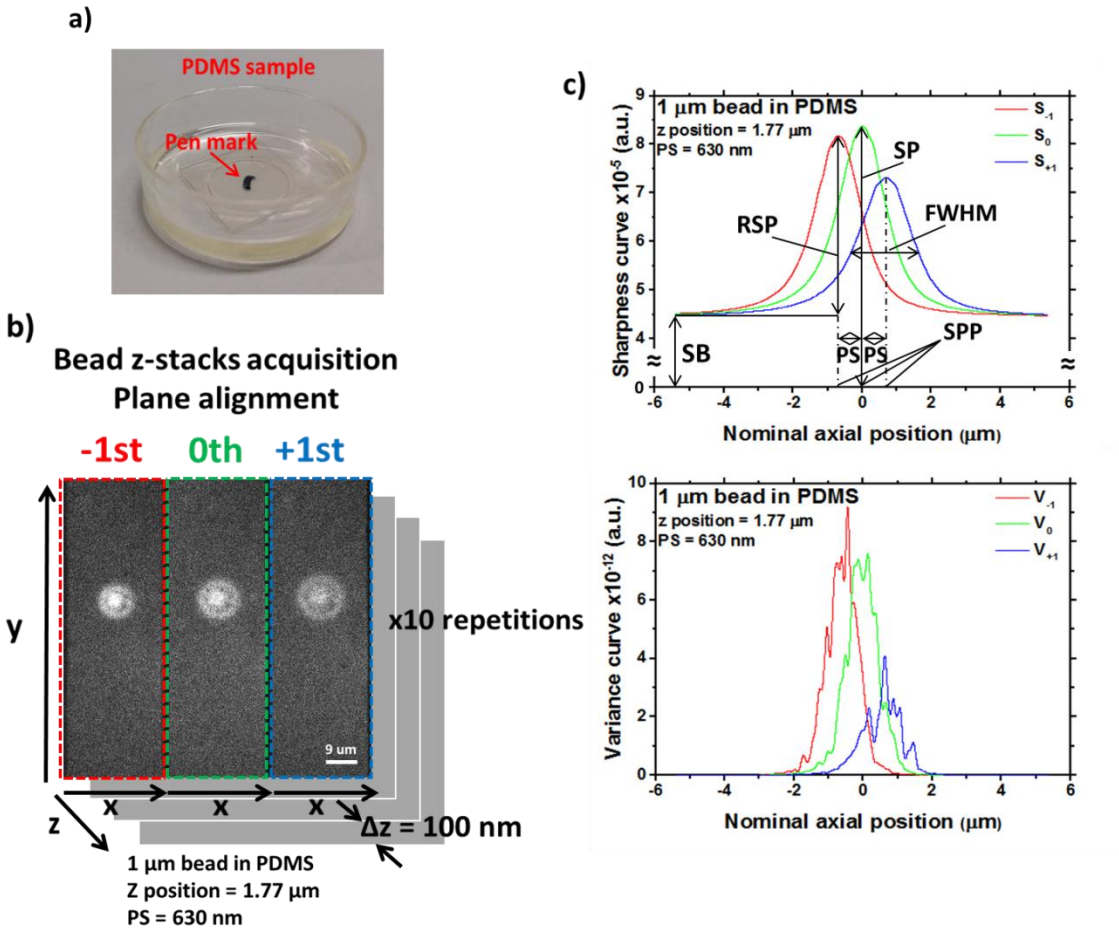

Figure 3.4 a) Picture showing one of the PDMS samples used for the experiments. The applied pen mark is visible. **b)** Scheme representing the typical data acquired via the multiplane relay for the sample shown in **a**, for the spherical aberration study presented in this chapter. In particular, the image represents a single frame of the z-stack acquired for a 1 µm bead in PDMS positioned 1.77 µm above the coverslip glass. PS = plane spacing. **c)** Sharpness curves (top) and variance curves (bottom) calculated for the same bead showed in **b**. SB = sharpness curve baseline, SP = sharpness peak height, RSP = relative sharpness peak height, SPP = sharpness peak position and FWHM = sharpness curve full width half-maximum.

As substrate materials agarose and poly-dimethylsiloxane (PDMS) polymers were selected [42, 43]. Agarose gel is widely used in biological laboratories for a variety of reasons (agarose gel electrophoresis, protein purification, etc. [42, 44]), while PDMS is commonly used for soft lithography, electronics and etc. [45, 46]. They have been chosen as substrate materials due to their transparency to visible light [47, 48] and quite different refractive indices (for agarose n = 1.33 at λ = 589 nm [49], while for PDMS n = 1.41 at λ = 589 nm [50]). Fluorescent beads emitting at 520 nm were

selected in order to match the used grating requirement. Also, in order to verify the impact of different size and brightness emitters, it was decided to use beads with diameters of 100 nm and 1 μm.

Agarose samples were prepared by adding 40 mg of agarose (Sigma-Aldrich, A2576) to 2 ml of distilled water, (2% mass of agarose in grams/volume of water in millilitres), and then either 10 μl of 100 nm yellow/green beads or 30 μl of 1 μm yellow/green beads were added directly from stock solution (Thermo Fisher Scientific, F8803 and F13081 respectively). This solution was, first, quickly manually stirred and put into a microwave for 30 s at max power to melt the agarose and then poured into a glass-bottomed dish for super-resolution microscopy (MatTek Corporation, P35G-0.170-14-C), with the top side of the coverslip manually pre-pen marked to have a reference for the surface position. Finally, the agarose samples have been left into a fridge at 4˚C for at least 15 - 20 min to let them cool down and solidify before the imaging. PDMS samples were made by mixing base and curing agent with a ratio 10:1 [50]. After manually stirring this solution for 10 min, an aliquot of 2 ml was taken and poured into a super-resolution glass-bottomed dish (pre-pen marked as the one used for the agarose sample) and the same amount of beads used for the agarose samples was added to it. At this point the sample was again manually stirred for 5 min and then put under low pressure (20 - 40 mbar) for 20 min to degas it and remove all the bubbles (this step was necessary, since PDMS is more viscous than agarose and can absorb higher quantities of gas). Finally, the PDMS samples have been cured at 45˚C for 7 h in an oven. Once cooled down in around 1 h, they were ready for the imaging. As an example, in fig. 3.4a a picture showing one of the PDMS samples used is presented.

As a quick comparison between the two samples, the agarose one is quick to prepare, but degrades within a couple of weeks and needs to be stored in a fridge, while the PDMS sample takes longer to be made, but it is more robust. Both need to be stored in a dark place to preserve the beads from photobleaching.

3.3.3 *Experimental method followed to acquire and study the data*

By using agarose and PDMS as substrate materials and 100 nm and 1 μm beads as emitters, four experimental conditions were created and investigated: 1 μm and 100 nm beads each in agarose and PDMS. For each of the four physical samples, 14 bead z-stacks have been acquired, with each bead at distinct different distances from the coverslip. The depths of the beads within the samples were evaluated by recording their axial positions relative to the in focus pen mark described previously. Considering that,

due to spherical aberration (which increases by increasing the depth within the sample and the mismatch), the best focus that can be observed is the circle of least confusion [51], it is important to realise that these positions should be considered only as nominal rather than actual axial positions, which cannot be evaluated in this way.

The z-stacks were recorded by focusing the beads on the central plane and then by moving the objective lens, with a nanometric precise piezo (Physik Instrumente**,** E-625 and P-721 PIFOC), by 100 nm steps over the ranges of ±3 and ±7 μm with respect to it, respectively for the 100 nm and 1 μm beads. All z-stacks in the same experimental conditions were recorded with the same exposure time, electron multiplying (em) gain and laser power, in order to keep them comparable. Specifically, all the z-stacks were imaged with an exposure time of 100 ms, while gain and laser power were changed among the different physical samples to avoid quick photo-bleaching, camera saturation and low signal to noise ratio (SNR) level. In particular, the used laser (Omicron, PhoxX 488-60) had a wavelength of 488 nm and laser powers at sample level of 42.6 μW and 2.1 μW, respectively for the 1 μm beads in agarose and PDMS, and 4.1 mW and 0.23 mW, respectively for the 100 nm beads in agarose and PDMS. The used em gains were, instead, 2,000 and 3,000, respectively for the 1 μm beads in agarose and PDMS, and 3,000 for both the 100 nm beads in agarose and PDMS. This is the gain value set via software and is equivalent to the real one achieved by the camera, as stated by the manufacturer [52]. All z-stacks were repeated 10 times to provide repeatability statistics and this has not caused observable photobleaching. In fig. 3.4b there is a z-stack acquisition scheme with an example frame acquired when the central plane was 3.8 μm below the position with the bead in focus in it, for a 1 μm bead in PDMS located a 1.77 μm from the coverslip glass. As observable and expected, the bead appears with different degrees of defocus in the three different planes. These z-stacks were used to calculate the relative sharpness curves of each imaged bead under each condition, through which the impact of spherical aberration on the perceived plane spacing, sharpness curve positions and shapes was evaluated. In fig. 3.4c sharpness and variance curves associated to the same z-stack used for fig. 3.4b are shown. These curves have been calculated, as explained in 2.4.3, by using the MUM plugin. The sharpness box was kept equal to 30x30 pixels and 150x150 pixels, respectively for the 100 nm and 1 μm beads and the background was not subtracted. The used acquisition parameters are summarised in next table (table 3.1):

Bead size	**Exp. time (ms)**	**em gain**	**Laser power at λ = 488 nm (mW)**	**BW (nm)**	**Obj. lens**	**Sharp. box side (pix)**	**PS (nm)**	**z-stack axial ext. (μm)**
100 nm	100	3,000	4.1 (A), 0.23 (P)	10	M = 100x, NA = 1.46, oil	30	630	±3 μm
1 μm		2,000 (A), 3,000 (P)	42.6 10^{-3} (A), 2.1 10^{-3} (P)			150		±7 μm

Table 3.1 Experimental parameters and conditions used. A = agarose, P = PDMS, M = magnification, BW = bandwidth, PS = plane spacing, NA = numerical aperture.

In the sharpness curve plot of fig. 3.3c the curve shape parameters studied are highlighted. Curve full-width half maxima (FWHM), sharpness peaks (SP, as the sum between the sharpness curve baseline, SB, and the relative sharpness peak to it, RSP) and plane spacing (PS) have been studied against the axial positions within the samples of the corresponding beads. Instead, the sharpness peak positions (SPP) have been compared to the corresponding axial positions obtained via centre of mass calculations for the same beads and this comparison has been studied with respect the bead axial positions.

3.4 Impact of mismatch-induced spherical aberration on bead cross sections and profiles

In order to understand the impact of spherical aberration on bead images and, as a consequence, on sharpness curves, lateral and axial cross sections and profiles have been observed at particular depths within the samples. This has been done for four 1 μm beads, two in agarose and two in PDMS, since these beads produce larger images than the 100 nm ones and can help to better appreciate how cross sections and profiles are affected.

In fig. 3.5 cross sections and profiles for two 1 μm beads in agarose imaged through the central plane located at axial distances from the coverslip equal to 0 μm and 28.62 μm are shown. The cross sections associated with the bead at z = 0 μm are shown on the left hand side of the figure, while those for the bead at z = 28.62 μm are on the other side. Also, the positions through which the lateral cross sections have been observed and the profiles have been calculated are identified in blue for the bead at z = 0 μm and in red for the one at z = 28.62 μm. Cross sections and profiles have been

obtained by using ImageJ. The cross sections shown belong to the first z-stack of every used z-stack series, while the profiles, tracked through the positions where the maximum signal was observable, have been calculated by using the same cross sections in the first three z-stacks of every used series to reduce the required computational time. The curves in the profile plots have been centred one respect to the other through their maxima and then this position has been set as zero. The scale of the x axes in the lateral profile plots has been transformed from pixels to micrometres by taking into account the pixel size and the objective lens magnification. For the axial profiles, instead, it was sufficient to take into account the axial distance between the images acquired in the z-stacks. Fig. 3.5d and 3.5f show the axial cross sections of the two beads. At first impression, the axial cross section for the bead at z = 0 μm seem shorter in comparison to the one for the bead at z = 28.62 μm. This can be confirmed by observing the axial profiles in fig. 3.5e, calculated through the horizontal lines in fig. 3.5d and 3.5f. The FWHM of these profiles, calculated as the distance between the two half-maxima points (where the maximum is not absolute, but relative to the lowest point in the profile), increases from 2.1 μm for the bead at z = 0 μm to 3.3 μm for the one at z = 28.62 μm. Simultaneously, the peak of the profiles gets reduced from around 3,400 image counts (IC) to almost 1,200 IC. Moving from the axial cross sections to the lateral ones, in fig. 3.5a and 3.5c the lateral cross sections through the best focal positions for, respectively, the beads at z = 0 μm and z = 28.62 μm are shown. The best foci have been selected as the axial positions where the peaks of the profiles in fig. 3.5b were maximised. The two cross sections in fig. 3.5a and 3.5c look similar to each other. However, by observing their profiles (fig. 3.5b), a difference is evident, since there is a strong reduction in the profile peaks from 3,080 IC to 1,170 IC as the axial position of the bead changes from 0 μm to 28.62 μm. In terms of FWHMs, instead, there is basically no change between the two beads and it is around 1.1 μm, even though the profile for the bead at 28.62 μm is fully contained within that for the bead at 0 μm. Together with the best focus, other two cross sections have been observed, one 4 μm before and one 4 μm after the best focus cross sections. The first comparison can be made between the two out of focus cross sections of each bead. Those before the best focus appear ring-like (fig. 3.5g and 3.5i), while those after seem more blurred (3.5h and 3.5j). This is an indication of the presence of spherical aberration [23, 24], in particular positive spherical aberration, where the ring-like pattern is closer to the tube lens (located on the left had side of the axial cross sections, fig. 3.5d and 3.5f) than the blurred pattern. In case of negative spherical aberration, the order of the patterns ring-like – blurred would have been

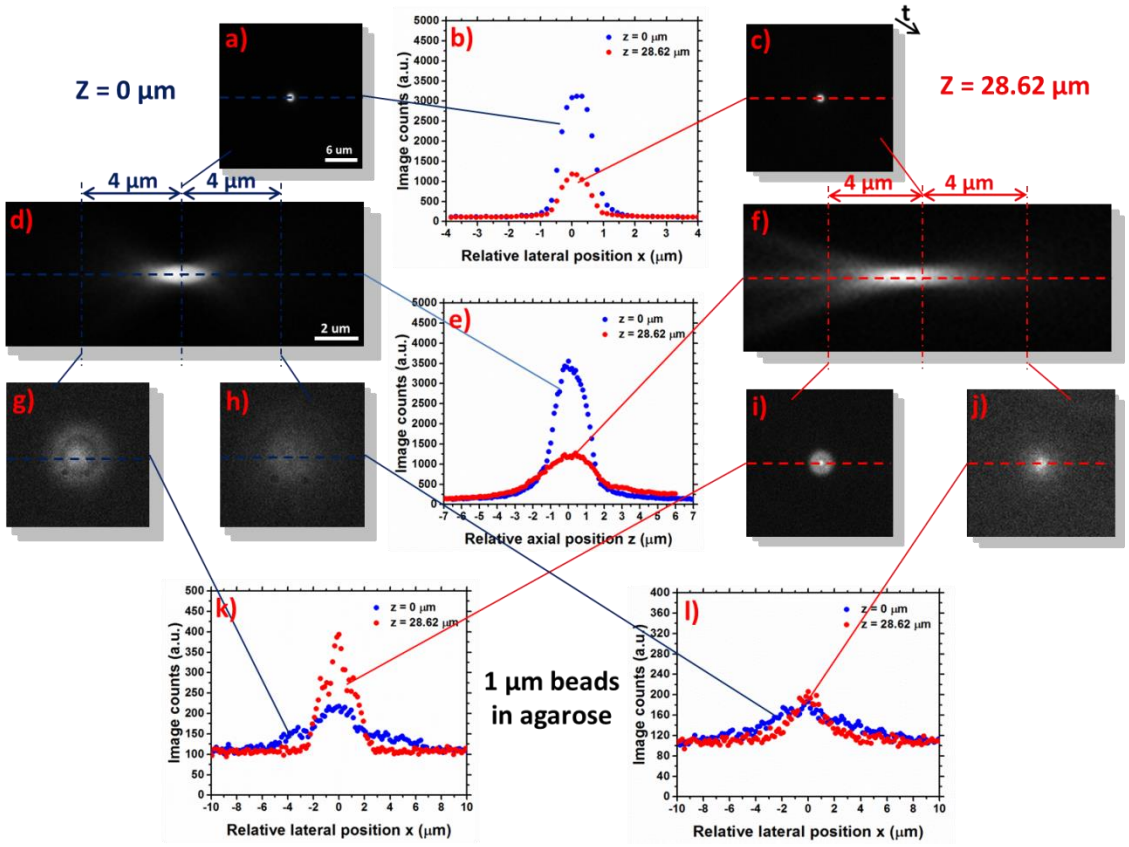

Figure 3.5 Axial and lateral cross sections and profiles of two 1 µm beads in agarose, positioned at z = 0 µm (left) and z = 28.62 µm (right) from the coverslip glass. Panels **d** and **f** show the axial cross sections of the two beads and the plots in **e)** are the axial profiles observed through the horizontal lines in **d** and **f**. The three vertical lines in **d** and **f** represent the positions of the lateral cross sections in the figure (**a**, **c**, **g**, **h**, **i** and **j**). In particular, the central ones are two best focal positions (showed in **a** and **c**), while the other two are positioned, respectively, 4 µm before (cross sections **g** and **i**) and 4 µm after (cross sections **h** and **j**) those positions. In panel **b** the lateral profiles through the horizontal lines on the cross sections in **a** and **c** are plotted. Instead, in panels **k** and **l** the lateral profiles through, respectively, the horizontal lines on the cross sections in **g**-**i** and in **h**-**j** are shown. The profiles for the beads at z = 0 µm and z = 28.62 µm have been plotted in, respectively, blue and red. All the profiles, tracked through the positions where the maximum signal was observable, have been calculate by using the same cross sections in the first three z-stacks of every used series. Exposure time = 100 ms, em gain = 2,000, laser power at sample = 42.6 µW at λ = 488 nm.

switched, while in the ideal and unrealisable case of no spherical aberration, both pattern would have been ring-like. The other comparison can be made between corresponding pattern before and after the best foci for the two beads at different axial

positions. Starting from the two ring-like cross sections, the one associated to the bead at z = 0 μm (fig. 3.5g) appears larger and less bright than the one for the bead at z = 28.62 μm (fig. 3.5i). This can be confirmed by observing the corresponding lateral profiles in fig. 3.5k, where, moving from the bead at z = 0 μm to that at z = 28.62 μm, the FWHM shrinks from 7.04 μm to 3.36 μm and the peak grows from 215 IC to 400 IC. The same observation can be made by looking at the cross sections in fig. 3.5h and 3.5j, where the one for the bead at z = 0 μm, again, seems larger and less bright than that for the bead at z = 28.62 μm. In this case, moving from the bead at 0 μm to that at 28.62 μm the FWHM gets reduced from 6.24 μm to 3.2 μm and the peak increases from 180 IC to 206 IC. Therefore, by observing the cross sections and the profiles in fig. 3.5 for the two beads at z = 0 μm and 28.62 μm in agarose, it can be concluded that the extensions of lateral and axial profiles tend to grow with the axial position of the observed beads, while the peak intensities tend to decrease.

In fig. 3.6 an equivalent of fig. 3.5 for two beads in PDMS is presented. These two beads are located at z = 1.77 μm (cross sections on the left hand side of fig. 3.6, blue profiles) and z = 28.09 μm (cross sections on the right hand side of fig. 3.6, red profiles) and, therefore, the axial distance between them is 26.32 μm, close to distance between the two beads in agarose in fig. 3.5 (28.62 μm). Starting from the comparison of the axial cross section in fig. 3.6d and 3.6f, now the difference appears less evident if compared to the two axial cross sections for the beads in agarose (fig. 3.5d and 3.5f). Indeed, by observing the comparison between axial profiles in fig. 3.6e, the FWHM now grows by 0.7 μm from 1.9 μm for the bead at z = 1.77 μm to 2.6 μm for the bead at z = 28.09 μm, while the same difference between the beads in agarose was around 1.2 μm (fig. 3.5e). Also the peaks of the profiles are very close to each other, growing from 4,225 IC to 4,655 IC, respectively for the bead at 1.77 μm and that at 28.09 μm, while in the agarose case a strong reduction was observed (fig. 3.5e). Regarding the lateral cross sections for the beads in focus (fig. 3.6a and 3.6c), they look very similar as those for the beads in agarose (fig. 3.5a and 3.5c). This can also be seen from the profiles in fig. 3.6b, but differently from those in fig. 3.5b, the profiles are basically overlapped, with FWHM equal to 0.96 μm and no reduction in the peak intensity, stable at 4,630 IC. Also the out of focus cross sections for the beads at z = 1.77 μm and 28.09 μm seem quite similar in fig. 3.6. There is still a difference between cross sections before and after the best focus positions, with fig. 3.6g and 3.6i ring-like and fig. 3.6h and 3.6j more blurred, indicating the presence of spherical aberration. However, if the cross sections before and after the best focal places are compared among them, now the

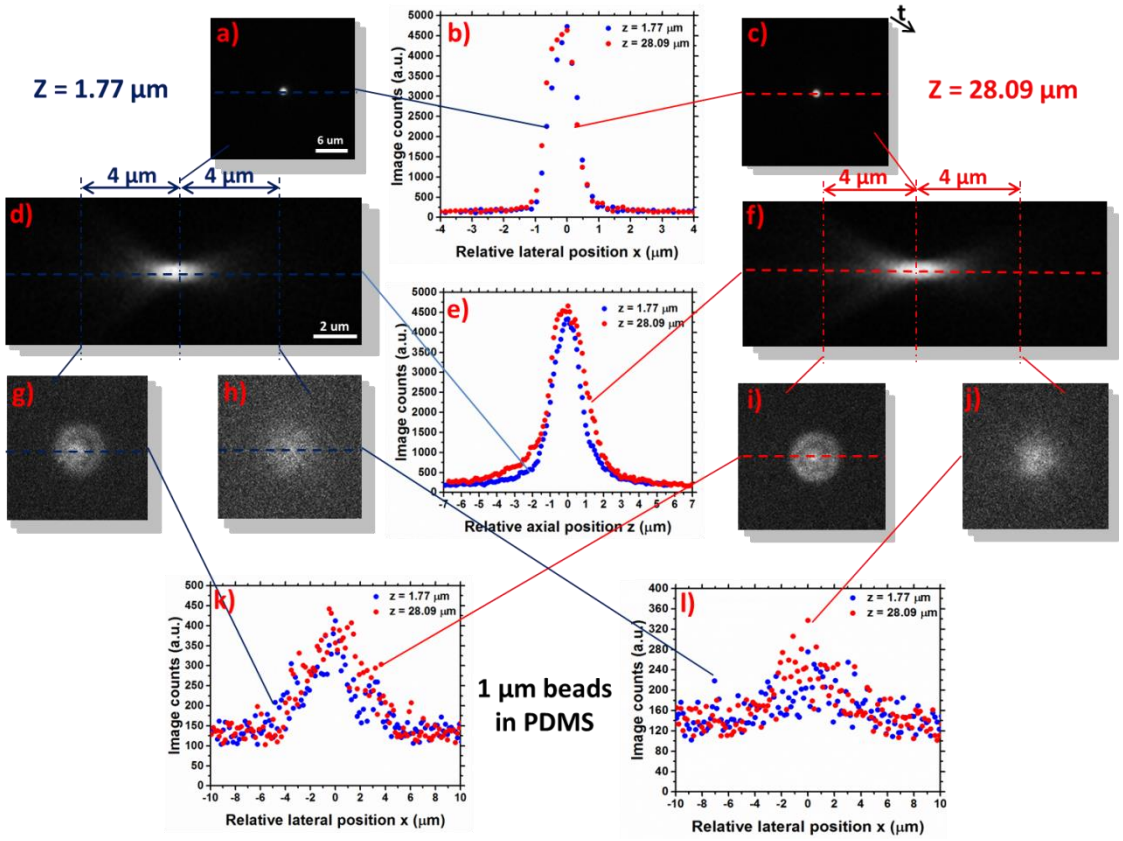

Figure 3.6 Axial and lateral cross sections and profiles of two 1 µm beads in polydimethylsiloxane (PDMS), positioned at z = 1.77 µm (left) and z = 28.09 µm (right) from the coverslip glass. Panels **d** and **f** are the axial cross sections of the two beads and the plots in **e)** are the axial profiles observed through the horizontal lines in **d** and **f**. The three vertical lines in **d** and **f** represent the positions of the lateral cross sections in the figure (**a**, **c**, **g**, **h**, **i** and **j**). In particular, the central ones are two best focal positions (showed in **a** and **c**), while the other two are positioned, respectively, 4 µm before (cross sections **g** and **i**) and 4 µm after (cross sections **h** and **j**) those positions. In panel **b** the lateral profiles through the horizontal lines on the cross sections in **a** and **c** are plotted. Instead, in panels **k** and **l** the lateral profiles through, respectively, the horizontal lines on the cross sections in **g-i** and in **h-j** are shown. The profiles for the beads at z = 1.77 µm and z = 28.09 µm have been plotted in, respectively, blue and red. All the profiles, tracked through the positions where the maximum signal was observable, have been calculate by using the same cross sections in the first three z-stacks of every used series. Exposure time = 100 ms, em gain = 3,000, laser power at sample = 2.1 µW at λ = 488 nm.

pattern in fig. 3.6g share the same sizes of that in fig. 3.6i and the same happens between the cross sections in fig. 3.6h and 3.6j. This can also be seen in the profile plots

in fig. 3.6k and 3.6l, where the curves for the beads at z = 1.77 µm and 28.09 µm are overlapped, with, respectively, FWHMs of around 5.92 µm and 6.4 µm and peaks of 390 IC and 280 IC. This was not the case for the profiles of the defocused cross sections of the beads in agarose (fig. 3.5k and 3.5l), which were getting wider FWHMs and their peaks were growing moving from the bead at 0 µm to that at 28.62 µm. Therefore, differently from the case for the two beads in agarose (fig. 3.5), the cross sections and the profiles for the two beads in PDMS (fig. 3.6) do not seem much different from each other, even if the axial distance between them (26.32 µm) is very close to the axial distance between the beads in agarose (28.62 µm).

The comparison between cross sections and profiles in fig. 3.5 and 3.6 leads to the conclusion that in agarose, over an axial range of 26 µm to 28 µm, bead axial cross sections tend to get more elongated and thinner as the axial depth of the beads within the material increases, while the same does not happen for beads in PDMS over the same axial range. This can be due to either the increased level of spherical aberration when agarose is used, since the refractive index mismatch between agarose (n = 1.33 at 589 nm [49]) and the used immersion oil (n = 1.518 at 23°C) is higher than that when PDMS (n = 1.41 at 589 nm [50]) is used, or it can be a matter of different levels of signal. In order to discriminate between these two possible causes, signal to noise ratios (SNR) and signal to background ratios (SBR) of all the images of the beads acquired in the four different experimental conditions (100 nm and 1 µm beads in agarose and PDMS) have been calculated when the beads were in focus in the central plane and studied as functions of the depths of the beads within the substrate materials, to see how they were changing.

There are several sources of noise [53]. Some originates from the stochastic nature of the photons and is called shot or Poisson noise [54]. Another source of noise is the electronic reading process of the camera, which introduces the read noise [54]. The camera heating will also generate some noise called dark noise [54]. Regarding the background, this also can have different origins, such as out of focus emitters, autofluorescence, light coming from the external environment, etc. In addition, it can be non-homogenously distributed in the field of view (FOV) and change dynamically in time [55]. For a more detailed discussion about noise and background in microscopy, refer to sec. 4.2.

The SBR was calculated by taking the averaged (over all the in focus images of the studied PSF in each z-stack series) background-subtracted integrated image count of a box containing the PSF under study and dividing it by the calculated amount of

background under the PSF itself. To do this, the average background per pixel was estimated by taking the average background value in a box not containing any PSF. The sizes of the boxes used for this purpose were equal to those that have been used to calculate the sharpness of the studied PSFs (30x30 pixels and 150x150 pixels, respectively for 100 nm and 1 μm beads). This done, to calculate the total background under each in focus PSF, instead, the number of pixels that were forming each bead image has been obtained by tracing a profile passing through the maximum pixel value of every PSF and counting the distance in pixels between the two points on the profiles just above the background level. This value has been used to draw a box centred on the PSF peak, within which the number of non-zero pixels after the background subtraction has been counted and multiplied by the average background per pixel. To evaluate the SNR, instead, it was necessary to, first, calculate the average (done as for the SBR) photon count of the studied PSFs within a box (with sizes as explained for the SBR), by using the formula [53] (eq. 3.7):

$$n_{ph} = \frac{ADC}{q}\frac{IC}{G}, \qquad \text{(eq. 3.7)}$$

where n_{ph} is the average photon count, IC is the average integrated image count (the same one used for the SBR), ADC is the analog to digital conversion factor of the used camera (12.7 e^-/IC [53]), q is the quantum efficiency (0.9 e^-/photon [53]) and G is the em gain used for the acquisition. Then, it was possible to estimate the SNR by using next equation [53] (eq. 3.8):

$$SNR = \frac{q\, n_{ph}}{\sqrt{2\, q\, n_{ph}}} = \sqrt{\frac{q\, n_{ph}}{2}}, \qquad \text{(eq. 3.8)}$$

where the numerator represents the amount of signal in terms of photo-electrons and the denominator is the associated Poisson noise (the 2 factor is an amplification factor due to the em shift register). The Gaussian read and the dark noises have been neglected [54]. The results are presented in fig. 3.7. The two plots in fig. 3.7a and 3.7b, in particular, are referred to, respectively, the beads in agarose and PDMS to which the cross sections and profiles in fig. 3.5 and fig. 3.6 are linked. The two beads in agarose in fig. 3.5 were positioned at nominal positions of 0 μm and 28.62 μm and, as it can be seen in fig. 3.7a, the SNR does not vary much between these positions, changing from

around 28.7 at z = 0 µm to 26 at z = 28.62 µm. The SBR, instead, increases from 12.2 to 18.4. So, the SNR is reduced by 2.7 and the SBR is increased by 6.2. Moving to the two beads in PDMS in fig. 3.6, these were located at nominal axial positions of 1.77 µm and 28.09 µm. At these two points the SNR is, respectively, equal to 28.7 and 31.2, so it increases by 1.5, while the SBR is equal to 14.7 and 16.4, so it grows by 1.7. Therefore, a slight reduction in SNR and an increase in SBR corresponds to a strong reduction in the peaks of the profiles for the beads in agarose (fig. 3.5), while there is basically no change between the profiles in fig. 3.6 for the beads in PDMS, even if there is a slight increase in SNR and SBR, it can be concluded that the change in terms of profiles between the beads in agarose is mostly due to the higher refractive index mismatch between agarose and immersion oil refractive indices, if compared to that between PDMS and immersion oil, at least over the first 26-28 µm of the nominal axial range.

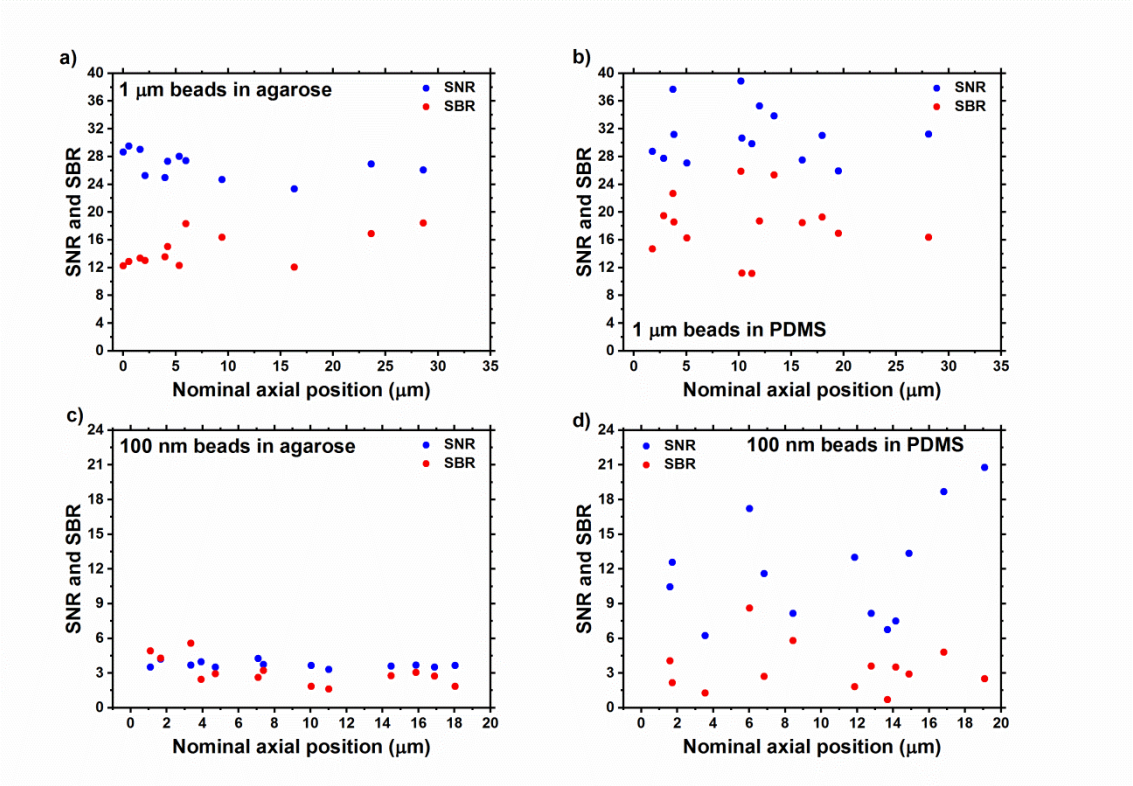

Figure 3.7 Evaluated SNR and SBR for beads located at different depths within the samples. **a)** 1 µm beads in agarose (exposure time = 100 ms, em gain = 2,000, laser power at sample = 42.6 µW at λ = 488 nm), **b)** 1 µm beads in PDMS (exposure time = 100 ms, em gain = 3,000, laser power at sample = 2.1 µW at λ = 488 nm), **c)** 100 nm beads in agarose (exposure time = 100 ms, em gain = 3,000, laser power at sample = 4.1 mW at λ = 488 nm) and **d)** 100 nm beads in PDMS (exposure time = 100 ms, em gain = 3,000, laser power at sample = 0.23 mW at λ = 488 nm).

So, the higher refractive index mismatch between agarose and the immersion oil has increased the level of spherical aberration, distorting the PSF shapes from ideal as the nominal axial position increased. This distortion produces an elongation of the PSF axial cross sections and profiles (fig. 3.5d, 3.5e and 3.5f), redistributing the energy from the best focal positions (which experience a reduction in profile peak) to the out of focus regions (whose profile peak increase). It also shrinks the lateral cross sections (fig. 3.5i and 3.5j). The latter is also connected to a change in perceived plane spacing (as it will be shown in section 3.4) due to the change in axial depth of the bead under study. The spherical aberration embedded in the PSF shapes has also an impact on the calculated sharpness curves, changing their profiles (this will be discussed in section 3.5). Finally, by considering the SNR and SBR curves in fig. 3.7, it can be noticed that there is not a massive change of these ratios over the shown nominal axial ranges. On average, the SNR is equal to 26.1 and 31.7, while the SBR is equal to 14.1 and 18.2, respectively for the 1 μm beads in agarose and PDMS. Instead, the SNR is equal to 3.7 and 11.6, while the SBR is equal to 3.1 and 3.5, respectively for the 100 nm beads in agarose and PDMS. As expected, the levels of SNR and SBR are higher for the 1 μm beads than for the 100 nm ones, since there is a higher number of emitted photons with the 1 μm beads. Also, the higher average SNR associated with the beads in PDMS means also higher level of noise and background (on average, the background per pixel is equal to 147 IC and 825 IC for, respectively, 1 μm and 100 nm beads in PDMS, and 108 IC and 129 IC for, respectively, 1 μm and 100 nm beads in agarose), which can explain the noisy out of focus profiles in fig. 3.6k and 3.6l and the higher variability between SNR and SBR values in the PDMS plots (fig. 3.7b and 3.7d) in comparison to those for the beads in agarose (fig. 3.7a and 3.7c). PDMS has been reported to have smaller extinction coefficient (hence absorption) in the visible light range than water [56, 57], which is the main component of the agarose gel samples, thus justifying the smaller SNR and SBR values for the beads in agarose.

Another important conclusion can be extracted from the cross sections and the profiles in fig. 3.5 and 3.6: There is no net evidence of other main aberrations [58] (apart from defocus and spherical aberration) such as coma, astigmatism, etc. Therefore, the study in this chapter has been limited to the impact of spherical aberration on the sharpness curves.

3.5 Impact of spherical aberration on sharpness peak positions

As on PSFs, spherical aberration has also an impact on the output of the sharpness algorithm and modifies the relative peak positions and shapes of the curves.

Peak position variations have been studied in two different ways: With respect to the sharpness peak positions in the other planes and with respect to the bead axial positions evaluated through axial centre of mass calculations. The former allows for a study of the perceived plane spacing, while the latter compares the responses, relatively to each other, of sharpness and centre of mass algorithms when indicating the evaluated axial positions in presence of spherical aberration. This has been possible since sharpness curves can indicate with nanometric accuracy the best focal positions of the PSFs. This can be seen, for example, in fig. 3.8, where the sharpness curves calculated for a 100 nm bead in PDMS located at the nominal axial positions of 1.6 μm have been plotted together with the corresponding average axial profiles observed in the three planes (evaluated as in sec. 3.4). All the curves in fig. 3.8 have been normalised by,

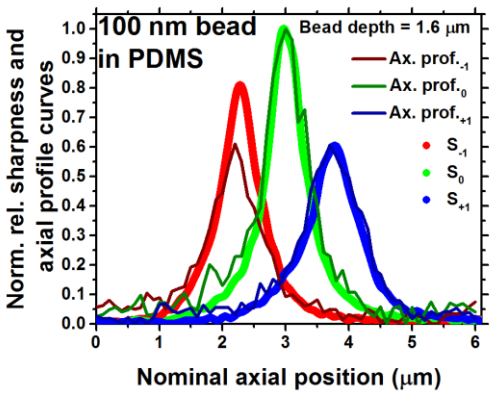

Figure 3.8 Sharpness curves and axial profiles observed through the three used axial planes for a 100 nm bead in PDMS, located at the nominal axial positions of 1.6 μm from the coverslip glass. These axial profiles have been obtained from the first three z-stacks of the acquired z-stack series. Exposure time = 100 ms, em gain = 3,000, laser power at sample = 0.23 mW at λ = 488 nm.

first, subtracting their minimal values (so to bring them to an equal zero reference) and, then, by dividing them for the maximum values in the central plane plots. As it can be observed, the sharpness and axial profiles curves are almost always overlapped. In particular, the average plane spacing calculated as average distance among the axial profile peaks (which can be considered the best focal positions) is around 750 nm, a value very close to 733 nm, which has been measured by using the sharpness peak

maxima. Instead, the average distance between axial profile and sharpness curve peak maxima is around only 62 nm.

3.5.1 *Plane spacing variation due to refractive index mismatch*

In fig. 3.9 two examples of axial cross sections and sharpness curves associated to two 100 nm beads in agarose, located at nominal axial depths of 1.09 μm (fig. 3.9a and 3.9b) and 15.86 μm (fig. 3.9c and 3.9d), are shown. The axial cross sections have been obtained via the software ImageJ, by reslicing the first z-stacks of the acquired z-stack series, while the associated plane spacing has been calculated by using a code written in Mathematica [59]. This code initially extracts the three sharpness curve peak values and positions associated to each acquired z-stack in the z-stack series. Then it calculates the PS for each z-stack as average of the differences between the positions of the S_0 and S_{-1} peaks and those of the S_{+1} and S_0 peaks. Finally, the PS for each z-stack series is evaluated by averaging the ten PS values obtained for each one of them. Moving from the sharpness curves and cross sections for the bead at z = 1.09 μm (fig. 3.9a and 3.9c) to those for the bead at 15.86 μm (fig. 3.9c and 3.9d), an increase in the distance among sharpness peak maxima and, therefore, plane spacing, can be observed. In particular, the plane spacing grows by around 145 nm, from 653 nm to 798 nm, as the nominal axial position of the bead increases by 14.77 μm. This is another effect of the increase in spherical aberration with the depth, which enlarges the axial separation among the PSFs in the three channel. This happens because the level of spherical aberration in each plane is different, since each one of them is positioned at a different distance from the objective lens. This can also be visualised by considering the simplified model described in sec. 3.2 (fig. 3.1) by eq. 3.6. A change in imaged plane position would have the effect of modifying the value of NF and, consequently, FSR. In addition, as explained in sec. 2.4.5 and 3.2, the level of spherical aberration in the $\pm 1^{st}$ planes varies from that in the 0^{th} one, since the objective lens has not been designed to image planes different from the nominal one and this will also have an effect on the observable PS. Regarding the shape of the PSF, by observing the cross sections in fig. 3.9b and 3.9d for the beads at the two axial positions, also here, as in fig. 3.5, an elongation of the cross section can be seen as the axial position of the bead increases. As shown (fig. 3.7), since there is almost no difference in SNR and SBR among beads at different nominal axial positions, this change in PSF shape cannot be directly attributed to changes in signal, but rather it is connected to different levels of spherical aberration, which increases with the bead depth within the sample [1]. This has an impact also on the shape of the

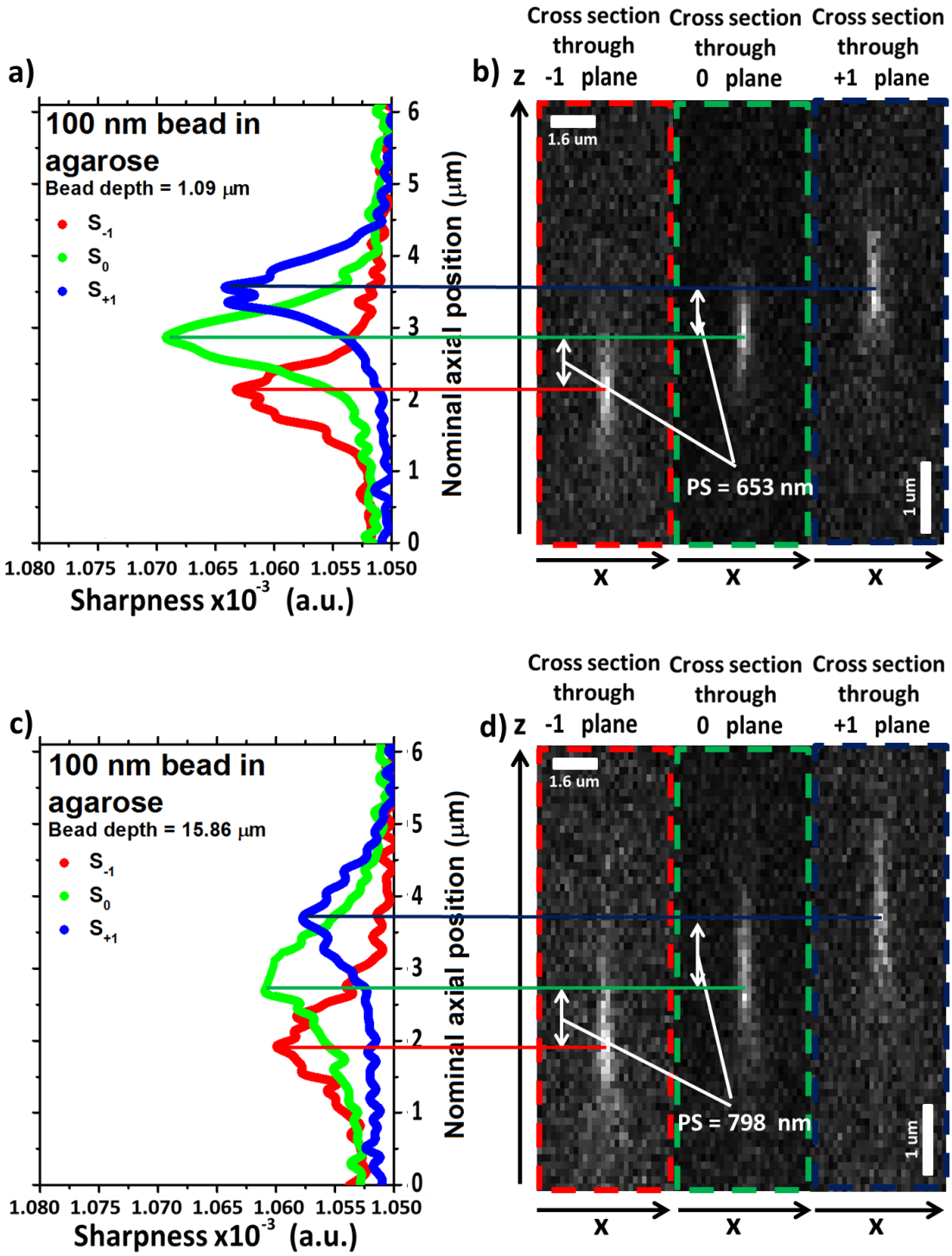

Figure 3.9 Sharpness curves (**a** and **c**) and axial cross sections (**b** and **d**) observed through the three used axial planes, for two 100 nm beads in agarose located at the nominal axial positions of (**a** and **b**) 1.09 μm and (**c** and **d**) 15.86 μm from the coverslip glass. The average calculated plane spacing is shown on the cross sections. The latter has been obtained from the first z-stacks of the acquired z-stack series. Exposure time = 100 ms, em gain = 3,000, laser power at sample = 4.1 mW at λ = 488 nm.

sharpness curves, which changes accordingly (fig. 3.8). Indeed, the curves in fig. 3.9a and 3.9c look different, with the curve for the bead at 1.09 µm having a higher peak than that at 15.86 µm (this will be shown in detail in sec. 3.6).

In fig. 3.10 the average calculated plane spacing at different nominal axial positions is presented for all the measured beads in the four experimental conditions. These data have been linearly fitted to evaluate the global rate of change of the PS as the axial position of the bead changes. All the fits in the four physical samples present a net increase in PS as the nominal axial position moves from 0 µm to 20 µm and the level of spherical aberration increases. However, this growth is stronger for the beads in

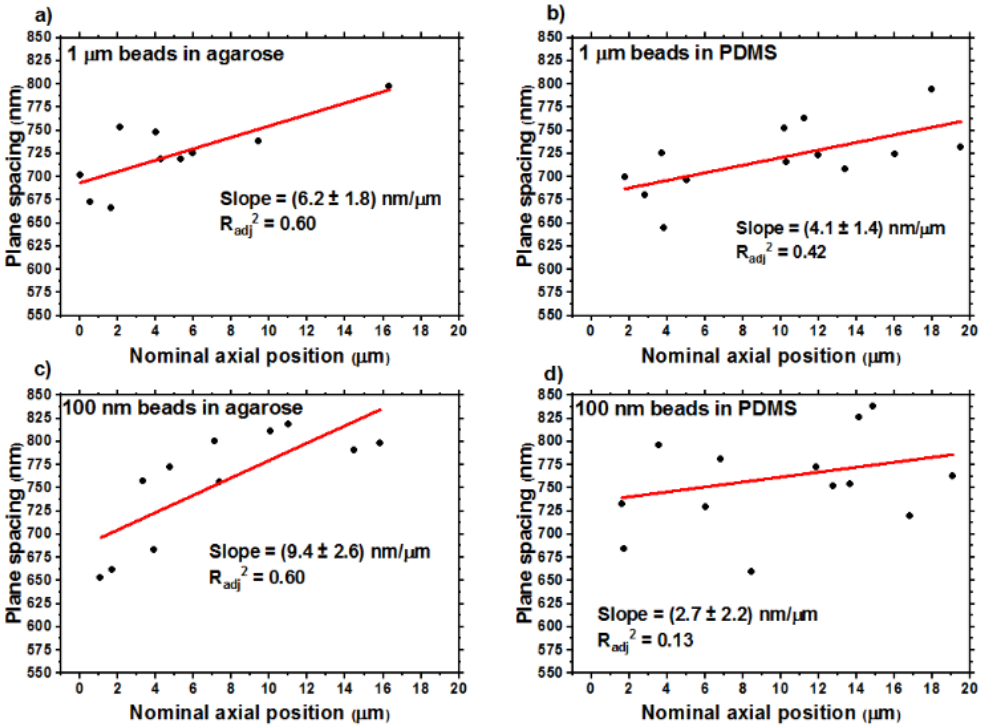

Figure 3.10 Evaluated average plane spacing for beads located at different depths within the samples. The red straight lines are linear fits through the data, whose slopes (with their standard deviations) and goodness (the adjusted R^2 values) are shown in the plots. **a)** 1 µm beads in agarose (exposure time = 100 ms, em gain = 2,000, laser power at sample = 42.6 µW at λ = 488 nm), **b)** 1 µm beads in PDMS (exposure time = 100 ms, em gain = 3,000, laser power at sample = 2.1 µW at λ = 488 nm), **c)** 100 nm beads in agarose (exposure time = 100 ms, em gain = 3,000, laser power at sample = 4.1 mW at λ = 488 nm) and **d)** 100 nm beads in PDMS (exposure time = 100 ms, em gain = 3,000, laser power at sample = 0.23 mW at λ = 488 nm).

agarose, where the slope is equal to (6.2 ± 1.8) nm/μm and (9.4 ± 2.6) nm/μm, respectively for the 1 μm (fig. 3.10a) and 100 nm (fig. 3.10c) beads, while it is equal to (4.1 ± 1.4) nm/μm and (2.7 ± 2.2) nm/μm, respectively for the 1 μm (fig. 3.10b) and 100 nm (fig. 3.10d) beads in PDMS. This difference is due to the reduced mismatch in refractive index between substrate material and immersion oil for the beads in PDMS. Indeed, as the refractive index mismatch increases, the difference between nominal and apparent focal position growths too (eq. 3.6 and fig. 3.1), thus raising the level of spherical aberration and the impact on the PS.

The variations in PS shown in fig. 3.10 could have also been affected by a change in system magnification through equation 2.4, due to the impact of different levels of spherical aberration. However, this has not been verified and no references to such a hypothetical phenomenon have been found in the literature.

3.5.2 *Sharpness curve and centre of mass axial localisation comparison*

Sharpness peak position variations due to spherical aberration can also be compared to axial position variations calculated through other algorithms. For the comparison it has been selected the axial centre of mass (CoM) algorithm [60] applied over the z-stack series, due to its ability to weight the geometric areas of an object and find its centre of balance. CoM will be used as a standard metric for evaluating the sharpness methodology.

If a system consisting of n objects with different masses located in different positions in space is taken into consideration, its CoM can be described, with respect to an origin in space, by the following equation (eq. 3.9):

$$\mathrm{CoM} = \frac{1}{\mathrm{M}}\left(\sum_{\mathrm{i}=1}^{\mathrm{n}} \mathrm{r_i m_i}\right), \qquad \text{(eq. 3.9)}$$

where M is equal to $\sum_{\mathrm{i}=1}^{\mathrm{n}} \mathrm{m_i}$ and is the total mass of the n objects with masses $\mathrm{m_i}$ in the system and $\mathrm{r_i}$ are the distances from the designed origin. A z-stack of images can be considered as a 3D system of objects distributed in space, where, in this case, the objects are the pixels. Every pixel has a "mass", which is its image count value, and is positioned at a particular distance from a pixel considered the origin, which can be identified in terms of row, column and z-stack frame (or page) number, since z-stacks are, in the case of the acquired data, 3D matrices [61]. Therefore, in order to calculate the axial CoMs of every z-stack series, all the beads in the z-stacks have first been extracted by cropping a box containing them, with sizes equal to the sizes used for the

sharpness curves calculated on the same beads (i.e. 30x30 pixels for 100 nm beads and 150x150 pixels for 1 μm beads). In addition to this lateral cropping, an axial one has also been applied. This has been necessary to avoid biased axial CoM values in the $\pm 1^{st}$ orders, where the beads are not axially centred with respect to the z-stacks. This axial cropping has been done by selecting, respectively for the 100 nm and 1 μm beads, ±10 frames and ±25 frames around the closest frames to the sharpness peak positions. This done, in order to identify the axial positions of each pixel, an index matrix, sharing the same sizes of the z-stack matrices, was created. This matrix has all the values in the first frame equal to 1, all those in the second one equal to 2, etc., since all the pixels in the first frame are at axial position $r_i = 1$ pix, all those in the second one are at $r_i = 2$ pix, etc. Once this axial index matrix has been set, by multiplying it pixel by pixel with all the cropped z-stacks in each z-stack series and dividing the sum of the pixels in the resulting matrices by the sum of the pixels in the original z-stacks, the axial CoMs have been obtained. Each z-stack series produced ten CoM values, which were averaged to find the average CoMs. This was done for all the three z-stack series observed through the three used axial planes. Finally, since all the axial CoMs were in units of frame numbers and the frame origin was identified with 1 rather than 0, all the axial CoM values were first reduced by one unit, so to shift their axial references to an origin equal to 0, and then these values were multiplied by 0.1 μm, i.e. the axial distance between frames in the z-stacks, in order to transform their units in micrometres. All this was done by using a code written in MATLAB [62].

As an example, in fig. 3.11 there is a comparison between the sharpness curve peak positions (red, green and blue solid lines, calculated as in sec. 3.5.1) and the CoM values (red, green and blue dashed lines) calculated for the a 100 nm bead in PDMS observed through all three planes, positioned at a nominal axial position of 1.6 μm. In fig. 3.11a the sharpness curves for this bead are shown, with the peak positions highlighted (red, green and blue spots) on the nominal axial position axis, while the cross sections in fig. 3.11b (extracted as explained in sec. 3.5.1) belong to the first z-stack of the z-stack series acquired for the used bead. As it can be noticed, sharpness peak and CoM positions are quite close to each other in all planes. This can be quantified by comparing the PS measured through the sharpness peak positions (sec. 3.5.1) to the equivalent one evaluated by using the CoM values for the three planes. The former is around 732 nm, while the latter 750 nm. Also, the average distances among sharpness peak positions and CoM values is only about 36 nm. Consequently, it can be

concluded that the sharpness peak position and the CoM algorithm are in good agreement with each other with nanometric accuracy.

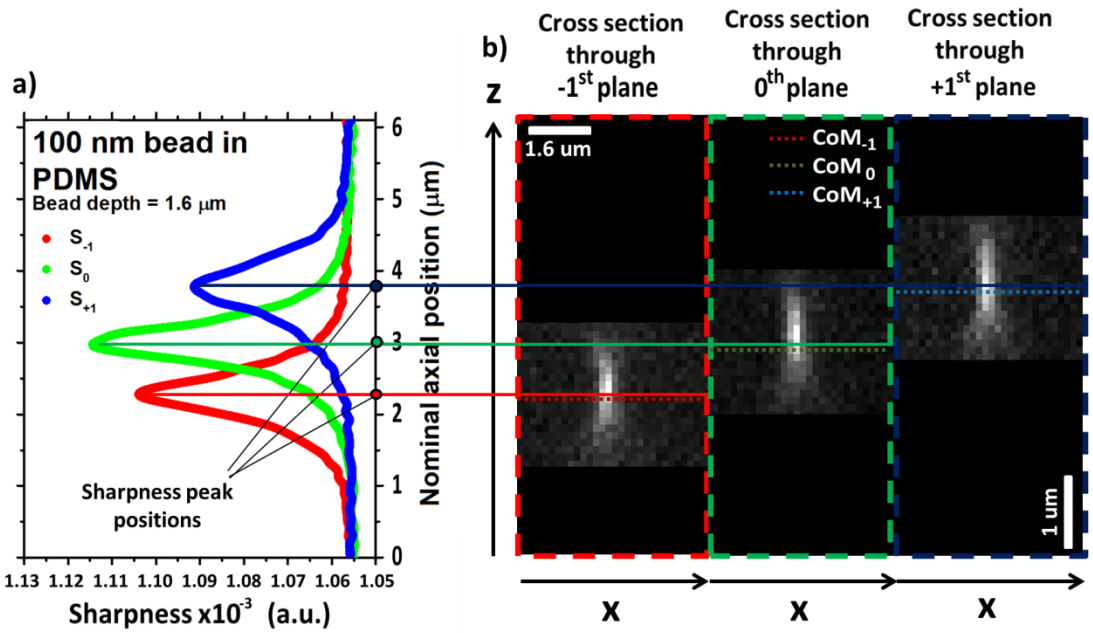

Figure 3.11 a) Sharpness curves and **b)** cropped axial cross sections observed through the three used axial planes for a 100 nm bead in PDMS, located at the nominal axial positions of 1.6 μm from the coverslip glass. The average calculated positions of the sharpness peaks (red, green and blue solid lines) and of the axial centres of mass (red, green and blue dashed lines) are shown on the cross sections. The latter has been obtained from the first z-stacks of the acquired z-stack series. Exposure time = 100 ms, em gain = 3,000, laser power at sample = 0.23 mW at λ = 488 nm.

In fig. 3.12 the differences between sharpness peak and CoM positions in the three planes and for the four experimental conditions studied have been plotted against the nominal axial positions of the imaged beads. As observable, it is not possible to see any particular trend as a function of the bead depth, since the values in all plots of fig. 3.12 seem to be randomly distributed around a difference of 0 nm. On average indeed, the total difference is equal to (0 ± 38) nm including all points in fig. 3.12.

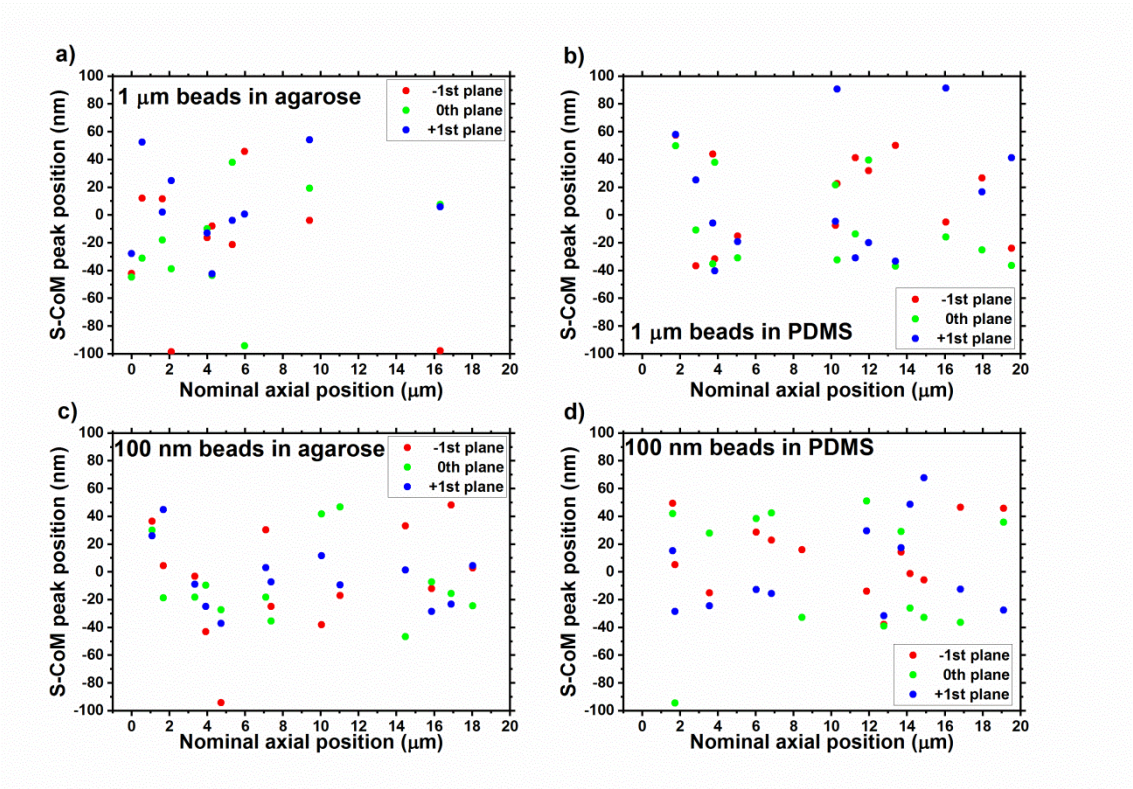

Figure 3.12 Difference between sharpness peak positions and axial centres of mass in all the three planes, for beads located at different depths within the samples. **a)** 1 μm beads in agarose (exposure time = 100 ms, em gain = 2,000, laser power at sample = 42.6 μW at λ = 488 nm), **b)** 1 μm beads in PDMS (exposure time = 100 ms, em gain = 3,000, laser power at sample = 2.1 μW at λ = 488 nm), **c)** 100 nm beads in agarose (exposure time = 100 ms, em gain = 3,000, laser power at sample = 4.1 mW at λ = 488 nm) and **d)** 100 nm beads in PDMS (exposure time = 100 ms, em gain = 3,000, laser power at sample = 0.23 mW at λ = 488 nm).

Concerning the CoM-based PS, this is shown in fig. 3.13 for all experimental conditions (black dots), together with the difference between the sharpness-based (fig. 3.10) and the CoM-based PS (red crosses). As in fig. 3.10, also here the PS values have been linearly fitted to show the global behaviour of the PS as a function of the depth. Due to the similarities between sharpness peak and axial CoM positions seen in fig. 3.12, also the CoM-based PS behaves similarly to that sharpness-based seen in fig. 3.10. As observable, also in this case the slopes associated to the agarose beads (fig. 3.13a and 3.13c) are higher than those for the PDMS ones (fig. 3.13b and 3.13d) due to the higher refractive index mismatch. In particular, these are equal to (9.0 ± 3.8) nm/μm and (10.4 ± 2.9) nm/μm, respectively for the 1 μm (fig. 3.13a) and 100 nm beads (fig. 3.13c)

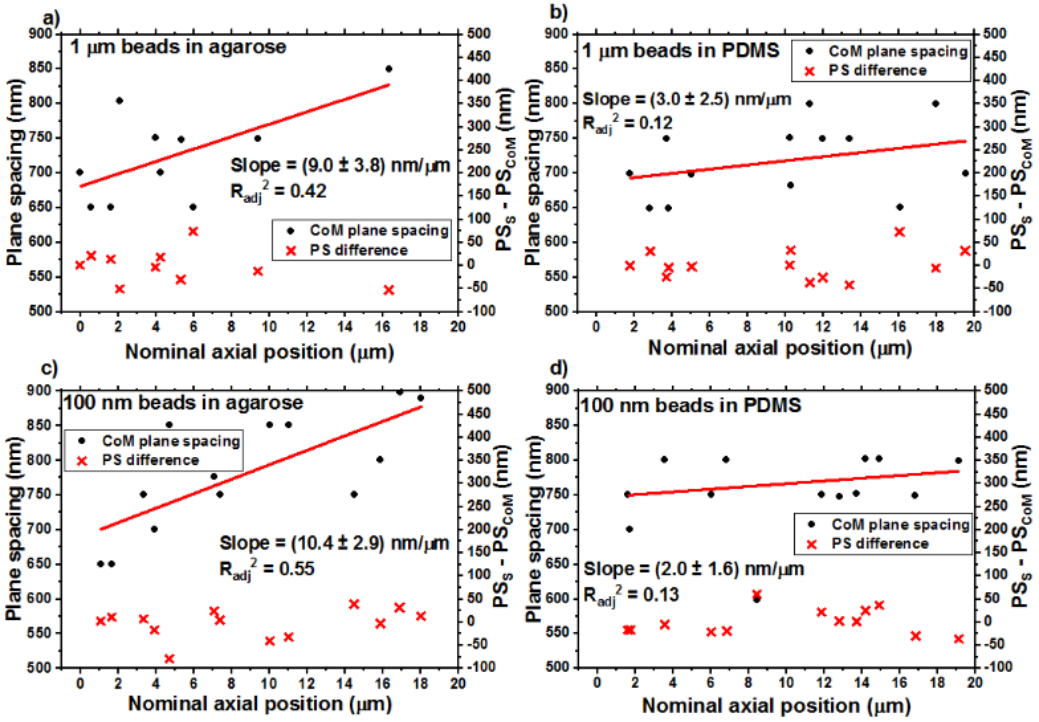

Figure 3.13 Evaluated average axial CoM-based plane spacing (black dots) and difference between sharpness-based and axial CoM-based plane spacing (red crosses) for beads located at different depths within the samples. The red straight lines are linear fits through the CoM-based plane spacing data, whose slopes (with their standard deviations) and goodness (the adjusted R^2 values) are shown in the plots. **a)** 1 µm beads in agarose (exposure time = 100 ms, em gain = 2,000, laser power at sample = 42.6 µW at λ = 488 nm), **b)** 1 µm beads in PDMS (exposure time = 100 ms, em gain = 3,000, laser power at sample = 2.1 µW at λ = 488 nm), **c)** 100 nm beads in agarose (exposure time = 100 ms, em gain = 3,000, laser power at sample = 4.1 mW at λ = 488 nm) and **d)** 100 nm beads in PDMS (exposure time = 100 ms, em gain = 3,000, laser power at sample = 0.23 mW at λ = 488 nm).

in agarose, and to (3.0 ± 2.5) nm/µm and (2.0 ± 1.6) nm/µm, respectively for the 1 µm (fig. 3.13b) and 100 nm (fig. 3.13d) beads in PDMS. These have been summarised in table 3.2, together with the slope values calculated for the sharpness-based PS:

PS slopes (nm/µm)	Agarose		PDMS	
	100 nm beads	**1 µm beads**	**100 nm beads**	**1 µm beads**
Sharpness-based	9.4 ± 2.6	6.2 ± 1.8	2.7 ± 2.2	4.1 ± 1.4
CoM-based	10.4 ± 2.9	9.0 ± 3.8	2.0 ± 1.6	3.0 ± 2.5

Table 3.2 Average slopes associated to the fits in fig. 3.10 and 3.13. Exposure time = 100 ms, em gain = 2,000 and 3,000, laser power at sample = 42.6 µW, 2.1 µW, 4.1 mW and 0.23 mW, λ = 488 nm.

Table 3.2 shows that both sharpness-based and CoM-based calculated slopes are generally in agreement, even though some differences are also visible due to the different response to the level of aberration of the two algorithms. In terms of difference in calculated PS between the two algorithms (fig. 3.13), as expected also in this case it is not possible to see any particular trend and the average among all calculated differences is around (0 ± 31) nm.

In conclusion, this section has shown how the perceived PS in a multifocal system increases with the level of mismatch-induced spherical aberration. This effect has been observed with both the sharpness and the CoM algorithm, which are generally in agreement.

3.6 Influence of spherical aberration on sharpness curve shapes

Spherical aberration distorts PSFs [3, 63, 64]. As seen in section 3.3, as the depth within the sample at which the emitter is located increases, the PSFs get more and more elongated over the optical axis, thinner in the image plane and asymmetric with respect to its best focus plane. This transformation cannot be ignored by the shape of the sharpness curves.

Sharpness curves get their shape transformed as the degree of spherical aberration changes. This is well represented in fig. 3.14, where the central sharpness curves of all the beads acquired in all used experimental conditions have been plotted by shifting their peak positions to the nominal axial depths at which they were acquired, in order to show their nominal axial position inside the samples. All curves in fig. 3.14 have been rescaled by subtracting the corresponding sharpness baseline value (fig. 3.4c) and dividing them by the highest sharpness peak value in each experimental condition. The sharpness curves associated to the beads in agarose (fig. 3.14a and 3.14c) are clearly more affected than those in PDMS (fig. 3.14b and 3.14d) over a nominal axial

range of 20 μm. This is a direct consequence of the higher refractive index mismatch in the former material, considering that there is not a consistent change in SNR and SBR among the different beads in the nominal axial range (fig. 3.7). However, while, on average, by increasing the depth within the sample the sharpness curves associated to the beads in agarose get lower, those for the beads in PDMS do not have the same behavour, but, instead, they seem to fluctuate. The latter behavour is also observable in the plots for the beads in agarose (fig. 3.14a and 3.14c), but mainly in the initial 7-8 μm of the nominal axial position axis, rather than over the whole 20 μm range. Consequently, it is not possible to attribute the change in sharpness peak exclusively to the variation in spherical aberration level. Regarding the variation in FWHM, this has

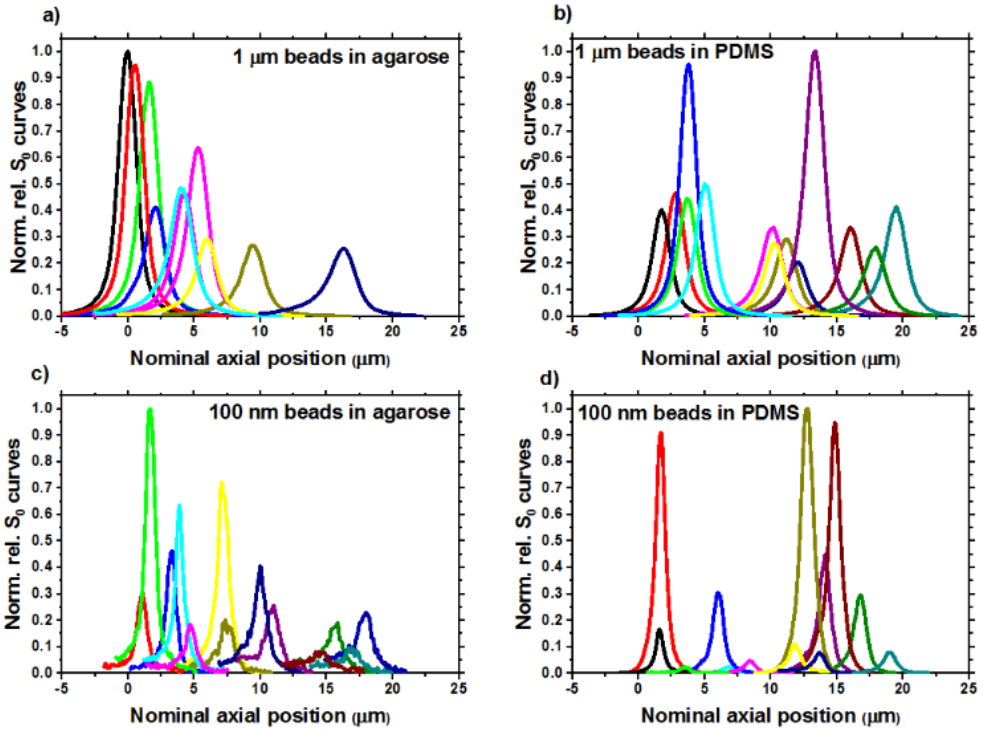

Figure 3.14 Calculated central plane sharpness curves for beads located at different depths within the samples. **a)** 1 μm beads in agarose (exposure time = 100 ms, em gain = 2,000, laser power at sample = 42.6 μW at λ = 488 nm), **b)** 1 μm beads in PDMS (exposure time = 100 ms, em gain = 3,000, laser power at sample = 2.1 μW at λ = 488 nm), **c)** 100 nm beads in agarose (exposure time = 100 ms, em gain = 3,000, laser power at sample = 4.1 mW at λ = 488 nm) and **d)** 100 nm beads in PDMS (exposure time = 100 ms, em gain = 3,000, laser power at sample = 0.23 mW at λ = 488 nm).

been highlighted by plotting in fig. 3.15 three relative (peak to baseline) central sharpness curves for each acquired experimental conditions, located close to the coverslip glass (0 μm to 1.77 μm from it, red curves), around ten micrometres from it (8.44 μm to 10.22 μm from it, green curves) and around twenty micrometres form it (18.04 μm to 23.66 μm from it, blue curves). These curves have been normalised then with respect to their sharpness peaks. As it can be observed, in all four panels of fig. 3.15 an increase in FWHM with the bead depth can be seen. However, this increase is more pronounced for the bead in agarose (fig. 3.15a and 3.15c), due to the higher level of mismatch-induced spherical aberration. This is in agreement with the increase in PSF elogantion with the bead depth shown in fig. 3.5 and 3.6. Another aspect that can be observed is the noise embedded in the curves for the 100 nm beads (fig. 3.15c and

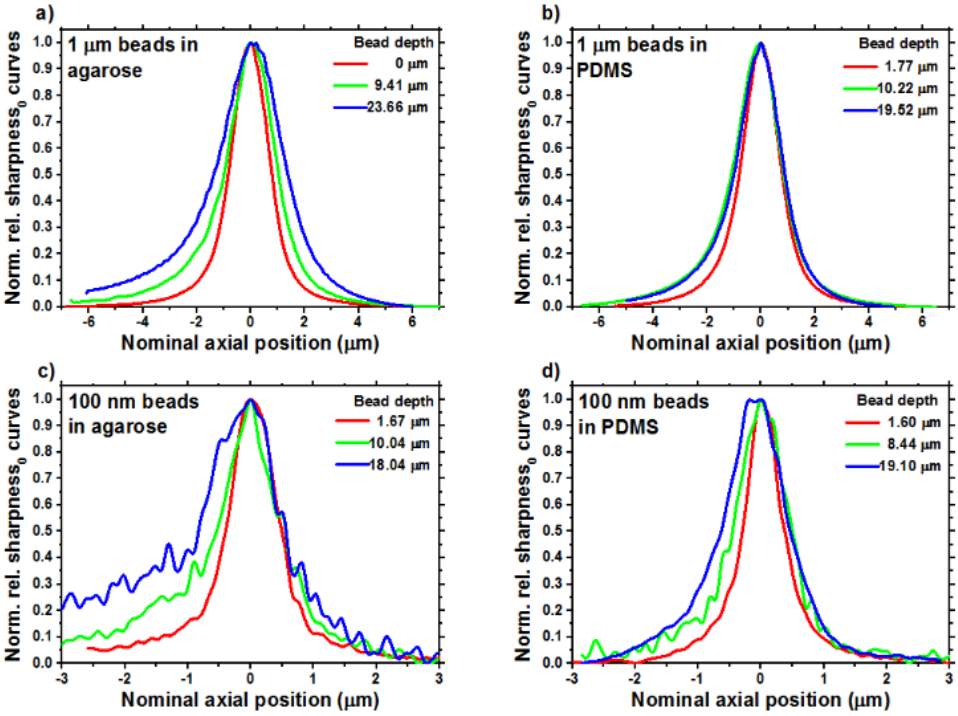

Figure 3.15 Normalised relative central sharpness curves for three beads located at nominal axial distances from the coverslip glass of around 0-2 μm (red curves), 8-10 μm (green curves) and 18-24 μm (blue curves). **a)** 1 μm beads in agarose (exposure time = 100 ms, em gain = 2,000, laser power at sample = 42.6 μW at λ = 488 nm), **b)** 1 μm beads in PDMS (exposure time = 100 ms, em gain = 3,000, laser power at sample = 2.1 μW at λ = 488 nm), **c)** 100 nm beads in agarose (exposure time = 100 ms, em gain = 3,000, laser power at sample = 4.1 mW at λ = 488 nm) and **d)** 100 nm beads in PDMS (exposure time = 100 ms, em gain = 3,000, laser power at sample = 0.23 mW at λ = 488 nm).

3.15d), if compared to the curves for the 1 μm ones (fig. 3.15a and 3.15b). This is due to the lower SNR and SBR associated to smaller beads, has shown in fig. 3.7.

To offer a global view of the change in sharpness curve shape over all the beads acquired in the first 20 μm nominal axial positions in the four experimental conditions, all the relative central sharpness curve peaks and FWHMs have been plotted in fig. 3.16. The sharpness peaks have been calculated, as explained in section 3.4.1, by using a Mathematica code that was selecting and averaging all the sharpness maxima (relative to the sharpness baseline values) associated to the sharpness curves calculated for the z-stacks in each z-stack series. Knowing the sharpness curve maximum values, the same code was then finding the positions of the two points of the curves closer to a value equal to half of the relative sharpness peaks, whose relative to each other distances are the FWHMs of the curves. The SNR values associated to the acquired beads (fig. 3.7) have been colour encoded in the FWHM data. As noticeable and anticipated in previous figure (fig. 3.15), the FWHM values in all plots increase with the depth, indicating how the PSFs change their shapes and get elongated (fig. 3.5 and 3.6). It is also clear that the FWHMs extracted for the beads in agarose (fig. 3.16a and 3.16c) grow faster than those for the beads in PDMS (fig. 3.16b and 3.16d). This can be quantified by linearly fitting these data. The slopes of the fits for the 1 μm (fig. 3.16a) and 100 nm (fig. 3.16c) beads in agarose are, respectively, equal to (44 ± 7) nm/μm and (33 ± 5) nm/μm, while those for the beads in PDMS are (21 ± 5) nm/μm and (17 ± 3) nm/μm, respectively for the 1 μm (fig. 3.16b) and 100 nm (fig. 3.16d) beads. Thus, the FWHM of the sharpness curves in agarose grows at around two times the speed of the FWHM for the sharpness curves in PDMS. In addition, the slopes for the 100 nm and the 1 μm bead in agarose are not very different from each other and the same can be said for the slopes for the 100 nm and 1 μm beads in PDMS. This is expected, since the impact of the spherical aberration does not depend on the size of the observed object [24]. Also, the linear fit seems to be a good approximation of the behaviour of the FWHM curves, since the R_{adj}^2 values are not that far from unity (0.82, 0.63, 0.78 and 0.67, respectively for the 1 μm beads in agarose and PDMS and the 100 nm beads in agarose and PDMS), at least over the nominal axial position range observed. By observing the colour encoded SNR data, it can also be confirmed that the latter does not impact the FWHM. Indeed, while, respectively with the 1 μm and 100 nm beads in agarose, the FWHM growth along with a tiny reduction in SNR from approximately 29 to 23 and from around 4 to 3, the same cannot be observed for the beads in PDMS, where the FWHM is still increasing,

independently from the random variations of the SNR. Consequently, the level of spherical aberration is the principal factor impacting the FWHM. Regarding the sharpness peaks, the difference between the curves for the beads in agarose (fig. 3.16a and 3.16c) and those for the beads in PDMS (fig. 3.16b and 3.16d) can be noticed. As already shown in fig. 3.14, the peaks extracted from the beads in agarose tend to decrease as the nominal axial depths of the associated beads grows and the signal slightly decreases, while the same cannot be observed for the peaks corresponding to the beads in PDMS (fig. 3.16b and 3.16d). In these plots, indeed, the sharpness peaks do not seem to get reduced, but rather they seem to fluctuate randomly and the same can be

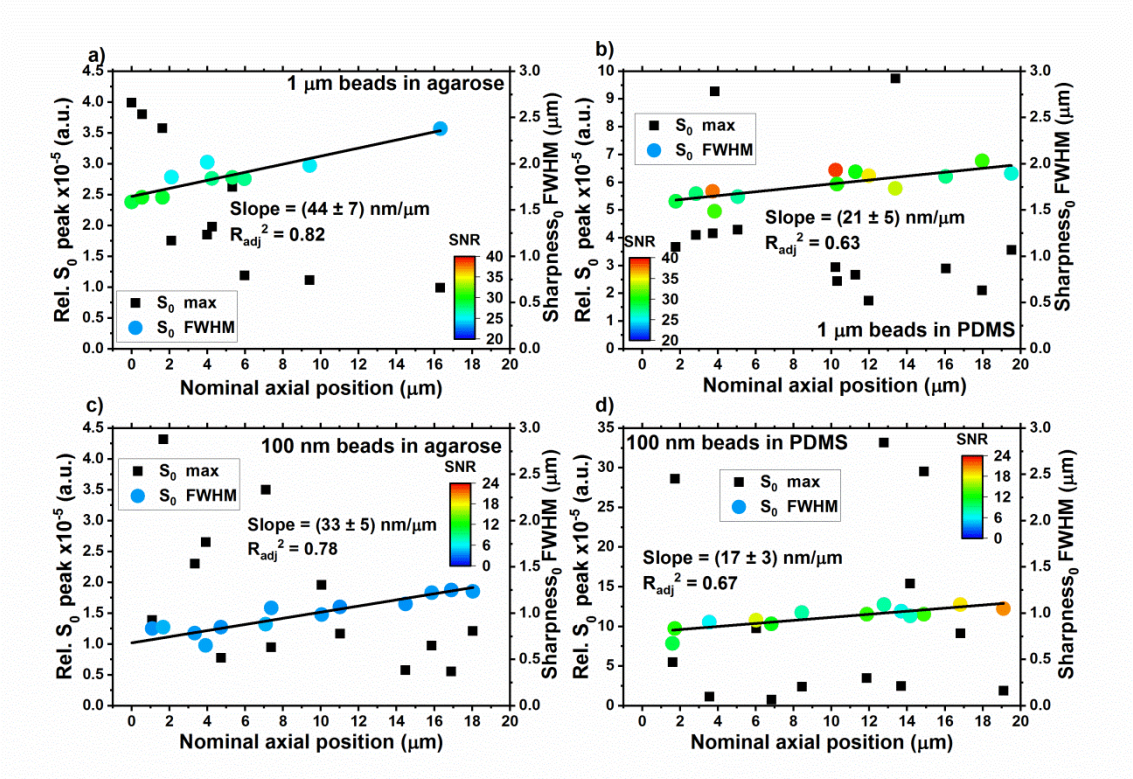

Figure 3.16 Evaluated relative central sharpness curve peak heights (left y axis, blue crosses) and FWHMs (right y axis, green crosses) for beads located at different depths within the samples. The straight lines are linear fits through the FWHM values, whose slopes (with their standard deviations) and goodness (the adjusted R^2 values) are shown in the plots. The associated SNR values have been colour encoded in the FWHM data. **a)** 1 µm beads in agarose (exposure time = 100 ms, em gain = 2,000, laser power at sample = 42.6 µW at λ = 488 nm), **b)** 1 µm beads in PDMS (exposure time = 100 ms, em gain = 3,000, laser power at sample = 2.1 µW at λ = 488 nm), **c)** 100 nm beads in agarose (exposure time = 100 ms, em gain = 3,000, laser power at sample = 4.1 mW at λ = 488 nm) and **d)** 100 nm beads in PDMS (exposure time = 100 ms, em gain = 3,000, laser power at sample = 0.23 mW at λ = 488 nm).

said for the beads at lower positions in the agarose plots (fig. 3.16a and 3.16c). In addition, the peaks associated to the beads in PDMS are higher than those for the beads in agarose. This suggests that, due to the lower refractive index mismatch between PDMS and immersion oil, the same peak reduction effect visible in the agarose plots could be observed at deeper axial positions with the beads in PDMS. However, it also indicates that other factors can influence the sharpness peak values.

To limit the influence of the levels of spherical aberration, in fig. 3.17 the relative sharpness peak heights extracted from the beads acquired within the first 10 µm from the coverslip glass have been plotted against the corresponding SNR and SBR (colour encoded) data. The data calculated for the 100 nm beads have been combined together (fig. 3.17a) and the same has been done for those for the 1 µm beads (fig. 3.17b). However, these have been kept separated, since the sharpness box size has been varied between 100 nm and 1 µm beads and this influences the sharpness peaks. As noticeable in fig. 3.17, the sharpness peaks generally tend to grow with the levels of the signal. Consequently, the latter can influence the sharpness peak height as well as the level of spherical aberration (fig. 3.16).

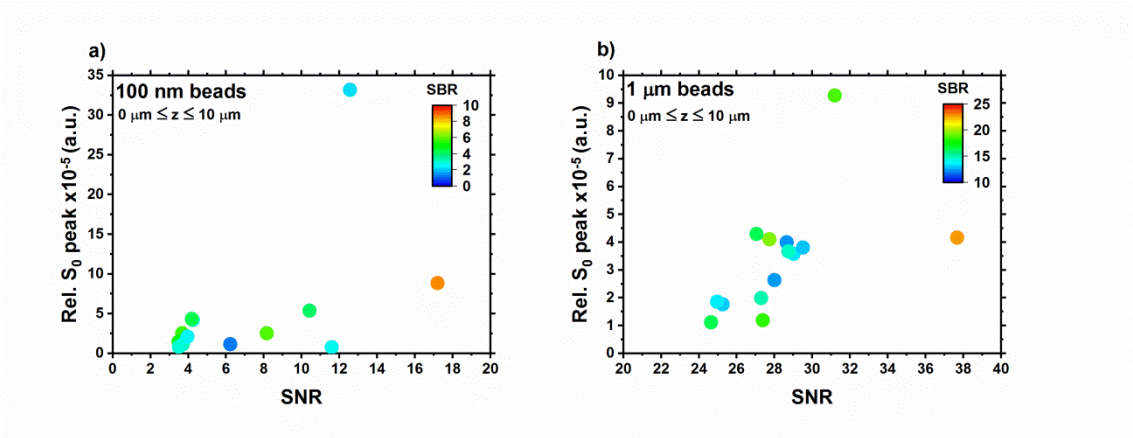

Figure 3.17 Evaluated relative central sharpness curve peak heights plotted against the corresponding SNR and SBR (colour encoded) values, for beads located within 10 µm from the coverslip glass. The data in **a** are associated to the 1 µm beads, while those in **b** to the 100 nm ones. Exposure time = 100 ms, em gain = 2,000 and 3,000, laser power at sample = 42.6 µW, 2.1 µW, 4.1 mW and 0.23 mW, $\lambda = 488$ nm.

3.6.1 *Correlation between sharpness peaks and FWHMs*

Some bell shaped curves, provided the area under them is conserved [65, 66], show a correlation between curve peaks and FWHMs: As one of the two parameters increases,

the other decreases and vice versa. This happens, for example, with both normalised Gaussian and Lorentzian functions. In the case of the normalised Gaussian function, the curve maximum (G_{max}) is equal to $1/[\sigma\sqrt{(2\pi)}]$ and its FWHM ($FWHM_G$) to $2\sigma\sqrt{(2\ln 2)}$, where σ is the standard deviation of the Gaussian function [65]. By combining these two equations it is possible to obtain the following expression (eq. 3.10):

$$G_{max} = 2\sqrt{\frac{\ln 2}{\pi}}\frac{1}{FWHM_G}, \qquad \text{(eq. 3.10)}$$

which shows the relation between G_{max} and $FWHM_G$. For the normalised Lorentzian curve a similar expression can be derived. Considering that the Lorentzian curve peak (L_{max}) is equal to $1/(\pi\gamma)$ and its FWHM ($FWHM_L$) to 2γ, with γ the Lorentzian standard deviation [66], the following relation can be built (eq. 3.11):

$$L_{max} = \frac{2}{\pi}\frac{1}{FWHM_L}. \qquad \text{(eq. 3.11)}$$

Both eq. 3.10 and 3.11 are independent from their corresponding standard deviations and represent a hyperbola [67], where, as one of the two parameters between peak and FWHM increases, the other decreases and vice versa.

Due to their shapes, Gaussian and Lorentzian curves could be used to provide a first order approximation of the sharpness curves. As an example, this is shown in fig. 3.18, where the central sharpness curve associated to a 100 nm bead in agarose located

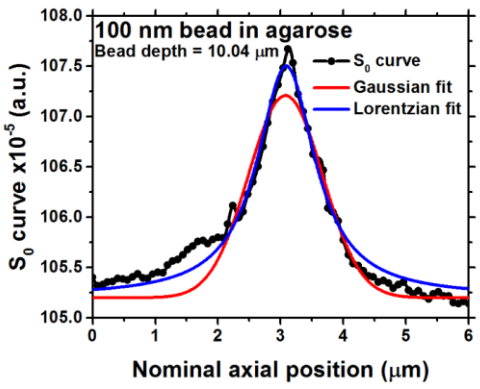

Figure 3.18 Generic Gaussian (red) and Lorentzian (blue) curves fitted to the central sharpness curve (black) associated to a 100 nm bead in agarose located at 10.04 μm from the coverslip glass. Exposure time = 100 ms, em gain = 3,000, laser power at sample = 4.1 mW at λ = 488 nm.

at 10.04 µm from the coverslip glass has been fitted by two generic Gaussian and Lorentzian profiles (fig. 3.18). As observable, neither the Gaussian nor the Lorentzian curve can provide an exact description of the sharpness curve, since the latter is distorted by the levels of the aberrations in the PSF. However, the degree of approximation is enough to investigate if an inverse relation between sharpness peaks and FWHMs similar to that described by eq. 3.10 and 3.11 could be valid for the sharpness curves and provide information on the PSF.

In fig. 3.19 all the relative sharpness peaks (S_{max}) and corresponding $FWHM_S$ ($FWHM_S$) associated to all calculated sharpness curves in the three used planes and for

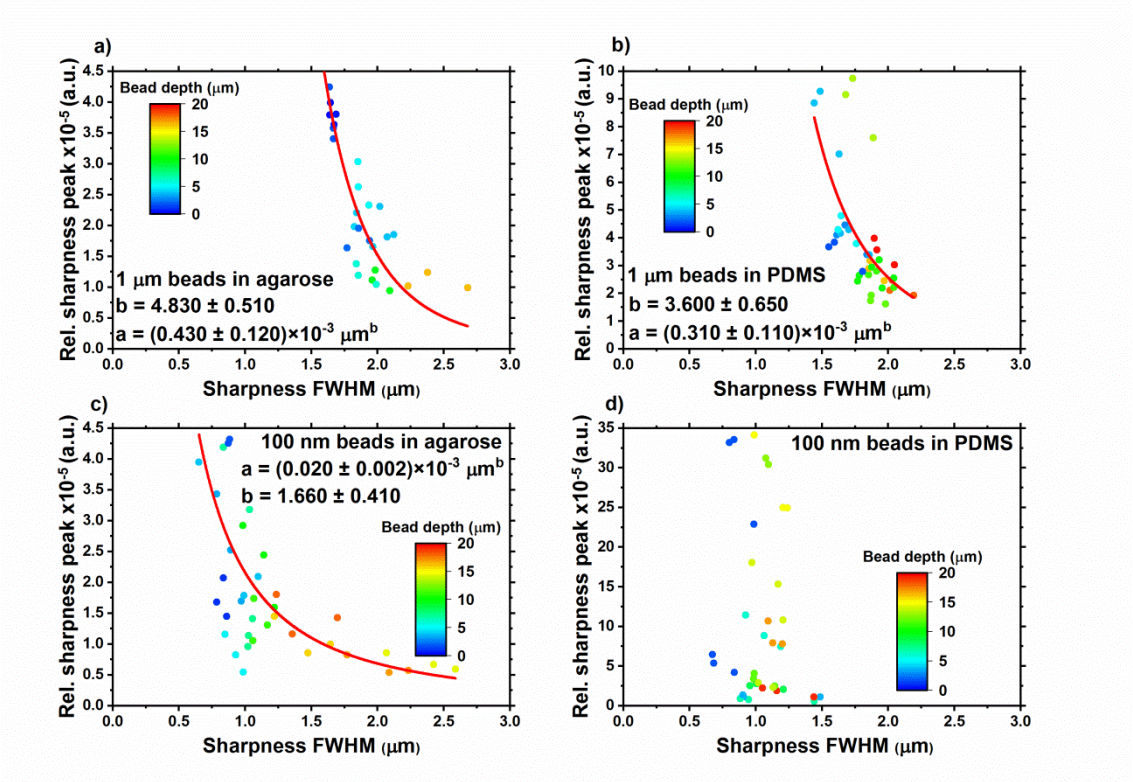

Figure 3.19 Relative sharpness curve peak heights plotted against the corresponding FWHM associated to beads located at different depths (colour encoded) within the samples. The red curves are non-linear fits (eq. 3.12) through the data, whose fitting results (a and b) and their standard deviations are shown in the plots. **a)** 1 µm beads in agarose (exposure time = 100 ms, em gain = 2,000, laser power at sample = 42.6 µW at λ = 488 nm), **b)** 1 µm beads in PDMS (exposure time = 100 ms, em gain = 3,000, laser power at sample = 2.1 µW at λ = 488 nm), **c)** 100 nm beads in agarose (exposure time = 100 ms, em gain = 3,000, laser power at sample = 4.1 mW at λ = 488 nm) and **d)** 100 nm beads in PDMS (exposure time = 100 ms, em gain = 3,000, laser power at sample = 0.23 mW at λ = 488 nm).

all the beads acquired in the four experimental conditions have been plotted against each other, together with the corresponding axial position of the bead colour encoded. These have been fitted by using the following relation (eq. 3.12):

$$S_{max} = \frac{a}{FWHM_S{}^b}, \qquad \text{(eq. 3.12)}$$

which is a hyperbola where the independent variable ($FWHM_S$) can have an exponent different from 1. This has been done to leave more degrees of freedom to the software (OriginPro) to find the best non-linear fits. The parameter b is dimensionless, while a is expressed in micrometres raised to the b. The a and b values obtained by the fits are shown in fig. 3.19. As it can be seen, the hyperbolic behaviour is more evident in the plots associated to the beads in agarose (3.19a and 3.19c) than in those for the beads in PDMS (3.19b and 3.19d). In the agarose plots, the sharpness peaks decrease as the FWHMs increase and this happens as the bead depth grows, as generally observed in fig. 3.14a, 3.14c, 3.16a and 3.16c. Regarding the plots for the beads in PDMS, instead (fig. 3.19b and 3.20d), the hyperbolic behaviour is more difficult to observe. This is due to the fact that, in this case, the FWHM grows more slowly with the bead depth and the sharpness peaks tend to fluctuate randomly (fig. 3.14b, 3.14d, 3.16b and 3.16d). Indeed, the points in fig. 3.19b and 3.19d are more grouped than those for the beads in agarose (fig. 3.19a and 3.19c). Concerning the fits, instead, unfortunately it has not been possible to fit the data relative to the 100 nm beads in PDMS, since the latter was not showing an enough extended hyperbolic profile to allow a good fit. The obtained fitting parameters are summarised in table 3.3:

	a x10^{-3} (µm^b)	**b**
1 µm beads in agarose	0.430 ± 0.120	4.830 ± 0.510
1 µm beads in PDMS	0.310 ± 0.110	3.600 ± 0.650
100 nm beads in agarose	0.020 ± 0.002	1.660 ± 0.410
100 nm beads in PDMS	NA	NA

Table 3.3 Fitting parameters **a** and **b** obtained by applying eq. 3.12 to the data in fig. 3.19. Exposure time = 100 ms, em gain = 2,000 and 3,000, laser power at sample = 42.6 µW, 2.1 µW, 4.1 mW and 0.23 mW, λ = 488 nm.

As noticeable in table 3.3, the a and b parameters calculated for the 1 μm beads in agarose ($(0.430 \pm 0.120)\cdot10^{-3}$ μm^b and 4.830 ± 0.510 respectively) are both higher than those obtained from the 1 μm beads in PDMS ($(0.310 \pm 0.110)\cdot10^{-3}$ μm^b and 3.600 ± 0.650 respectively). This could be linked to the fact that the rate of change of the PSF with the depth-induced spherical aberration is higher in the agarose samples than in the PDMS ones, due to the higher refractive index mismatch with respect to that of the immersion oil (fig. 3.5 and 3.6). Regarding the a and b parameters calculated for the 100 nm beads in agarose ($(0.020 \pm 0.002)\cdot10^{-3}$ μm^b and 1.660 ± 0.410 respectively), these are considerably smaller than those obtained with the 1 μm beads (table 3.3). This could be connected to the fact that the level of the signal associated to the 100 nm beads is smaller than that for the 1 μm ones (fig. 3.7). Consequently, both a and b parameters seem to be linked to the levels of spherical aberration and signal of the PSFs. Ideally, they could be used to characterise the PSF from the point of view of the rate of deformation due to the mismatch-induced spherical aberration. However, further investigations are necessary to verify the description provided.

In conclusion, this section has shown and quantified the impact on the PSF of different levels of mismatch-induced spherical aberration by mean of the shape of the sharpness curves, which have been used as a metric for this purpose. These, on average, tend to reduce their peaks and become wider as the level of depth-induced spherical aberration increases (fig. 3.5, 3.6 and 3.19) and, as expected, this effect is much more evident as the sample - immersion medium refractive index mismatch grows (fig. 3.16).

3.7 Summary and considerations

In this chapter the impact on multifocal microscopy of spherical aberration induced by refractive index mismatch between sample and immersion medium has been presented. After introducing the principle behind the generation of mismatch-induced spherical aberration (sec. 3.2) and describing how the used multiplane system has been assembled and tested (sec. 3.3), it has been shown how this affects the shape of PSFs (sec. 3.4) distorting them and that this distortion increases with the refractive index mismatch and with the depth of the observed object within the material (fig. 3.5 and 3.6). Then, the effect of mismatch-induced spherical aberration on the system plane spacing has been presented (sec. 3.5), indicating that, as the level of spherical aberration increases, the plane spacing grows accordingly (fig. 3.10). This has also been verified by mean of axial CoM calculations, which are in agreement with the results obtained with the sharpness algorithm (fig. 3.12) and have confirmed the increase in plane spacing (fig.

3.13). Finally, the impact of spherical aberration on PSFs has been quantified through the shape of sharpness curves (sec. 3.6). These, in agreement with what shown in fig. 3.5 and 3.6, have clearly shown a linear growth in FWHM as the depth-induced spherical aberration was increasing (fig. 3.16) and that this effect becomes more important as the sample – immersion medium refractive index mismatch is raised. Regarding the change in sharpness peaks, these on average tend to decrease as the level of spherical aberration grows. However, they are also affected by the level of the signal (fig. 3.17). Sharpness peaks and FWHMs show a hyperbolic relation (eq. 3.12 and fig. 3.19).

In conclusion, the results in terms of plane spacing and sharpness curve shape variations indicate that minimising the sample – immersion medium refractive index mismatch is important in MUM, since this allows to reduce the impact of spherical aberration on the PSF and, consequently, can help to improve the accuracy of MUM systems. In addition, knowing how the sharpness FWHM and peak and the PS vary with the axial depth of the emitter could also allow to generate correction factors that could be applied to the sharpness calibration curves to increase the accuracy of the calculated axial positions. However, as already mentioned in sec. 3.4.3, the impact of the axial depth on those parameters has been observed with respect to the nominal rather than actual axial position, due to the effect of the spherical aberration. Consequently, to generate such correction factors the actual against nominal axial position curve and how this varies with the refractive index mismatch should be known. Hypothetically, this curve could be generated by accurately axially shifting through known positions a plate immersed in a known refractive index sample that contains illuminated sub-diffraction holes and observing how the perceived nominal axial position varies. Setting up such an experiment, however, would offer several challenges, due, for example, to the production of such a perforated plate and to the very high accuracy required during the measurements.

In the next chapter the impact of the level of the signal on the performances of MUM will be presented.

3.8 References

[1] S. F. Gibson and F. Lanni, “Experimental test of an analytical model of aberration in an oil-immersion objective lens used in 3-dimensional light-microscopy,” Journal of the Optical Society of America A - Optics Image Science and Vision,

vol. 8, no. 10, pp. 1601-1613, 1991.

[2] M. J. Booth and T. Wilson, "Refractive-index-mismatch induced aberrations in single-photon and two-photon microscopy and the use of aberration correction," Journal of Biomedical Optics, vol. 6, pp. 266-272, 2001.

[3] E. Wolf, "The diffraction theory of aberrations," Reports on Progress in Physics, vol. 14, p. 95, 1951.

[4] K. N. Fish, "Total Internal Reflection Fluorescence (TIRF) Microscopy," Current Protocols in Cytometry, vol. 50, no. 1, pp. 12.18.1-12.18.13, 2009.

[5] E. J. Botcherby, R. Juskaitis, M. J. Booth and T. Wilson, "Aberration-free optical refocusing in high numerical aperture microscopy," Optics Letters, vol. 32, no. 14, pp. 2007-2009, 2007.

[6] M. Abramowitz, K. R. Spring, H. E. Keller and M. W. Davidson, "Basic principles of microscope objectives," Biotechniques, vol. 33, no. 4, pp. 772-+, 2002.

[7] A. v. d. Horst, "Spherical aberrations due to refractive-index mismatch — Influence on optical trapping and confocal imaging," in High-refractive index particles in counter-propagating optical tweezers - manipulation and forces, Utrecht University, 2006, pp. 37-56.

[8] B. E. A. Saleh and M. C. Teich, "Postulates of ray optics," in Fundamentals of photonics, 2nd ed., Wiley-Interscience, 2007, pp. 3-6.

[9] E. W. Weisstein, "Parallel Postulate," in CRC Concise encyclopedia of mathematics, 2nd ed., CRC Press, 2002, pp. 2142-2143.

[10] I. Agricola and T. Friedrich, "Elementary geometrical figures and their properties," in Elementary geometry, American Mathematical Society, 2008, pp. 9-98.

[11] B. E. A. Saleh and M. C. Teich, "Ray optics," in Fundamentals of photonics, 2nd ed., Wiley-Interscience , 2007, pp. 1-37.

[12] B. E. A. Saleh and M. C. Teich, "Simple optical components," in Fundamentals of photonics, 2nd ed., Wiley-Interscience, 2007, pp. 6-17.

[13] B. E. A. Saleh and M. C. Teich, "Wave optics," in Fundamentals of photonics, Wiley-Interscience, 2007, pp. 38-73.

[14] B. E. A. Saleh and M. C. Teich, "Electromagnetic optics," in Fundamentals of photonics, Wiley-Interscience, 2007, pp. 150-196.

[15] "Zemax OpticStudio," [Online]. Available:

https://www.zemax.com/products/opticstudio. [Accessed September 2018].

[16] "CODE V Optical Design Software," [Online]. Available: https://www.synopsys.com/optical-solutions/codev.html. [Accessed September 2018].

[17] S. Abrahamsson, J. Chen, B. Hajj, S. Stallinga, A. Y. Katsov, J. Wisniewski, G. Mizuguchi, P. Soule, F. Mueller, C. D. Darzacq, X. Darzacq, C. Wu, C. I. Bargmann, D. A. Agard, M. Dahan and M. G. L. Gust, "Fast multicolor 3D imaging using aberration-corrected multifocus microscopy," Nature Methods, vol. 10, pp. 60-63, 2013.

[18] P. A. Dalgarno, H. I. C. Dalgarno, R. Lambert, L. Paterson, D. C. Logan, D. P. Towers, R. J. Warburton and A. H. Greenaway, "Multiplane imaging and three dimensional nanoscale particle tracking in biological microscopy," Optics Express, vol. 18, pp. 877-884, 2010.

[19] S. Ram, J. Chao, P. Prabhat, E. S. Ward and R. J. Ober, "Overcoming the depth discrimination barrier in widefield microscopes: 3D single molecule tracking with high axial accuracy," Single Molecule Spectroscopy and Imaging, vol. 6862, pp. O8620-O8620, 2008.

[20] M. J. Booth, "Adaptive optics in microscopy," Philosophical Transactions of the Royal Society A - Mathematical Physical and Engineering Sciences, vol. 365, no. 1861, pp. 2829-2843, 2007.

[21] F. A. Jenkins and H. E. White, "Spherical aberration of a thin lens," in Fundamentals of optics, 4th ed., McGraw-Hill, 2001, pp. 153-157.

[22] D. Malacara and B. J. Thompson, "Aspheric Lenses," in Handbook of optical engineering, Marcel Dekker, Inc., 2001, pp. 142-143.

[23] D. G. Abdelsalam and M. Stanislas, "Spherical aberration measurement of a microscope objective by use of calibrated spherical particles," Applied Optics, vol. 56, no. 16, pp. 4766-4771, 2017.

[24] F. A. Jenkins and H. E. White, "Spherical aberration of a thin lens," in Fundamentals of optics, 4th ed., McGraw-Hill Higher Education, 2001, pp. 153-157.

[25] Blanchard, PM; Greenaway, AH, "Simultaneous multiplane imaging with a distorted diffraction grating," Applied Optics, vol. 38, no. 32, pp. 6692-6699, 1999.

[26] D. C. O'shea, "Reducing aberrations," in Elements of modern optical design, John

Wiley & Sons, 1985, pp. 204-219.

[27] S. Djidel, J. K. Gansel, H. I. Campbell and A. H. Greenaway, "High-speed, 3-dimensional, telecentric imaging," Optics Express, vol. 14, pp. 8269-8277, 2006.

[28] B. E. A. Saleh and M. C. Teich, "Image formation," in Fundamentals of photonics, Wiley-Interscience, 2007, pp. 127-137.

[29] I. H. Malitson, "Interspecimen comparison of the refractive index of fused silica," Journal of the Optical Society of America, vol. 55, no. 10, pp. 1205-1209, 1965.

[30] "ThermoFisher Scientific," [Online]. Available: https://www.thermofisher.com/it/en/home/life-science/cell-analysis/fluorophores.html. [Accessed September 2018].

[31] E. Hecht, "The diffraction grating," in Optics, 4th ed., Addison Wesley, 2002, pp. 476-485.

[32] A. Tahmasbi, S. Ram, J. Chao, A. V. Abraham, F. W. Tang, E. S. Ward and R. Ober, "Designing the focal plane spacing for multifocal plane microscopy," OPTICS EXPRESS, vol. 2, no. 14, pp. 16706-16721, 2014.

[33] A. Tahmasbi, J. C. S. Ram, A. V. Abraham, E. S. Ward and R. Ober, "An information-theoretic approach to designing the plane spacing for multifocal plane microscopy," Three-Dimensional and Multidimensional Microscopy: Image Acquisition and Processing XXII, vol. 9330, no. 933011, 2015.

[34] "Micro-Manager," [Online]. Available: https://micro-manager.org/. [Accessed June 2019].

[35] D. Dussault and P. Hoess, "Noise performance comparison of ICCD with CCD and EMCCD cameras," Infrared Systems and Photelectronic Technology, vol. 5563, pp. 195-204, 2004.

[36] "CAIRN," [Online]. Available: https://www.cairn-research.co.uk/. [Accessed September 2018].

[37] "Thorlabs 1 in lens tubes," [Online]. Available: https://www.thorlabs.com/newgrouppage9.cfm?objectgroup_id=3307. [Accessed September 2018].

[38] "Thorlabs 6 mm rods," [Online]. Available: https://www.thorlabs.com/newgrouppage9.cfm?objectgroup_id=4125. [Accessed September 2018].

[39] "Applied Image Inc," [Online]. Available: https://www.appliedimage.com/wp-

content/uploads/2017/09/USAF-1951-Test-Target-T-20_v1-04.pdf. [Accessed September 2018].

[40] "ImageJ," [Online]. Available: https://imagej.nih.gov/ij/. [Accessed September 2018].

[41] H. I. C. Dalgarno, P. A. Dalgarno, A. C. Dada, C. E. Towers, G. J. Gibson, R. M. Parton, I. Davis, R. J. Warburton and A. H. Greenaway, "Nanometric depth resolution from multi-focal images in microscopy," Journal of the Royal Society Interface, vol. 8, no. 60, pp. 942-951, 2011.

[42] P. Serwer, "Agarose gels - Properties and use for electrophoresis," Electrophoresis, vol. 4, pp. 375-382, 1983.

[43] J. E. Mark, H. R. Allcock and R. West, in Inorganic polymers, 2nd ed., Oxford University Press, 2005, pp. 154-214.

[44] P. Z. d. Azevedo, T. F. Sylvestre, R. D. Cavalcante, L. R. d. Carvalho, D. V. Moris, M. L. C. S. d. Oliveira and R. P. Mendes, "Evaluation of the double agar gel immunodiffusion test and of the enzyme-linked immunosorbent assay in the diagnosis and follow-up of patients with chronic pulmonary aspergillosis," Plos One, vol. 10, p. e0134841, 2015.

[45] D. Qin, Y. N. Xia and G. M. Whitesides, "Soft lithography for micro- and nanoscale patterning," Nature Protocols, vol. 5, pp. 491-502, 2010.

[46] B. W. Zhang, Q. Dong, C. E. Korman, Z. Y. Li and M. E. Zaghloul, "Flexible packaging of solid-state integrated circuit chips with elastomeric microfluidics," Scientific Reports, vol. 3, p. 1098, 2013.

[47] M. L. Byron and E. A. Variano, "Refractive-index-matched hydrogel materials for measuring flow-structure interactions," Experiments in Fluids, vol. 54, p. 1456, 2013.

[48] J. C. McDonald and G. M. Whitesides, "Poly(dimethylsiloxane) as a material for fabricating microfluidic devices," Accounts of Chemical Research, vol. 35, pp. 491-499, 2002.

[49] M. L. Byron and E. A. Variano, "Refractive-index-matched hydrogel materials for measuring flow-structure interactions," Experiments In Fluids, vol. 54, no. 2, 2013.

[50] "Dow Corning," [Online]. Available: http://www.farnell.com/datasheets/1599873.pdf. [Accessed 2018].

[51] W. T. Welford, Aberrations of optical systems, Adam Hilger, 1991, pp. 109-139.

[52] Andor - Oxford Instruments, Andor Ixon Ultra 897 - Hardware Guide, ver. 1.3, Andor, 2015.

[53] M. Hirsch, R. J. Wareham, M. L. Martin-Fernandez, M. Hobson and D. J. Rolfe, "A stochastic model for electron multiplication charge-coupled devices - From theory to practice," Plos One, vol. 8, no. 1, p. e53671, 2013.

[54] D. Dussault and P. Hoess, "Noise performance comparison of ICCD with CCD and EMCCD cameras," Infrared Systems and Photelectronic Technology, vol. 5563, pp. 195-204, 2004.

[55] J. G. White, W. B. Amos and M. Fordham, "An evaluation of confocal versus conventional imaging," Journal of Cell Biology, vol. 105, no. 1, pp. 41-48, 1987.

[56] G. M. Whitesides and S. K. Tang, "Fluidic Optics," SPIE Digital Library, vol. 6329, 2006.

[57] W. M. Irvine and J. B. Pollack, "Infrared optical properties of water and ice spheres," Icarus, vol. 8, pp. 324-360, 1968.

[58] J. M. Geary, "Aberrations in general," in Introduction to lens design, Willmann-Bell, Inc. , 2002, pp. 65-84.

[59] "Wolfram Mathematica," [Online]. Available: http://www.wolfram.com/mathematica/. [Accessed September 2018].

[60] H. R. Harrison and T. Nettleton, "Centre of mass," in Principle of engineering mechanics, 2nd ed., Edward Arnold, 1994, pp. 25-26.

[61] A. M. G. Solo, "Multidimensional matrix mathematics: Notation, representation, and simplification, Part 1 of 6," Proceedings of the World Congress on Engineering 2010 Vol III , pp. 1824-1828, 2010.

[62] "MathWorks MATLAB," [Online]. Available: https://ch.mathworks.com/. [Accessed September 2018].

[63] V. N. Mahajan, "Symmetry properties of aberrated point-spread functions," Journal of the Optical Society of America A - Optics Image Science and Vision, vol. 11, pp. 1993-2003, 1994.

[64] S. F. Gibson and F. Lanni, "Experimental test of an analytical model of aberration in an oil-immersion objective lens used in three-dimensional light microscopy," Journal of the Optical Society of America A - Optics Image Science and Vision, vol. 9, pp. 154-166, 1992.

[65] G. Casella and R. L. Berger, "Continuous distributuion," in Statistical inference,

2nd ed., Duxbury advanced series, 2002, pp. 98-111.

[66] N. L. Johnson and N. B. S. Kotz, "Cauchy distribution," in Continuous univariate distributions volume 1, 2nd ed., John Wiley & Sons, Inc., 1994, pp. 298-336.

[67] C. Y. Young, "The hyperbola," in Precalculus, John Wiley & Sons, Inc., 2010, pp. 860-872.

Chapter 4

Imaging limits of diffraction multifocal microscopy

4.1 Chapter overview

After the study, presented in chapter 3, of the impact of spherical aberration on multiplane microscopy, here the limits to imaging of this technique are tackled. In particular, the performances (fig. 4.11) of the Dalgarno multiplane relay and of the sharpness algorithm are studied in the same four experimental conditions explored in chapter 3 (100 nm and 1 μm beads in agarose and PDMS), but under different photon flux regimes. This has shown a linear and an exponential behaviour (eq. 4.8 and 4.14, fig. 4.40) for, respectively, the axial range and precision as a function of the signal level and a clear SNR_0 threshold (sec. 4.4.3) below which the axial range collapses to 0 μm and the axial precision tends to infinity. The impact of the plane spacing on the speed at which the axial range grows with the SNR is also shown (fig. 4.41). The results found (sec. 4.7) are valid for the Dalgarno multiplane setup and the sharpness algorithm when an accuracy within 100 nm is required, but they can be generally used as a guidance in case other similar multiplane setups/algorithms are used. A set of two equations has also been generated to allow a quick evaluation of the expected axial range and precision, given the parameters of the multiplane system are known.

4.2 Influence of signal level on multiplane microscopy

Signal, noise and background levels are extremely important in optical microscopy [1, 2], regardless of the imaging technology. In order to capture the images observable through an optical microscope, digital cameras such as charged coupled devices (CCDs) [3] and scientific complementary metal oxide semiconductors (sCMOSs) [4] are commonly used. These devices are provided with several pixels, which generate some electron-hole pairs every time photons emitted from the samples (i.e. the signal) hit them [5]. In case a CCD camera is used, the electron content accumulated in each pixel is then continuously shifted along a particular direction from one pixel to another, until the readout register is reached. The latter, then, further transfers these electrons to the output node, where the content of each pixel is read and digitalised [6]. Regarding sCMOS cameras, instead, each single column has its own readout structure, where the contents of each pixel is sent to an amplifier and then to an analog to digital converter (ADC) [7]. CCD cameras can be equipped with an electron multiplying system (emCCD) to amplify the signal [8]. This is especially convenient in situations (e.g. single molecule detection) where the amount of signal is quite low to be efficiently

detected and there is a requirement to amplify the photon signal with respect to the noise. However, the em gain cannot be raised indefinitely, since it amplifies the background too and further reduces the possibility to distinguish this from the signal. In addition, also the em gain introduces a noise factor [4].

Every time a signal is recorded, there is always some noise associated to it and coming from different sources [9]. Some noise originates from the stochastic nature of the photons arriving, which is called shot noise or Poisson noise [10], since it follows Poisson statistics. This noise is amplified by the em gain and grows with the signal [8]. Another source of noise is introduced by the electronic signal reading process, and it is called read noise [10]. This noise in general follows Gaussian statistics. Its contribution is usually smaller than the one provided by the Poisson noise at high photon flux regimes (it is not amplified by the em gain) and, as a consequence, it becomes more important at low signal levels. Also the heating of the camera while operating can generate some noise called dark noise, due to inherent thermal excitation of electrons [10]. This noise too can be boosted by the em gain, but cooling down the camera during the acquisition can make it negligible.

Since noise is unavoidable [10] and grows with the signal, signal and noise need to be considered simultaneously to optimise the data acquisition [11]. This can be done by considering the signal to noise ratio (SNR) [9], which measures how many times the signal is higher than the noise. The SNR needs to be maximised in order to improve the ability to localise emitters under study with high accuracy and precision and this can be achieved by setting the experimental parameters accordingly. For example, the power of the excitation source (e.g. a laser source) could be raised to increase the rate of photons emitted by the sample or the camera ET could be increased to allow the camera chip to collect more photons. Both these actions will enhance the SNR. However, as the power of the excitation source is increased, the emitter photobleaching time [12] (i.e. the time over which the emitters can emit photons at the required wavelengths) is reduced. This is a drawback for those applications where there is a requirement to observe the behaviour of single emitters [13] (e.g. single molecule applications) over extended temporal intervals. Regarding the camera ET, instead, high values will compromise the temporal resolution, which, in turn, will make more difficult the study of fast moving phenomena [14]. Also the sample can be optimised to increase the SNR. This could be done, for example, by choosing bright emitters with high photon emission rates and long photobleaching times or by using them in non-absorbing media [15]. However, emitter and media choices follow also other criteria, which can depend on sample needs

(e.g. if the emitter needs to be expressed in a cell to be attached to a target protein to study [13]) or on emission wavelength requirements [16].

In addition to noise, together with the desired signal, there is always unwanted signal, generally called background [9, 17, 18]. Background has different sources. It can come from out of focus emitters, autofluorescence, light coming from the external environment, etc. Due to its nature, it can also be non-uniformly distributed in the field of view (FOV) and can dynamically change in time [19]. This poses serious limitation to imaging, since it can be easily confused with the wanted signal and can complicate the background subtraction operation necessary for its removal [20]. As with the noise, the signal can also be compared to the background through the signal to background ratio (SBR), which states how many times the signal is above the background level [17]. The SBR could be increased by using bright emitters or by lowering the background through the reduction of the emitter density or quenching the autofluorescence [21].

In multiplane microscopy the potential problems caused by noise and background levels are, in general, worsened, since the signal is split between the different planes involved, reducing both SNR and SBR in each plane [22]. Background and Poisson noise are also split among the diffraction orders, however, the camera and dark noise are not, thus the net effect is always a reduction in the overall SNR. Noise and background can, in particular, cause problems in the defocused images typically acquired in multifocus microscopy. Indeed, in defocused PSFs the signal is further spread over an increasing number of pixels, which reduces the average SNR per pixel. This imposes a strong limitation on what multiplane microscopy can achieve in terms of axial and lateral localisation accuracy of out of focus objects.

In this chapter, the impact on the performance of the sharpness algorithm applied to the Dalgarno diffractive multiplane imaging system in terms of axial range (i.e. the range over which it is possible to calculate the expected nominal axial position) and axial precision (i.e. the average axial precision within the axial range) has been studied under different conditions and for same four experimental conditions used in the previous chapter: 1 μm and 100 nm beads three-dimensionally dispersed in agarose and PDMS. First, the performance of the multiplane relay and sharpness algorithm have been considered at different camera ETs, since this parameter is crucial to control both signal level and temporal resolution [23, 24]. To explore extremely low photon levels and observe how the used multiplane system behaves in this regime, the limits of the system have been pushed further down by using neutral density filters [25]. Then, the impact of different bandwidth filtering to correct for the chromatic aberration grating-

induced has been studied. Finally, the effect of objective lens with different magnification and NA has been investigated.

4.2.1 *Definition of the method used to calculate the SNR and SBR*

All the results have been interpreted by taking into consideration the levels of SNR and SBR. Since the SNR and SBR vary as the PSFs are defocused, it is not possible to assign single SNR and SBR values to each PSF. Therefore, the SNR and SBR values have only been calculated for the beads in focus (positions identified as the frames with the highest image count values in the bead lateral profiles) in either the central or outer planes and these values have been used as a relative metric to compare the different imaging conditions. The SBR was calculated by taking the average (over all the in focus images of the studied PSF in each z-stack series acquired as in section 3.2.2) background-subtracted integrated image count value of a box containing the PSF under study and dividing it by the calculated amount of background under the PSF itself. To do this (fig. 4.1a), the average background per pixel was estimated by taking the average background value in a box not containing any PSF in the same frame of the first z-stack series where the in focus PSF was located (the average background per pixel was basically constant among the acquired z-stack series), while the box containing the PSF was centred on the PSF maximum value. The sizes of the boxes used for this purpose were equal to those that have been used to calculate the sharpness of the studied PSFs. The effect of the background subtraction is shown on the lateral bead profiles in fig. 4.1b and 4.1c, tracked through the horizontal dashed line in the selected bead region (fig. 4.1a). The background level in fig. 4.1b (vertical dark yellow line) is around the value calculated with the background box (fig. 4.1a), which is equal to 103 image counts (IC) for the 1 μm bead in agarose used as example in fig. 4.1a (frame from the first z-stack of the used z-stack series, ET = 100 ms, em gain = 2,000, laser power at sample = 42.56 μW at λ = 488 nm, plane spacing 630 nm). This value was subtracted from all the pixel values in the selected bead areas before calculating the integrated intensities in all the ten frames with the bead in focus in each z-stack series. The corresponding lateral bead profile after background subtraction is presented in fig. 4.1c. The average integrated intensity per z-stack series was then calculated by averaging all the ten integrated intensity values obtained. Bead profiles, integrated intensities and average background per pixel were calculated by using the software ImageJ [26]. To calculate the total background under each in focus PSF, instead (semi-transparent red area in fig. 4.1b), it was necessary to know the number of pixels that

were forming each bead image. This was done by counting the distance in pixels between the two points on the bead profiles just above the background level (red

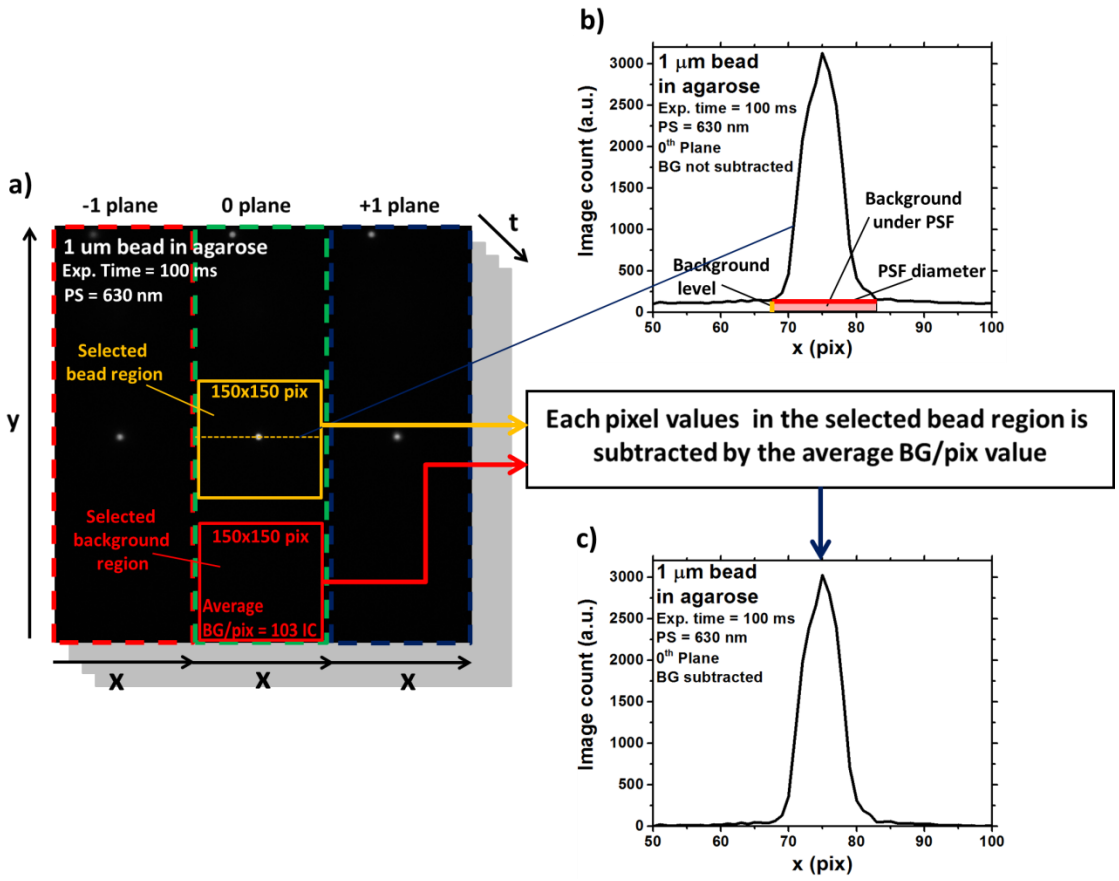

Figure 4.1 a) Example frame from the first z-stack of a bead z-stack series showing a 1 µm bead in agarose in focus in the central plane. On the frame the boxes (150x150 pix^2) used to delimit the bead region (dark yellow, centred at the bead maximum value) and to calculate the average background per pixel (red, area without beads) are drawn. **b)** Lateral profile for the bead in focus in the 0^{th} plane in **a**, observed through the central dashed line (tracked where the signal was maximised) in the bead region box. On this profile plot the average background per pixel level (vertical dark yellow line), the PSF diameter (horizontal red line, as the length over which the signal is higher than the background per pixel level) and the background under the PSF (semi-transparent red area) are indicated. **c)** Same profile as in **b**, but tracked after that each pixel in the selected bead region in **a** was subtracted by the average background per pixel (BG/pix or B_{pix}) calculated (103 IC). ET = 100 ms, em gain = 2,000, laser power at sample = 42.56 µW at λ = 488 nm.

horizontal line in fig. 4.1b). This value has then been used to create a box centred on the PSF peak, within which the number of non-zero pixels after the background subtraction

has been counted and multiplied by the average background per pixel to obtain the total background under the PSF. The ratio between the average integrated intensity and the total background under the bead image was finally calculated to get the SBR.

Regarding the SNR, this has been calculated by, first, evaluating the average photon count by using the same average integrated intensity used for the SBR through the formula [9] (eq. 3.7):

$$n_{ph} = \frac{ADC}{q}\frac{ic}{G}, \qquad \text{(eq. 3.7)}$$

where n_{ph} is the average photon count, ic is the average background-subtracted integrated image count, ADC is the analog to digital conversion factor of the camera (equivalent to 12.7 e^-/IC for the emCCD camera used, Andor EMCCD Ixon Ultra 897), q is the quantum efficiency (equal to 0.9 e^-/photon, again, for the emCCD camera utilised) and G is the em gain used for the acquisition. Then, the SNR was obtained by the next equation [9] (eq. 4.1):

$$SNR = \frac{q\, n_{ph} G}{\sqrt{2\, q\, n_{ph} G^2 + {G_N}^2}}, \qquad \text{(eq. 4.1)}$$

where the signal at the numerator represents the amount of photo-electrons, obtained by multiplying the photon count by the quantum efficiency and the em gain, and the noise at the denominator is composed by two terms, the Poisson noise (left hand side) and the Gaussian read noise (right hand side). The 2 factor in the denominator of eq. 4.1 is an amplification factor due to the em shift register [9]. In all the calculations made, G_N has been neglected, considering it is not multiplied by the gain and therefore it is much lower than the Poisson component. By neglecting G_N eq. 4.1 can be simplified and, by substituting eq. 3.7 into eq. 4.1, an equation for the SNR in terms of image count ic can be obtained (eq. 4.2):

$$SNR = \sqrt{\frac{ADC}{2G}}\sqrt{ic}. \qquad \text{(eq. 4.2)}$$

Eq. 4.2 is important, since it can lead to an equation for the average SNR per pixel (SNR_{pix}). Indeed, the SNR calculated from the integrated intensity of a PSF can just

give an estimation of the associated total SNR in a frame. However, this signal is spread over an increasing number of pixels as the PSF gets defocused [27], thus reducing the SNR_{pix}. This is an important limiting factor in multiplane microscopy, where the use of defocused images is needed, and leads to a reduction in axial localisation precision, as well as to a reduction in axial range. In order to calculate SNR_{pix}, it is needed to divide ic in eq. 4.2 by the number of pixels involved in the PSF image N_{pix}, which, in turn, is equal to the number of pixels calculated to estimate the total background for the SBR (eq. 4.3):

$$\mathrm{SNR_{pix}} = \sqrt{\frac{\mathrm{ADC}}{2\mathrm{G}}}\sqrt{\frac{\mathrm{ic}}{\mathrm{N_{pix}}}} = \frac{\mathrm{SNR}}{\sqrt{\mathrm{N_{pix}}}}. \qquad \text{(eq. 4.3)}$$

Therefore, SNR_{pix} can be calculated from the total SNR in the frame by dividing the latter by the square root of the number of pixels involved in the PSF. Obviously, since the signal is not evenly distributed in the PSF, but rather it is concentrated around its centre (PSFs are Airy functions [27], sec. 1.3.4), also the SNR_{pix} will increase as pixels closer to the PSF centres are observed. Consequently, the average SNR_{pix} calculated with eq. 4.3 can just give an estimate of the SNR_{pix} profile in each frame. Regarding the average SBR per pixel (SBR_{pix}), this is equivalent to the overall SBR per frame. This can be shown by equation 4.5, which is a mathematical representation of the SBR definition given above in this section:

$$\mathrm{SBR} = \frac{\mathrm{ic}}{\mathrm{B_{pix}N_{pix}}} = \frac{\mathrm{ic_{pix}}}{\mathrm{B_{pix}}} = \mathrm{SBR_{pix}}, \qquad \text{(eq. 4.4)}$$

where ic is the average integrated intensity calculated as explained before, B_{pix} is the average background per pixel and N_{pix} is the number of pixels involved. By dividing ic by N_{pix} the average ic per pixel can be calculated (ic_{pix}) and the ratio between the latter and B_{pix} gives SBR_{pix}, which is equal to SBR. This relation holds only between the total SBR in the frame and the average SBR_{pix}, but it is not valid for the actual SBR of each pixel, which will increase as the SNR_{pix} for pixels closer to the PSF centres.

4.3 Experimental methods used to estimate the limits to imaging of a diffraction multifocal system

Microscope, emCCD camera, multifocal diffraction relay, samples (1 μm and 100 nm beads in agarose and PDMS) and z-stack data acquisition methodology used to acquire the data presented in this chapter are the same as in section 3.2.2.

For these experiments, it was decided to limit the depth of the beads within the substrate materials (i.e. agarose and PDMS) to 10 μm from the coverslip, in order to avoid spherical aberration dominating. Ideally, all the beads should have been positioned at the same distance from the coverslip, in order to keep constant the spherical aberration in the two materials, but, unfortunately, manufacturing such samples is challenging and beyond the scope of this work.

4.4 Importance of the camera exposure time to control the performances of a diffraction multifocal microscope: A study at different plane spacing

In microscopy, one of the most common ways to modify SNR and SBR of images is by changing the camera ET [23, 24], which is the set time over which the photon flux coming from the sample is collected by a camera as signal. Therefore, it is crucial to assess the influence on sharpness curve shapes and the variations of diffraction multifocal system performances at different ETs, in order to understand how the system responds to several photon flux regimes.

In order to study the multiplane relay and the sharpness algorithm from this point of view, several bead z-stacks have been acquired in the four experimental conditions (100 nm and 1 μm beads in agarose and PDMS), with various camera ETs (38 ms, 70 ms, 100 ms, 130 ms and 160 ms) and through three different distorted diffraction gratings, with PS 80 nm, 320 nm and 630 nm (i.e. with focal lengths, respectively, 7,579.67 mm, 1,894.92 mm and 962.50 mm), to evaluate also the effect of PS on the system performance. Laser powers at samples were 8.56 mW and 0.76 mW, respectively for 100 nm beads in agarose and PDMS, and 42.56 μW and 2.07 μW, respectively for 1 μm beads in agarose and PDMS, at a wavelength of 488 nm, while the camera em gain was set on 3,000 for all experimental condition apart the 1 μm beads in agarose, were a value of 2,000 was used. All the z-stacks were acquired via an oil immersion objective (Zeiss, 440782-9800-000), with magnification 100x and NA 1.46, with dichroic mirror (Semrock, Di03-R488-t1-25x36) and emission filter (Semrock, FF01-535/50-25) inserted in the imaging path of the microscope to separate excitation and emission light, and with a further 10 nm bandwidth filter (Semrock, FF01-520/5-25,

centred on 520 nm), to remove the chromatic aberration introduced by the gratings. Bead z-stacks were acquired with the same procedure explained in the section 3.2.2, scanning the objective ten times over a range of ±3 μm and ±7 μm (respectively for 100 nm and 1 μm beads), centred on the axial position with the beads in focus in the central plane, and with an axial spacing of 100 nm among the images in the stacks. All the sharpness curves were calculated by using sharpness boxes (SBs) of 150x150 pixels and 30x30 pixels, respectively for 1 μm and 100 nm beads. These acquisition parameters have been summarised in the next table (table 4.1):

<table>
<tr><th>Bead size</th><th>ET (ms)</th><th>em gain</th><th>Laser power at λ = 488 nm (mW)</th><th>BW (nm)</th><th>Obj. lens</th><th>SB side (pix)</th><th>PS (nm)</th><th>z-stack axial ext. (μm)</th></tr>
<tr><td>100 nm</td><td rowspan="2">38, 70, 100, 130, 160</td><td>3,000</td><td>8.56 (A), 0.76 (P)</td><td rowspan="2">10</td><td rowspan="2">M = 100x, NA = 1.46, oil</td><td>30</td><td rowspan="2">80, 320, 630</td><td>±3 μm</td></tr>
<tr><td>1 μm</td><td>2,000 (A), 3,000 (P)</td><td>42.56 10^{-3} (A), 2.07 10^{-3} (P)</td><td>150</td><td>±7 μm</td></tr>
</table>

Table 4.1 Experimental parameters and conditions used with the multi-ET study. A = agarose, P = PDMS, M = magnification, SB = sharpness box, PS = plane spacing, NA = numerical aperture, ET = exposure time, BW) bandwidth.

In fig. 4.2 some example lateral cross sections extracted from the first z-stacks of two z-stack series, acquired with ETs of 38 ms (fig. 4.2a, 4.2d and 4.2g) and 160 ms (fig. 4.2c, 4.2f and 4.2i) are shown for two 1 μm beads in agarose, observed in the central plane and with PS equal to 630 nm. The corresponding lateral profiles, observed through the horizontal lines in the lateral cross section panels and averaged among the three corresponding frames in the first three z-stacks of the z-stack series, are presented in fig. 4.2b, 4.2e and 4.2h. The cross sections in fig. 4.2d and 4.2f have been extracted from the best focus positions, where the bead profiles in fig. 4.2e were maximised. Instead, those in fig. 4.2a and 4.2c have been extracted 3.5 μm before the best focus (i.e. closer to the coverslip glass), while those in fig. 4.2g and 4.2i 3.5 μm after (i.e. further from the coverslip glass). The first difference between lateral profiles for beads acquired at 38 ms and 160 ms is, as expected, in the amount of signal detected. Starting from the in focus beads (fig. 4.2e), the profile peak grows from around 750 IC to 3,200 IC, as the

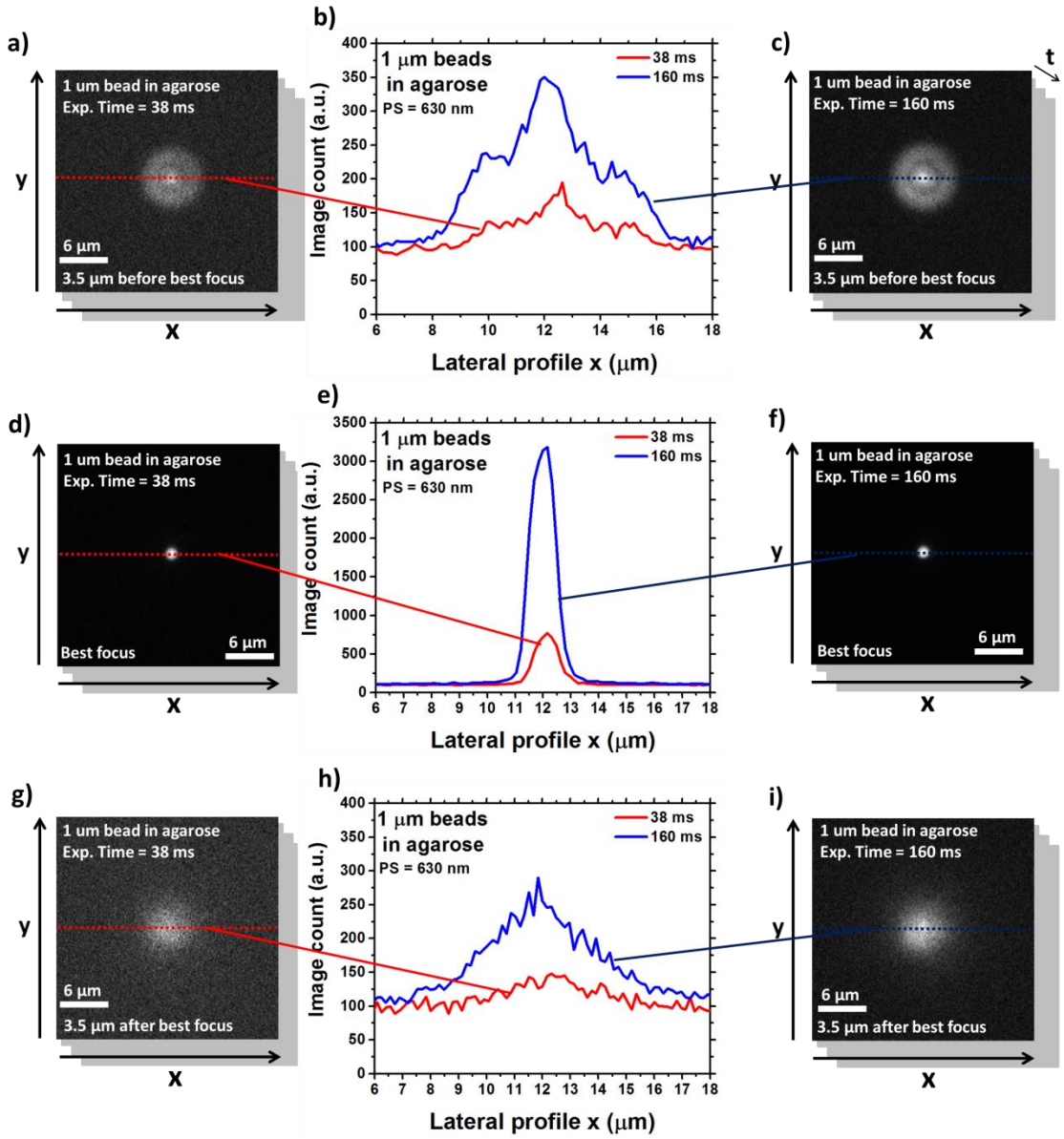

Figure 4.2 Lateral cross sections and profiles (observed through the horizontal lines in the cross section panels) of two 1 µm beads in agarose acquired with ETs of 38 ms (left) and 160 ms (right). **d** and **f** show PSF images in their best focuses with panel **e** showing the corresponding cross sections. **a** and **c** show PSF images 3.5 µm before their best focuses (i.e. closer to the coverslip glass) with panel **b** showing the corresponding cross sections. **g** and **i** show PSF images 3.5 µm after their best focuses with panel **h** showing the corresponding cross sections. Exp. time = 38 ms or exp. time = 160 ms, laser power at sample = 42.56 µW at λ = 488 nm, em gain = 2,000, PS = 630 nm.

ET increases from 38 ms to 160 ms. The same can be observed on the profiles for the out of focus cross sections (fig. 4.2b and 4.2h). In fig. 4.2b the signal peak increases from 180 IC to 350 IC, while in fig. 4.2h it rises from 140 IC to 280 IC, as the ET goes

from 38 ms to 160 ms. This increase in signal is clearly due to the increase in ET from 38 ms to 160 ms, which, in turn, allows a growth in SNR, since the photon collection time has been raised. The SNR, in the case of the beads in focus in fig. 4.2d and 4.2f, is more than doubled from 14 to 28.1. This is also the case for the SBR, which grows from 5.7 to 12. In terms of profile FWHMs, instead (measured as explained in sec. 3.4), in general there is no difference between curves acquired at 38 ms and 160 ms ETs. These observed variations in profile peak are substantially different from those shown in section 3.3 (chap. 3, fig. 3.5), which were not supported by relevant differences in SNR and SBR, but were due to different levels of spherical aberration. In this case the main cause for the modification in profile peak is just the difference in signal levels, considering the two beads are now distant less than 10 µm from each other. This is a further confirmation that the change in PSF shapes observed in the previous chapter was exclusively caused by the amount of spherical aberration. However, also the images of the beads in fig. 4.2 are affected by positive spherical aberration, as shown by the fact that the out of focus cross sections acquired before the best focus ones are ring-like (fig. 4.2a and 4.2c), while those after are blurred (fig. 4.2g and 4.2i) [28, 29].

In fig. 4.3 the axial profiles (averaged among the three corresponding cross sections from the first three z-stacks of the z-stack series) and cross sections for the same 1 µm beads in agarose shown in fig. 4.2 are presented, together with the corresponding sharpness curves. Fig. 4.3a and 4.3b are associated with the bead acquired with 38 ms ET, while fig. 4.3c and 4.3d to the 160 ms case. As for the lateral profiles, the axial profile peaks increase in terms of signal, moving, in the case of the profiles in the central planes, from around 800 IC to 3,200 IC as the exposure goes from 38 ms to 160 ms. Regarding the FWHM of the two central axial profiles, also this parameter is basically unchanged as for the lateral profiles and equal to around 2 µm for the two beads acquired with 38 ms and 160 ms ETs. In fig. 4.4b the total SNR per axial position has been plotted for the two 1 µm beads in agarose acquired with ETs of 38 ms and 160 ms presented in fig. 4.2 and 4.3. As expectable, at all axial positions the SNR associated to the bead acquired with 160 ms ET is higher than that associated to the beads acquired with the 38 ms one. Another aspect visible in fig. 4.4 is the asymmetry of the SNR curves with respect to the central axial position, where the best focus is located (around frame 70). This is due to the presence of the spherical aberration

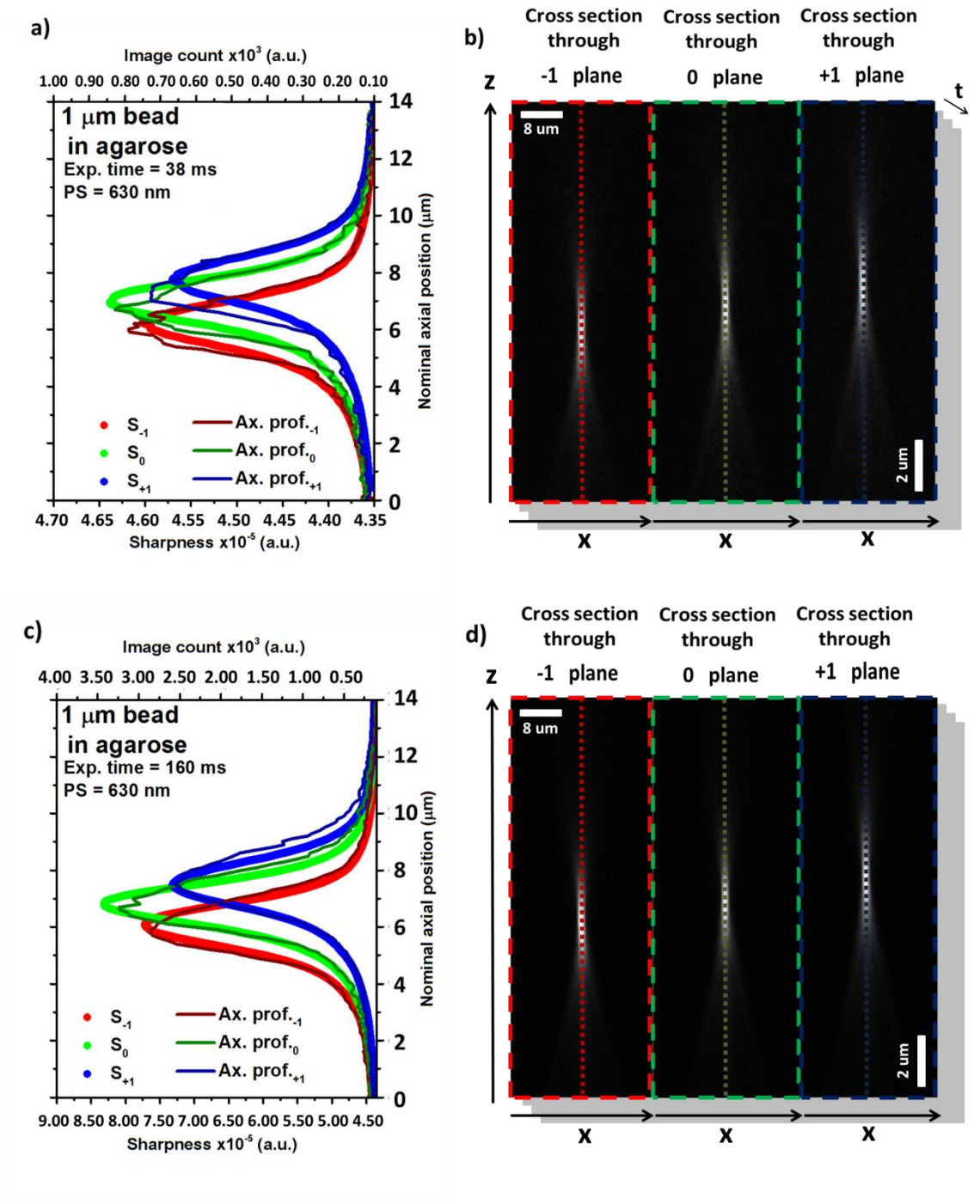

Figure 4.3 Sharpness curves with axial profiles (**a** and **c**) and axial cross sections (**b** and **d**) observed through the three used axial planes, for two 1 μm beads in agarose acquired with an ETs of (**a** and **b**) 38 ms and (**c** and **d**) 160 ms. The cross sections have been obtained from the first z-stack of the acquired z-stack series. The axial profiles have been observed through the three vertical lines in **b** and **d**, where they were maximised and are averaged among the three corresponding cross sections from the first three z-stacks of the z-stack series. Laser power at sample = 42.56 μW at λ = 488 nm, em gain = 2,000, PS = 630 nm.

already mentioned and visible in fig. 4.2, which breaks the symmetry of the PSF itself (as it can be seen in the profiles in fig. 4.4a, where from positions 0 μm to 6 μm the image count values are clearly higher than from 8 μm to 14 μm) and of the energy distribution in the image [27]. The change in axial profiles seen in fig. 4.3 has also an impact on the sharpness curves (fig. 4.3a and 4.3c), which change their peak values

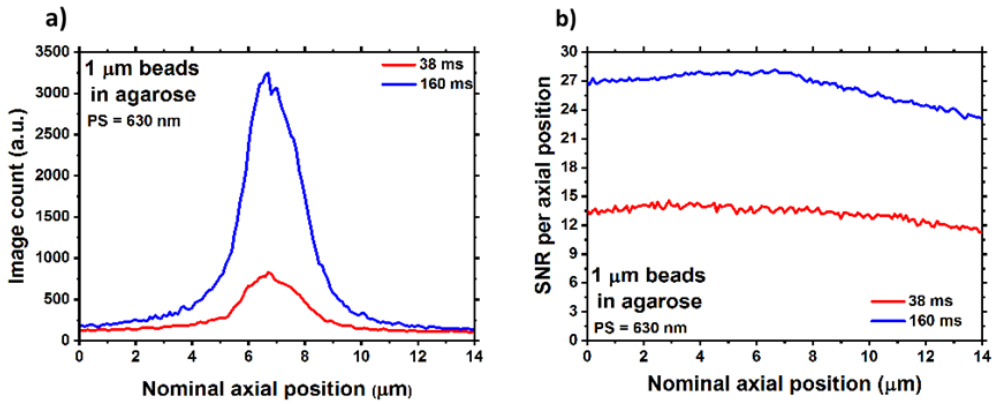

Figure 4.4 a) Axial profiles observed through the central green vertical lines in fig. 4.3b and 4.3d and **b)** evaluated SNR per axial position for two 1 μm beads in agarose acquired with an ET of 38 ms (red curves) and 160 ms (blue curves). Laser power at sample = 42.56 μW at λ = 488 nm, em gain = 2,000, PS = 630 nm.

accordingly. Indeed, in the case of the curves associated to the central planes, the sharpness peak is higher for the bead acquired with 160 ms ET (8.50 10^{-5} a.u.), than for that acquired with the 38 ms one (4.65 10^{-5} a.u.). This is expected, since higher image count values can make the image sharper. A consequence of this is the fact that, as the axial profile peaks change among the three different planes, the sharpness peaks change too, as it can be seen in both fig. 4.3a and 4.3c. In particular, the profile peaks in the -1st orders are higher than those in the +1st orders, since the -1st plane is closer to the objective lens and, as a consequence, has a higher numerical aperture (NA), which increases the collection of photons [30]. However, the highest axial profile peaks are those for the beads observed through the central planes. This, as it will be demonstrated in section 4.4, is due to the fact that there is no residual lateral chromatic aberration in the central plane, thus concentrating the photons on a smaller area and increasing the profile peak values. Concerning the central sharpness FWHMs, also these values are unchanged for the two ETs considered and equal to 2 μm, the same values obtained for the corresponding axial profiles.

The SNR curves in fig. 4.4b need more attention. They only show a slow decrease as the axial position changes from the central one, where the beads are around their best focuses, even if the images get heavily defocused. This happens because the total number of collected photons varies slowly along z. However, as explained in sec. 4.2 and 4.3, as the degree of defocus increases, the signal is spread over a larger number of pixels, thus reducing the average SNR_{pix} and SBR per frame and lowering the performances of the sharpness algorithm. To show how the SNR_{pix} and the SBR change with defocus, it is needed to know the number of pixels occupied by the PSF in every axial position, to then use eq. 4.3. As an example, this has been done for the two 1 µm beads in agarose acquired with ETs of 38 ms and 160 ms and observed through their central planes (PS of 630 nm) presented above. To calculate the number of pixels per PSF, the lateral profiles (traced as in fig. 4.2) associated to the latter have been fitted in some selected frames with a generic Gaussian function [31] of the form (eq. 4.5):

$$y(x) = Ae^{-\frac{(x-x_0)^2}{2\sigma^2}}, \qquad \text{(eq. 4.5)}$$

where A and x_0 are, respectively, the amplitude and the peak position of the curve, while σ is the standard deviation. By multiplying the latter by $2\sqrt{(2\ln(2))}$ the associated FWHM has then been obtained and used to calculate the radius and the circular area of the PSF in pixels. An example fit is shown in fig. 4.5a, where the lateral profile is the same plotted in fig. 4.2e for the bead acquired at 160 ms ET. This allowed to calculated a FWHM of 0.1 mm (6.4 pix) and an area of $7.9 \cdot 10^{-3}$ mm^2 (32.2 pix). The SNR_{pix} (eq. 4.3) and the SBR (eq. 4.4) have then been calculated with the PSF area obtained. The resulting SNR_{pix} and SBR per axial position are presented in fig. 4.5b and 4.5c, respectively. As observable, both SNR_{pix} and SBR increase moving toward the focal position, where the area occupied by the PSF is reduced. As expected, the values associated to the bead acquired with an ET of 160 ms are higher than those for the bead at 38 ms. In particular, the SNR_{pix} has peak values of around 1.1 and 1.7, respectively at 38 ms and 160 ms ETs, while the SBR of 2.2 and 8.8, again at 38 ms and 160 ms ETs respectively.

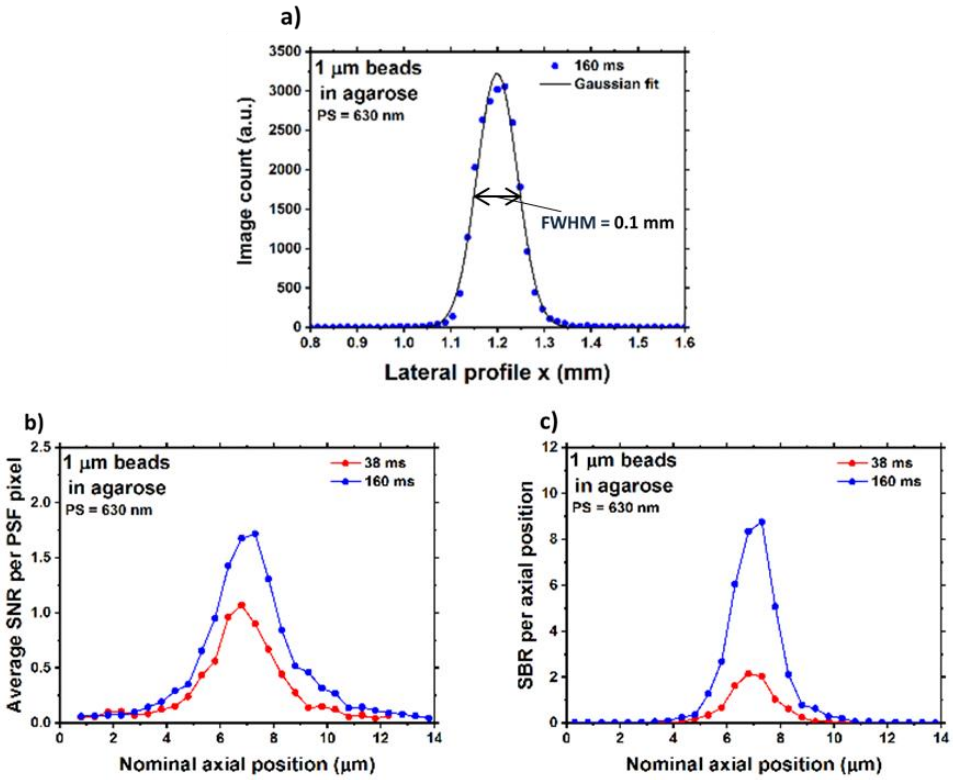

Figure 4.5 a) Example of a fit performed through eq. 4.5 to a lateral PSF profile (fig. 4.2e) associated to a 1 µm bead in agarose acquired with an ET of 160 ms. The extracted FWHM is shown. **b)** Evaluated SNR_{pix} per axial frame for two 1 µm beads in agarose acquired with an ET of 38 ms (red curves) and 160 ms (blue curves). **c)** Evaluated SBR per axial frame for two 1 µm beads in agarose acquired with an ET of 38 ms (red curves) and 160 ms (blue curves). Laser power at sample = 42.56 µW at λ = 488 nm, em gain = 2,000, PS = 630 nm.

The growth in SNR and SBR observed between the two 1 µm beads in agarose presented above can, in general, be observed as the ET increases in all the four experimental conditions studied. This can be seen in fig. 4.6, where SNR and SBR, calculated for the beads in focus in the central planes, have been plotted against the acquisition ET used for some selected PS. The beads shown in fig. 4.6a have been acquired with a PS of 80 nm, those in fig. 4.6b with one of 320 nm and those in fig. 4.6c and 4.6d with a PS of 630 nm. Moving from 38 ms to 160 ms exposure time, the SNR grows from 15.5 to 27.7, from 20.3 to 36.0, from 3.2 to 6.5 and from 9.0 to 14.2, respectively for the data in fig. 4.6a, 4.6b, 4.6c and 4.6d. Regarding the SBR, in the same range this increases from 7.7 to 8.5, from 11.8 to 17.3, from 1.7 to 3.3 and from 1.4 to 3.5, again respectively for the data in fig. 4.6a, 4.6b, 4.6c and 4.6d. As expected, the values associated to the 1 µm beads are higher than those for the 100 nm ones.

Those calculated for the beads in PDMS, instead, are generally higher than those for the beads in agarose, due, as explained in sec. 3.4, to the fact that the PDMS has a lower absorption in the visible range than water [32, 33], i.e. the main component of the agarose samples (sec. 3.3.2). The increase in SNR with the ET is, as said, due to the fact that the number of collected photons increases (eq. 3.7). The increase in SBR, instead, is due to the fact that the signal increases faster than the background with the ET. For example, moving from 38 ms and 160 ms ET in fig. 4.6b, the signal presents a 3-fold increase, while the background a double one. This happens since the sample autofluorescence (at the detected wavelength) and the external environment light are

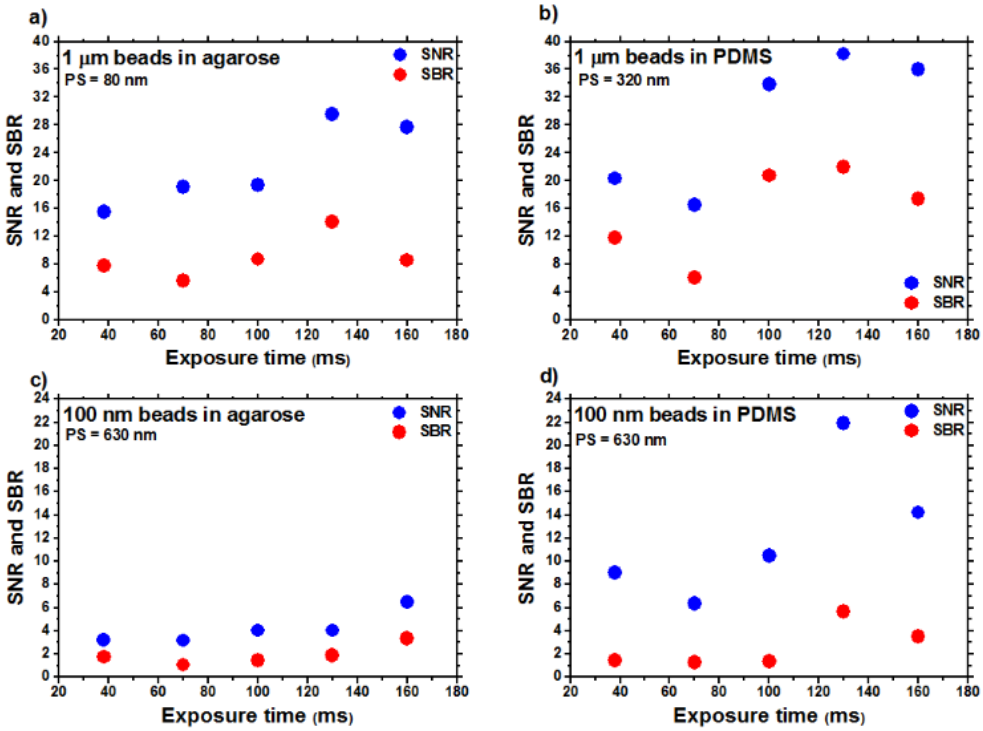

Figure 4.6 Evaluated SNR and SBR for bead z-stacks acquired with different ETs and some selected PS. **a)** 1 µm beads in agarose (PS = 80 nm, laser power at sample = 42.56 µW at λ = 488 nm, em gain = 2,000), **b)** 1 µm beads in PDMS (PS = 320 nm, laser power at sample = 2.07 µW at λ = 488 nm, em gain = 3,000), **c)** 100 nm beads in agarose (PS = 630 nm, laser power at sample = 8.56 mW at λ = 488 nm, em gain = 3,000) and **d)** 100 nm beads in PDMS (PS = 630 nm, laser power at sample = 0.76 mW at λ = 488 nm, em gain = 3,000).

negligible, while the signal coming from out of focus sources is weak due to the low density of emitters in the sample.

The fact the SNR and SBR do not grow monotonically with the ET but, instead, show a certain scatter is due to multiple reasons, such as the different physical position of the beads in the sample and the non-identical fluorophore density on each bead. This can be shown by evaluating the average SNR and SBR and the relative standard deviations associated to beads imaged in the same conditions. In fig. 4.7 the average SNR and SBR values calculated among all the beads presented in fig. 3.7 that have been acquired within the first 10 µm from the coverslip are shown, together with the associated standard deviations. As observable, in general the standard deviations associated to all SNR and SBR average values calculated for the four used physical samples span across several SNR/SBR units. This is due to the variability of the signal coming from different beads, even when acquired in similar conditions.

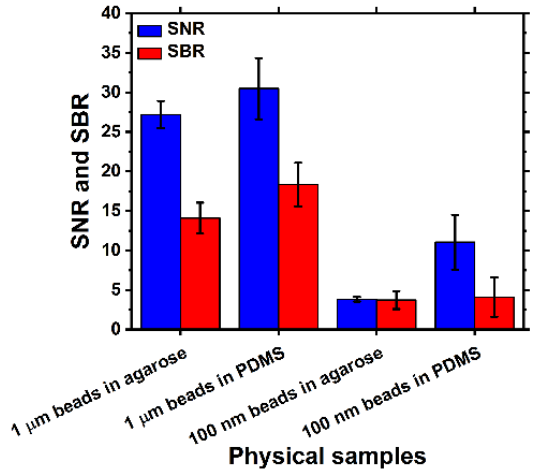

Figure 4.7 Average SNR and SBR values calculated by using the beads in the first 10 µm from the coverslip presented in fig. 3.7 and for all the studied physical samples. The error bars represent the relative standard deviations. Exposure time = 100 ms, em gain = 2,000 and 3,000, laser power at sample = 42.6 µW, 2.1 µW, 4.1 mW and 0.23 mW at λ = 488 nm.

4.4.1 *Impact of the level of the signal on the shape of the sharpness curves*

As already seen in fig. 4.3, different ETs can lead to variations in the sharpness curve peaks. In particular, the latter increases with the ET and, thus, the signal level, since the sharpness is a function of signal intensity (eq. 2.36). As an example, in fig. 4.8 the relative (peak to baseline) sharpness curves associated to beads acquired with ETs of 38 ms and 160 ms and with the same PS used for fig. 4.6 are compared in the four experimental conditions studied. These curves have been scaled with respect to the

peaks of the central curves acquired with ET 160 ms. In all quadrants of fig. 4.8 the curve peaks for the beads acquired with 38 ms ET are around 10% of those for the beads acquired with the 160 ms one. This, as anticipated, is expected, since higher levels of signal allow for higher pixel values, which make the beads appear as sharper. Another aspects observable is the influence of the SNR on the smoothness of the sharpness curves, as evidenced by the noise present in the curves in fig. 4.8c. Indeed, the curves associated to the 100 nm beads in agarose are those with the lowest level of

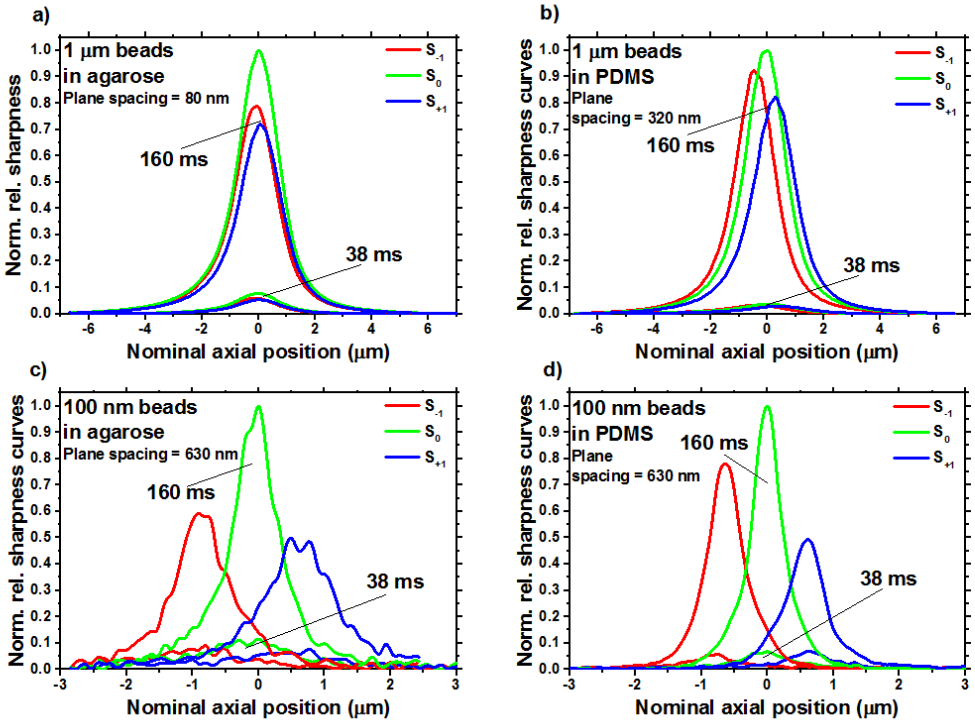

Figure 4.8 Calculated sharpness curves for bead z-stacks acquired with 38 ms and 160 ms ETs and some selected PS. **a)** 1 µm beads in agarose (PS = 80 nm, laser power at sample = 42.56 µW at λ = 488 nm, em gain = 2,000), **b)** 1 µm beads in PDMS (PS = 320 nm, laser power at sample = 2.07 µW at λ = 488 nm, em gain = 3,000), **c)** 100 nm beads in agarose (PS = 630 nm, laser power at sample = 8.56 mW at λ = 488 nm, em gain = 3,000) and **d)** 100 nm beads in PDMS (PS = 630 nm, laser power at sample = 0.76 mW at λ = 488 nm, em gain = 3,000).

SNR (fig. 4.6c). As observable, the overall axial coverage of each set of three sharpness curves can be extended by increasing the PS. Indeed, as the latter grows, the degree of overlap between sharpness curves is reduced, thus extending the axial range they cover. This is clearly visible by comparing fig. 4.8a and 4.8b. In fig. 4.8a, where the PS is 80 nm, the $\pm 1^{st}$ sharpness curves are fully covered by the 0^{th} one, while the same does

not happen in fig. 4.8b, where, thanks to a PS of 320 nm, the ±1st sharpness curves are partially shifted outside the range of the 0th curve, thus raising the axial extension of the three sharpness curve set. This is important, since it can help to improve the performances of the sharpness algorithm in terms of axial range, as it will be shown in sec. 4.4.2.

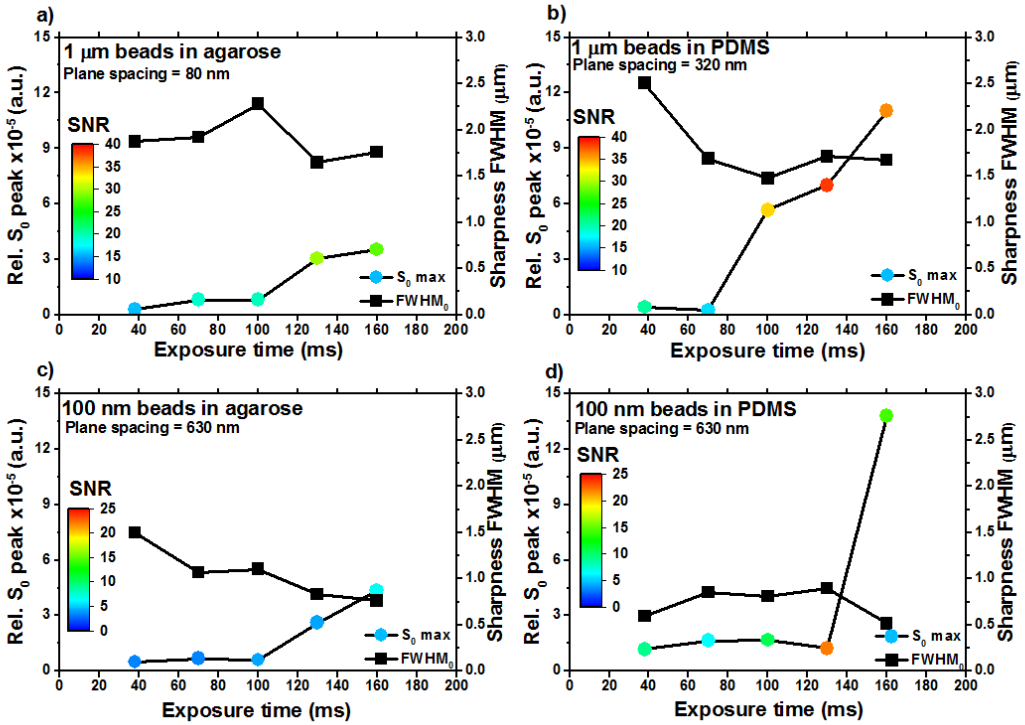

Figure 4.9 Evaluated relative sharpness curve peak heights (left y axis, circles) and FWHMs (right y axis, squares) of the sharpness curves in the central planes, for bead z-stacks acquired with different ETs and some selected PS. The SNR has been colour encoded in the sharpness peak curves. **a)** 1 µm beads in agarose (PS = 80 nm, laser power at sample = 42.56 µW at λ = 488 nm, em gain = 2,000), **b)** 1 µm beads in PDMS (PS = 320 nm, laser power at sample = 2.07 µW at λ = 488 nm, em gain = 3,000), **c)** 100 nm beads in agarose (PS = 630 nm, laser power at sample = 8.56 mW at λ = 488 nm, em gain = 3,000) and **d)** 100 nm beads in PDMS (PS = 630 nm, laser power at sample = 0.76 mW at λ = 488 nm, em gain = 3,000).

In fig. 4.9 all the relative S_0 curve peaks and FWHMs (extracted as explained in sec. 3.4 and sec. 3.6) of the sharpness curves associated to the beads acquired with all the different ETs and experimental conditions and for the same PS as in fig. 4.8 are

shown. The SNR has been colour encoded in the sharpness peak data. Starting from the sharpness peak curves, in general these tend to increase with the exposure time in all the four experimental conditions, simultaneously with an increase in SNR. The FWHM, instead, does not show a net increasing or decreasing behaviour with respect to exposure time and SNR. This is in agreement with what shown in fig. 4.3, where, moving from the bead acquired with an ET of 38 ms to that with one of 160 ms the sharpness peaks were increasing, while the FWHMs were substancially unchanged.

To better visualise the behaviour of sharpness peaks and FWHMs with respect to the signal level, in fig. 4.10 these have been plotted as in fig. 3.17 with respect to the SNR and with the SBR colour encoded. Fig. 4.10a and 4.10b show, respectively, the sharpness peak and FWHM values associated to the central curves of all the 1 μm beads acquired with the different ETs and PS, while fig. 4.10c and 4.10d show the corresponding values for the 100 nm beads. The values for the 100 nm and 1 μm beads have been kept separated, since bead and sharpness box sizes modify the shape of the sharpness curves. In fig. 4.10a the sharpness peaks obtained from the 1 μm beads clearly increase with the SNR and the SBR. In particular, these grow from around $5 \cdot 10^{-7}$ a.u. at a SNR of 14 and a SBR of 6 to around $11 \cdot 10^{-5}$ a.u. at a SNR of 36 and a SBR of 17. However, this growth in sharpness peak is not very pronounced until a SNR around 20 and a SBR around 8.8 are reached, where the increase becomes faster. This behaviour can also be observed in fig. 4.10c, for the peaks associated to the 100 nm beads. Up to a SNR around 15 and a SBR around 2 the majority of the sharpness peaks is below a value around $3 \cdot 10^{-5}$ a.u., while values around $14 \cdot 10^{-5}$ a.u. are reached at a SNR of 22 and a SBR of 5.7. Consequently, it can be concluded that both SNR and SBR can drive an increase in sharpness peak, since a growth in signal and/or a reduction in background can make a PSF appear as sharper. The values for the FWHMs (fig. 4.10b and 4.10d), instead, fluctuate around an average position, but do not distinctly increase or decrese with respect to the signal. The average FWHM associated to the 1 μm beads is equal to (1.8 ± 0.2) μm, while that for the 100 nm beads to (0.9 ± 0.2) μm, with the former clearly larger due to the size of the beads. The fact that the FWHM does not change with the signal is not surprising as said, since all beads were acquired within the first 10 μm from the coverslip and, thus, the amount of introduced spherical aberration is not able to strongly distort PSFs and sharpness curves (e.g. fig. 3.5, 3.6 and 3.18).

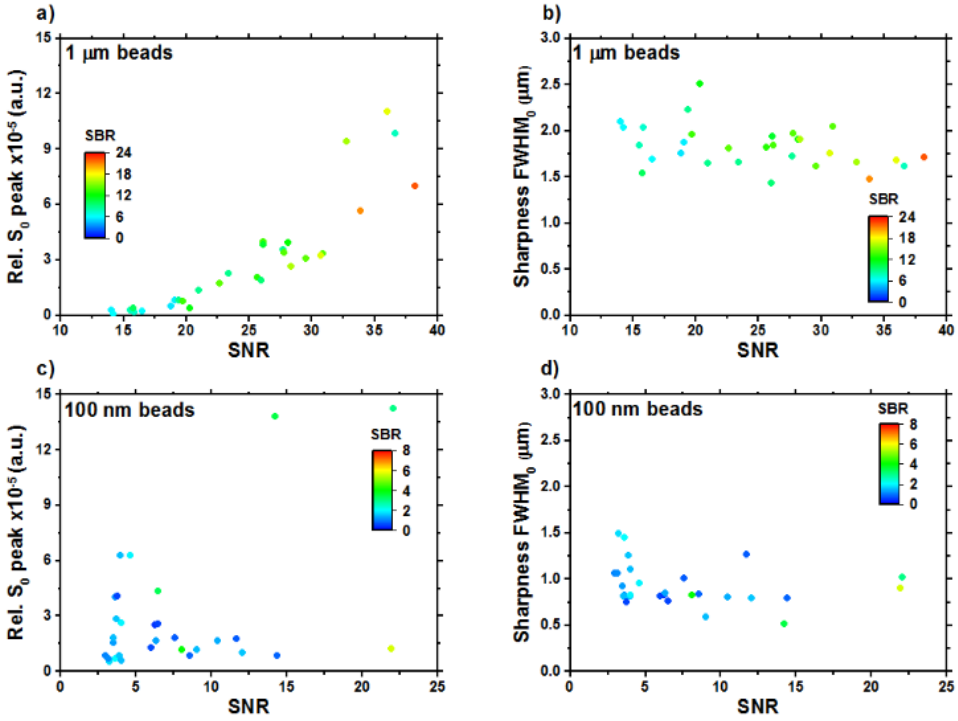

Figure 4.10 Relative sharpness peak heights and FWHMs of the sharpness curves in the central planes plotted against the corresponding SNR and SBR values, for all bead z-stacks acquired in agarose and PDMS, with the different ETs and PS. The SBR has been colour encoded in the sharpness peak curves. The data in **a** and **b** are associated to the 1 µm beads, while those in **c** and **d** to the 100 nm ones. PS = 80 nm, 320 nm and 630 nm. Laser power at sample = 42.56 µW, 2.07 µW, 8.56 mW and 0.76 mW. λ = 488 nm. em gain = 2,000, 3,000. ET = 38 ms, 70 ms, 100 ms, 130 ms and 160 ms.

4.4.2 *Impact of the level of the signal on the performances of the sharpness algorithm*

The impact of different ETs and, as a consequence, of different signal levels, has been studied also on the performances of the sharpness algorithm and multiplane system, in terms of axial range and precision achievable. As explained in sec. 4.2, the axial range indicates the range over which the system is able to calculate the expected nominal axial position, while the axial precision is the average localisation precision within the axial range. By using the ImageJ multiplane plugin described in 2.4.3, axial ranges and average axial precisions have been calculated for all the 1 µm and 100 nm bead z-stacks acquired with the different ETs. All the images of the beads at different axial positions in the multiplane z-stack series have, first, been 2D localised (i.e. over x and y in the image plane) through their centres of mass (all the parameters to do that have been changed with the samples, in order to get the highest possible number of automatic 2D

localisations every time). This done, their axial positions have been calculated via the sharpness algorithm with the independent method (sec. 2.5.3) and the calibration curves generated for each sample (some of them are shown, e.g., in fig. 4.8), with the SBs (which had the same sizes of the boxes used to calculate the corresponding sharpness curves) centred on the centres of mass positions. Each average axial position has then been obtained by averaging all the values calculated for the same nominal axial position in each of the ten different z-stacks in the z-stack series. The standard deviations calculated with these averages have been used as the precisions on the axial positions. For each z-stack in the z-stack series only the values within 100 nm from their expected nominal axial positions (i.e. with axial accuracy $\leq$ 100 nm) have been selected to evaluate the axial ranges. The latter, in general, is roughly symmetric relatively to the central plane positions (as the SNR curves in fig. 4.4b) and shorter than the z-stack axial extensions, due to the lack of photons at very defocused positions that does not allow to get accurate positioning. The used axial range, therefore, is the range over which it is possible to calculate the nominal axial positions with at least 100 nm accuracy. The average axial range was then calculated by averaging all the axial ranges calculated for each z-stack in the z-stack series. Finally, the standard deviations on the positions within the axial ranges were averaged to obtain the reference axial precisions for each bead acquired with the different ETs. In fig. 4.11 examples of axial accuracy, range and precision calculations are shown for two 1 μm beads in agarose, acquired with a PS of 630 nm and ETs of 38 ms (fig. 4.11a, 4.11c and 4.11e) and 160 ms (fig. 4.11b, 4.11d and 4.11f). Starting from fig. 4.11a and 4.11b, here the calculated average (among all acquired z-stacks) axial accuracies and the associated precisions on them (calculated as standard deviations) have been plotted against the nominal axial positions. As observable, the axial accuracy assumes values below 100 nm over a certain central range, which represents the axial range and grows with the signal level. On average, the axial accuracy in the axial range region is equal to (39.6 ± 27.6) nm and to (41.7 ± 29.1) nm, respectively for the bead acquired with an ET of 38 ms (fig. 4.11a) and 160 ms (fig. 4.11b). To better highlight the axial ranges, in fig. 4.11c and 4.11d the calculated against nominal axial positions have been plotted for, respectively, the beads acquired at 38 ms and 160 ms ETs. The central white regions are those where the accuracy (i.e. the difference between calculated and nominal values in each position) is smaller or equivalent to 100 nm, while the coloured ones (red for the bead acquired with 38 ms ET and blue for the other one) are those where the accuracy exceeds 100 nm. The error bars are the axial precisions calculated in each position. As it can be seen, the axial

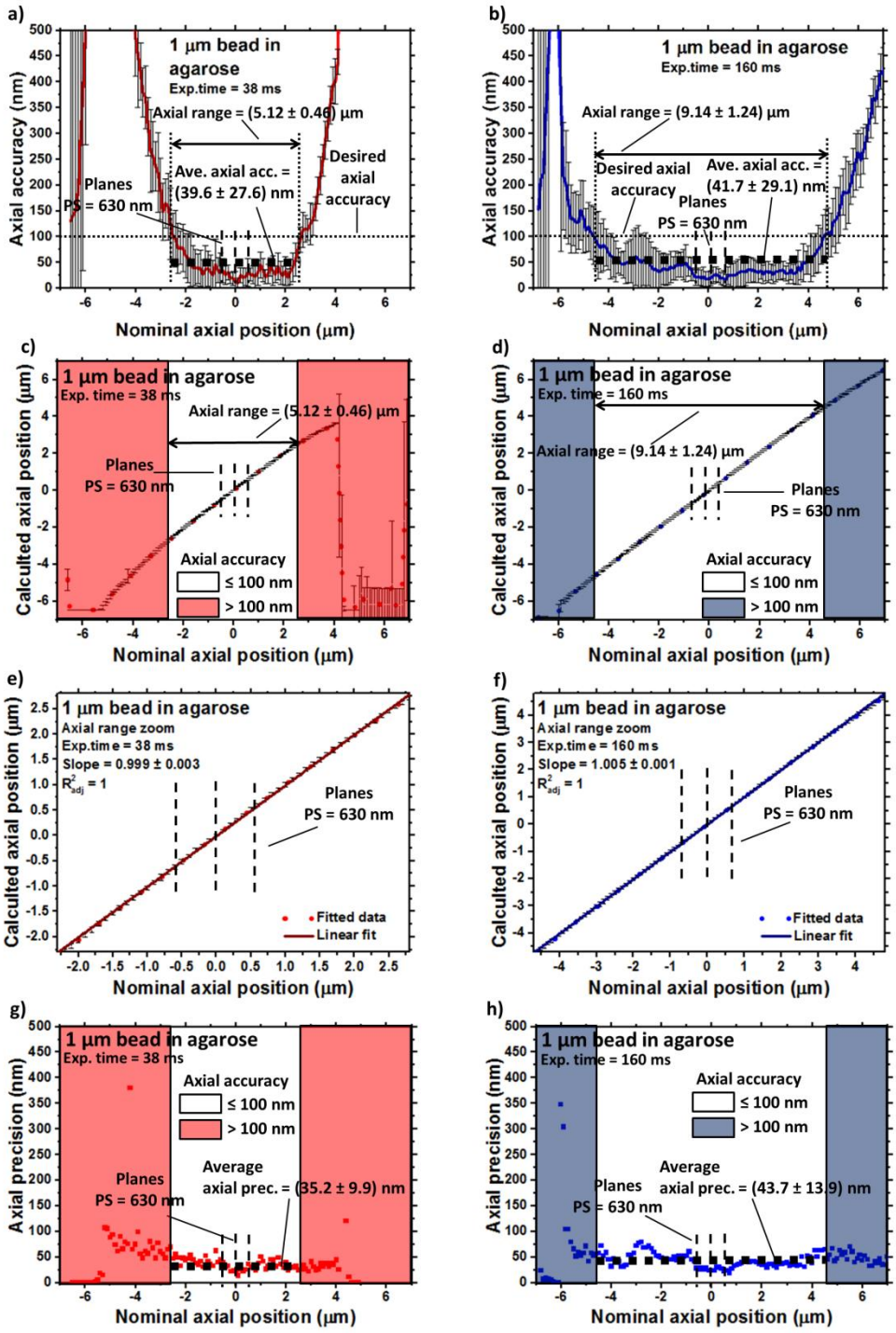

Figure 4.11 Axial accuracy, precision and calculated against nominal axial positions for two 1 µm beads in agarose acquired with ETs of (**a**, **c**, **e** and **g**) 38 ms and (**b**, **d**, **f** and **h**) 160 ms. In **a** and **b** the curves represent the axial accuracies against nominal axial positions associated to the two used beads. The set 100 nm axial accuracy limit, the corresponding axial range regions and the average axial accuracies within it are shown, together with the plane positions. The error bars are the precisions on the calculated accuracies. In **c** and **d** the red and blue areas are the axial regions were the axial accuracies were bigger than 100 nm. In **e** and **f** only the regions in, respectively, **c** and **d**

were the axial accuracies are smaller than 100 nm have been plotted. These plots have been linearly fitted (red fit for the bead acquired with 38 ms ET and blue fit for the other one). In **c** and **d** the lengths of the axial ranges have been indicated and in all panels the error bars represent the average axial precision in each acquired axial position. In **g** and **h** the axial precisions, respectively for the beads acquired with 38 ms and 160 ms ETs and represented by the error bars in **c**, **d**, **e** and **f**, have been plotted against the nominal axial positions. As in **c** and **d**, the region with accuracy larger than 100 nm have been highlighted. The average axial precisions and its standard deviation in the region with accuracy $\leq$ 100 nm (axial range regions) have been reported. The axial precision axes have been zoomed in to show the first 500 nm, where the precisions in the axial range regions are located. Laser power at sample = 42.56 μW at λ = 488 nm, em gain = 2,000, PS = 630 nm.

range for the bead acquired with 160 ms ET (fig. 4.11d) is more extended than that for the bead acquired with the 38 ms one (fig. 4.11c). In particular, the first one is equal to (9.14 ± 1.24) μm, while the second one only to (5.12 ± 0.46) μm, almost halved. The overall SNR for the beads in focus in the central planes, as said above, grows from 14 to 28.1, as the ET moves from 38 ms to 160 ms. As shown in fig. 4.4b, this value does not change massively with the axial position (in the observed range). Therefore, higher SNR values raise the SNR_{pix} at all axial positions (fig. 4.5b and 4.5c) and improve the accuracy on the calculations for the axial range. It is important to notice that the axial ranges are several times more extended than the distance between the ±1st planes, indicating that the multiplane system can, with enough photons, easily work with severely defocused images. The plots in fig. 4.11c and 4.11d are linear in the axial range regions and tend to deviate from linearity outside them, where the error bars get wider. This can be seen in fig. 4.11e and 4.11f, where the respectively axial range regions in fig. 4.11c and 4.11d have been expanded and linearly fitted. Both these fits have slopes and R_{adj}^2 around 1 and the error bars (i.e. the axial precisions) are very small, indicating high accuracy and precision on the localisations in the axial ranges. In particular, the axial precisions have been plotted in fig. 4.11g and 4.11h, respectively for the data in fig. 4.11c and 4.11d. The average axial precisions in the axial range regions, indicated with horizontal dashed lines, are (35.2 ± 9.9) nm and (43.7 ± 13.9) nm, respectively for the beads acquired with 38 ms and 160 ms ETs.

In fig. 4.12 all axial ranges and precisions calculated for the beads acquired with all the used ETs and experimental conditions and for the same PS as in fig. 4.9 are

shown. The axial range curves have been colour encoded with the corresponding SNR values. As observable, the axial range, in general, grows with the ET and the SNR in all experimental conditions. Simultaneously, also the axial precision tends to improve as ET and SNR increase. As expected, axial range and precision values associated to the 1 µm beads are generally better than those calculated for the 100 nm ones, due to the higher level of the signal.

To observe the global variation of axial range and precision with respect to the level of the signal, these have been plotted against SNR and SBR in fig. 4.13, for all used PS and experimental conditions. Fig. 4.13a and 4.13b show, respectively, how the axial range increases with both SNR and SBR. The axial range increases from around 0.5 µm at a SNR of 3 and a SBR of 0.5 to around 9 µm at a SNR of 37 and a SBR of

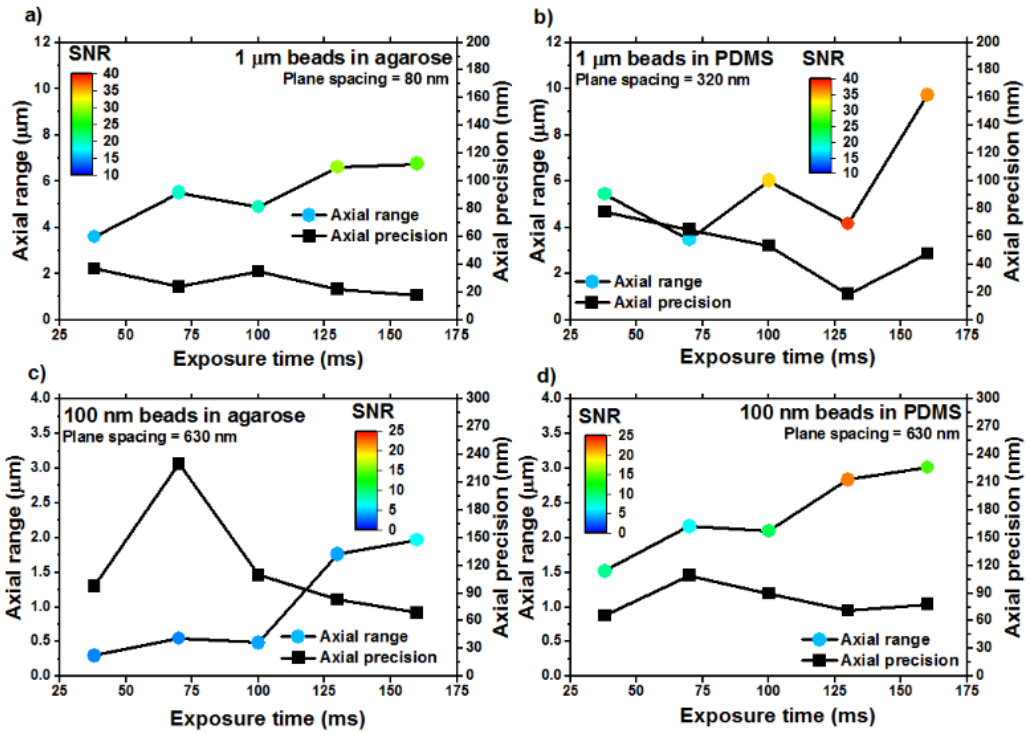

Figure 4.12 Evaluated axial ranges (left y axis, circles) and precisions (right y axis, squares) for bead z-stacks acquired with different ETs and some selected PS. The SNR has been colour encoded in the axial range curves. **a)** 1 µm beads in agarose (PS = 80 nm, laser power at sample = 42.56 µW at λ = 488 nm, em gain = 2,000), **b)** 1 µm beads in PDMS (PS = 320 nm, laser power at sample = 2.07 µW at λ = 488 nm, em gain = 3,000), **c)** 100 nm beads in agarose (PS = 630 nm, laser power at sample = 8.56 mW at λ = 488 nm, em gain = 3,000) and **d)** 100 nm beads in PDMS (PS = 630 nm, laser power at sample = 0.76 mW at λ = 488 nm, em gain = 3,000).

approximately 17. By linearly fitting the data for the different PS in fig. 4.13a, the general increase in axial range with respect to the signal can be quantified. The linear fits present slopes of (170 ± 30) nm, (210 ± 30) nm and (250 ± 30) nm, respectively for the PS of 80 nm, 320 nm and 630 nm. Therefore, in the PS and SNR ranges observed, the axial range grows faster with respect to the signal as the PS increases. Larger PS, thanks to the reduced overlap among sharpness curves and the consequent increased axial coverage (fig. 4.8), can help to achieve wider axial ranges. However, the advantage offered by larger PS is lost as the SNR is reduced, since the linear fits tend to

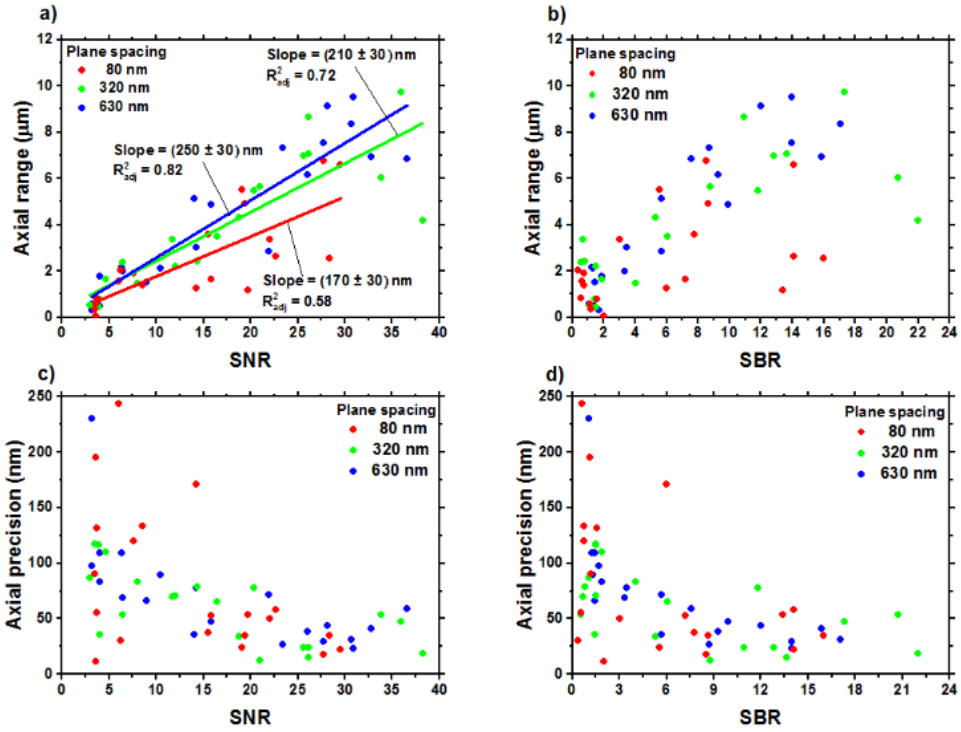

Figure 4.13 Evaluated axial ranges (**a** and **b**) and precisions (**c** and **d**) plotted against the corresponding SNR (**a** and **c**) and SBR (**b** and **d**) values, for all bead z-stacks acquired with the different ETs and PS. The straight lines in **a** are linear fits through the axial range values for the different PS, whose slopes (with their standard deviations) and goodness (the adjusted R^2 values) are shown. PS = 80 nm, 320 nm and 630 nm. Laser power at sample = 42.56 µW, 2.07 µW, 8.56 mW and 0.76 mW. λ = 488 nm. em gain = 2,000, 3,000. ET = 38 ms, 70 ms, 100 ms, 130 ms and 160 ms.

overlap in that case. This is due to the fact that at low signal levels the reduction in sharpness curve peak heights can allow the curves in the 0^{th} orders to cover those in the $\pm1^{st}$ ones (fig. 4.8c). This reduces the total axial coverage of the sharpness curves to that

of the central one and, hence, removes the ability of larger PS to achieve wider axial ranges. Regarding the axial precision values, these are presented against the SNR and the SBR in fig. 4.13c and 4.13d, respectively. As observable, differently from the axial range, the axial precision does not vary with respect to the PS, since the latter does not affect the collected photon budget. It can also be noticed that the axial precision does not vary much as the SNR is reduced from around 37 to approximately 12 and the SBR from 20 to around 8. On average, in this range the axial precision is around (42 ± 25) nm. In the same SNR and SBR ranges the axial range varies by around 6 µm, instead. However, as the signal is further reduced, the axial precision tends to rise quickly. At a SNR around 5 and SBR around 1.5 the axial precision reaches 230 nm. This behaviour could be described by an exponential function. However, to obtain a proper fit to the data, it is first necessary to expand the latter toward lower signal levels. This can also allow to find the signal threshold below which the axial range tends to 0 µm. This will be approached in the next section by using neutral density (ND) filters.

4.4.3 *Pushing the limits of sharpness algorithm performances with neutral density filters*

To further push the limits of the multiplane relay under study and of the sharpness algorithm, the multi-ET experiment in the previous section has been expanded by making use of neutral density (ND) filters [25]. The allowed transmission (T) is controlled by the optical density (OD) of the filter, which is its absorbance (A), through the equation (eq. 4.2):

$$T = 10^{-OD}. \qquad \text{(eq. 4.6)}$$

ND filters can be stacked such that the total OD is the sum of the ODs of each individual filter (eq. 4.7):

$$T_N = \prod_{i=1}^{N} T_i = 10^{-\sum_{i=1}^{N} OD_i}. \qquad \text{(eq. 4.7)}$$

In order to study the system at extreme low photon flux levels several different absorption neutral density filters have been inserted into the optical path of the distorted diffraction relay, just before the narrow bandpass filter. The ET has been set on 38 ms and the PS to 630 nm, while all other camera and optical setup parameters have not been changed with respect to those shown in table 4.1. The PS of 630 nm has been

selected to start from the widest possible axial range and avoid a quick collapse of the performance as the OD increases. For each of the experimental conditions used, several z-stacks have been acquired (as in previous section) with different OD filters (including a z-stack acquired without ND filter).

Once all the z-stacks have been acquired, the associated sharpness curves have been calculated to then, in turn, evaluate axial ranges and precisions as functions of the signal. Ideally, the sharpness curves in each experimental conditions should have been calculated by using the same SB sizes already used, i.e. 150x150 pix^2 and 30x30 pix^2 for, respectively, 1 μm and 100 nm beads, in order to have only the transmission as variable. However, this was not possible for this study, since the reduction in signal level was leading, in this extreme case, the acquired images to be completely dominated by the background, whose weight was rapidly increasing with the disappearing of the PSF from the SB. The latter effect is visible on the sharpness curves. As an example, in fig. 4.14 the sharpness curves associated to a 1 μm bead in agarose, acquired with a ND filter with OD = 1 (i.e. T = 10%) and calculated by using different SB sizes are

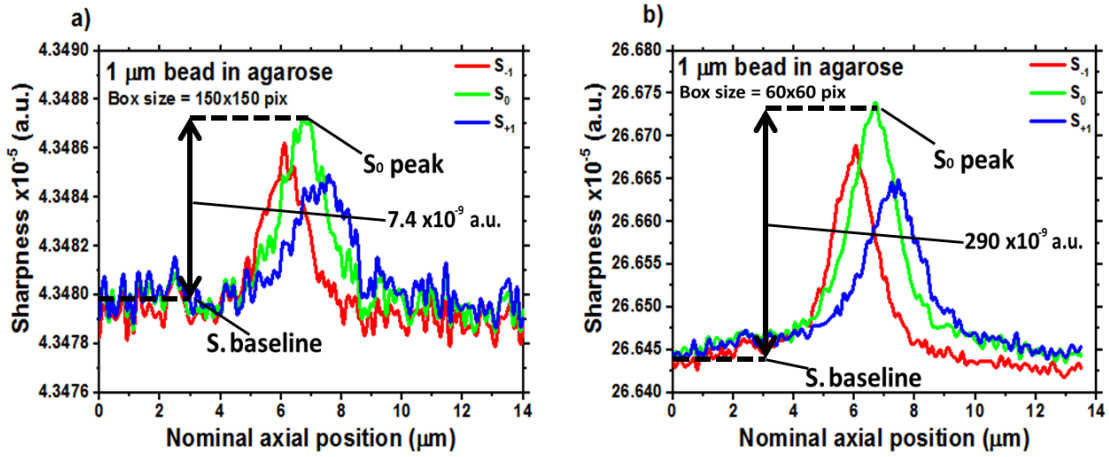

Figure 4.14 Sharpness curves associated to a 1 μm bead in agarose observed through a ND filter with OD = 1 and calculated by using box sizes of **a)** 150x150 pix^2 and **b)** 60x60 pix^2. The relative central sharpness peaks are indicated in the plots. PS = 630 nm, laser power at sample = 42.56 μW at λ = 488 nm, em gain = 2,000, ET = 38 ms.

presented. In fig. 4.14a the SB has been kept equal to 150x150 pix^2, which is the one used so far for the 1 μm beads, while in fig. 4.14b it has been reduced to 60x60 pix^2, to diminish the impact of the background on the sharpness curves. The difference is net. When the signal is reduced to 10% of the original one at 38 ms ET (which imposes a reduction of the SNR from 14 to 4.9 in this case), the relative central sharpness peak

value in fig. 4.14a becomes very small (≈ $7.4 \cdot 10^{-9}$ a.u.) and is just above the sharpness baseline, which effectively represents the sharpness value of the background within the used SB. Instead, by reducing the SB sizes (fig. 4.14b), the relative central sharpness peak increases (≈ $290 \cdot 10^{-9}$ a.u.), making the sharpness associated to the signal more distinguishable from that of the background. This has a consequence on the performances of the sharpness algorithm. By keeping the box size unchanged, the axial range associated to the bead used for the sharpness curves in fig. 4.14a is 0 μm, since the accuracy for all calculated axial positions is always over 100 nm. In particular, the sharpness algorithm calculates the axial position to be equal to 0 μm at all nominal axial positions, due to the fact that, with the curves in fig. 4.14a, all the positions are confused with a position where there is almost only background. Instead, by using the curves in fig. 4.14b the axial range becomes equal to 1.38 μm, with an axial precision of 98.77 nm. This second result is technically more correct, since the SB size should be changed to include the entire PSF, but no extra-background that can be avoided. Indeed, what should be observed is the variation in performances due to the reduction in photon count, rather than that due to the extra-weight of the background in the SB. This adjustment in SB size was not required for the multi-ET study, since the reduction in signal was not such to need it. Therefore, the following SB sizes and ODs have been used (table 4.2):

1 μm beads in agarose		**1 μm beads in PDMS**		**100 nm beads in agarose**		**100 nm beads in PDMS**	
OD	**SB side (pix)**	**OD**	**SB side (pix)**	**OD**	**SB side (pix)**	**OD**	**SB side (pix)**
0	150	0	150	0	30	0	30
1	60	0.5	150	1	20	0.2	30
1.5	40	1	100	1.5	20	0.6	20
1.7	20	1.5	60	1.7	10	0.8	10

Table 4.2 ODs and corresponding SBs used for the ND filter study in the different experimental conditions. SB = sharpness box, OD = optical density.

In fig. 4.15 axial ranges and precisions, calculated as in the previous section (sec. 4.4.2), are presented for the beads acquired through the different ND filters and for the four experimental conditions studied. These have been plotted against their SNR values and the calculated SBR has been colour encoded into the axial range data. As

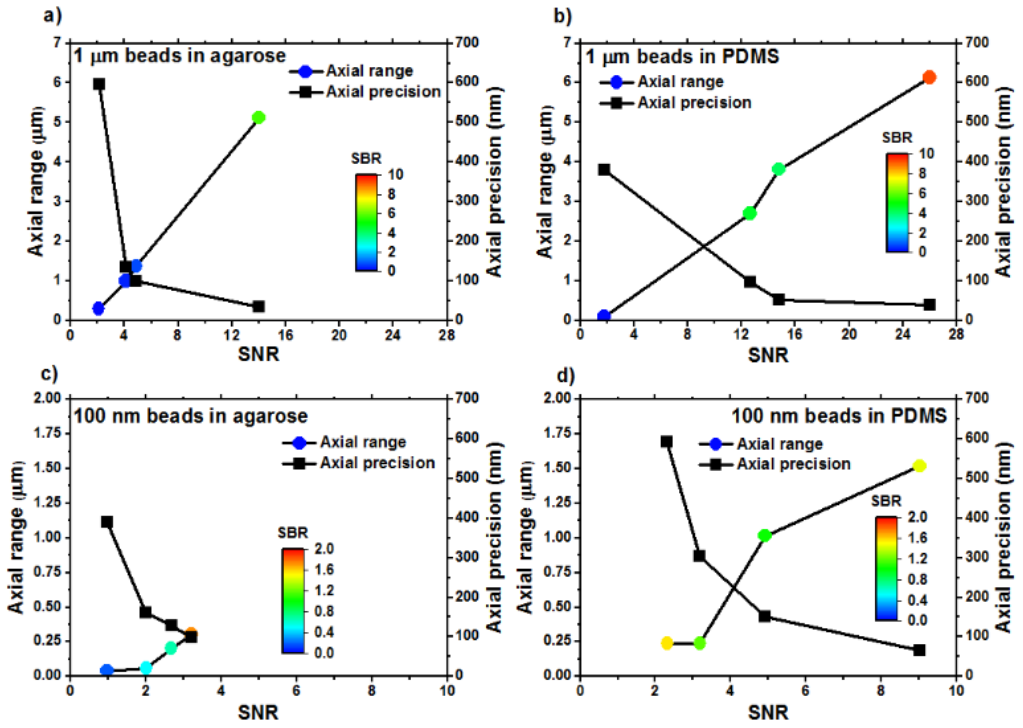

Figure 4.15 Evaluated axial range (left y axis, crosses) and average precision in it (right y axis, squares) against their SNR, for beads observed through different ND filters and with PS = 630 nm. The SBR is colour encoded in the axial range data. **a)** 1 µm beads in agarose (laser power at sample = 42.56 µW at λ = 488 nm, em gain = 2,000), **b)** 1 µm beads in PDMS (laser power at sample = 2.07 µW at λ = 488 nm, em gain = 3,000), **c)** 100 nm beads in agarose (laser power at sample = 8.56 mW at λ = 488 nm, em gain = 3,000) and **d)** 100 nm beads in PDMS (laser power at sample = 0.76 mW at λ = 488 nm, em gain = 3,000).

already shown in fig. 4.13, the axial range increases linearly with the signal, while the axial precision behaves non-linearly. However, in this case the use of ND filters has allowed to push the SNR below 3 and the SBR under 0.5 and reach axial ranges around 40 nm (fig. 4.15c) and precision of 600 nm (fig. 4.15d).

As in fig. 4.13, all data for the four experimental conditions in fig. 4.15 can be joined to show single axial range and precision plots associated to the ND filter study. These are, respectively, presented in fig. 4.16a and 4.16b. By linearly fitting the axial range data in fig. 4.16a, it is possible to extract the threshold SNR_0 at which the axial range with accuracy within 100 nm collapses to 0 µm. SNR_0 results to be equal to 1.23 ± 0.71, which corresponds to 3.36 ± 1.75 photons (eq. 4.1). The SBR, instead, at this threshold level approaches 0. ND filter data are, as said, an extension toward lower

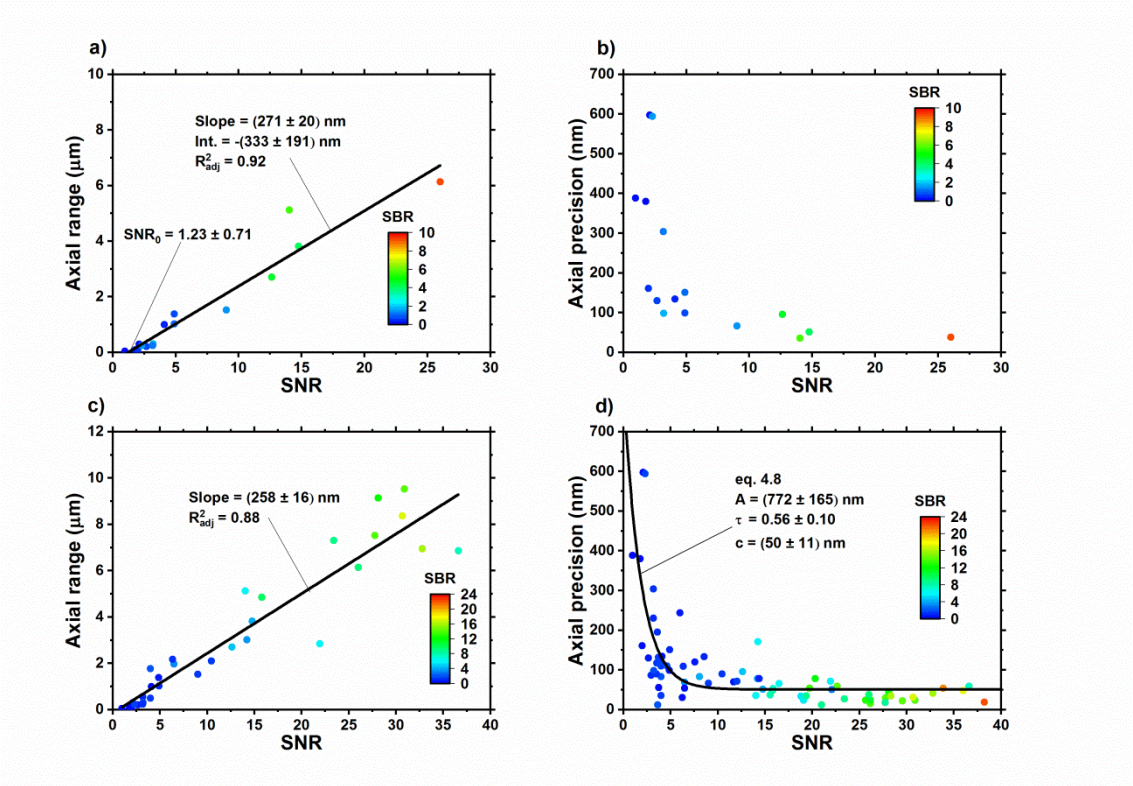

Figure 4.16 Evaluated axial ranges (**a**) and precisions (**b**) associated to the ND filter study and plotted against the corresponding SNR and SBR values. In **c**, instead, the results in **a** have been plotted together with those in fig. 4.13a and 4.13b for a PS of 630 nm, while in **d** those in **b** have been combined with those in fig. 4.13c and 4.13d. The straight lines in **a** and **c** are linear fits through the axial range values. Some extrapolated results are shown. The fit in **d** has been achieved by using eq. 4.8 and the corresponding extrapolated values are shown. PS = 80 nm, 320 nm and 630 nm. Laser power at sample = 42.56 µW, 2.07 µW, 8.56 mW and 0.76 mW. λ = 488 nm. em gain = 2,000, 3,000. ET = 38 ms.

signal levels of the multi-ET data. These two, consequently, can be joined together. Fig. 4.16c shows the axial range data in fig. 4.16a together with those at PS = 630 nm in fig. 4.13a, while fig. 4.16d presents the axial precision values in fig. 4.16b with those in fig. 4.13c at all PS. The data in fig. 4.16c have been linearly fitted, rendering a slope of (258 ± 16) nm per SNR unit, which is comparable to that obtained in fig. 4.13a. The data in fig. 4.16d, as mentioned, show a clear non-linear behaviour, instead. To quantify the latter, the axial precision (AP) data have been fitted by the following exponential function (eq. 4.8):

$$\mathrm{AP}(\mathrm{SNR}) = \mathrm{A}\, e^{-\tau\, \mathrm{SNR}} + \mathrm{c}. \qquad \text{(eq. 4.8)}$$

In eq. 4.8, A + c and c represent the values reached by the AP at, respectively, very low and high signal levels. τ, instead, is the characteristic decay constant of the curve: the higher this value, the lower the signal level needed to observe a rapid exponential increase of the AP. The fit has led to the following values: A = (772 ± 165) nm, τ = 0.56 ± 0.10 per SNR unit and c = (50 ± 11) nm. By setting an hypothetical threshold on the AP of 100 nm, this value is not reached until the SNR is reduced to around 5 and the SBR to approximately 1.2. The fit in fig. 4.16c indicates that to reach useful axial ranges that can be used in biological studies, e.g. equal to 3 μm at least [34], the SNR should be greater-than or equal to around 12, with corresponding SBR of 4.6 and AP of 51 nm. This SNR value, if compared to the results in fig. 4.12, can be easily reached by the 1 μm beads, even at low ETs, but hardly by the 100 nm ones, for which the ET and/or laser power should be increased, limiting the temporal resolution and worsening the photobleaching problem. Considering that the 100 nm beads can be brighter than fluorescent molecules and quantum dots [35], it could be even harder to reach the needed signal level with the latter with the used multiplane system. In addition, if the imaging is done in a cellular environment, the worsened SBR can just reduce the overall performance [17].

In conclusion, this section has shown the influence of the signal level on the performances of a multiplane system. As seen, the impact of the SNR on the PSF profiles (fig. 4.2 and 4.3) imposes a variation on the shape of the sharpness curves (fig. 4.10). This can be seen in terms of variation of the sharpness peak heights, which show a rapid increase after a SNR of around 20 is reached (fig. 4.10). The FWHM, instead, does not vary in the SNR range observed. This, as said, is not surprising, considering that all the beads lie within 10 μm from the coverslip glass and, hence, the variations introduced by spherical aberration are not important (fig. 3.18). Regarding the performance, the axial range tends to decrease linearly with respect to the signal (fig. 4.13), while the axial precision grows exponentially with it (eq. 4.8, fig. 4.16). Larger PS can help to reach wider axial ranges, thanks to the fact that this increases the axial coverage of the sharpness curves (fig. 4.8). This is important, since it can allow to improve the axial range without increasing laser power and/or ET, thus reducing temporal resolution and photobleaching problems. However, this advantage is progressively lost as the signal level decreases (fig. 4.13a).

The next section will show a study of the multifocal system performances under different levels of chromatic correction, by using filters of various bandwidths inserted in the diffraction relay.

4.5 Behaviour of a non-chromatically corrected diffraction multifocal microscope

The fundamental component of the multiplane relay under study is the quadratically distorted diffraction grating [36], which, thanks to the detour phase introduced, acts as a lens in the non-zero diffraction orders with order-dependent focal length, as explained in section 2.3.1, allowing the imaging of different axial planes at sample level. The physical behaviour of diffraction gratings is governed by the grating equation [37] (eq. 2.3):

$$d_0 \sin \theta_m = m \lambda, \qquad \text{(eq. 2.3)}$$

which states that the diffraction angle θ_m is a function of the diffraction order m, of the central grating period d_0 and of the wavelength λ, for light normally incident on the grating. In particular, this wavelength dependence imposes that each spectral component of light is diffracted at different output angles, introducing chromatic smearing in the $\pm 1^{st}$ planes, where m is not equal to zero. In addition, due to the opposite sign of m for the $\pm 1^{st}$ orders, the chromatic smearing will appear symmetric between them. This phenomenon is visible in fig. 4.17.

Fig. 4.17a shows a section of a camera frame with a 1 μm bead in PDMS in focus (i.e. where the IC was maximised) in the central plane. This has been extracted from the first bead z-stack of a ten z-stack series, acquired without any filter inserted in the diffraction relay (for a total measured bandwidth of 50 nm, due to the filters in the microscopes) and with laser power at sample of 2.07 μW at λ = 488 nm, em gain of 3,000 and ET of 100 ms. As observable, the image of the bead has the expected round shape only in the central plane, while it is elongated in the lateral ones, due to the chromatic smearing. Also, the images in the $\pm 1^{st}$ planes are one specular to the other as described. To make the effect of the chromatic smearing clearer, images of the bead in focus in each one of the three planes and their corresponding lateral profiles along the directions where these were maximised are presented in fig. 4.17b and 4.17c, respectively. The profile in fig. 4.17c (averaged among the three corresponding cross sections from the first three z-stacks of the z-stack series) with the highest peak is that for the bead in focus in the central plane in fig. 4.17b (3,800 ic), since the images of the

bead at the different wavelengths are all overlapped in that case. Vice versa, the peak drops down to around 1,800 ic and 1,600 ic for the profiles associated to the bead in focus in the -1st and +1st planes in fig. 4.17b respectively, considering the images at the

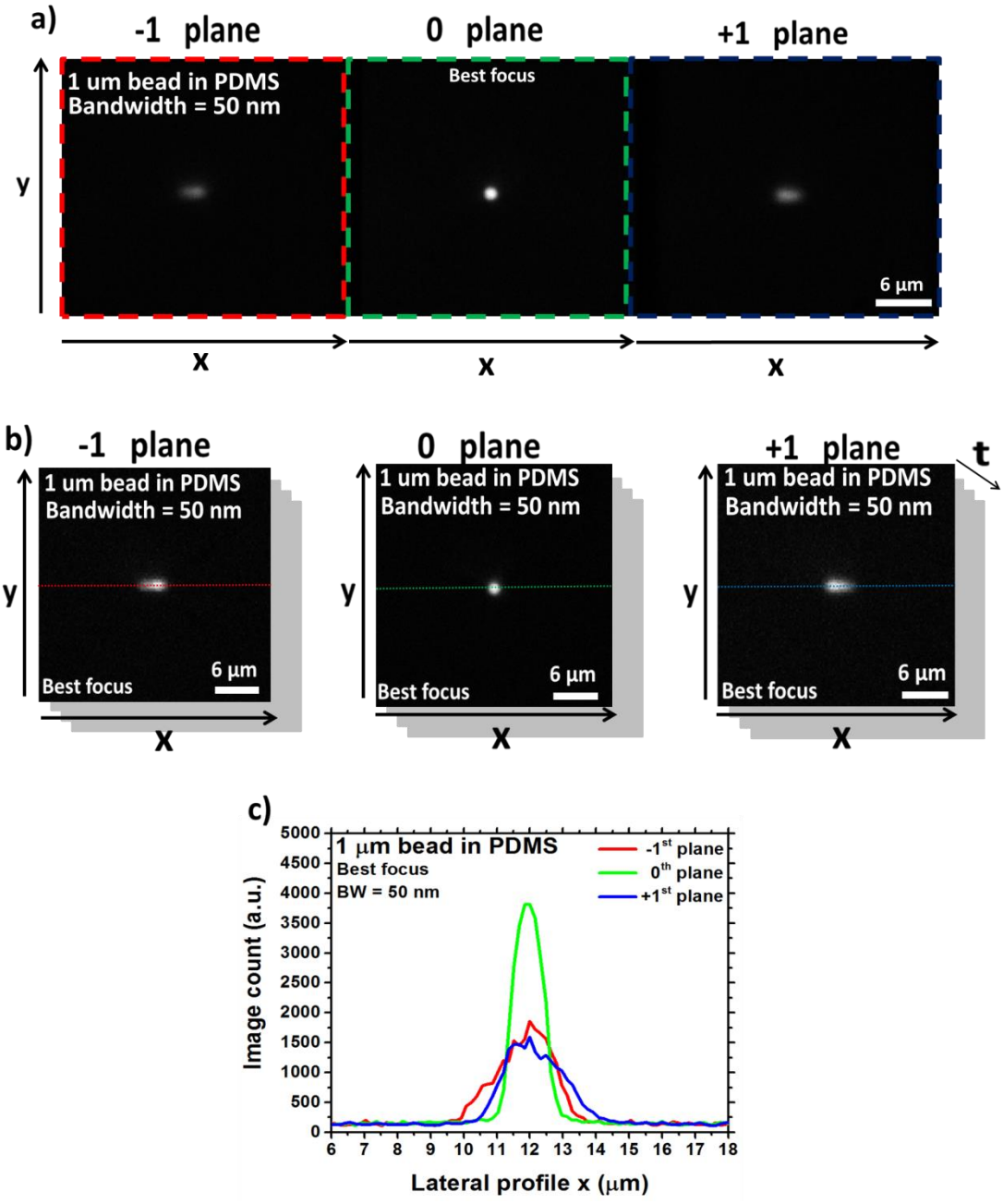

Figure 4.17 a) Image showing a 1 µm bead in PDMS observed through a BW of 50 nm and in focus in the central plane. **b)** Lateral cross sections showing the same bead in **a** in focus in the three different planes used. The images in **a** and **b** have been extracted from the first z-stack of the acquired z-stack series. **c)** Lateral profiles observed through the horizontal lines in **b**, where they were maximised. These are averaged among the three corresponding cross sections from the first three z-stacks of the z-stack series. Laser power at sample = 2.07 µW at λ = 488 nm, em gain = 3,000, ET = 100 ms.

different wavelengths are laterally spread on the camera chip now. This spreading can also be measured in terms of FWHM of the lateral profiles of the PSF in focus in the three different planes. Indeed, it is equal to roughly 1 μm and 2.25 μm, respectively for the bead in focus in the 0^{th} and $\pm1^{st}$ planes (fig. 4.17b and 4.17c). Obviously, the fact that the PSF is elongated in the $\pm1^{st}$ orders has also an effect on the average SNR_{pix}, which (for the bead in fig. 4.17b) decreases from 2.2 in the 0^{th} order to around 1.7 in the $\pm1^{st}$ ones.

As already shown in chapter 2, in order to correct for this particular lateral chromatic aberration, which would reduce the lateral localisation accuracy and increase the PSF overlapping, optical solutions have been introduced, either by using compensatory dispersion and diffraction optics [34] or by narrowing the image spectral band [38]. This second solution (adopted in the relay under study) keeps the system compact, relatively simple to build/align and cheaper compared to the compensatory optics system. However, these advantages come at the expense of the photon budget, whose value gets lower as the bandwidth filter gets narrower. In order to evaluate the performances of the multiplane diffraction relay (i.e. the achievable axial range and average axial precision in it) with different degrees of lateral chromatic aberration correction, this has been tested with and without different bandpass filters inserted in it. These filters had a bandwidth of 10 nm (Semrock, FF01-520/5-25), 25 nm (Semrock, FF01-525/15-25) and 60 nm (Semrock, FF03-525/50-25) and their transmission against wavelength curves are shown in fig. 4.18d, together with a horizontal line positioned at transmission 1 that represents the condition without filter. In the imaging path of the microscope there is also a dichroic mirror (Chroma, T505lpxt), with 50% emission edge at 505 nm (fig. 4.18b), and another emission filter (fig. 4.18a), with bandwidth of 50 nm (Semrock, FF01-535/50-25), inserted into the filter cube. These have the role of separating the laser (excitation at 488 nm) from the emission light (bead emission peak at 515 nm) and pre-select the light emitted in the desired range, respectively. All the filters listed above can transmit the wavelength of 520 nm, where the grating is balanced (sec. 3.3), and part of the emission spectrum of the used beads (fig. 4.18c), whose peak is at 515 nm. The combination of all used filters and of the bead spectrum gives the total transmission bandwidths for the system (fig. 4.18e), which have a transmission peak of around 70% at 520 nm and grow, mostly toward longer wavelengths, from 10 nm to 50 nm with the bandwidth of the filters in the relay (fig. 4.18d). The change in system bandwidth has a strong effect on PSF lateral cross sections and profiles in the $\pm1^{st}$ orders. In fig. 4.18g, 4.18h, 4.18i and 4.18j the lateral

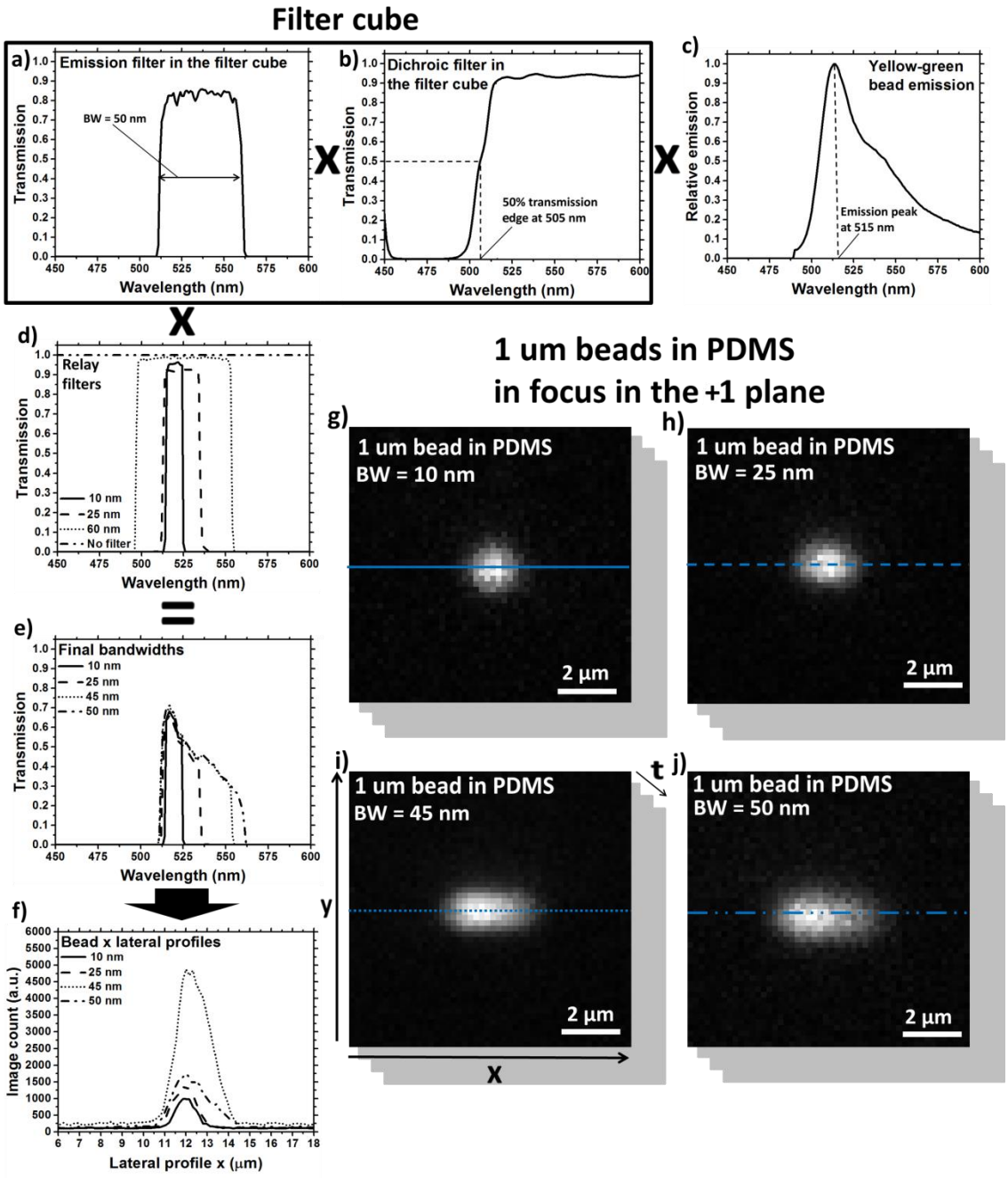

Figure 4.18 Transmission against wavelength profiles for **a** the emission filter and **b** the dichroic mirror used in the microscope filter cube and for **d** all the different emission filters used in the diffraction relay. In **c** the relative emission of the used beads is presented. In **e** the final bandwidths given by the multiplications of all the used filters and the bead emission spectrum are shown. The lateral cross sections observed through different BWs for 1 μm beads in PDMS in focus in the +1st plane are shown in **g** for BW = 10 nm, in **h** for BW = 25 nm, in **i** for BW = 45 nm and in **j** for BW = 50 nm. These have been extracted from the first z-stack of the acquired z-stack series. In **f** the lateral profiles tracked through the lines in **g**, **h**, **i** and **j** are presented. These have been observed where they were maximised and are averaged among the three corresponding

cross sections from the first three z-stacks of the z-stack series. Laser power at sample = 2.07 μW at λ = 488 nm, em gain = 3,000, ET = 100 ms.

cross sections (extracted from the first z-stack of their z-stack series) of the 1 μm beads in PDMS observed in focus in the $+1^{st}$ plane are shown for system bandwidths (BWs) of 10 nm, 25 nm, 45 nm and 50 nm, respectively. The lateral profiles, instead, are shown in fig. 4.18f (averaged as those in fig. 4.17c) and have been tracked through the horizontal lines on the cross sections in fig. 4.18, where they were maximised. The FWHM of these profiles goes from 1.35 μm for BW = 10 nm to 2 μm for BW = 50 nm. As the system BWs in fig. 4.18e increases toward longer wavelengths, the diffraction angle grows too (eq. 2.3), thus elongating the profiles on the right-hand side of that for the bead observed through a BW of 10 nm (the opposite happens in the -1^{st} order, eq. 2.3). Moving away from the peaks, the bead profiles decay in intensity as the fluorophore emission does in fig. 4.18c. In terms of profile peaks, these should grow with the BW, as more photons are collected. Effectively, this is the case for BWs of 10 nm, 25 nm and 45 nm, where the peak goes from around 1,000 ic to 4,750 ic. For BW = 50 nm, instead, there is a decrease to 1,750 ic. This behaviour is not due to a reduction in the number of allowed photons, since the BW has grown. It is simply due to the fact that the bead observed with BW = 45 nm is brighter than that acquired with BW = 50 nm, considering the SNR of the first is 42.5, while that of the second one is 27.3.

The lateral elongation of the PSF observed for the beads in focus in fig. 4.17 becomes less evident as the PSF gets defocused, due to the introduction of the defocus aberration. In fig. 4.19 three bead lateral cross sections from different axial positions are shown. These have been extracted from the -1^{st} plane of the first z-stack acquired for the 1 μm bead in PDMS with BW = 50 nm and are presented with their corresponding lateral profiles over x and y directions (horizontal and vertical lines on the cross sections, tracked as those in fig. 4.17). Cross section and profiles in fig. 4.18c and 4.18d are associated to the bead in focus, while those in fig. 4.18a - 4.18b and 4.18e - 4.18f to the bead imaged, respectively, 3 μm before and after the best focal position in that plane. As observable, while x and y profiles are clearly different for the bead in focus (fig. 4.19c – 4.19d), with the first one with a FWHM of 2.25 μm and the second one of 1 μm, the x and y profiles for the beads out of focus in fig. 4.19b and 4.19f are basically overlapped. This is also visible on the cross sections in fig. 4.19a and 4.19e, whose shape is circular. This can be explained by considering the reduction in SNR_{pix} as the

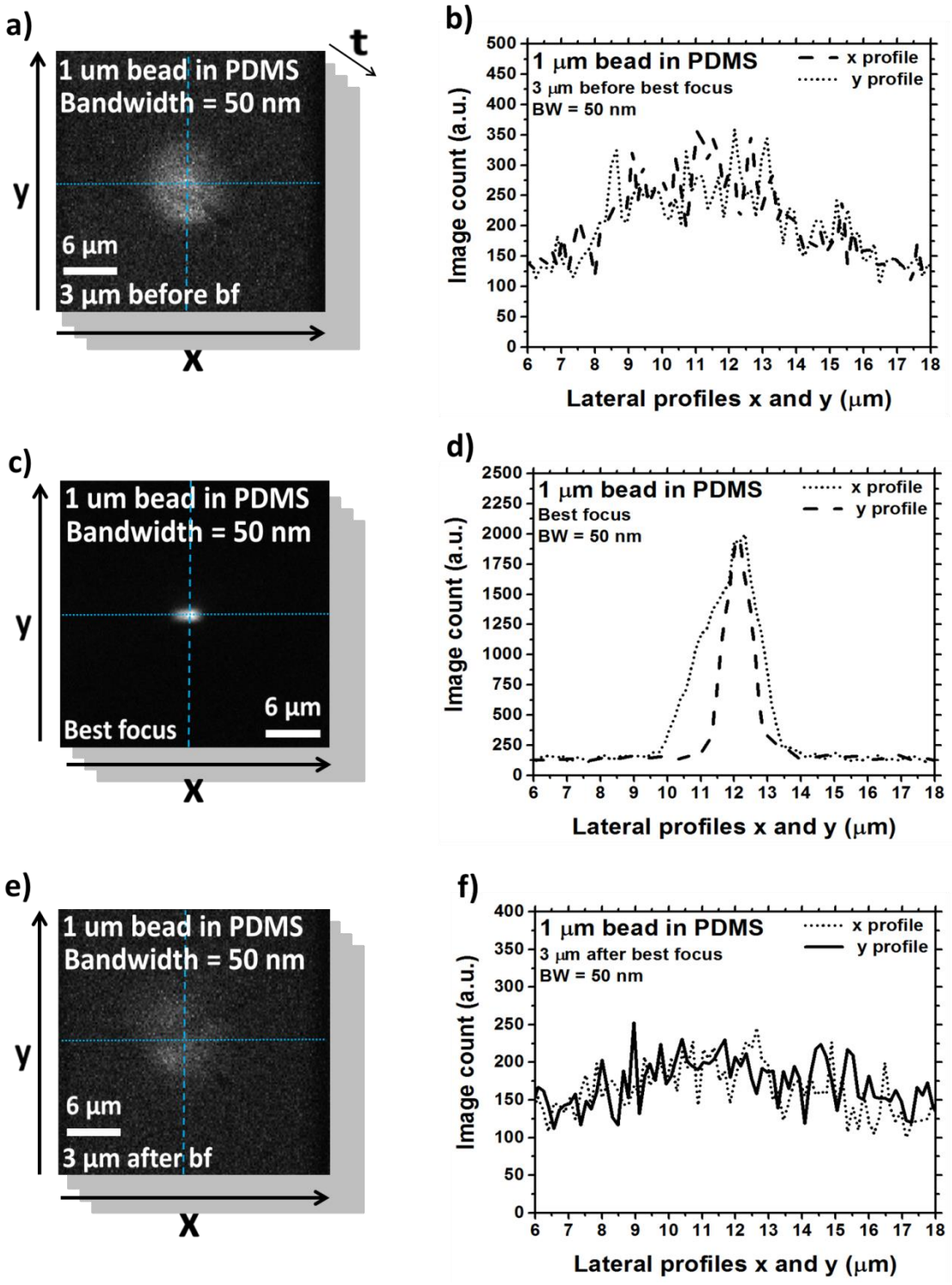

Figure 4.19 Lateral cross sections and profiles (over x and y directions) of a 1 µm bead in PDMS, observed through a BW of 50 nm and in the -1st plane. **c** and **d** show, respectively, cross section and lateral profiles for the bead in focus, **a** and **b** for the bead 3 µm before the best focus and **e** and **f** 3 µm after it. The cross sections have been extracted from the first z-stack of the acquired z-stack series, while the profiles are observed through the lines in **a**, **c** and **e**, where they were maximised. These are averaged among the three corresponding cross sections from the first three z-stacks of

the z-stack series. Laser power at sample = 2.07 μW at λ = 488 nm, em gain = 3,000, ET = 100 ms.

PSF moves out of focus and the emission profile in fig. 4.18c. Indeed, the average SNR_{pix}, as shown in fig. 4.5b, decays as the PSF is defocused, but this reduction in signal is more pronounced for those wavelengths whose relative emission is lower than the maximum one (fig. 4.18c), taking to the gradual disappearing of the chromatic smearing in the out of focus regions.

Regarding the impact of different BWs on axial cross sections, profiles and sharpness curves, this is due to the change in SNR combined with that in BWs. Fig. 4.20b and 4.20d show the axial cross sections (extracted as those in fig. 4.3) associated to 1 μm beads in PDMS acquired with BWs of, respectively, 10 nm and 50 nm, while the corresponding axial profiles (calculated as in fig. 4.3) and sharpness curves are in fig. 4.20a and 4.20c. The profile peaks associated to the bead in fig. 4.20c and 4.20d (BW = 50 nm) are higher than those for the bead in fig. 4.20a and 4.20b (BW = 10 nm), since the former has a SNR of 27.3 and the latter of 18.2. The central profile peak in fig. 4.20a is 1,100 ic, while that in fig. 4.20c is 4,000 ic. The same behaviour can be observed for the sharpness curves (for all 1 μm beads a SB of 150x150 pix^2 has been used), whose peaks are higher for the bead acquired with BW = 50 nm ($4.85 \cdot 10^{-5}$ a.u.

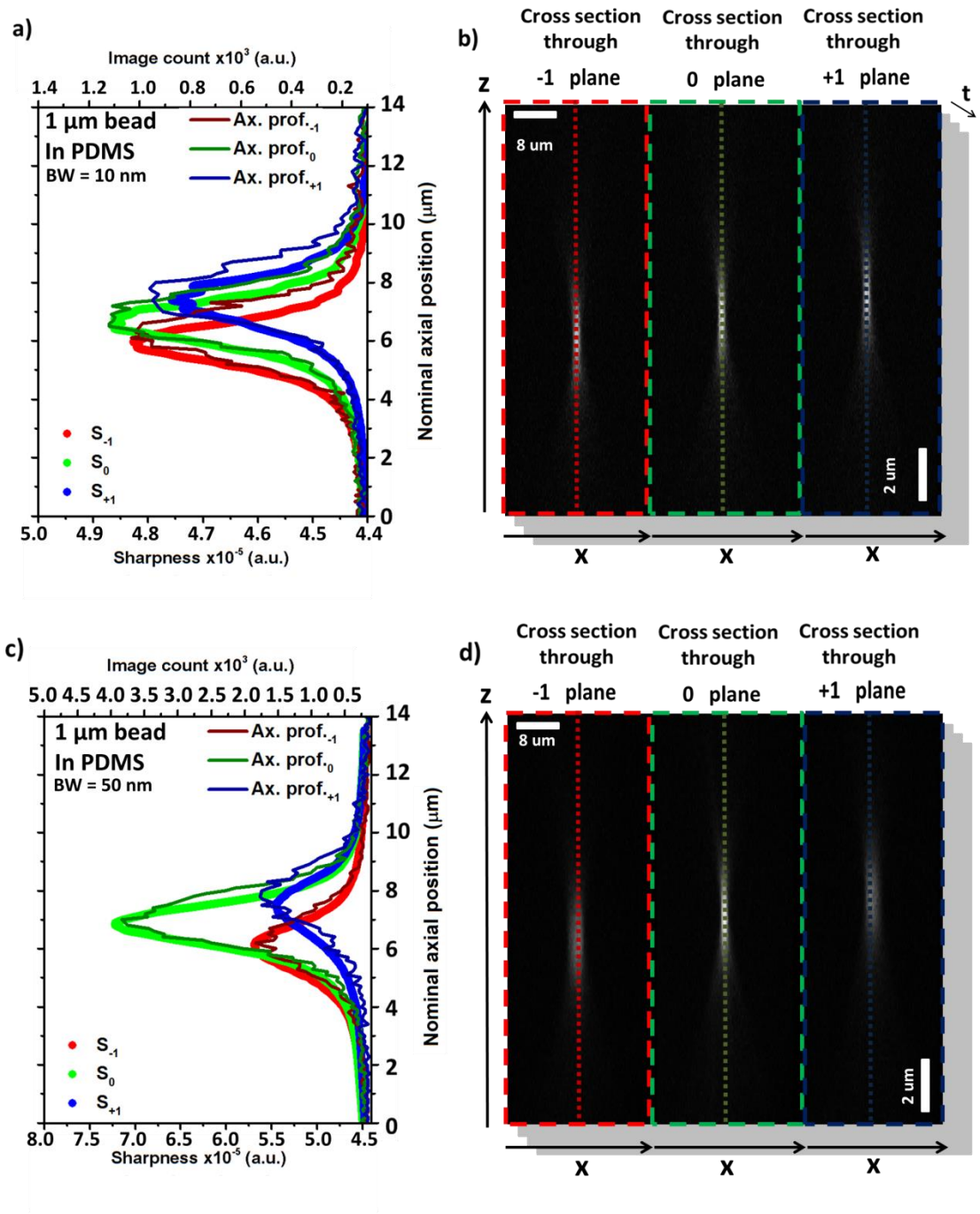

Figure 4.20 Sharpness curves with axial profiles (**a** and **c**) and axial cross sections (**b** and **d**) observed through the three used axial planes, for two 1 µm beads in PDMS acquired through BW of (**a** and **b**) 10 nm and (**c** and **d**) 50 nm. The cross sections have been obtained from the first z-stacks of the acquired z-stack series. The axial profiles have been observed through the three vertical lines in **b** and **d**, where they were maximised and are averaged among the three corresponding cross sections from the first three z-stacks of the z-stack series. Laser power at sample = 2.07 µW at λ = 488 nm, em gain = 3,000, ET = 100 ms.

for the central curve in fig. 4.20a and $7.25 \cdot 10^{-5}$ a.u. for the corresponding one in fig. 4.20c). Another aspect to observe is the difference in peak heights between axial profile/sharpness curves in the $\pm 1^{st}$ and the 0^{th} planes, which increases with the BW. As the BW increases, the relative peak heights of the non-zeroth orders profile and sharpness curves decrease with respect to those in the zeroth order, indicative of a reduced overall image sharpness due to the increasing lateral chromatic aberration. This is clearly visible in fig. 4.21, where the relative normalised sharpness curves associated to the 1 μm beads in PDMS acquired with the different BW are presented. Therefore, it can be concluded that the central sharpness and axial profile curves have higher peaks

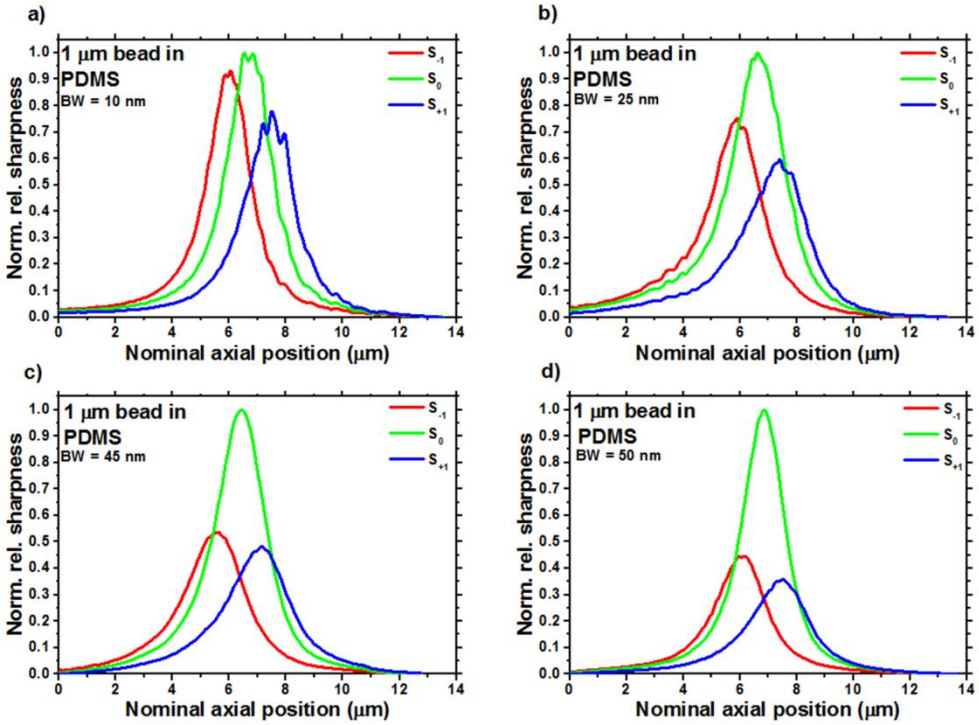

Figure 4.21 Calculated sharpness curves for 1 μm beads in PDMS observed through bandwidths of **a)** 10 nm, **b)** 25 nm, **c)** 45 nm and **d)** 50 nm. Laser power at sample = 2.07 μW at λ = 488 nm, em gain = 3,000, ET = 100 ms.

than those in the $\pm 1^{st}$ orders due to the total absence of diffraction grating-induced chromatic aberration in the 0^{th} order.

Together with the 1 μm beads in PDMS, the response of the system to different BWs (the same shown in fig. 4.17) has also been studied by using 1 μm beads in agarose and 100 nm beads in agarose and PDMS, as in previous sections. The z-stack series have been acquired by using the same procedure and acquisition conditions

described in sec. 4.4 in terms of objective lens, filter cube, laser power and em gain, while the ET was fixed on 100 ms. The grating with focal length of 962.50 mm (PS = 630 nm) has been used. As in sec. 4.4, the sharpness curves have been calculated for all acquired z-stacks by using sharpness boxes of 30x30 pix^2 and 150x150 pix^2, respectively for the 100 nm and 1 μm beads. This has been summarised in table 4.3:

Bead size	**ET (ms)**	**em gain**	**Laser power at λ = 488 nm (mW)**	**BW (nm)**	**Obj. lens**	**SB side (pix)**	**PS (nm)**	**z-stack axial ext. (μm)**
100 nm	100	3,000	8.56 (A), 0.76 (P)	10, 25, 45, 50	M = 100x, NA = 1.46, oil	30	630	±3 μm
1 μm		2,000 (A), 3,000 (P)	$42.56\ 10^{-3}$ (A), $2.07\ 10^{-3}$ (P)			150		±7 μm

Table 4.3 Experimental parameters and conditions used with the multi-BW study. A = agarose, P = PDMS, M = magnification, SB = sharpness box, PS = plane spacing, NA = numerical aperture, ET = exposure time, BW) bandwidth.

In fig. 4.22 the SNR and SBR values evaluated in the -1^{st} order and associated to the beads acquired in the different experimental conditions have been plotted against the corresponding BW. As observable, apart from some outliers, in general the SNR tends to increase with the BW. The SBR, instead, does not behave similarly, even if this was the case with the multi-ET study (fig. 4.6). For example, by considering the data in fig. 4.22a, both the signal and the background have a 3-fold increase moving from BW = 10 nm to BW = 50 nm, thus keeping the SBR almost unchanged (6.2 and 6.4, respectively). This could be due to an increase in autofluorescence of the samples at wavelengths different from that at which the grating is balanced (520 nm). However, even though it has been reported that agarose and PDMS samples show some little autofluorescence in the visible [39, 40], not study of the emission of these materials as function of the wavelength has been found and, hence, this cannot be demonstrated.

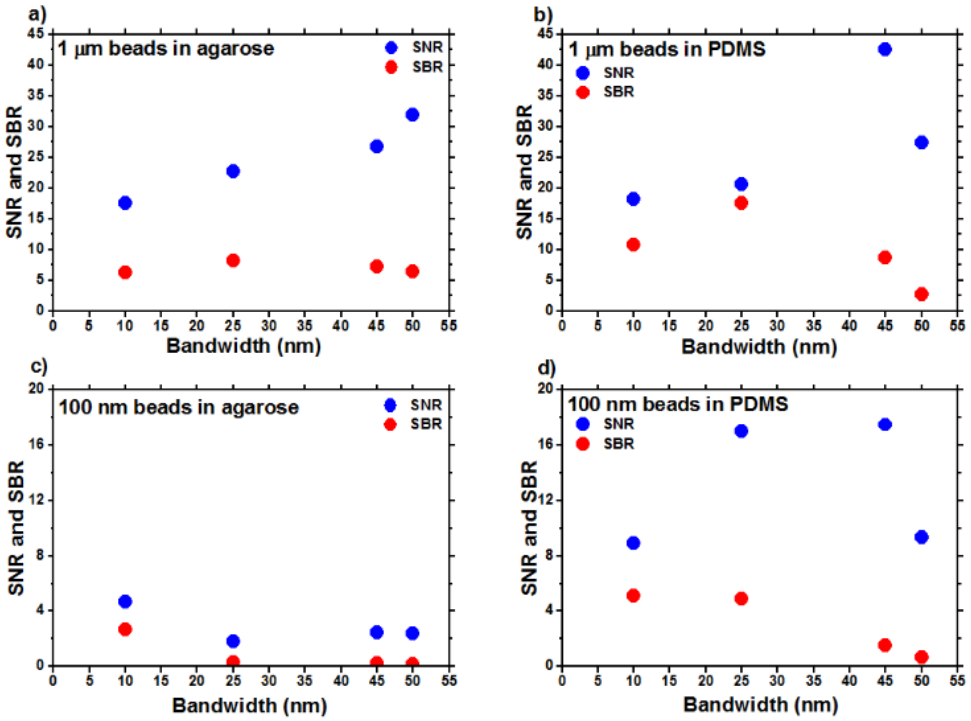

Figure 4.22 Evaluated SNR and SBR for bead z-stacks acquired with different BWs and PS = 630 nm. **a)** 1 µm beads in agarose (laser power at sample = 42.56 µW at λ = 488 nm, em gain = 2,000), **b)** 1 µm beads in PDMS (laser power at sample = 2.07 µW at λ = 488 nm, em gain = 3,000), **c)** 100 nm beads in agarose (laser power at sample = 8.56 mW at λ = 488 nm, em gain = 3,000) and **d)** 100 nm beads in PDMS (laser power at sample = 0.76 mW at λ = 488 nm, em gain = 3,000).

The analysis of the shape of the sharpness curves is presented in fig. 4.23, where the relative sharpness peaks and FWHMs are presented for all the four experimental conditions against their associated BWs. The data presented are for the beads observed in the -1st plane, thus including the effect of the chromatic aberration. The SNR values have been colour encoded in the sharpness peak data. As observable, the FWHM data tend to grow with the BW in all four experimental conditions. This result is not surprising, since, as explained in sec. 2.4.4, the BW generates axial chromatic smearing in the non-zeroth orders [41], which is directly proportional to it and is embedded in the shape of the sharpness curves. For example, the FWHMs of the axial profiles in the -1st planes in fig. 4.20 grow from 2.5 µm at BW = 10 nm (fig. 4.20a) to 2.9 µm at BW = 50 nm (fig. 4.20c), while those for the axial profiles in the 0th order are both around 2.1 µm. This FWHM enlargement cannot be attributed to the increase in signal

level, since it has not been observed with the multi-ET study in fig. 4.10, where the BW was not changed. In the plots of fig. 4.23 the growth in FWHM with the BW has been quantified by using linear fits, obtaining slopes equal to (15 ± 8) nm/nm, (11 ± 8) nm/nm, (9 ± 9) nm/nm and (3 ± 6) nm/nm, respectively for the curves in fig. 4.23a, 4.23b, 4.23c and 4.23d. Even though the R_{adj}^2 values are not close to unit (0.44,

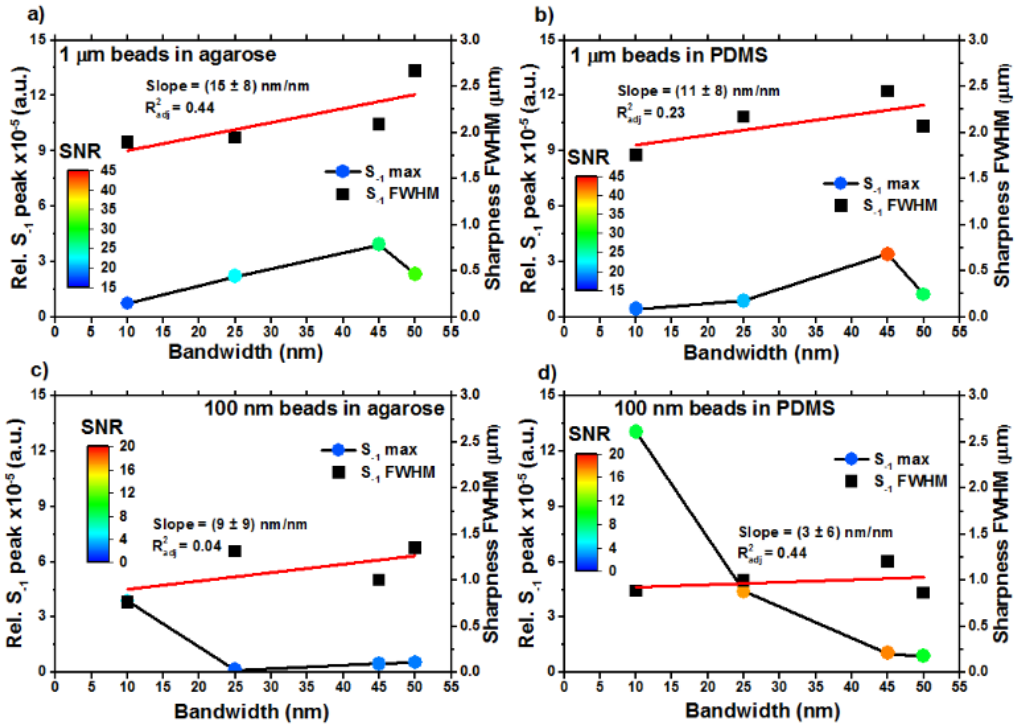

Figure 4.23 Evaluated relative sharpness curve peak heights (left y axis, circles) and FWHMs (right y axis, squares) of the sharpness curves in the -1st planes, for bead z-stacks acquired with different bandwidths and PS = 630 nm. The SNR (evaluated in the -1st plane) has been colour encoded in the sharpness peak curves. The red straight lines are linear fits through the FWHM values, whose slopes (with their standard deviations) and goodness (the adjusted R^2 values) are shown in the plots. **a)** 1 µm beads in agarose (laser power at sample = 42.56 µW at λ = 488 nm, em gain = 2,000, ET = 100 ms), **b)** 1 µm beads in PDMS (laser power at sample = 2.07 µW at λ = 488 nm, em gain = 3,000, ET = 100 ms), **c)** 100 nm beads in agarose (laser power at sample = 8.56 mW at λ = 488 nm, em gain = 3,000, ET = 100 ms) and **d)** 100 nm beads in PDMS (laser power at sample = 0.76 mW at λ = 488 nm, em gain = 3,000, ET = 100 ms).

0.23, 0.04 and 0.44, ordered as the slopes above), probably due to the low number of points per fit, the calculated slopes, considering their standard deviations, are quite close to each other and take to an average value of (9.5 ± 7.8) nm/nm. This indicates that the FWHM has grown, on average, by (475 ± 390) nm as the BW has reached 50 nm. This increase in FWHM is larger than the one expected to be generated by the axial chromatic smearing. Indeed, eq. 2.30 states that:

$$\frac{\Delta PS}{PS_c} = \frac{\Delta\lambda}{\lambda_c}, \qquad \text{(eq. 2.30)}$$

which means that the ratio between the BW $\Delta\lambda$ and its central wavelength λ_c (where the grating is balanced in this case) is equal to the ratio between the axial chromatic smearing introduced (ΔPS) and the plane spacing PS_c associated to λ_c. Therefore, for a λ_c of 520 nm, a BW of 50 nm and a PS_c of 630 nm a ΔPS of around 60 nm was expected. The larger increase in FWHM in the non-zeroth orders could be due to the fact that PSFs are also laterally chromatic aberrated and this might have had an effect. In addition, the increase in BW might have introduced some wavelength depended aberrations [42] that have not been taken into account. However, these aspects have not been investigated.

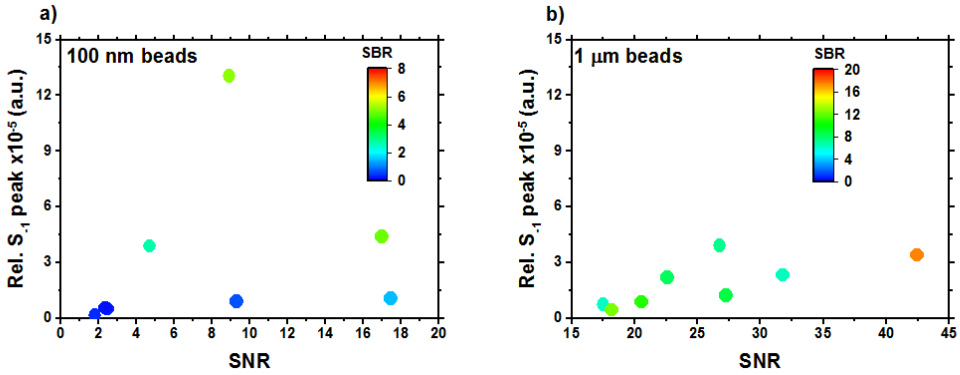

Figure 4.24 Relative sharpness peak heights of the sharpness curves in the -1st planes plotted against the corresponding SNR and SBR values, for all bead z-stacks acquired in agarose and PDMS, with the different BWs and PS = 630 nm. The SBR has been colour encoded in the sharpness peak curves. The data in **a** are associated to the 100 nm beads, while those in **b** to the 1 µm ones. Laser power at sample = 42.56 µW, 2.07 µW, 8.56 mW and 0.76 mW. λ = 488 nm. em gain = 2,000, 3,000. ET = 100 ms.

Regarding the sharpness peaks, these in general grow with the signal level as seen with the data acquired for the multi-ET study (fig. 4.10). This can be observed in fig. 4.24, where the sharpness peaks associated to the 100 nm (fig. 4.24a) and 1 μm (fig. 4.24b) beads have been plotted against the corresponding SNR and SBR values. The peaks associated to the 1 μm beads grow from around $0.5 \cdot 10^{-5}$ a.u. at a SNR of 18 and a SBR of 6 to around $3.4 \cdot 10^{-5}$ a.u. at a SNR of 42.5 and a SBR of 17.5. This growth is less pronounced that that seen in fig. 4.10, due, as said, to the fact that the lateral chromatic aberration reduces the image sharpness (fig. 4.20 and 4.21). Similarly, those for the 100 nm beads in general increase from around $0.1 \cdot 10^{-5}$ a.u. at a SNR of 1.8 and a SBR of 0.3 to around $4.4 \cdot 10^{-5}$ a.u. at a SNR of 17 and a SBR of 5.

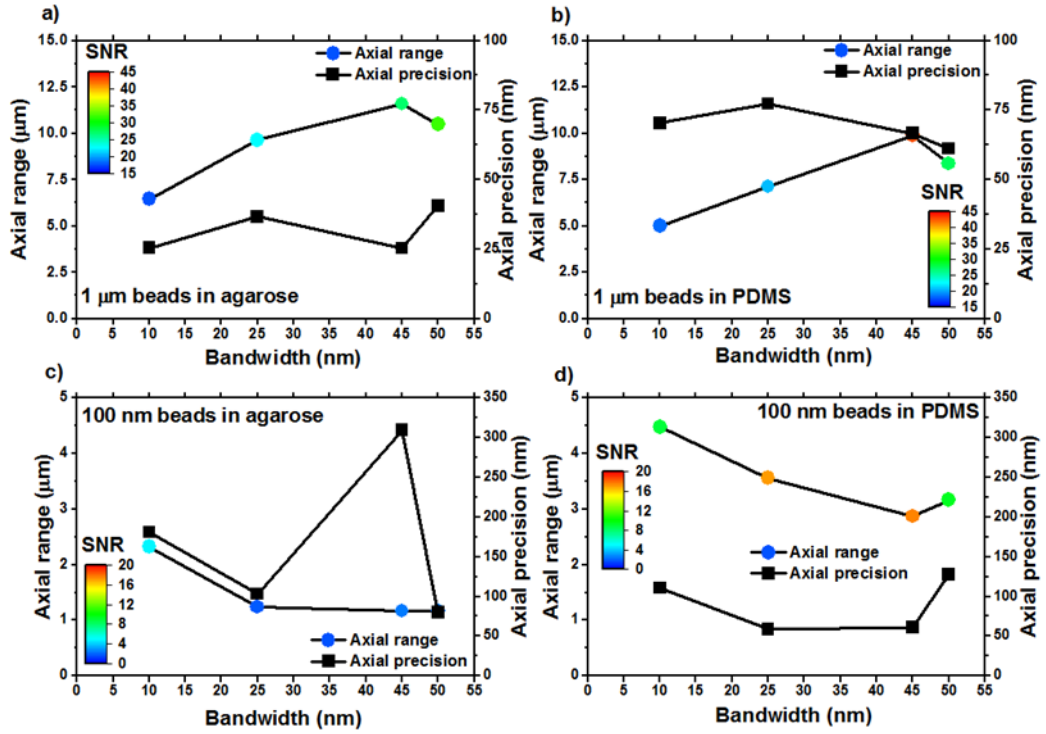

Figure 4.25 Evaluated axial ranges (left y axis, circles) and precisions (right y axis, squares) for bead z-stacks acquired with different bandwidths and PS = 630 nm. The SNR (evaluated in the -1st plane) has been colour encoded in the axial range curves. **a)** 1 μm beads in agarose (laser power at sample = 42.56 μW at λ = 488 nm, em gain = 2,000, ET = 100 ms), **b)** 1 μm beads in PDMS (laser power at sample = 2.07 μW at λ = 488 nm, em gain = 3,000, ET = 100 ms), **c)** 100 nm beads in agarose (laser power at sample = 8.56 mW at λ = 488 nm, em gain = 3,000, ET = 100 ms) and **d)** 100 nm beads in PDMS (laser power at sample = 0.76 mW at λ = 488 nm, em gain = 3,000, ET = 100 ms).

As for the multi-ET study (sec. 4.4.2), also in this case the performance of the sharpness algorithm have been investigated. The achievable axial ranges and average axial precisions within them have been evaluated through the different BWs used in the four experimental conditions. The results are presented in fig. 4.25, with the SNR colour encoded in the axial range data. As done for the results at different ETs (fig. 4.13), these data can be combined to show the global behaviour of the performance as a function of the level of the signal. This is presented in fig. 4.26, where axial range (fig. 4.26a) and precision (fig. 4.26b) have been plotted against the corresponding SNR and SBR values. As expected, both axial range and precision improve with the signal. The axial range increases from around 1.2 μm at a SNR of 1.8 and a SBR of 0.3 to around 9.9 μm at a SNR of 42.5 and a SBR of 17.4. As already shown in fig. 4.13 and 4.16, this increase is linear with the signal and has a speed of (273 ± 38) nm per SNR unit, a value comparable to those extrapolated before. Regarding the axial precision, this worsens from 67 nm to around 310 nm as the signal is reduced, following a behaviour similar to that observed in sec. 4.4.3 (fig. 4.16).

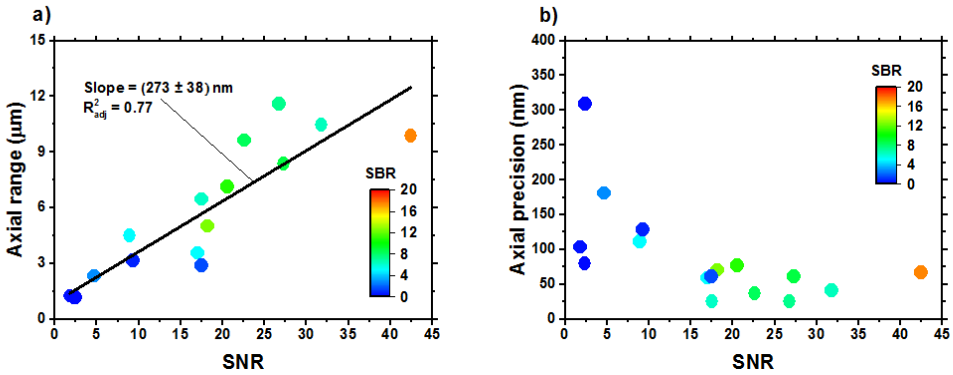

Figure 4.26 Evaluated axial ranges (**a**) and precisions (**b**) associated to the multi-BW study and plotted against the corresponding SNR and SBR values. The straight line in **a** is a linear fit through the axial range values, whose slope (with its standard deviation) and goodness (the adjusted R^2 value) are shown. PS = 630 nm. Laser power at sample = 42.56 μW, 2.07 μW, 8.56 mW and 0.76 mW. λ = 488 nm. em gain = 2,000 and 3,000. ET = 100 ms.

By observing the results in fig. 4.26, it can be concluded that chromatically spread PSFs can still be axially localised within an accuracy of 100 nm, even though they are composed by the overlap of multiple laterally shifted PSFs generated at different wavelengths. This is possible since the sharpness curves are able to embed the chromatic smearing into them (fig. 4.20) and localise the chromatically aberrated PSFs

successfully. However, even if it could seem appropriate to use a BW as wide as possible to raise the signal level and improve axial range and precision, there are also some drawbacks. One of these is represented by the worsening of the lateral localisation accuracy due to the PSF elongation, considering that all three planes should be used to maximise the number of used photons. This has been quantified by comparing the lateral centres of mass (CoMs) calculated by using all three planes (aligned by using the alignment file generated by the MUM algorithm) to the CoMs evaluated by using the images in the central plane only, where the chromatic aberration grating-induced has no effect. To this end, the 1 μm beads in PDMS acquired with BWs of 10 nm (fig. 4.27a) and 50 nm (fig. 4.27b) have been used to calculate the CoMs in both x and y directions, where the x direction is that where the chromatic spreading appears. In fig. 4.27 the absolute values of the difference between the three plane CoMs (indicated as x_{tot} and y_{tot}) and those obtained through the central planes only (called x_{cen} and y_{cen}) have been plotted against the nominal axial positions. The values of x_{cen} and y_{cen} have been used as references, thus the curves in fig. 4.27 are considered as accuracies (x_{acc} and y_{acc}). All

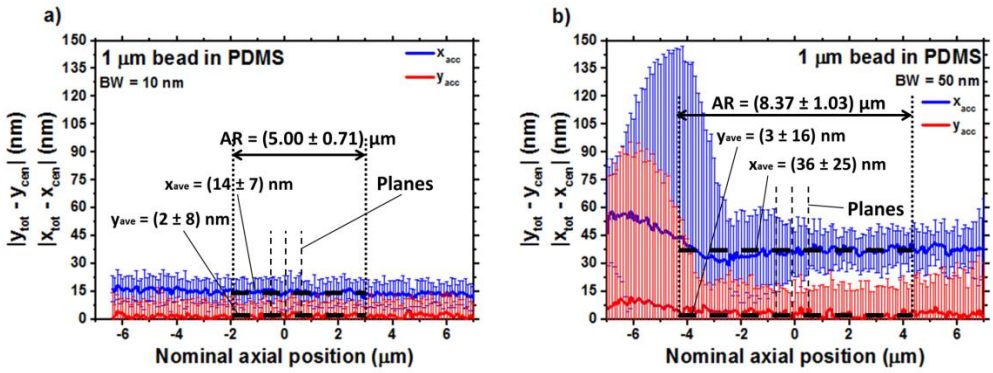

Figure 4.27 Average lateral localisation accuracies over x and y directions, calculated as absolute difference between the lateral localisation positions obtained by evaluating the CoMs of the beads observed through all three planes simultaneously and in the central plane only with a code written in MATLAB. This has been done for all axial positions and for 1 μm beads in PDMS acquired through BWs of **a)** 10 nm and **b)** 50 nm. The error bars are the standard deviations on the average accuracies. The axial ranges and the average lateral accuracies in them are shown, together with the position of the planes. Laser power at sample = 2.07 μW at λ = 488 nm, em gain = 3,000, ET = 100 ms, PS = 630 nm.

CoM values have been obtained by using the same MATLAB code presented in sec. 3.3.2, which has been rearranged to evaluate the lateral CoM instead of the axial one. In

this case the values obtained in pixels have been subtracted by 0.5 pix to refer them to an origin of 0 pix and then transformed in micrometres by multiplying them by 0.16 μm/pix. The final x_{tot}, x_{cen}, y_{tot} and y_{cen} values have then be obtained by using the same averaging procedure described in sec. 3.5.2 for the axial CoM. The error bars in fig. 4.27 are the standard deviations on x_{acc} and y_{acc} calculated at all nominal axial positions. To facilitate the observation of the differences in lateral localisation accuracies, the average values for x_{acc} and y_{acc} have been calculated within the axial range regions (shown in fig. 4.27, together with the plane positions). These are equal to (14 ± 7) nm and (2 ± 8) nm, respectively for the average x_{acc} and y_{acc} in fig. 4.27a, and to (36 ± 25) nm and (3 ± 16) nm, respectively for the average x_{acc} and y_{acc} in fig. 4.27b. As noticeable, the average x_{acc} has worsened by more than 2.5 times moving from BW = 10 nm to BW = 50 nm, due to the chromatic spreading. This reduction in lateral accuracy could be avoided by using only the central plane to get the x-y positions. However, this would come at the expenses of the lateral precision, since the number of used photons for that purpose will be roughly reduced to one third and will worsen with the degree of defocus of the imaged object. Another problem could be the increasing rate of PSF overlapping in a context where multiple objects are imaged simultaneously, due to the chromatic elongation. This could be a problem especially when the study of densely packed systems is needed (the bead flow application presented in next chapter is one of them), where PSF overlapping would add artefacts to the calculated axial and lateral positions.

In the next section a study of the multifocal system performance observed by using different microscope objective lenses will be presented.

4.6 Importance of objective lenses in diffraction multifocal microscopy

Microscope objectives are one of the most important and complex components of a microscope [30]. They are responsible for the amount of photons collected from the sample through their numerical aperture (NA), for the correction of aberrations (spherical, comatic, chromatic, field curvature, etc.) and, together with tube lens and/or eyepiece, for the image magnification introduced. Consequently, they play a key role in multiplane microscopy [36, 43]. In order to quantify the influence of the microscope objectives on the performance of the diffraction multiplane system under study, it has been decided to perform a multi-objective experiment. Four objectives lenses have been selected: a 20x magnification, 0.8 NA, dry objective (Zeiss, 420650-9901-000), a 63x magnification, 1.2 NA, water immersion objective (Zeiss, 441777-9970-000, with the

relative immersion water with n = 1.334 at 23°C, Zeiss, 444969-0000-000), a 63x magnification, 1.4 NA, oil immersion objective (Zeiss, 440762-9904-000) and the so far used 100x magnification, 1.46 NA, oil immersion objective (Zeiss, 440782-9800-000). These four objectives have a transmission at 520 nm of, respectively, 0.95, 0.78, 0.83 and 0.73. As in previous sections, the same four experimental conditions have been investigated (100 nm and 1 μm beads in agarose and PDMS), by using the grating with focal length of 962.50 mm (PS = 630 nm at M = 100x). For each experimental condition, one bead z-stack series per objective lens (within 10 μm from the coverslip) has been acquired by following the previous describe procedures. However, due to the increase in PS with the reduction in M (eq. 2.24), it has been necessary to increase the z-stack acquisition ranges for those beads acquired with objectives whose M was smaller than 100x. In particular, respectively for the 20x, 63x and 100x objectives and with respect to the beads in focus in the central planes, these were equal to ±30 μm, ±10 μm and ±7 μm for the 1 μm beads, and to ±30 μm, ±5 μm and ±3 μm for the 100 nm ones. Regarding the imaging parameters, for all the experimental conditions the em gain has been set to 3,000 and the ET to 100 ms, while the laser powers at 488 nm, measured before the objective lenses, were equal to 21.4 μW and 3.56 μW, respectively for the 1 μm beads in agarose and PDMS, and to 357 μW and 105.6 μW, respectively for the 100 nm beads in agarose and PDMS. To calculate the sharpness curves, apart from the 1 μm beads imaged through the 20x objective, the same procedure described in previous sections has been used. For the 1 μm beads imaged via the 20x objective, instead, it was necessary to reduce the size of the sharpness box from 150x150 pix^2 to 30x30 pix^2. This was needed due to the increased FOV, since a box of 150x150 pix^2 would have included more than one bead. These parameters have been summarised in table 4.4:

Bead size	**ET (ms)**	**em gain**	**Laser power at λ = 488 nm (µW)**	**BW (nm)**	**Obj. lens**	**SB side (pix)**	**z-stack axial ext. (µm)**
100 nm	100	3,000	357 (A), 106.5 (P)	10	M = 20x, NA = 0.8, dry M = 63x, NA = 1.2, water M = 63x, NA = 1.4, oil M = 100x, NA = 1.46, oil	30	±30 µm ±5 µm ±3 µm
1 µm			21.4 (A), 3.56 (P)			30, 150	±30 µm ±10 µm ±7 µm

Table 4.4 Experimental parameters and conditions used with the multi-objective lens study. A = agarose, P = PDMS, M = magnification, BW = bandwidth, NA = numerical aperture, SB = sharpness box, ET = exposure time.

Both NA and magnification can vary the observed SNR_{pix} and, consequently, the system performances. Indeed, as the NA increases, the number of collected photons grows too, since the cone of collected light is enlarged, thus raising the SNR_{pix}. Instead, the opposite happens with the magnification (M), whose reduction leads to an increase in SNR_{pix}, considering the emitter image is concentrated on a smaller number of pixels. This means that the SNR_{pix} achievable with an objective lens results from the balance between the light concentration imposed by the M and light collection dictated by NA. This can be further explained by considering the following mathematical model. An emitter (e.g. an organic fluorophore, a fluorescent protein, a quantum dot, etc.) emits photons over all the possible directions in space, i.e. over a solid angle of 4π sr (fig. 4.28a). However, the majority of these photons is lost, since only the fraction emitted within the collection cone described by the NA of the objective lens can be collected. If the semi-aperture angle associated to the NA is ϑ_{NA}, the corresponding solid angle θ_{NA} (i.e. the fraction of the surface of the emission sphere with radius R = 1 in fig. 4.28a intersected by the NA collection cone) will be equal to ([44], eq. 4.9):

$$\theta_{NA} = 2\pi(1 - \cos\vartheta_{NA}). \qquad \text{(eq. 4.9)}$$

By dividing θ_{NA} by the entire solid angle 4π sr, it is possible to estimate the fraction of light intercepted by the objective lens. Once the light has been collected, it is needed to transmit the latter through the microscope and the diffraction relay to the camera. The number of photons n_{ph} hitting the camera chip will be equal to (eq. 4.10):

$$n_{ph} = N_{ph}\, T_{tot}\, \frac{\theta_{NA}}{4\pi} = \frac{1}{2} N_{ph}\, T_{tot}\, (1 - \cos \vartheta_{NA}), \qquad \text{(eq. 4.10)}$$

where N_{ph} is the total number of photons emitted by the emitter and T_{tot} is the total system transmission. Eq. 4.10 is based on the fact that only the fraction of photons collected by the objective lens and transmitted through the entire system will reach the camera. By using eq. 4.1 and 4.11 the overall SNR can be calculated (eq. 4.11):

$$SNR = \sqrt{\frac{q\, n_{ph}}{2}} = \frac{1}{2}\sqrt{q\, N_{ph}\, T_{tot}\, (1 - \cos \vartheta_{NA})}, \qquad \text{(eq. 4.11)}$$

with q the quantum efficiency of the camera (eq. 4.11 takes into account the Poisson noise only). To evaluate the SNR_{pix}, it is necessary to estimate to number of pixels illuminated N_{pix} (eq. 4.3), which will depend on the system magnification M. Considering only extended objects for simplicity (i.e. larger than the PSF associated to the microscope [27]), the radius r of the image of an emitter with radius e_r will be approximately equal to $|M| \cdot e_r$, due to the M. Therefore, the number of illuminated pixels N_{pix} can be evaluated as the number of pixels within a circle of radius r (fig. 4.28b) by using eq. 4.12:

$$N_{pix} = \pi \left(\frac{|M|\, e_r}{S_{pix}} \right)^2, \qquad \text{(eq. 4.12)}$$

with S_{pix} the camera pixel size. N_{pix} should be an integer number, since a pixel will result fully illuminated even if it has been only partially hit by the incoming photons. However, it has been decided to allow non-integer values for N_{pix} as well, so to avoid the further complication of the model. By combining eq. 4.11 and 4.13 into eq. 4.3, it is possible to obtain a final equation to model SNR_{pix} as a function of both NA and M (eq. 4.13):

$$\mathrm{SNR_{pix}} = \frac{\mathrm{SNR}}{\sqrt{\mathrm{N_{pix}}}} = \frac{\mathrm{S_{pix}}}{2\,|\mathrm{M}|\,\mathrm{e_r}}\sqrt{\frac{\mathrm{q\,N_{ph}\,T_{tot}\,(1-\cos\vartheta_{NA})}}{\pi}}. \qquad \text{(eq. 4.13)}$$

As it can be seen from eq. 4.13, as the M is reduced, the SNR_{pix} increases. However, a simultaneous reduction in ϑ_{NA} (i.e. in NA) will reduce the numerator in the square root of eq. 4.13 and, thus, the SNR_{pix}. Commonly, cell microscopy objective lenses have high NAs associated to high Ms and vice versa. Therefore, the sign of the change in SNR_{pix} as a function of the change in M and NA depends on the relative speed at which these two variable are modified. To plot eq. 4.13 and visualise its behaviour it is needed to estimate T_{tot} and N_{ph}. T_{tot} is the total transmission of the system at the emission wavelength desired (λ = 520 nm), thus it can be calculated by multiplying all the transmissions at that wavelength of the components the light encounters when travelling from the sample to the camera chip. In the system under study this are the objective lens (T_{obj}, listed above), the dichroic mirror (T_{dic} = 0.90), the emission filter (T_{em} = 0.90), the tube lens (its transmission is unknown, so it has been assumed equal to 1), the filter in the relay (T_{Frel} = 0.95), the two doublet lenses in the relay ($T^2_{doub} = 0.81^2$) and the diffraction grating (T_{grat} = 0.87/3, since the light is split into three channels). The transmissions of the emitter support material (e.g. agarose or PDMS), coverslip glass, objective immersion medium and diffraction grating material have been ignored for simplicity. In addition, since each one of the used objectives has a different transmission, it has been decided to use the average among them as T_{obj} (thus T_{obj} = 0.82) to reduce the number of variables. This, multiplied by the other transmissions, gives a T_{tot} equal to 0.12. Regarding N_{ph}, to avoid incorrect estimations it has been decided to rescale eq. 4.13 by dividing it by $\sqrt{N_{ph}}$. The parameters q, S_{pix} and e_r, instead, have been set equal to, respectively, 0.9 e^-/photon, 16 µm/pix (i.e. those associated to the used camera) and 0.5 µm (i.e. as in case of a 1 µm bead). In fig. 4.28c eq. 4.13 has been plotted as a function of |M| and of the NA semi-aperture angle. As expected and clear from eq. 4.13, $SNR_{pix}/\sqrt{N_{ph}}$ grows with the NA and as the M decreases. However, it is also clear that, when M and NA are both reduced or increased simultaneously, the sign of the change in SNR_{pix} can vary as mentioned. If a decrease in NA is compensated or overcome by a reduction in M, the overall SNR_{pix} will not change or will increase, while the opposite will happen if the described compensation effect fails. For example, in the blue path in fig. 4.28c $SNR_{pix}/\sqrt{N_{ph}}$ can vary from 0.029,

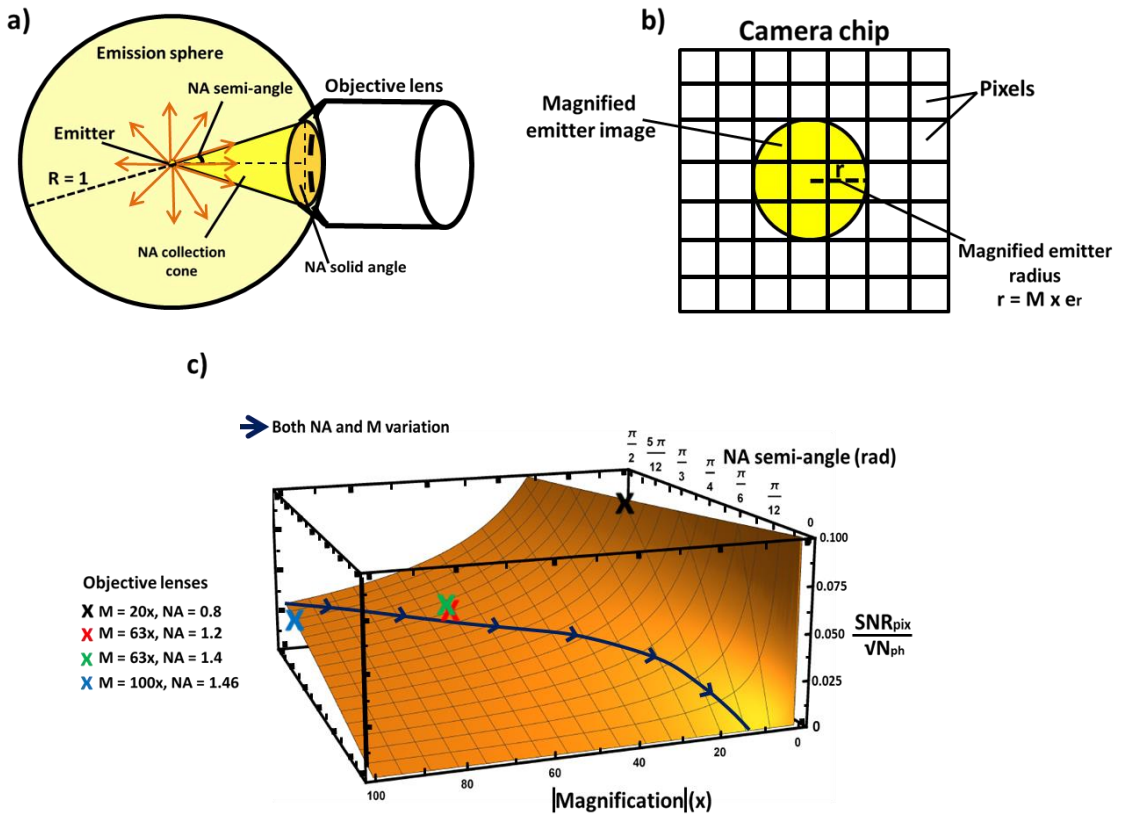

Figure 4.28 a) Schematic representation of the cone of light collected by an objective lens. The fraction of the emission sphere surface (centred on the emitter and with radius R = 1) intersected by the collection cone is equal to the solid angle through which light is collected and is a function of the NA semi-angle aperture. **b)** Scheme showing the magnified image of an emitter (with radius r equal to M times the emitter radius e_r, where M is the objective lens magnification) and the corresponding illuminated camera pixels. **c)** Curve simulated by using eq. 4.13, showing the $SNR_{pix}/\sqrt{N_{ph}}$ as a function of the NA semi-aperture angle and of the magnitude of the |M| of the objective lenses (T_{tot} = 0.12, q = 0.9 e^-/photon, S_{pix} = 16 µm/pix, e_r = 0.5 µm). The evidenced variation direction on the plot indicates a direction where both NA and M are changed (blue arrow) to produce a continuous reduction in $SNR_{pix}/\sqrt{N_{ph}}$.

at M = 100x and $\vartheta_{NA} = 10\pi/21$ rad (e.g. NA ≈ 1 with n_{im} = 1, eq. 1.6), to 0.014, at M = 20x and $\vartheta_{NA} = \pi/24$ rad (e.g. NA ≈ 0.13 with n_{im} = 1, eq. 1.6). At the ϑ_{NA} angles, Ms and T_{obj} associated to the objectives listed above (respectively, $5\pi/17$ rad and 20x, $5\pi/14$ rad and 63x, $10\pi/27$ rad and 63x and $5\pi/12$ rad and 100x, eq. 1.6) $SNR_{pix}/\sqrt{N_{ph}}$ (eq. 4.13) is equal to 0.101, 0.035, 0.037 and 0.024 respectively (fig. 4.28c), thus indicating a theoretical strong increase with the 20x dry objective. However, by considering the SNR_{pix} values calculated for the beads acquired for the four experimental conditions when in focus in the central plane (fig. 4.29), this behaviour is

not observed. Indeed, in both figures 4.29a and 4.29b with the 1 μm beads the SNR_{pix} values associated to the 20x objective are similar to those calculated for the 100x objective and around 2.3 – 2.6. This indicates that there are other major factors associated to the 20x objective and not simulated by eq. 4.13 that are able to reduce the signal level. The model in eq. 4.13, indeed, is largely simplified and can only provide a qualitative explanation on the behaviour of SNR_{pix} as a function of NA and M when imaging extended objects. The reduction in signal associated to the 20x objective lens has not allowed the direct observation of single 100 nm beads with it, but only of bead clusters. This has been verified by comparing the diameter of the observable objects to that expected by considering the diffraction limit with this objective, which should be

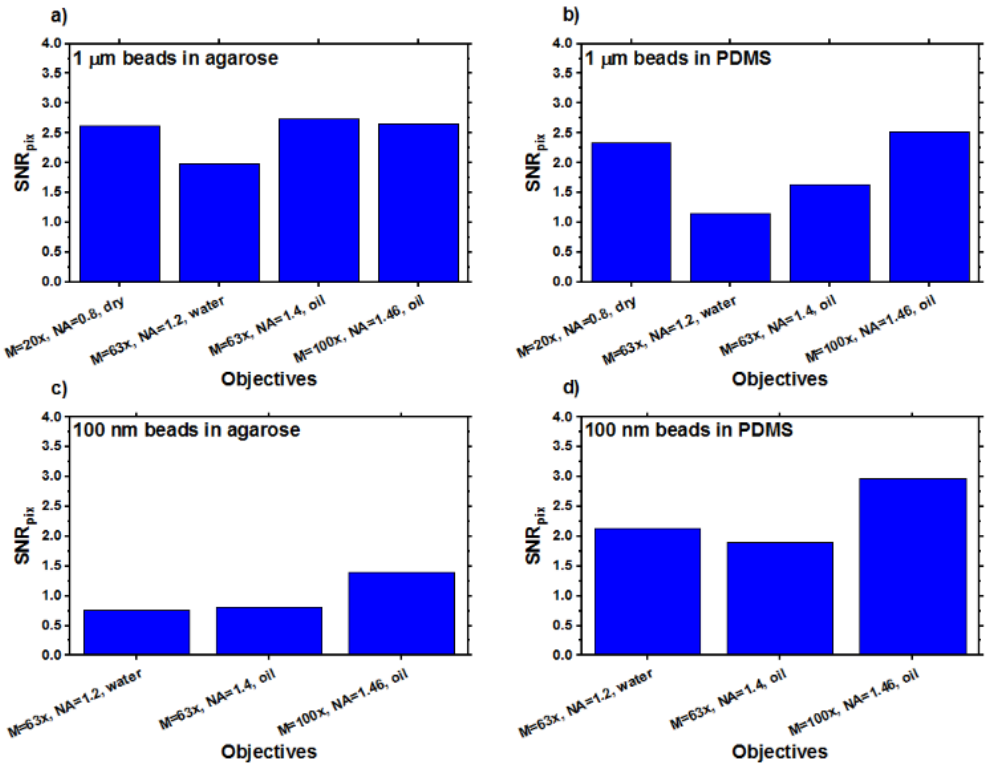

Figure 4.29 Evaluated SNR_{pix} for bead z-stacks acquired with different objective lenses. **a)** 1 μm beads in agarose (laser power before objective lenses = 21.4 μW at λ = 488 nm, em gain = 3,000, ET = 100 ms), **b)** 1 μm beads in PDMS (laser power before objective lenses = 3.56 μW at λ = 488 nm, em gain = 3,000, ET = 100 ms), **c)** 100 nm beads in agarose (laser power before objective lenses = 357 μW at λ = 488 nm, em gain = 3,000, ET = 100 ms) and **d)** 100 nm beads in PDMS (laser power before objective lenses = 105.6 μW at λ = 488 nm, em gain = 3,000, ET = 100 ms).

around 1 pix (eq. 1.8). In both cases (i.e. with the 100 nm beads in agarose and PDMS) the imaged objects resulted several pixels wider than that. Therefore, to avoid the inclusion of bead clusters in the analysis it has been decided to exclude the emitters observed with the 20x objectives and the 100 nm bead samples. The SNR_{pix} values calculated for the 100 nm beads acquired by using the other objectives are shown in fig. 4.29c and 4.29d, respectively for the beads in agarose and PDMS. These, on average, grow with the objective NA. Regarding the overall SNR and SBR values calculated for

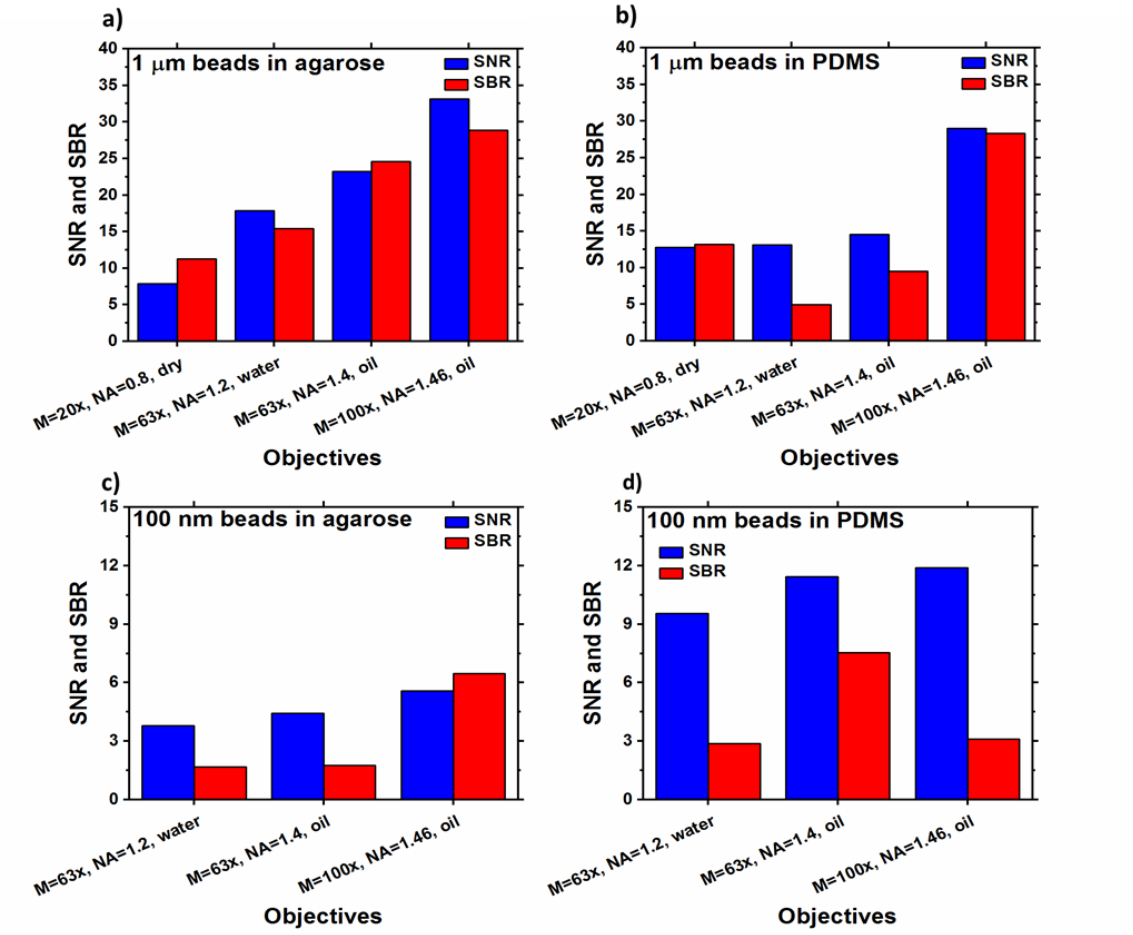

Figure 4.30 Evaluated SNR and SBR for bead z-stacks acquired with different objective lenses. **a)** 1 μm beads in agarose (laser power before objective lenses = 21.4 μW at λ = 488 nm, em gain = 3,000, ET = 100 ms), **b)** 1 μm beads in PDMS (laser power before objective lenses = 3.56 μW at λ = 488 nm, em gain = 3,000, ET = 100 ms), **c)** 100 nm beads in agarose (laser power before objective lenses = 357 μW at λ = 488 nm, em gain = 3,000, ET = 100 ms) and **d)** 100 nm beads in PDMS (laser power before objective lenses = 105.6 μW at λ = 488 nm, em gain = 3,000, ET = 100 ms).

the different experimental conditions, these are shown in fig. 4.30. As observable and expected, in general both SNR and SBR values tend to grow in all experimental conditions as the NA of the associated objective lens increases.

In order to show the impact of the used objective lenses on the PSFs, in fig. 4.31 the lateral cross sections profiles of the 1 μm beads in PDMS acquired with the different objectives and in the central plane are presented. Fig. 4.31a, 4.31b, 4.31c and 4.31d are associated to the 20x objective, fig. 4.31e, 4.31f, 4.31g and 4.31h to the 63x water immersion objective, fig. 4.31i, 4.31j, 4.31k and 4.31l to the 63x oil immersion objective and fig. 4.31m, 4.31n, 4.31o and 4.31p to the 100x objective. All cross section panels have been extracted from the central planes. In fig. 4.31b, 4.31f, 4.31j and 4.31n the beads are in focus (identified as in the previous sections), while fig. 4.31a, 4.31e, 4.31i and 4.31m show them 3 μm before the best focus and fig. 4.31c, 4.31g, 4.31k and 4.31o 3 μm after it. Fig. 4.31d, 4.31h, 4.31l and 4.31p show the lateral profiles tracked through the horizontal lines in the cross section panels. As expected, all the profiles associated the out of focus cross sections (red and blue curves) have smaller peaks and wider FWHMs than the corresponding profiles measured on the in focus beads (green curves). Regarding the differences among the PSFs imposed by the different objectives, these can be quantified by comparing the different lateral profiles and cross sections. Starting from the in focus profile peaks, these constantly grow as the NA increases from 1,600 ic (fig. 4.31d) to 4,250 ic (fig. 4.31p). At the same time, the FWHMs of the same profiles increase too from 3 pix to 7 pix, due to the increase in M. The same behaviour can be observed with the other experimental conditions. Another difference imposed by the objective lenses can be found by observing the out of focus lateral cross sections. Those acquired for the oil immersion objectives (fig.4.31i, 4.31k, 4.31m and 4.31o) present the ring-like profile before the best focal position (i.e. closer to the tube lens), while the opposite happens with those associated to the dry and water immersion objectives (fig.4.31a, 4.31c, 4.31e and 4.31g). As explained in previous chapter (sec. 3.4), this indicates the sign of the spherical aberration (SA) of the system [28, 29]. In particular, the SA is negative with the dry and water immersion objectives, while it is positive with the oil immersion ones.

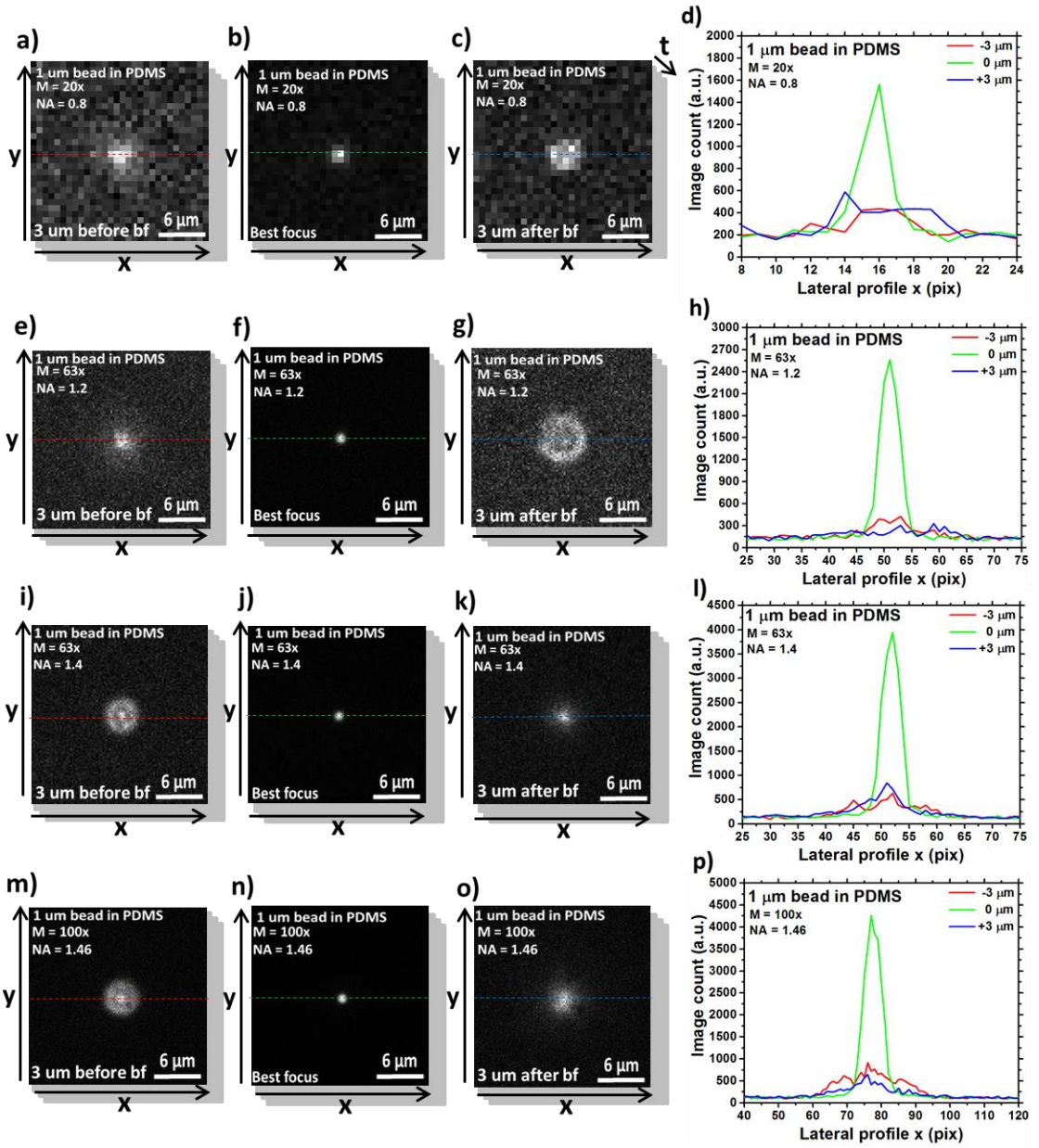

Figure 4.31 Lateral cross sections and profiles of 1 µm beads in PDMS, observed, in the 0^{th} plane, through objective lenses with M = 20x and NA = 0.8 (**a**, **b**, **c**, and **d**, dry objective lens), M = 63x and NA = 1.2 (**e**, **f**, **g**, and **h**, water immersion objective lens), M = 63x and NA = 1.4 (**i**, **j**, **k**, and **l**, oil immersion objective lens) and M = 100x and NA = 1.46 (**m**, **n**, **o**, and **p**, oil immersion objective lens). Panels **b**, **f**, **j** and **n** show the cross sections for the beads in focus (identified as the positions where the intensity is maximised), while panels **a**, **e**, **i** and **m** show the cross sections for the beads observed 3 µm before the focus and panels **c**, **g**, **k** and **o** show the cross sections for the beads observed 3 µm after the focus. The cross sections have been extracted from the first z-stacks of the acquired z-stack series, while the profiles in **d**, **h**, **l** and **p** are observed through the lines in the cross section panels, where they were maximised. These are averaged among the three corresponding cross sections from the first three z-stacks of

the z-stack series. Laser power before objective lenses = 3.56 μW at λ = 488 nm, em gain = 3,000, ET = 100 ms.

To evaluate the influence of the objective lenses on axial cross sections and profiles, some examples of them (extracted and calculated as in previous sections) are shown in fig. 4.32, together with the calculated sharpness curves. Fig. 4.33a and 4.33b are associated to the 1 μm bead in PDMS acquired with the 20x objective, while fig. 4.33c and 4.33d to the 1 μm bead in PDMS acquired with the 63x water immersion one. The axial profiles in fig. 4.32a and 4.32c present several differences. One of the most evident ones is the distance among the profile peaks associated to the different planes. On average, this is equal to 11.98 μm and to 1.94 μm, respectively for the profiles in fig. 4.32a and 4.32c. This is an expected increase and is due to the inverse relation between the PS and the M (eq. 2.24). Another difference, as already shown in fig. 4.31, is in the profile peak heights, which are higher for the profiles associated the bead acquired with the higher NA. This difference in NA has, in turn, raised the SNR of the bead in fig. 4.32d to 14.6, while that of the bead in fig. 4.32b is equal to 12.8. This is also visible on the axial profiles, since those in fig. 4.32a are clearly noisier than those in fig. 4.32c. Finally, another important divergence between the axial profiles in fig. 4.32a and 4.32c is given by their axial extensions, since the profiles for the bead acquired with the 20x objective are more elongated than those acquired with the 63x one. This can be estimated by considering their FWHMs, which are equal to 3.01 μm and to 1.83 μm, respectively for the central profiles in fig. 4.32a and 4.32c, and is due to the increase of the depth of field (DoF) with the reduction in NA (eq. 1.9). Regarding the sharpness curves, since they are built on the PSFs, their behaviour is similar to that of the corresponding axial profiles. However, it should be observed that, differently from the axial profiles, the peaks of the sharpness curves in fig. 4.32a are higher than those in fig. 4.32c. For example, for the central curve in fig. 4.32a the peak is equal to $1.10 \cdot 10^{-3}$ a.u., while for the same curve in fig. 4.32c to $5.15 \cdot 10^{-5}$ a.u., i.e. a smaller value. This depends on the fact that a smaller sharpness box has been used for the beads acquired with the 20x objective. Indeed, by reducing the sharpness box the relative weight of an emitter with respect to the background is increased, thus making it appear as sharper in comparison to when a wider sharpness box is used. The same happens to the sharpness baseline, which in fig. 4.32a is higher ($1.06 \cdot 10^{-3}$ a.u.) than in fig. 4.32c ($4.45 \cdot 10^{-5}$ a.u.).

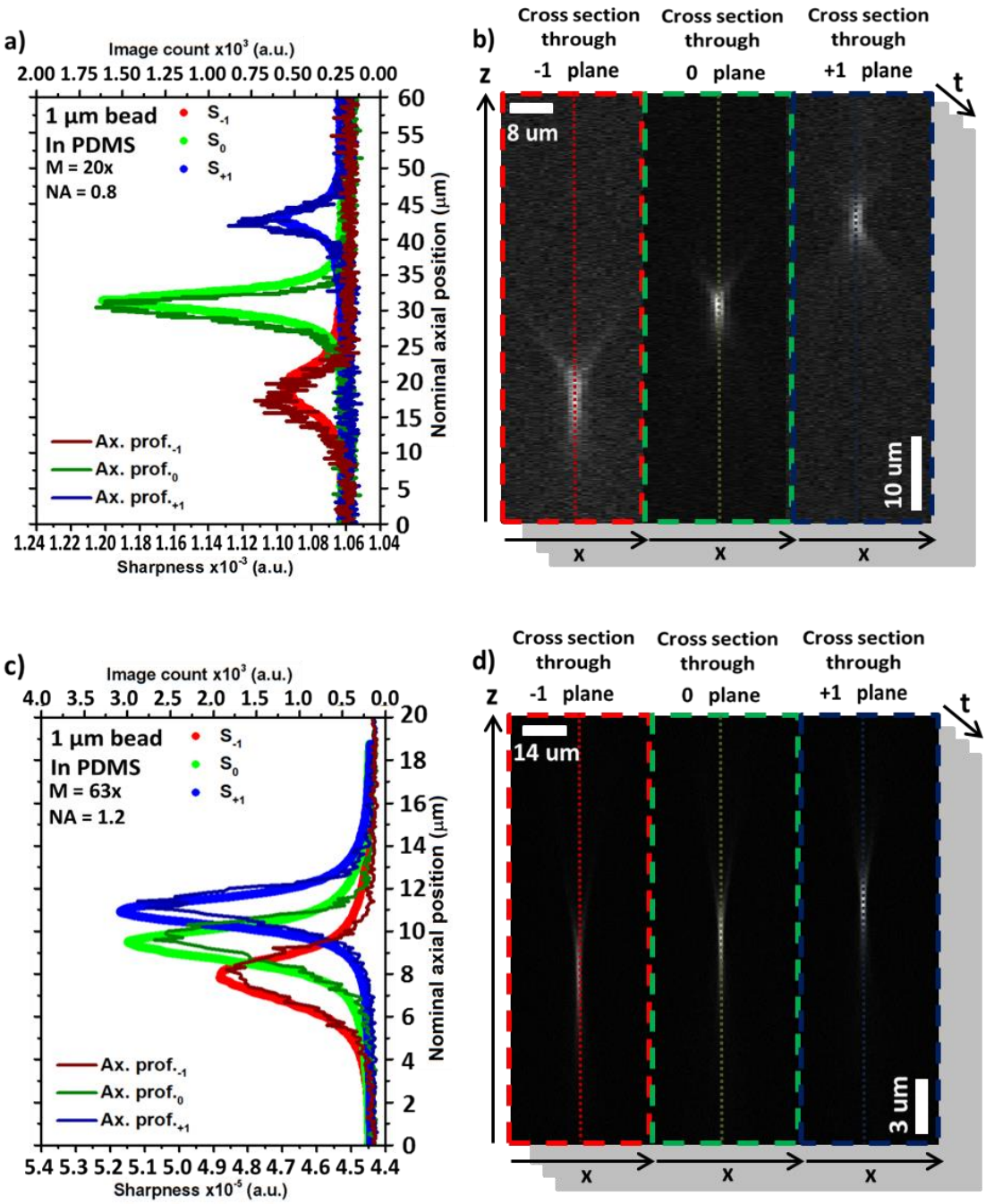

Figure 4.32 Sharpness curves with axial profiles (**a** and **c**) and corresponding axial cross sections (**b** and **d**) observed through the three used axial planes, for two 1 µm beads in PDMS acquired with objective lenses with M = 20x and NA = 0.8 (**a** and **b**, dry objective lens) and with M = 63x and NA = 1.2 (**c** and **d**, water immersion objective lens). The cross sections have been obtained from the first z-stacks of the acquired z-stack series. The axial profiles have been observed through the three vertical lines in **b** and **d**, where they were maximised and are averaged among the three corresponding cross sections from the first three z-stacks of the z-stack series. Laser power before objective lenses = 3.56 µW at λ = 488 nm, em gain = 3,000, ET = 100 ms.

In fig. 4.33, all the relative normalised sharpness curves calculated for the 1 µm beads in PDMS and acquired with all the used objectives are presented. The curves in fig. 4.33a, 4.33b, 4.33c and 4.33d are, respectively, associated to the beads imaged with the 20x, the 63x water immersion, the 63x and the 100x oil immersion objective lenses. As anticipated (fig. 4.32) and widely expected, it is possible to see the increase in PS with the reduction in M (eq. 2.24). Another aspect to notice is the fact that the curves in fig. 4.33a and 4.33b present a S_{+1} peak higher than the S_{-1} one (and in fig. 4.33b the S_{+1} peak is also higher than the S_0 peak), while those in fig. 4.33c and 4.33d show the usual behaviour where the S_0 peak is the highest one and the S_{-1} peak is higher than that of the S_{+1} curve (e.g. as in fig. 4.8 and 4.21). This behaviour is common among all the studied experimental conditions and is linked to the levels of aberration correction imposed by

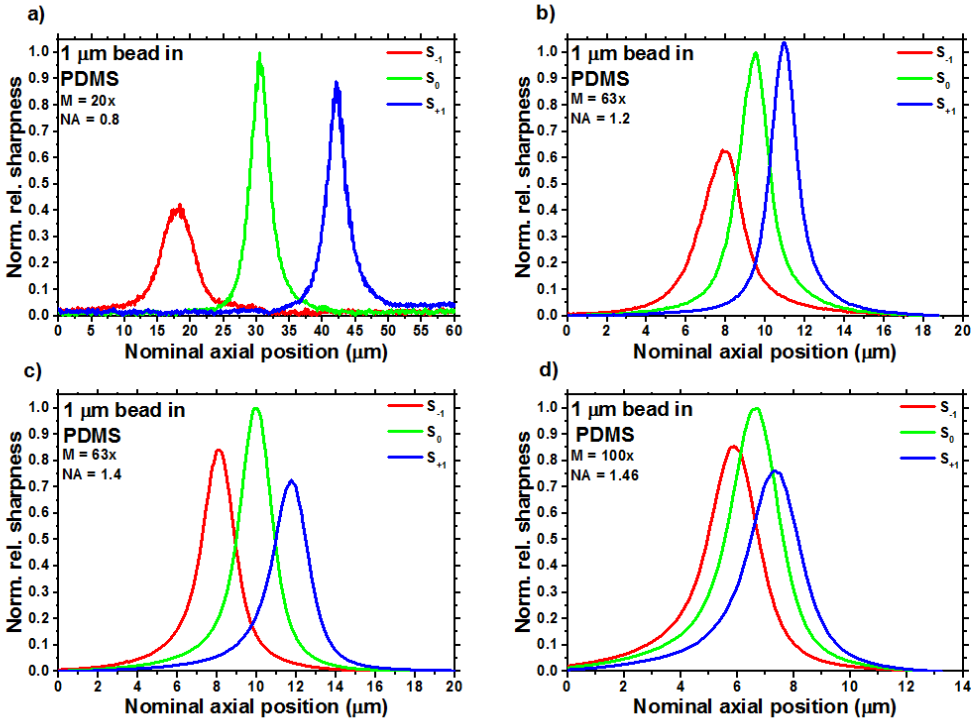

Figure 4.33 Calculated sharpness curves for 1 µm beads in PDMS observed with objective lenses with **a)** M = 20x and NA = 0.8 (dry objective lens), **b)** M = 63x and NA = 1.2 (water immersion objective lens), **c)** M = 63x and NA = 1.4 (oil immersion objective lens) and **d)** M = 20x and NA = 0.8 (oil immersion objective lens). Laser power before objective lenses = 3.56 µW at λ = 488 nm, em gain = 3,000, ET = 100 ms.

the different objective lenses used. However, this aspect has not been studied in detail.

In fig. 4.34 all the PS measured in the different experimental conditions and with the different used objectives have been plotted against the nominal objective magnification, together with the theoretical curve (eq. 2.24):

$$PS = \frac{{f_{eff}}^2}{f_g}\frac{1}{M^2}, \qquad \text{(eq. 2.24)}$$

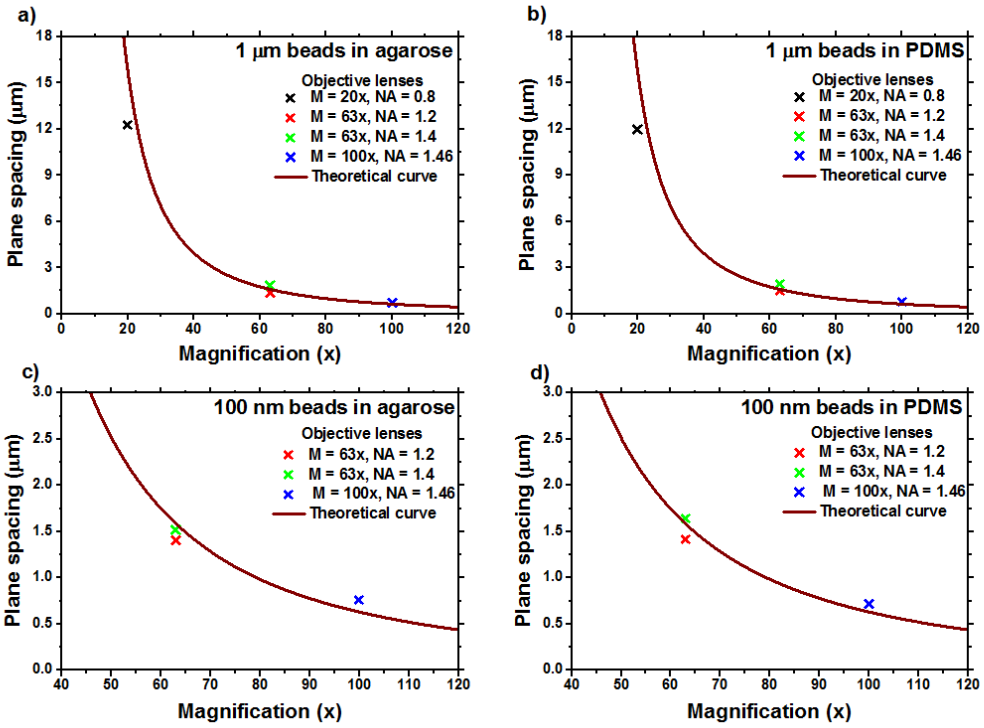

Figure 4.34 Evaluated average PS for beads observed through different objectives lenses. The theoretical curve for the PS as a function of the used magnification (eq. 2.24) has been shown for comparison. **a)** 1 µm beads in agarose (laser power before objective lenses = 21.4 µW at λ = 488 nm, em gain = 3,000, ET = 100 ms), **b)** 1 µm beads in PDMS (laser power before objective lenses = 3.56 µW at λ = 488 nm, em gain = 3,000, ET = 100 ms), **c)** 100 nm beads in agarose (laser power before objective lenses = 357 µW at λ = 488 nm, em gain = 3,000, ET = 100 ms) and **d)** 100 nm beads in PDMS (laser power before objective lenses = 105.6 µW at λ = 488 nm, em gain = 3,000, ET = 100 ms).

where f_{eff} is the effective focal length of the relay (77.87 mm, eq. 2.16) and f_g is the diffraction grating focal length (±962.50 mm, eq. 2.15). As observable in all plots of fig.

4.34, in general there is agreement between the measured and the theoretical PS curve as a function of the magnification. However, the measured PSs show some differences with respect to the theoretical expected values. In particular, the 20x and the 63x water immersion objectives show PSs lower than expected, while those associated to the 100x one are slightly higher. In general, this variations are probably caused by some issues as

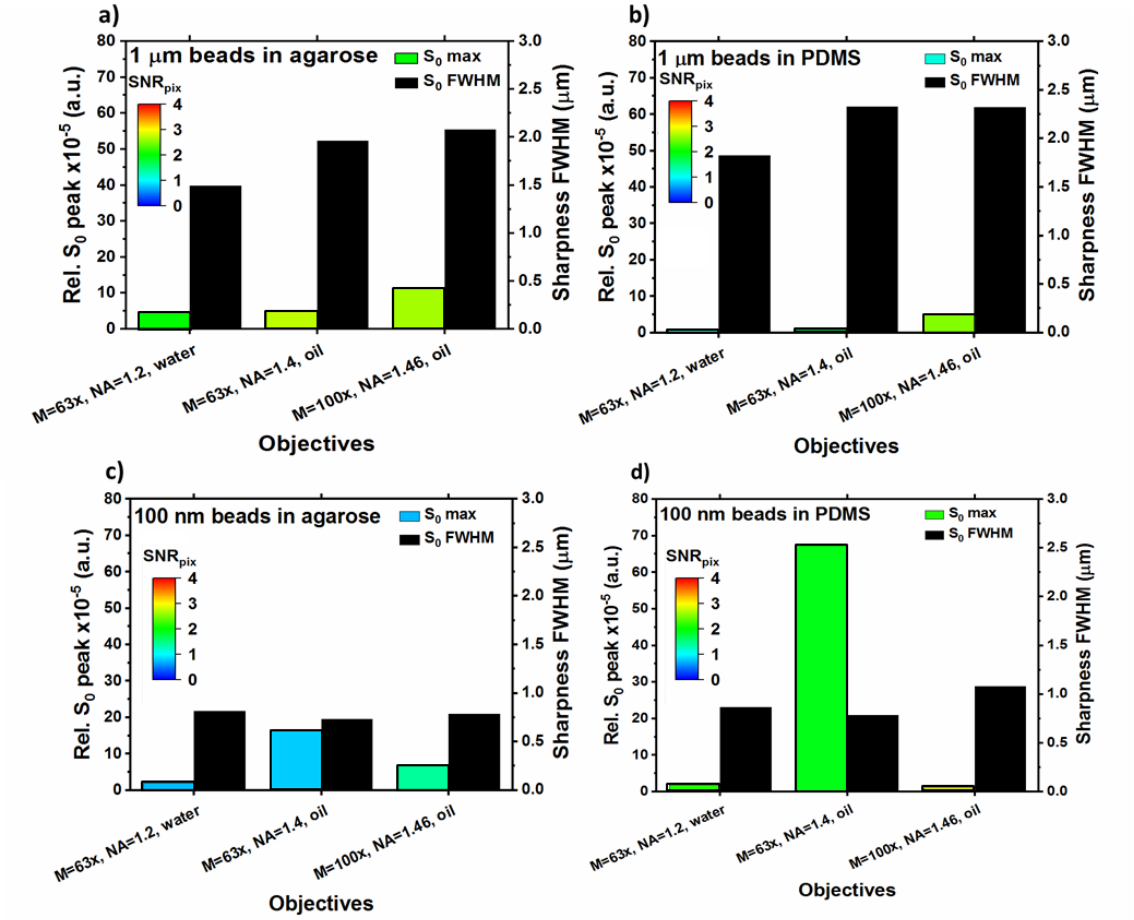

Figure 4.35 Evaluated relative sharpness curve peak heights (left y axis, circles) and FWHMs (right y axis, squares) of the sharpness curves in the 0th planes, for bead z-stacks acquired with different objective lenses. The SNR_{pix} (evaluated in the 0th plane) has been colour encoded in the sharpness peak curves. **a)** 1 μm beads in agarose (laser power before objective lenses = 21.4 μW at λ = 488 nm, em gain = 3,000, ET = 100 ms), **b)** 1 μm beads in PDMS (laser power before objective lenses = 3.56 μW at λ = 488 nm, em gain = 3,000, ET = 100 ms), **c)** 100 nm beads in agarose (laser power before objective lenses = 357 μW at λ = 488 nm, em gain = 3,000, ET = 100 ms) and **d)** 100 nm beads in PDMS (laser power before objective lenses = 105.6 μW at λ = 488 nm, em gain = 3,000, ET = 100 ms).

the relay not providing a M exactly equal to 1x, the camera and/or grating not being perfectly in the correct positions, etc. In addition, it should also be considered that the PS varies with the axial position of the emitter within the sample, as shown in fig. 3.10 and 3.14, due to the spherical aberration.

As in previous sections, also in this case the relative central sharpness peaks and FWHMs have been studied for the beads acquired in all the four experimental conditions. In fig. 4.35, these have been plotted against the used objective lenses. The SNR_{pix} has been colour encoded in the relative sharpness peak data, in order to take into account the simultaneous variation of the M and NA. The data calculated for the 20x objective will be shown separately (fig. 4.39), since a different sharpness box has been used in that case. Starting from the FWHM values, these, on average, tend to increase moving from the 63x water immersion objective to the 100x one. In general, due to the increase in DOF with the reduction in NA (eq. 1.9), the opposite was expected as seen in fig. 4.32 with 1 µm beads in PDMS imaged with the 0.8 NA and 1.2 NA objectives. It is possible that also this behaviour is dictated by the different levels of aberration correction introduced by the objective lenses. Indeed, as seen in fig. 3.18, different levels of spherical aberration vary the FWHMs of the sharpness curves, which change

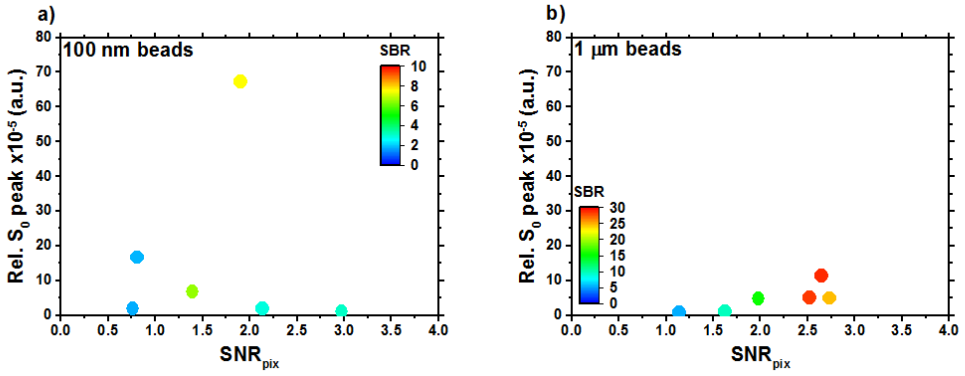

Figure 4.36 Relative sharpness peak heights of the sharpness curves in the 0^{th} planes plotted against the corresponding SNR_{pix} and SBR values, for all bead z-stacks acquired in agarose and PDMS and with the different objective lenses. The SBR has been colour encoded in the sharpness peak curves. The data in **a** are associated to the 100 nm beads, while those in **b** to the 1 µm ones. Laser power before objective lenses = 357 µW, 106.5 µW, 21.4 µW and 3.56 µW. λ = 488 nm. em gain = 3,000. ET = 100 ms.

accordingly. However, this aspect has not been studied in depth for the multi-objective lens study. Regarding the sharpness peaks, these can be interpreted in term of the corresponding signal levels, as in previous sections (fig. 4.10 and 4.24). In fig. 4.36 the

relative sharpness peak values in fig. 4.35 have been plotted against the associated SNR_{pix} and SBR values. As observable, also in this case the sharpness peak is driven by the level of the signal for both the 100 nm (fig. 4.36a) and the 1 μm (fig. 4.36b) beads. The values calculated for the 1 μm beads start to increase at a SNR_{pix} around 1.7 and SBR of 15.4, while those for the 100 nm beads show a peak at a SNR_{pix} of 1.9 and SBR around 7.5.

Moving to the performances of the sharpness algorithm as a function of the used objective lens, in fig. 4.37 the axial ranges and precisions calculated for all the beads

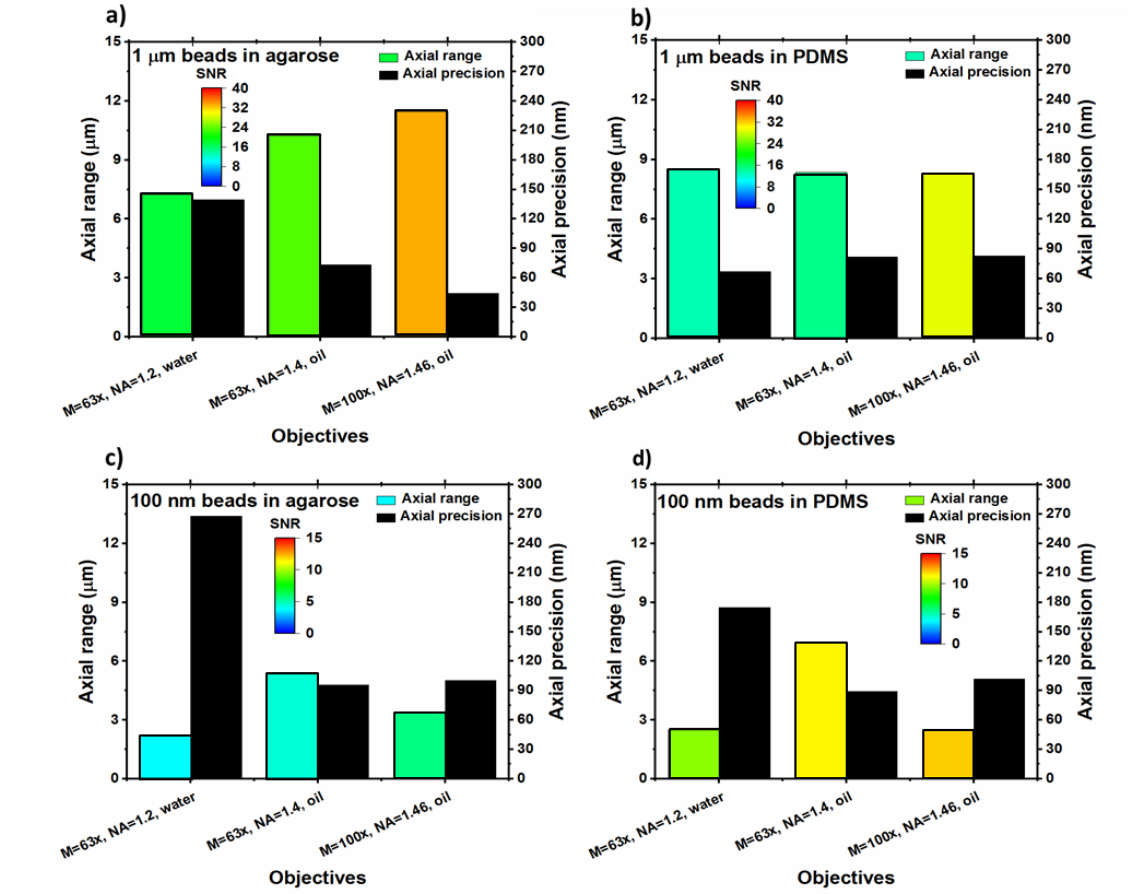

Figure 4.37 Evaluated axial ranges (left y axis, circles) and precisions (right y axis, squares) for bead z-stacks acquired with different objective lenses. The SNR (evaluated in the 0^{th} plane) has been colour encoded in the axial range curves. **a)** 1 μm beads in agarose (laser power before objective lenses = 21.4 μW at λ = 488 nm, em gain = 3,000, ET = 100 ms), **b)** 1 μm beads in PDMS (laser power before objective lenses = 3.56 μW at λ = 488 nm, em gain = 3,000, ET = 100 ms), **c)** 100 nm beads in agarose (laser power before objective lenses = 357 μW at λ = 488 nm, em gain = 3,000, ET = 100 ms) and **d)** 100 nm beads in PDMS (laser power before objective lenses = 105.6 μW at λ = 488 nm, em gain = 3,000, ET = 100 ms).

acquired in the four experimental conditions are shown. For the same reason explained above, the data associated to the 20x objective have been exclude from this plot and will be shown separately (fig. 4.39). The SNR has been colour encoded in the axial range data. As done previously (fig. 4.13, 4.16 and 4.26), these data can be studied with respect to the corresponding signal levels. This is shown in fig. 4.38, where the axial range and precision results in fig. 4.37 have been grouped and plotted against the associated SNR and SBR values. The axial ranges calculated with M of 63x (fig. 4.38a) and 100x (fig. 4.38b) have been kept separated, since different Ms change the PS (eq. 2.24) and this has an effect on the axial range as shown in fig. 4.13. As expected and seen in previous cases, in both fig. 4.38a 4.38b the axial range grows with the SNR and SBR. It is also clear that this growth is faster with the 63x objectives, due to the increased PS and axial extension of the sharpness curves (fig. 4.8 and 4.34). This has

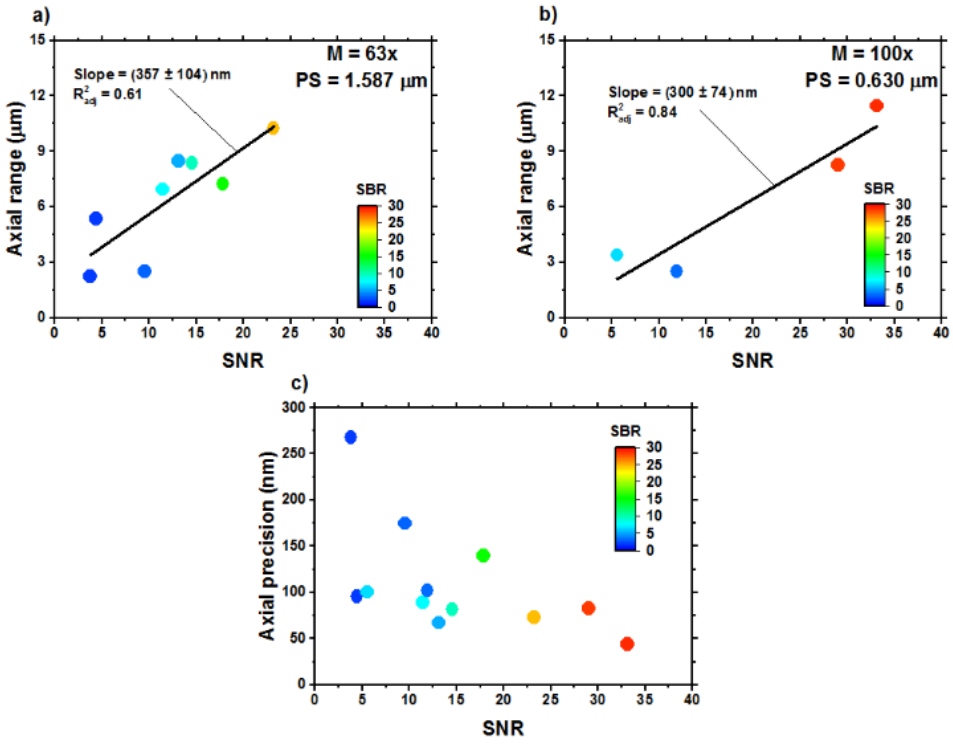

Figure 4.38 Evaluated axial ranges calculated for the data acquired with M of 63x (**a**) and 100x (**b**) and axial precisions (**c**) associated to the multi-objective lens study and plotted against the corresponding SNR and SBR values. The straight line in **a** and **b** are a linear fit through the axial range values, whose slope (with its standard deviation) and goodness (the adjusted R^2 value) are shown. Laser power before objective lenses = 357 µW, 106.5 µW, 21.4 µW and 3.56 µW. λ = 488 nm. em gain = 3,000. ET = 100 ms.

been quantified by using linear fits that have produced slopes of (300 ± 74) nm and (357 ± 104) nm, respectively with PS of 0.630 μm (M = 100x, fig. 4.38b) and 1.587 μm (M = 63x, fig. 4.38a). The slope associated to PS = 630 nm is higher than those calculated in previous sections with the same PS (fig. 4.13, 4.16 and 4.26). This is due to the fact that only four points have been used to calculate the value in fig. 4.38b that, consequently, is probably less accurate. Concerning the axial precision results (fig. 4.38c), also these data present the same behaviour already observed (fig. 4.13, 4.16 and 4.26), showing a general worsening as the signal is reduced. In particular, the axial precision moves from around 44 nm to 268 nm as the SNR reduces from 33 to 3.8 and the SBR from 28.8 to 1.7.

Finally, in fig. 4.39 the data calculated for the 20x dry objective are presented for the 1 μm beads in agarose and PDMS. These data are presented separately due to the

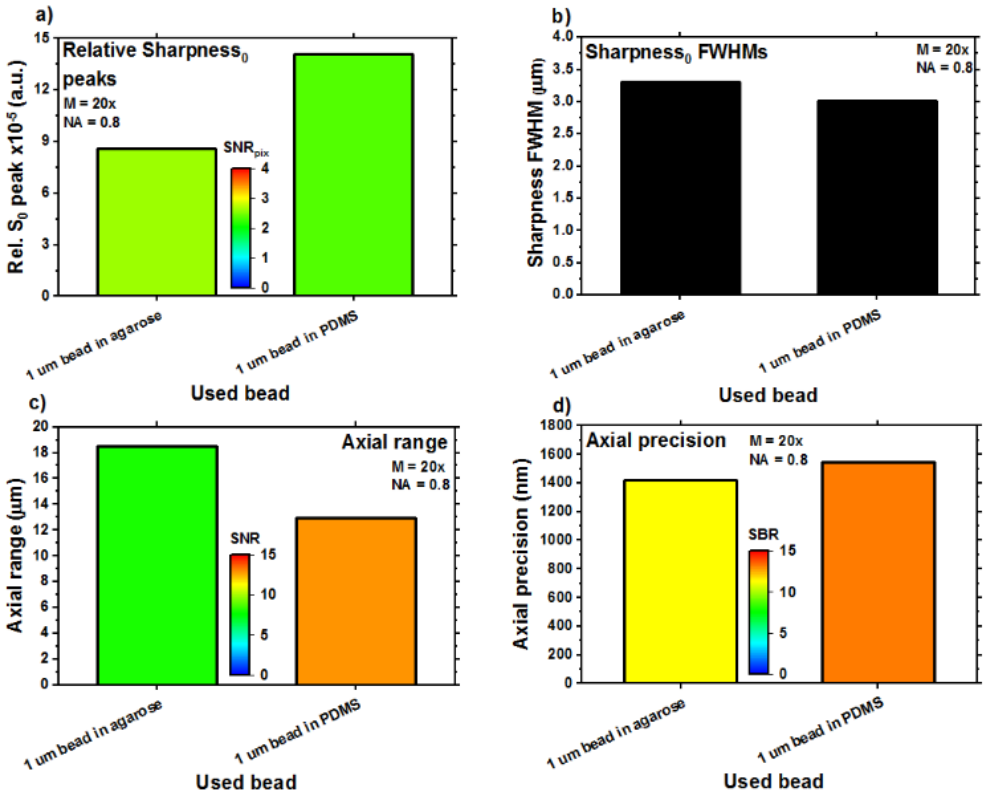

Figure 4.39 Evaluated central relative sharpness curve peak heights (**a**) and FWHMs (**b**) of 1 μm beads in agarose (laser power before objective lenses = 21.4 μW at λ = 488 nm, em gain = 3,000, ET = 100 ms) and PDMS (laser power before objective lenses = 3.56 μW at λ = 488 nm, em gain = 3,000, ET = 100 ms) acquired with an objective lens with M = 20x and NA = 0.8 (dry objective lens). In **c** and **d** the corresponding axial ranges and precisions are shown. The SNR_{pix} has been colour encoded in **a**, the SNR in **c** and the SBR in **d**.

fact their sharpness curves were calculated by using a smaller sharpness box. In fig. 4.39a the central relative sharpness peaks have been colour encoded by the SNR_{pix}, while the axial range (fig. 4.39c) and precision (fig. 4.39d) results by, respectively, the SNR and SBR values. The S_0 peak associated to the bead in PDMS is higher than that for the bead in agarose due to the higher SNR and SBR levels. Regarding the FWHMs (fig. 4.39b), these values are clearly wider than those calculated with the other objectives (fig. 4.35) and on average are equal to (3.2 ± 0.2) μm. This, as shown in fig. 4.32, is mainly due to the massively extended DOF achieved with the reduced NA (eq. 1.11).

Fig. 4.39c presents the axial ranges achieved with the 20x objectives. In this case it has been necessary to raise the required accuracy from 100 nm to 1,000 nm, to avoid the axial ranges to be equal to 0 μm. This behaviour was not expected, since the SNR, SBR and SNR_{pix} values associated to the beads in fig. 4.39 are not considerably lower than those shown in fig. 4.37. This indicates that some other non-investigated factors can strongly influence the axial range. The average axial range in fig. 4.39c is equal to (15.7 ± 2.8) μm. This value is larger than those seen in fig. 4.37, but it cannot be attributed to the extended PS, since it derives from the worsened accuracy. As a consequence of the increase in accuracy threshold, also the axial precisions in fig. 4.39d have strongly worsened in comparison to those in fig. 4.37 and have reached an average value of (1,481 ± 64) nm.

In conclusion, the aim of the multi-objective lens study was to evaluate the impact of the microscope objectives on the performances of the Dalgarno [38] multiplane system. As widely expected, the simultaneous reduction in M and NA has had the effect of extending the PS (sec. 2.4.3, fig. 4.34) and the DOF (eq. 1.9, fig. 4.32), as clearly visible on the sharpness curves (fig. 4.33). From the point of view of the performance, axial range and precision improve has already observed in previous sections as the signal grows (fig. 4.38). The former, in particular, has shown a faster increase with respect to the signal level at larger PS, thus confirming the result already observed in fig. 4.13. This improvement in axial range, however, has not been observed by using the 20x objective lens, for which it has been required to lower the set accuracy to 1 μm. Nonetheless, with this objective it has been possible to substantially expand the axial range to around 15.7 μm, even if at the expenses of the axial precision that has worsened to around 1,481 nm. This could be convenient for applications where the axial range is more important than the precision and lower accuracies are acceptable.

4.7 Global behaviour of the performances with respect to the signal level and the plane spacing

The studies presented in this chapter have shown how the performances of the diffraction multifocal system under study vary with different ETs (sec. 4.4), ND filters (sec. 4.4.3), BWs (sec. 4.5) and objective lenses (sec. 4.6). These experiments, however, are not disconnected among them. As shown in fig. 4.13, 4.16, 4.26 and 4.39, indeed, axial range and precision can be studied in terms of signal level, presenting similar behaviours as the latter varies. This indicates that these results can be combined to observe the global variation of the performances with respect to the signal. This is presented in fig. 4.40, against the corresponding SNR and SBR values. In fig. 4.40a all axial ranges calculated by using a PS of 630 nm have been plotted, while all axial precisions, apart from those obtained by using the 20x objective lens (fig. 4.39), are shown in fig. 4.40b. A linear fit to the data in fig. 4.40a provides a slope of (277 ± 16) nm per SNR unit, which is comparable to those already observed in previous sections (fig. 4.13a, 4.16a, 4.16c, 4.26a and 4.38b). Similarly, by fitting the data in fig.

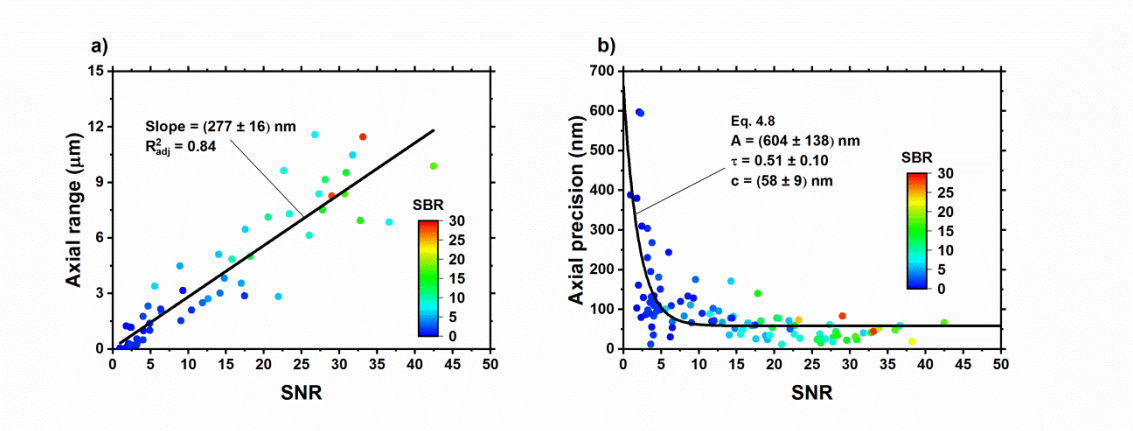

Figure 4.40 Evaluated axial ranges (**a**) and precisions (**b**) associated to all data (apart from those for the 20x objective) presented in this chapter and plotted against the corresponding SNR and SBR values. In **a** the axial range data are those acquired with PS = 630 nm and the straight line is a linear fit, whose slope (with its standard deviation) and goodness (the R_{adj}^2 value) are shown. The fit in **b** has been achieved by using eq. 4.8 and the corresponding extrapolated values are shown. PS = 630 nm. PS = 80 nm, 320 nm and 630 nm. Laser power at sample = 42.56 µW, 2.07 µW, 8.56 mW and 0.76 mW. Laser power before objective lenses = 357 µW, 106.5 µW, 3.56 µW. λ = 488 nm. em gain = 2,000, 3,000. ET = 38 ms, 70 ms, 100 ms, 130 ms, 160 ms. λ = 488 nm. em gain = 2,000, 3,000.

4.40b with eq. 4.8, the parameters obtained are in agreement with those achieved from the fit in fig. 4.16d and are as follow: A = (604 ± 138) nm, τ = 0.51 ± 0.10 per SNR unit and c = (58 ± 9) nm. Therefore, it can be concluded that the global behaviour shown in fig. 4.40 is not biased by the data of one of the studies that composes it, since these are all in agreement. However, it is also clear that there is a certain degree of scatter in the data around the fits, meaning that the studied system is susceptible to many other factors not considered (e.g. non-perfect homogeneity of the matrix materials and of the bead distributions) and these results can only be a general guide.

By grouping the different data shown in previous sections (sec. 4.4 and 4.6) and in fig. 4.13 and 4.38 the global impact of the PS on the speed at which the axial range grows with the signal can also be visualised. In fig. 4.41 the slopes of the fits in fig. 4.13a (for the PS of 80 nm and 320 nm), 4.38a and 4.40a have been plotted against the corresponding nominal PS. As noticeable, these data increase linearly in the observed PS interval. A linear fit to them presents an R_{adj}^2 around 0.94, a slope (m_{PS}) of 0.12 ± 0.02 and an intercept (q_{PS}) of (174 ± 16) nm per SNR unit when PS = 0 µm. This indicates that at very small PS values (near 0 µm) the axial range growth reduces to (174 ± 16) nm per SNR unit and that the speed at which the axial range increases with the SNR grows, in turn, by around 12 nm per SNR unit every time the PS is enlarged by

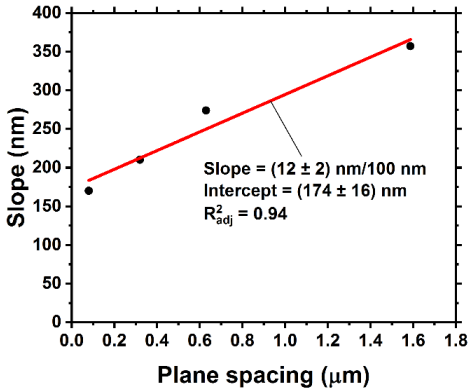

Figure 4.41 Slopes of the linear fits to the axial range data in fig. 4.13a, 4.38a and 4.40a plotted against the corresponding nominal PS. The straight line is a linear fit, whose slope (with its standard deviation) and goodness (the R_{adj}^2 value) are shown. PS = 630 nm. PS = 80 nm, 320 nm and 630 nm. Laser power at sample = 42.56 µW, 2.07 µW, 8.56 mW and 0.76 mW. Laser power before objective lenses = 357 µW, 106.5 µW, 3.56 µW. λ = 488 nm. em gain = 2,000, 3,000. ET = 38 ms, 70 ms, 100 ms, 130 ms, 160 ms. λ = 488 nm. em gain = 2,000, 3,000.

100 nm. This aspect, as already explained in sec. 4.4.2, is important, since it indicates the possibility to extend the axial range without increasing parameters as laser power and/or ET, which can cause problems in terms of photobleaching rate, phototoxicity and temporal resolution. Obviously, this does not mean the PS can be enlarged without limit to increase the axial range. Indeed, the PS should always allow the PSF to be observable through more than one plane simultaneously, otherwise the multiplane ability of the system would be lost.

The increase in axial range (AR) with the SNR and the PS can be synthesised into a single equation that summarises the behaviours visible in fig. 4.40a and 4.41 and allows to quickly estimate the AR (as for the AP with eq. 4.8), given the parameters of the multiplane system are known. Indeed, by exploiting the equation of a straight line [45], the AR can be expressed as (eq. 4.14):

$$\mathrm{AR}(\mathrm{PS}, \mathrm{SNR}) = (\mathrm{m_{PS}}\,\mathrm{PS} + \mathrm{q_{PS}})\,(\mathrm{SNR} - \mathrm{SNR_0}), \qquad \text{(eq. 4.14)}$$

where m_{PS} indicates the speed at which the axial range growth per SNR unit increases with the PS, q_{PS} the speed at which the axial range grows with the SNR in the limit of very small PS values and SNR_0 the SNR threshold at which the AR is reduced to 0 µm.

The results presented in fig. 4.40 and 4.41 and the SNR_0 threshold are valid for the studied multifocal setup and algorithm. However, they also provide a general reference to estimate the performances of similar multiplane systems with respect to the signal level when an accuracy within 100 nm is required.

4.8 Summary and considerations

This chapter has been dedicated to the study of the performances of the Dalgarno multiplane system [38] in terms of achievable axial range and precision as a function of the signal levels. The latter has been varied in a controlled manner by modifying the system ET and BW and by using different ND filters, objective lenses and four experimental conditions (100 nm and 1 µm beads in agarose and PDMS).

In general, SNR and SBR have shown an impact on the shape of the sharpness curves, whose peaks tend to increase with the signal (fig. 4.10a, 4.10c, 4.24 and 4.36). The curve FWHMs, instead (fig. 4.10b and 4.10d), do not directly vary as SNR and SBR are modified. This behaviour was expected, since the spherical aberration in the system was not able to strongly distort the PSFs as in fig. 3.5, 3.6 and 3.18. However,

the effect of different BW (eq. 2.3) and NA (eq. 1.9) is clear on them (fig. 4.23, 4.33, 4.36 and 4.39), which increase as the BW is raised and the NA is reduced.

In terms of performance, as expected raising the levels of SNR and SBR is beneficial for axial range and precision (fig. 4.13, 4.16, 4.26 and 4.38), which improve. In particular, in all studies the axial range shows linear increases with the signal, while the axial precision presents exponential behaviours (eq. 4.8). This, as explained in sec. 4.7, is due to the fact that these results are not strictly linked to the conducted test and, hence, to the multifocal system and axial localisation algorithm used and can be used as a guidance for other similar multiplane systems. This permits to combine all studies together to find the global behaviour of the performance with respect to the signal, providing a characteristic decay constant τ of around 0.51 per SNR unit (fig. 4.39b). By pushing down the photon flux with the ND filters (sec. 4.4.3), a SNR_0 threshold of around 1.23 has been found (fig. 4.16a), below which the axial range collapses to 0 µm. This aspect, however, can be improved by worsening the required accuracy (fig. 4.39). Regarding the speed at which the axial range grows with the signal, this increases with the PS (fig. 4.13a, 4.38a, 4.38b and 4.41), since the latter varies the axial extension of the sharpness curves (fig. 4.8). However, this advantage is progressively lost as the signal level decreases (fig. 4.13a) and is valid within a limited PS range to avoid the loss of the multifocal properties.

The studies presented in this chapter have also allowed to generate two equations that can permit to rapidly evaluate the expected axial range and precision of the multiplane system investigated, given parameters as A, τ and c for the AP (eq. 4.8) and m_{PS}, q_{PS} and SNR_0 for the AR (eq. 4.14) are known or have been estimated.

Next chapter will be dedicated to a possible application of multiplane microscopy. A flow of fluid around a cell will be three-dimensionally reconstructed by tracking some beads flowing into it. This can, in turn, allow to calculate velocity and shear stress maps around the cell and understand the forces this interacts with in such contests.

4.9 References

[1] C. J. R. Sheppard, M. Gu and M. Roy, “Signal-to-noise ratio in confocal microscope systems,” Journal of Microscopy - Oxford, vol. 168, no. 3, pp. 209-218, 1992.

[2] J. C. Waters, "Accuracy and precision in quantitative fluorescence microscopy," Journal of Cell Biology, vol. 185, no. 7, pp. 1135-1148, 2009.

[3] J. R. Janesick, scientific charge-coupled devices, SPIE Press, 2001.

[4] F. Long, S. Zeng and Z. L. Huang, "Localization-based super-resolution microscopy with an sCMOS camera Part II: Experimental methodology for comparing sCMOS with EMCCD cameras," Optics Express, vol. 20, no. 16, pp. 17741-17759, 2012.

[5] H. Zimmermann, "Active-pixel sensors," in Integrated silicon optoelectronics, 2nd ed., Springer, 2010, pp. 104-114.

[6] J. R. Janesick, in Scientific charge-coupled devices, SPIE Press, 2001, pp. 22-25.

[7] S. A. Taylor, "CCD and CMOS imaging array technologies - Technology review," Xerox Limited, 1998.

[8] QImaging, "Electron-Multiplying (EM) gain," QImaging, 2013.

[9] M. Hirsch, R. J. Wareham, M. L. Martin-Fernandez, M. Hobson and D. J. Rolfe, "A stochastic model for electron multiplication charge-coupled devices - From theory to practice," Plos One, vol. 8, no. 1, p. e53671, 2013.

[10] D. Dussault and P. Hoess, "Noise performance comparison of ICCD with CCD and EMCCD cameras," Infrared Systems and Photelectronic Technology, vol. 5563, pp. 195-204, 2004.

[11] Photometrics, "Keep the noise down! Low noise: An integral part of high-performance," Photometrics, 2010.

[12] N. B. Vicente, J. E. D. Zamboni, J. F. Adur, E. V. Paravani and V. H. Casco, "Photobleaching correction in fluorescence," Journal of Physics: Conference Series, vol. 90, p. 012068, 2007.

[13] M. L. Martin-Fernandez and D. T. Clarke, "single molecule fluorescence detection and tracking in mammalian cells: The state-of-the-art and future perspectives," International Journal of Molecular Sciences, vol. 13, no. 11, p. 14742–14765, 2012.

[14] P. P. Mondal, "Temporal resolution in fluorescence imaging," Frontiers in Molecular Biosciences, vol. 1, no. 11, 2014.

[15] M. Monici, "Cell and tissue autofluorescence research and diagnostic applications," Biotechnology Annual Review, vol. 11, pp. 227-256, 2005.

[16] D. Baddeley, D. Crossman, S. Rossberger, J. E. Cheyne, J. M. Montgomery, I. D. Jayasinghe, C. Cremer, M. B. Cannell and C. Soeller, "4D super-resolution microscopy with conventional fluorophores and single wavelength excitation in optically thick cells and tissues," Plos One, vol. 6, no. 5, p. e20645, 2011.

[17] D. R. Sandison and W. W. Webb, "background rejection and signal-to-noise optimization in confocal and alternative fluorescence microscopes," Applied Optics, vol. 33, no. 4, pp. 603-615, 1994.

[18] M. Monici, "Cell and tissue autofluorescence research and diagnostic applications," Biotechnology Annual Review, vol. 11, pp. 227-256, 2005.

[19] J. G. White, W. B. Amos and M. Fordham, "An Evaluation of Confocal Versus Conventional Imaging," Journal of Cell Biology, vol. 105, no. 1, pp. 41-48, 1987.

[20] T. W. Chen, B. J. Lin, E. Brunner and D. Schild, "In situ background estimation in quantitative fluorescence imaging," Biophysical Journal, vol. 90, no. 7, p. 2534–2547, 2006.

[21] A. S. Davis, A. Richter, S. Becker, J. E. Moyer, A. Sandouk, J. Skinner and J. K. Taubenberger, "Characterizing and diminishing autofluorescence in formalin-fixed paraffin-embedded human respiratory tissue," Journal of Histochemistry & Cytochemistry, vol. 62, no. 6, pp. 405-423, 2014.

[22] H. I. C. Dalgarno, P. A. Dalgarno, A. C. Dada, C. E. Towers, G. J. Gibson, R. M. Parton, I. Davis, R. J. Warburton and A. H. Greenaway, "Nanometric depth resolution from multi-focal images in microscopy," Journal Of The Royal Society Interface, vol. 8, no. 60, pp. 942-951, 2011.

[23] Photometrics, "Evolve EMCCD for super-resolution microscopy," Photometrics, 2009.

[24] S. Swift and L. Trinkle-Mulcahy, "To bin or not to bin: Balancing the trade-off between signal intensity, spatial and time resolution in biological imaging," RMS infocus, no. 26, pp. 4-14, 2012.

[25] Thorlabs, "Absorptive neutral density filters," Thorlabs, 2001.

[26] "ImageJ," [Online]. Available: https://imagej.nih.gov/ij/. [Accessed September 2018].

[27] S. F. Gibson and F. Lanni, "Experimental test of an analytical model of aberration in an oil-immersion objective lens used in 3-dimensional light-microscopy," Journal of the Optical Society of America A - Optics Image Science and Vision,

vol. 8, no. 10, pp. 1601-1613, 1991.

[28] D. G. Abdelsalam and M. Stanislas, "Spherical aberration measurement of a microscope objective by use of calibrated spherical particles," Applied Optics, vol. 56, no. 16, pp. 4766-4771, 2017.

[29] F. A. Jenkins and H. E. White, "spherical aberration of a thin lens," in Fundamentals of optics, 4th ed., McGraw-Hill Higher Education, 2001, pp. 153-157.

[30] M. Abramowitz, K. R. Spring, H. E. Keller and M. W. Davidson, "Basic principles of microscope objectives," Biotechniques, vol. 33, no. 4, pp. 772-+, 2002.

[31] G. Casella and R. L. Berger, "Continuous distributuion," in Statistical Inference, 2nd ed., Duxbury advanced series, 2002, pp. 98-111.

[32] G. M. Whitesides and S. K. Tang, "Fluidic optics," SPIE Digital Library, vol. 6329, 2006.

[33] W. M. Irvine and J. B. Pollack, "Infrared optical properties of water and ice spheres," Icarus, vol. 8, pp. 324-360, 1968.

[34] S. Abrahamsson, J. Chen, B. Hajj, S. Stallinga, A. Y. Katsov, J. Wisniewski, G. Mizuguchi, P. Soule, F. Mueller, C. D. Darzacq, X. Darzacq, C. Wu, C. I. Bargmann, D. A. Agard, M. Dahan and M. G. L. Gust, "Fast multicolor 3D imaging using aberration-corrected multifocus microscopy," Nature Methods, vol. 10, pp. 60-63, 2013.

[35] M. A. Model and J. K. Burkhardt, "A standard for calibration and shading correction of a fluorescence microscope," Cytometry, vol. 44, no. 4, pp. 309-316, 2001.

[36] P. M. Blanchard and A. H. Greenaway, "Simultaneous multiplane imaging with a distorted diffraction grating," Applied Optics, vol. 38, no. 32, pp. 6692-6699, 1999.

[37] E. L. C. Palmer, in Diffraction grating handbook, 6th ed., Newport Corporation, 2005, pp. 20-25.

[38] P. A. Dalgarno, H. I. C. Dalgarno, R. Lambert, L. Paterson, D. C. Logan, D. P. Towers, R. J. Warburton and A. H. Greenaway, "Multiplane imaging and three dimensional nanoscale particle tracking in biological microscopy," Optics Express, vol. 18, pp. 877-884, 2010.

[39] P. A. Jaeger, C. McElfresh, L. R. Wong and T. Ideker, "Beyond agar: Gel substrates with improved optical clarity and drug efficiency and reduced

autofluorescence for microbial growth experiments," Applied and Environmental Microbiology, vol. 81, no. 16, pp. 5639-5649, 2015.

[40] A. Piruska, I. Nikcevic, S. H. Lee, C. Ahn, W. R. Heineman, P. A. Limbach and C. J. Seliskar, "The autofluorescence of plastic materials and chips measured under laser irradiation," LAB ON A CHIP, vol. 5, no. 12, pp. 1348-1354, 2005.

[41] P. M. Blanchard and A. H. Greenaway, "Broadband simultaneous multiplane imaging," Optics Communications, vol. 183, no. 1-4, p. 29–36, 2000.

[42] R. E. Fischer and B. Tadic-Galeb, "Review Of Specific Geometrical Aberrations And How To Get Rid Of Them," in Optical system design, McGraw-Hill, 2000, pp. 61-94.

[43] S. Djidel, J. K. Gansel, H. I. Campbell and A. H. Greenaway, "High-speed, 3-dimensional, telecentric imaging," Optics Express, vol. 14, pp. 8269-8277, 2006.

[44] E. W. Weisstein, "Spherical Cap," in CRC Concise encyclopedia of mathematics, 2nd ed., CRC Press, 1999, pp. 2775-2776.

[45] C. Y. Young, "Lines," in Precalculus, John Wiley & Sons, Inc., 2010, pp. 73-86.

Chapter 5

Multifocal microscopy applied to evaluate the fluid shear stress on a cell

5.1 Chapter overview

After the study of the limits of a Dalgarno multifocal microscope presented in chap. 4, this chapter is dedicated to the application of multifocal microscopy (MUM) as a method to perform micro-particle image velocimetry (μPIV) [1], specifically applied for the first time to reconstruct velocity and shear stress fields generated by a fluid flow around a cell.

MUM has been, first, validated as method by reconstructing the flow velocity profile inside a parallel plate flow chamber (PPFC, eq. 5.4, sec. 5.3) along the flow direction and as a function of the axial distance from the coverslip. This has shown that MUM, within the first 10 μm from the coverslip, can achieve an average accuracy on the calculated velocities of (0.42 ± 0.32) μm/s, while the same measurement performed with a confocal microscope has reached a slightly improved average accuracy of (0.30 ± 0.13) μm/s (table 5.3 and fig. 5.11). At higher axial distances from the coverslip, instead, confocal microscopy is significantly more accurate than MUM. Despite this, MUM has achieved better results than those shown in the literature (table 5.1) for other 4D microscopy techniques and shown its superiority in terms of temporal resolution.

After this test, MUM has been applied to reconstruct velocity and shear stress fields (eq. 5.8 ,5.9, 5.10 and 5.11) around a fixed HeLa cell [2]. This has clearly shown the perturbation to the laminar flow due to the presence of the cell (the velocities over directions perpendicular to that of the flow reached around 30 μm/s) and the shear stress around the latter (fig. 5.16, 5.17 and 5.18), which varied between 0.5 Pa and 3 Pa. The features visible in the velocity and shear stress fields obtained are comparable to those observable in the literature [3, 4]. However, the reconstructed fields show also some unexpected fluctuations that indicate a reduction in accuracy due to false axial localisations.

5.2 Mechanical interactions between fluids and cells

The mechanical interaction between fluids and cells is widely documented in the literature. It encompasses the interaction between blood and blood vessels [5], lymph and lymphatic vessels [6, 7], bacteria and any liquid external environment [8], etc. It

includes also the studies performed in bioreactors to exert mechanical cues [9], as, e.g., those on stem [10] and bone cells [11]. In general, all these systems are linked by the fact that, when liquids flow around cells, they impart some shear stress [12], causing mechanical and biochemical responses. The shear stress is caused by the component of the force imparted by the flow parallel to the surface on which the force is exerted. Mathematically, it can be expresses as (eq. 5.1):

$$S = \frac{F_{\backslash\backslash}}{A}, \qquad \text{(eq. 5.1)}$$

where S is the shear stress, $F_{\backslash\backslash}$ is the component of the force parallel to the surface and A is the surface area. S is expressed in Pa and is a scalar quantity. S can be generated both between the different layers of a fluid, which can flow at different speeds, and between the fluid and the solid surface that contains it [13]. In the latter case it is termed wall shear stress (S_w).

In blood vessels there is a constant dynamic balance between the wall shear stress generated by the blood pressure and the biological response to preserve homeostatic conditions [14]. The fact that S_w can acutely dilate the vessel is fully established, however the exact mechanism through which vessels sense and transduce mechanical stimuli (mechanotransduction [15]) is not fully comprehended [5] and several mechanisms involving biochemical and protein receptors exist [16, 17]. In general, perturbations to the homeostatic equilibrium via unexpected mechanical stimuli (exercise, hypertension, etc.) can either lead to the adaptation or the damaging of vessels [16]. In parallel to the blood circulatory systems, many living species include a lymphatic system [7], which transports a substance called lymph. In mammals the lymphatic system has three main roles [6]: it removes the interstitial fluid from tissues and the fatty acids from the digestive system and transports immune cells to and from the lymph nodes. Differently from the blood circulatory system, the lymphatic one does not have a centralised pumping system, but, instead, it relies on lymphatic vessel contractions, which, in turn, are activated by the wall shear stress generated by the lymph. The activation S_w varies among animal species and lymphatic system regions. Consequently, it has been hypothesised that the different regional sensitivities of the lymphatic system to the S_w are needed to optimise the lymph transport [6]. S_w is also known to play a role in bacterial adhesion on target cells [18]. For example, the presence of S_w can activate a strengthening of the adhesion of bacteria [8], which moves from loose to firm upon a 10-fold S_w increase.

The interaction between fluids and cells can also be artificially generated to impose defined mechanical stimuli [15]. This can be done by using bioreactors, which are systems where cells are stimulated in a controlled manner to reproduce the biological environment [9]. In a bioreactor mechanical stimuli can be provided in different ways [19, 20], including fluid perfusion, electrical cues, etc. An example includes the study of bone cells [21], where bone mass gain and adaption are observed upon mechanical stimuli [22]. Such work has shown that the absence of mechanical loads can induce a reduction in bone mass. This is possible since the information regarding the mechanical forces is detected and collected by the bone cells and transmitted to the cell nucleus via different pathways to be elaborated [23]. One of these pathways is mediated by the Ca^{2+} ion [24] and is observable with stem bone cells such as human mesenchymal stem cells (hMSCs) [10] and with pre-osteoblast cells such as MC3T3-E1 [25]. When these cells are mechanically stimulated in perfusion chambers [9], which are bioreactors where the mechanical cue is generated via a perfused medium [1], they move from their initial stationary state (fig. 5.1a) and produce morphological and biochemical responses (fig. 5.1b). This is due to the fact that the parabolic flow velocity profile established in the

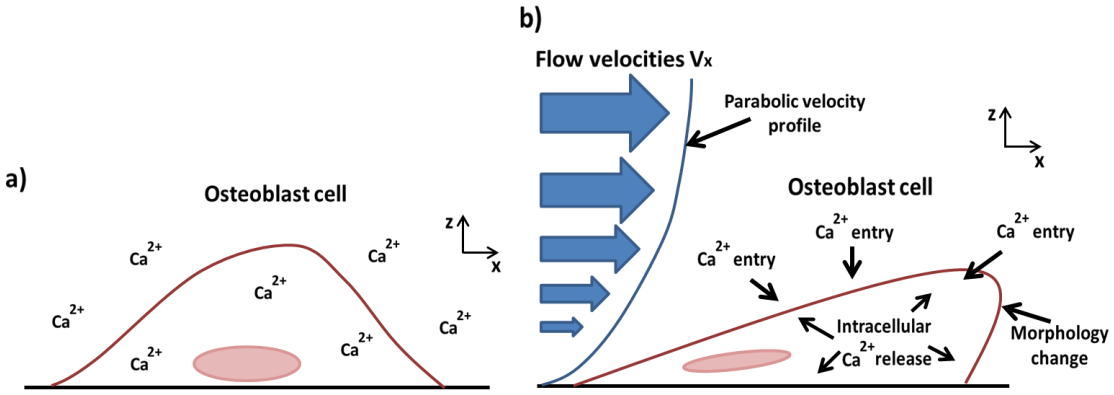

Figure 5.1 Schematic representation of an osteoblast cell before (**a**) and after (**b**) the application of a laminar flow to generate fluid shear stress (FSS). The latter causes morphological (e.g. shape adaptation) and biochemical (e.g. intracellular Ca^{2+} release and Ca^{2+} uptake from the external environment) responses.

chamber (i.e. a laminar flow [13]) generates wall shear stress on the cells. This mechanical stimulation provokes, in turn, the uptake from the external environment and from intracellular stores of Ca^{2+} ions [24], which are used to start the signalling cascade and transmit the shear stress information to the nucleus [23]. Once this information has been transmitted, the cells can decide the best strategies to adapt to the shear stress (e.g.

via cell elongation to reduce the interactions with the flow [26]). In bone cells other pathways exist to transmit the mechanical information to the nucleus, but not all of them are fully understood [27].

To study and comprehend the biochemical and morphological responses of cells to mechanical stimuli, it is important to monitor the behaviour of the flow and, consequently, of the shear stress around the cells. This could be done by using an imaging technique called micro-particle image velocimetry (μPIV) [1], which allows the acquisition and tracking of the flow, in order to reconstruct the local velocities and shear stresses exerted on cells.

5.2.1 *Mechanotransduction through in vitro perfusion systems*

As mentioned, perfusion chambers, also called in vitro perfusion systems [9], are common bioreactors used to apply mechanical cues on cells via the perfusion of a medium [1]. An example of perfusion chamber is the parallel plate flow chamber (PPFC) shown in fig. 5.2a. The PPFC has a rectangular channel, within which the cells are seeded. The perfusion medium is injected into one extreme of this rectangular channel through a tube, which could be connected to a syringe. On the other extreme of the rectangular channel another tube collects the output flow. To perform μPIV, in an inverted microscope the PPFC is positioned above the microscope objective lens (fig. 5.2a), which observes the flow from the bottom side of the channel. Both widefield and confocal [1] microscopes have been used for μPIV. The first one can quickly (depending on the camera acquisition speed [28]) acquire an entire 2D image simultaneously, while the second one needs to scan the imaged plane point by point [29], but it possesses superior axial sectioning ability. To track the behaviour of the flow some bright emitters such as fluorescent beads can be inserted to observe the local behaviour of the fluid and follow its stream lines [1]. The density of the inserted emitters should be as close as possible to that of the fluid, in order to minimise the effect of the buoyancy [1]. In addition, the perfusion media should be transparent to the light emitted by the fluorescent emitters, so to minimise light scattering and absorption. Another factor to consider is the emitter concentration in the media [1]. This should be sufficiently high to allow such a spatial sampling that permits the accurate reconstruction of the flow velocity profile and, as a consequence, of the forces exerted. The reconstruction of the flow profile around a cell requires the acquisition of a 3D field of view (FOV). This can be done either by continuously scanning the imaging plane axially within the flow channel or by imaging the flow at different axial positions over

fixed intervals of time [30, 31] (fig. 5.2c). In both cases, however, it is not possible to image simultaneously the entire volume to study, since the imaged planes cannot be acquired simultaneously with single plane widefield and confocal microscopy (fig. 5.2c). This, in turn, could lead to the loss of information in case of fast evolving 3D systems that need to be constantly imaged. Therefore, an acquisition speed as fast as

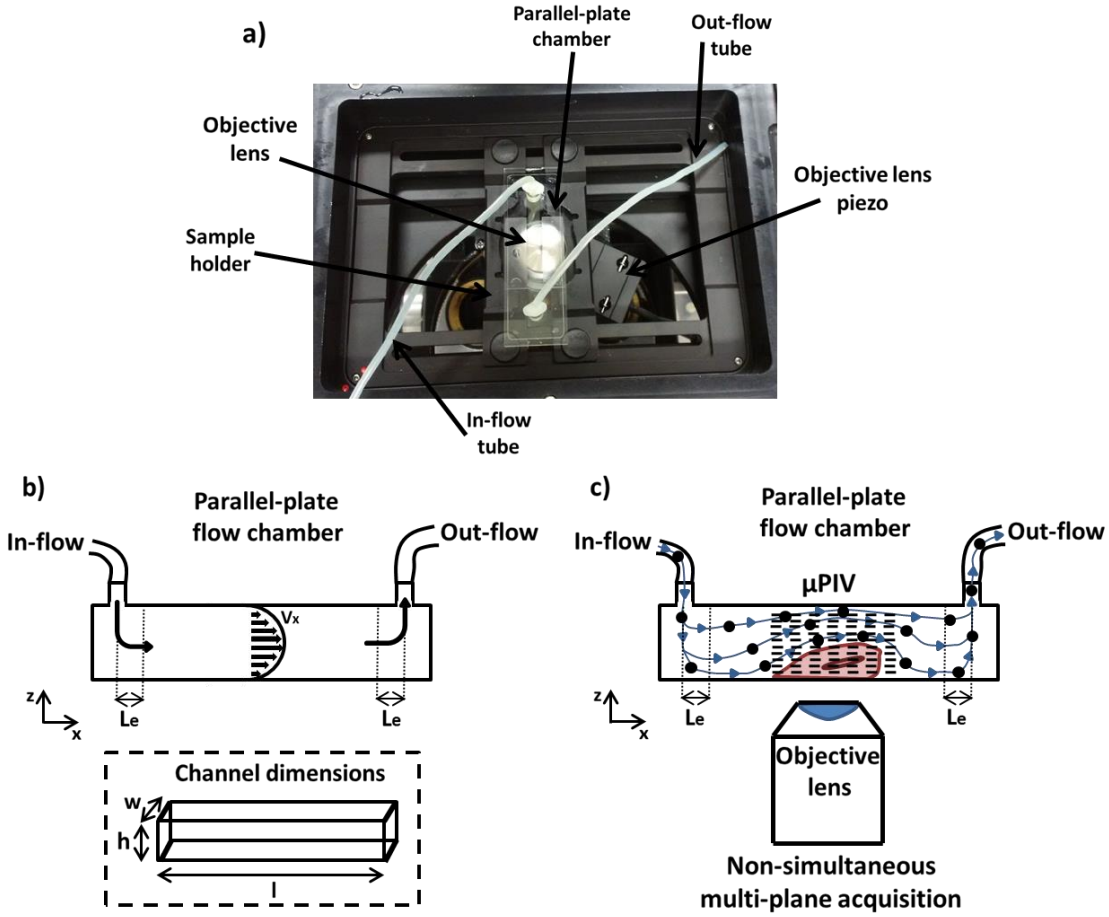

Figure 5.2 a) Picture showing a parallel plate flow chamber (PPFC) positioned on top of the sample holder of a widefield microscope. This image shows the input and output flow tubes, the objective lens and the nanometric accurate piezo to axially displace the latter. **b)** Schematic representation of the flow velocity profile of a fluid flowing inside a PPFC and of the dimensions of the rectangular channel. w = width, h = height, l = length. **c)** Schematic representation of a fluid containing beads and flowing inside a PPFC containing a cell. The flow is imaged by acquiring multiple planes non-simultaneously with a microscope (µPIV). L_e is the entrance length after which the laminar flow is fully developed.

possible might be fundamental to understand the responses of the biological system to the mechanical stimuli.

To image a three-dimensional flow over time (4D imaging) and avoid the temporal resolution constrains above mentioned, µPIV and micro-particle tracking velocimetry (µPTV, a technique where the interest is focused on evaluating the speed of individual tracks, rather than on reconstructing the velocity fields [32]) have been performed via different 3D microscopy techniques. In particular, techniques as stereo-microscopy, optical tomography, digital holography, PSF engineering, defocus and multifocal microscopy have been applied [33, 34, 35, 36, 37, 38, 39, 40]. In stereo-microscopy the object plane is observed simultaneously over two different angles, thus rendering two images that are captured via an equivalent number of detectors [41, 42]. The introduced angular offset generates a lateral one between the two images, which can allow to evaluate, via a complex pre-calibration, the lateral and axial positions of the emitters. In stereo-microscopy the axial range is limited by the depth of field (DoF) of the system, which should consequently be maximised. However, the latter is inversely proportional to the axial resolution ([43], eq. 1.9), thus imposing some limits. Even though this technique allows the access to the axial dimension, the presence of the angular offset introduces aberrations (e.g. image distortion [44]), which reduce the accuracy of the localisation. Similarly to stereo-microscopy, in tomographic imaging the imaged plane is observed over several observation angles (at least four [34]) and via multiple detectors [45]. The quite long used DoFs (e.g. by setting the system NA at around 0.06 [45]) allow a three-dimensional imaging. In tomographic µPIV/PTV, however, the volume reconstruction is an ill-posed problem [46], which does not have unique solutions and reduced the accuracy of the localisations. In digital holography, instead, both pieces of information about the intensity as well as the phase of the collected signal are acquired [34, 47], thus allowing for the 3D localisation of the emitters within the DoF of the objective lens. This is achieved by recording and analysing the interference pattern generated between a beam transmitted through the sample and a reference one. However, in digital holography the localisation accuracy is very sensitive to the noise and can be further worsened by the interference among the patterns generated by the different emitters in the recorded signal [34]. To acquire the axial dimension in real time µPIV/PTV has also been combined with PSF engineering techniques [33, 34]. In particular, in [48, 49] some astigmatism has been introduced by inserting a cylindrical lens in the optical path to encode the axial positions in the ellipticity of the PSF [50], while in [51] an amplitude mask has been inserted in the back focal plane of the objective lens to generate triple-spot PSFs whose sizes and orientations are linked to the axial position of the emitters. The latter PSF engineering

method, however, has the drawbacks of severely reducing the photon flux through the amplitude mask and produces a lateral movement of the PSF on the detector with the axial position, thus requiring a more complex calibration [34]. In addition, the triple-spot feature increases the possibilities of confusing different emitter images among them, but this problem can be reduced by varying the geometry of the intensity mask to change the PSF shape [34]. In the literature the direct use of non-engineered PSFs to evaluate the axial positions of the emitters by measuring the defocused PSF diameters is also reported [34, 52, 53, 54]. As expected, this technique requires the focal plane to lie outside the micro-fluidic channel to avoid the depth discrimination problem [34, 55, 56]. Finally, some authors have also reported the use of multiplane microscopy to perform µPIV/PTV [35, 36, 37, 38, 39, 40]. In particular, in [39, 40] a variable plane number and position system has been used to evaluate the influence of solvent evaporation on polymer deposition in different regions, while a combined biplane - PSF engineering system (cubic PSF [57]) presented in [35, 36, 37, 38] has been applied to preliminarily study the blood flow trajectories in a live zebrafish [58] embryo. In terms of uncertainties achieved on the velocity over the flow direction by these different real time 3D microscopy techniques, the following values are reported for general comparison (table 5.1):

4D microscopy technique	**Flow velocity uncertainty (µm/s)**
Stereo-microscopy	$3.6 \cdot 10^3$ [41]
Optical tomography	$86 \cdot 10^3$ [34, 45]
Digital holography	$305 \cdot 10^3$ [59]
PSF engineering - Astigmatic	3.3 [48]
PSF engineering – Triple spot family	NA
Defocused PSF	1.9 [53]
Multiplane microscopy	NA
Multiplane microscopy with PSF engineering	NA

Table 5.1 Example of flow velocities uncertainties reported in the literature [34, 41, 45, 48, 53, 59] for some 4D microscopy techniques applied to µPIV/PTV (NA indicates no data have been found).

Clearly, techniques as defocus and astigmatic PSF engineering achieve better performances in term of flow velocity accuracy in comparison to stereo-microscopy,

optical tomography and digital holography, considering the former is in the range of μm/s, while the latter in that of mm/s.

Generally, to control as much as possible the mechanical cues imposed by the fluids, a laminar flow within the PPFC is desired. To determine if the flow is laminar, a parameter called Reynolds number (Re) is used [60]. For PPFC the Re is measured by using the following formula [61] (eq. 5.2):

$$\mathrm{Re} = \frac{\rho V_f}{\mu W}, \qquad \text{(eq. 5.2)}$$

where ρ and μ are, respectively, density and viscosity of the perfusion medium, V_f is the flow velocity at which the perfusion medium is injected into the PPFC and w is the width of the PPFC (fig. 5.2b). If Re is smaller than 2,300 the flow is considered laminar [61]. A laminar flow has a parabolic velocity profile inside a PPFC (fig. 5.2b), which is maximised at the centre of the channel and theoretically equal to 0 μm/s on the walls of the PPFC [13]. Even if Re < 2,300, close to the entrance aperture where the flow is injected the profile is not perfectly laminar and the same happens close to the exit aperture [61]. For symmetric PPFC, the distance from the input and output apertures after which the flow regime becomes perfectly laminar is called entrance length (L_e) and is equal to (fig. 5.2a and 5.2b, eq. 5.3):

$$L_e = 0.04\ h\ \mathrm{Re} = 0.04\frac{\rho h V_f}{\mu W}, \qquad \text{(eq. 5.3)}$$

where h is the height of the PPFC (fig. 5.2b). It is important not to image the flow closer than L_e to the inlet and outlet flows, otherwise the observed flow will not be laminar. In absence of obstacles such as cells within the PPFC, the flow will tend to be mono-dimensional [61], i.e. it will tend to flow mainly along the direction of the length of the channel. If the ratio h/w is smaller than 0.05, the flow can be considered mono-dimensional with an accuracy of 97.5% [61]. The equation that governs the flow velocity profile of a laminar flow inside a PPFC as a function of the distance from the coverslip, i.e. $V_x(z)$, is [13] (eq. 5.4):

$$V_x(z) = \frac{6 V_f}{h^3 w}(hz - z^2), \qquad \text{(eq. 5.4)}$$

which is valid far from the perturbations to the flow and for a mono-dimensional flow along x. As it can be seen, $V_x(z)$ is the equation of a parabola along z. At z = 0 µm and z = h (i.e. on the walls of the PPFC), $V_x(z)$ = 0 µm/s. Vice versa, at z = h/2 (i.e. in the middle of the channel) $V_x(z)$ is maximised and equal to ($V_{x,max}$ eq. 5.5):

$$V_{x,max} = \frac{3V_f}{2hw}. \qquad \text{(eq. 5.5)}$$

Knowing $V_x(z)$ it is possible to calculate the shear stress generated by the flow in the x-z plane, i.e. $S_{xz}(z)$ [13] (eq. 5.6):

$$S_{xz}(z) = \mu \frac{dV_x(z)}{dz} = \frac{6\mu V_f}{h^3 w}(h - 2z). \qquad \text{(eq. 5.6)}$$

Differently from $V_x(z)$, $S_{xz}(z)$ is a linear function of z that is equal to 0 Pa in the middle of the channel (i.e. at z = h/2), while it is maximised on the walls of the PPFC (i.e. at z = 0 µm and z = h), where it becomes equal to (eq. 5.7):

$$S_{xz,w} = \pm \frac{6\,\mu V_f}{h^2 w} \qquad \text{(eq. 5.7)}$$

and is called wall shear stress ($S_{xz,w}$) [62]. The ± sign in eq. 5.7 indicates that the $S_{xz,w}$ assumes opposite values on the top and bottom walls of the PPFC, but the magnitude of the stress remains the same.

Fig. 5.3 shows the behaviour of $V_x(z)$ and $S_{xz}(z)$ in case of a PPFC as the µ-Slide I $^{0.2}$ Luer from Ibidi (fig. 5.2a), where h = 200 µm and w = 5 mm (h/w = 0.04), and of a perfusion medium perfused at V_f = 1.0 µl/min and with µ = 0.5 Pa·s and ρ = 1.1 g/ml (Re = $7.30 \cdot 10^{-6}$, L_e = 0.058 nm). As it can be seen, $V_x(z)$ has a parabolic profile maximised in the middle of the chamber and reduced to 0 µm/s at the edges.

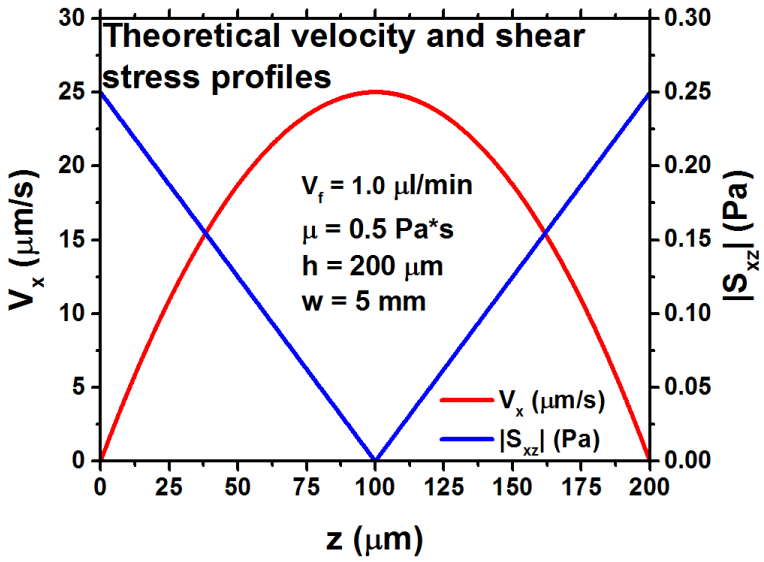

Figure 5.3 Theoretical V_x and $|S_{xz}|$ against axial position curves (eq. 5.4 and 5.6, respectively), built by using the following flow and PPFC parameters: V_f = 1.0 µl/min, µ = 0.5 Pa·s, h = 200 µm, w = 5 mm.

Conversely, $S_{xz}(z)$ shows the linear profile maximised on the walls and equal to 0 Pa in the centre.

In case the laminar flow is perturbed by an obstacle such as a cell, the flow in the perturbed region is no longer mono-dimensional and velocity components perpendicular to the flow direction (i.e. V_y and V_z) are introduced. Consequently, since the flow is deviated over multiple directions, the shear stress applied on the cell acts over several planes. This produces three velocity fields, i.e. $V_x(x,y,z)$, $V_y(x,y,z)$ and $V_z(x,y,z)$, whose composition gives the total velocity magnitude ($V_{mag}(x,y,z)$, eq. 5.8):

$$V_{mag}(x,y,z) = \sqrt{V_x{}^2(x,y,z) + V_y{}^2(x,y,z) + V_z{}^2(x,y,z)} \qquad \text{(eq. 5.8)}$$

and the velocity vector field ($V_{vec}(x,y,z)$). The shear stress introduced in the x-y, x-z and y-z planes, i.e., respectively, $S_{xy}(x,y,z)$, $S_{xz}(x,y,z)$ and $S_{yz}(x,y,z)$, is given by (eq. 5.9, 5.10 and 5.11):

$$S_{xy}(x,y,z) = \mu\left(\frac{\partial V_x(x,y,z)}{\partial y} + \frac{\partial V_y(x,y,z)}{\partial x}\right), \qquad \text{(eq. 5.9)}$$

$$S_{xz}(x,y,z) = \mu\left(\frac{\partial V_x(x,y,z)}{\partial z} + \frac{\partial V_z(x,y,z)}{\partial x}\right) \qquad \text{(eq. 5.10)}$$

and

$$S_{yz}(x,y,z) = \mu\left(\frac{\partial V_y(x,y,z)}{\partial z} + \frac{\partial V_z(x,y,z)}{\partial y}\right). \qquad \text{(eq. 5.11)}$$

To have a clear picture of the shear forces around a cell, the shear stress in all the three planes indicated above needs to be calculated.

This chapter discusses the application of multifocal microscopy (MUM) as a method to perform µPIV (fig. 5.4). As explained in previous chapters (sec. 1.3.9 and 2.2), MUM is a widefield microscopy able to image simultaneously a 3D FOV. Consequently, its application to µPIV can provide considerably advantages in terms of acquisition speed, since the axial scanning of the imaged plane is not needed. This is a fundamental requirement for quickly evolving systems, which might need continuous and simultaneous observations at multiple axial positions.

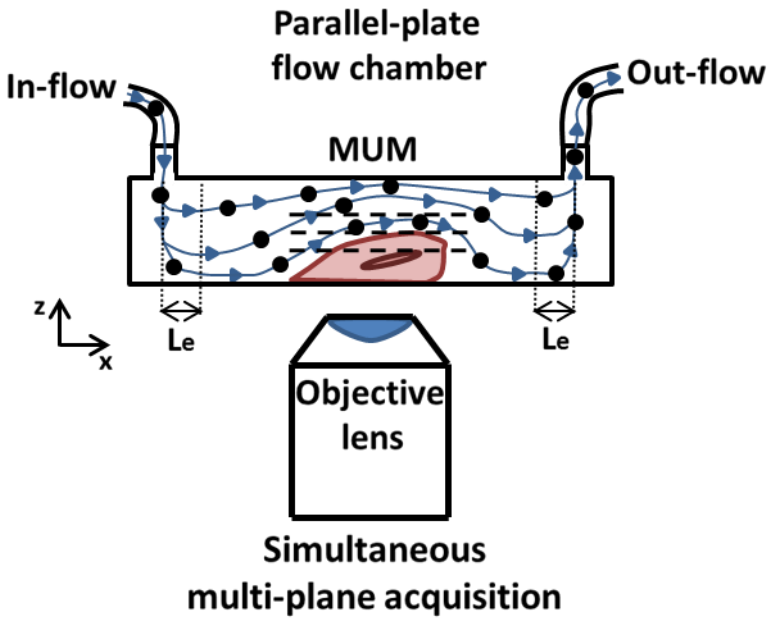

Figure 5.4 Schematic representation of a fluid containing beads and flowing inside a PPFC containing a cell. The flow is imaged by acquiring multiple planes simultaneously with a multiplane microscope (MUM). L_e is the entrance length after which the laminar flow is fully developed.

In next sections MUM will be first validated as a microscopy method for µPIV against the expected theoretical behaviour (eq. 5.4) and that observed with a confocal microscope. Then, it will be applied to reconstruct velocity (eq. 5.8) and shear stress fields (eq. 5.9, 5.10 and 5.11) around a test fixed cell for the first time. Testing MUM over confocal microscopy for µPIV is important, since, although the latter has superior sectioning abilities [63], it suffers from limited acquisition speed, considering it cannot image the entire field of view simultaneously and more than one plane per time. The

work in this chapter has been done in collaboration with Dr Kamel Madi from the University of Manchester.

5.3 Reconstruction of the axial velocity profile inside a parallel plate flow chamber via the Dalgarno multiplane microscope

In order to validate MUM as a technique to perform µPIV, it has been decided to use it to reconstruct the velocity against axial distance profile (e.g. fig. 5.3) of a fluid flowing inside a PPFC and compare this to that obtained by using a confocal microscope and the theoretical model (eq. 5.4).

The perfusion medium has been made by mixing by hand for 5 min 10 ml of Dulbecco's phosphate - buffered saline (DPBS, Gibco, 15326239), 3 g of dextran from Leuconostoc species (Sigma - Aldrich, 31392-50G) and 250 µl of yellow/green fluorescent 1 µm beads (Thermo Fisher Scientific, F13081) inside a Falcon tube (Corning, 352098). Dextran is a polysaccharide [64] and has been used to raise the viscosity and, consequently, the shear stress imposed by the solution (eq. 5.6). Indeed, the viscosity of the DPBS is very low (it can be assumed to be similar to that of water, $\mu = 8.90 \cdot 10^{-4}$ Pa·s) and, for the experiment with the fixed cell (sec. 5.4), would have not generated a level of shear stress around the cell high enough to discriminate it from that generated by the noise in the measurements. For example, with a PPFC with h = 100 µm and w = 5 mm (Ibidi, µ-Slide I $^{0.1}$ Luer) and with a media with $\mu = 8.90 \cdot 10^{-4}$ Pa·s and injected at V_f = 1.0 µl/min, $|S_{xz,w}|$ would be equal to only $1.5 \cdot 10^{-3}$ Pa (eq. 5.7). 1 µm beads have been chosen, since they have been demonstrated to allow high performances in terms of axial range and precision, due to the high photon emission rate (chap. 4). The concentration of beads in the perfusion medium is around $1.5 \cdot 10^{-12}$ M (neglecting the volume increase due to the dextran). The viscosity of this medium has been measured by using a rheometer at the University of Manchester (TA Instruments, HR-3) by Dr Kamel Madi and Dr Andrew Smith and resulted to be 0.5 Pa·s. The density (ρ) and the refractive index (n) of this perfusion medium were not measured. However, in the literature [64] it is possible to find some empirical equations that can calculate them given the dextran concentration. In particular, ρ (at room temperature and 1 atm) is equal to (eq. 5.12):

$$\rho = 0.99717 \frac{g}{ml} + 0.00398133 \frac{g}{ml} d + 0.00001597 \frac{g}{ml} d^2 \quad \text{(eq. 5.12)}$$

and n (at a wavelength of 589.29 nm, 1 atm and room temperature) to (eq. 5.11):

$$n = 1.33299 + 0.00151005\ d + 0.000006372\ d^2, \qquad \text{(eq. 5.13)}$$

where d is the number of grams of dextran per 100 g of solution. In this case d = 22.64 (assuming the density of the DPBS and the bead stock solution are equal to that of water, i.e. 1 g/ml) and, consequently, ρ = 1.10 g/ml (eq. 5.12) and n = 1.37 (eq. 5.13).
As perfusion chamber, a PPFC with dimensions h = 200 µm, w = 5 mm and length (l) = 50 mm has been selected (Ibidi, µ-Slide I $^{0.2}$ Luer, fig. 5.2a and 5.2b). The medium was perfused by using a syringe pump (Harvard Apparatus, 11 plus 70-2012) and, for the MUM validation test, two different V_f have been used: 0.5 µl/min and 1.0 µl/min. The syringe pump was pushing a syringe (BD Plastipak, 300013) containing the perfusion medium. The syringe was connected to the PPFC through a precision tip (Nordson EFD, 7018169), a 0.8 mm internal diameter silicone tube (Ibidi, 10841, fig. 5.2a) and a tube - PPFC male connector (Ibidi, 10824, fig. 5.2a). The output flow was collected using the same male connectors and silicon tubing (fig. 5.2a) into an Eppendorf tube. The PPFC was positioned below the sample holder (fig. 5.2a), fixed to it by using cable ties and oriented in order to show the beads flowing along the longer sides of the MUM channels (e.g. fig. 5.6).

Knowing the density and the viscosity of the perfusion medium, the dimensions of the PPFC and the flow velocities, the Reynolds numbers (Re, eq. 5.2) and entrance lengths (L_e, eq. 5.3) can be calculated. Respectively at V_f = 0.5 µl/min and 1.0 µl/min, Re is equal to $3.65 \cdot 10^{-6}$ and $7.30 \cdot 10^{-6}$, while L_e to 0.029 nm and 0.058 nm. Since the calculated Re values are much smaller than 2,300 and the L_e values are much shorter than half the length of the channel (25 mm), where the objective lens is roughly positioned, the imaged flow is undoubtedly laminar [13]. In addition, since the ratio h/w is equal to 0.04, i.e. it is much smaller than 1, the flow can be considered one-dimensional [13]. As a consequence, the velocity components along directions different from that of the flow can be considered negligible (this is valid in absence of obstacles in the flow as cells).

To calculate the axial positions of the beads in the flows acquired with the Dalgarno multiplane system using the sharpness algorithm [65], it is necessary to create a set of sharpness calibration curves with the 1 µm beads. In terms of optical system, the same objective lens, filters, diffraction grating, dichroic mirror, multifocal relay, laser system, emCCD, microscope and etc. described in sec. 3.3 has been used. Therefore, the plane spacing was equal to 630 nm. To build the calibration sample, a support material

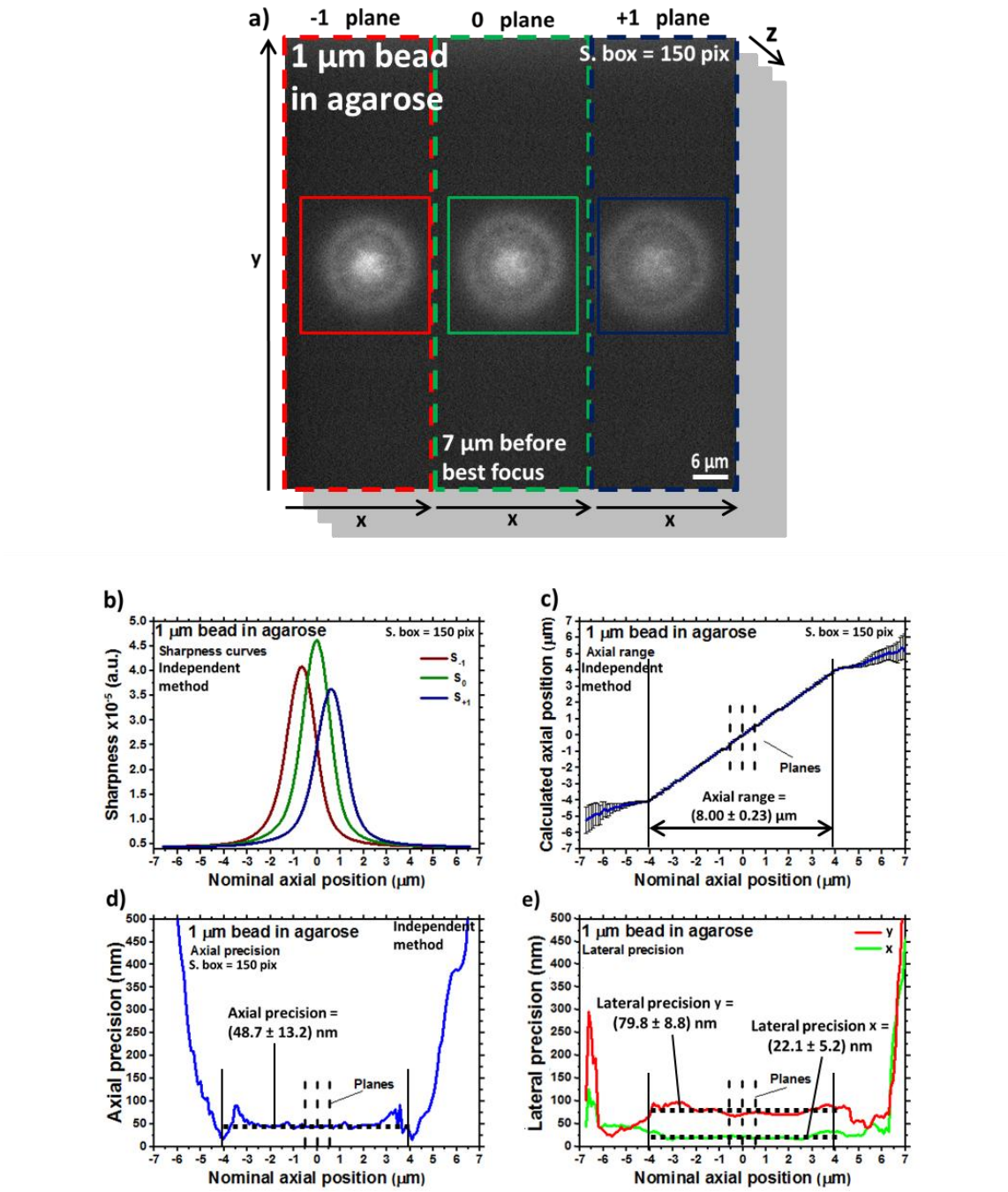

Figure 5.5 a) Axial cross section showing the 1 µm bead in agarose used to build the sharpness curves in **b** and observed through the diffraction multiplane relay under study. The image in the central plane is located 7 µm before the best focal position. This image has been extracted from the first z-stack of the z-stack series acquired to calculate the corresponding sharpness curves. **b)** Sharpness curves calculated to reconstruct the flow velocity profiles. A sharpness box of 150 pix has been used. **c)** Calculated axial position against nominal axial position curve. **d)** Axial precision against nominal axial position curve. **e)** Lateral precision over x and y directions against nominal axial position curves, calculated from the bead used to build the calibration curves in **b**.

Laser power at sample = 87.18 μW at λ = 488 nm, em gain = 2,000, ET = 100 ms, PS = 630 nm (shown in **c**, **d** and **e**).

whose refractive index matches that of the used dextran solution (n_{dex} = 1.37) would be ideal to reduce the localisation artefacts, since the impact of the spherical aberration on the sharpness values would be similar (chap. 3). However, both support materials presented in previous chapters (agarose and PDMS, sec. 3.3.2) have refractive indices different from that one (n_{PDMS} = 1.41 and n_{agar} = 1.33) and in both cases the mismatch between the refractive indices is the same ($|n_{PDMS/agar} - n_{dex}| \approx 0.04$). Therefore, agarose has been preferred to PDMS only due to the fact it can be produced more easily (sec. 3.3.2). The agarose sample has been made by following the same procedures explained in sec. 3.3.2. A bead positioned within the first 10 μm from the bottom of the glass-bottomed dish has been chosen, to minimise the impact of the spherical aberration induced by the refractive index mismatch between the immersion oil and the agarose (chap. 3). The following imaging parameters have been used for the calibration sample: Exposure time (ET) = 100 ms, em gain = 2,000 and laser power at sample = 87.18 μW at λ = 488 nm. Laser power, ET and em gain have been set on these values to produce high quality sharpness curves, in order to reduce the noise present on their profiles (chap. 4). A series of ten z-stacks has been acquired to build the sharpness curves, following the procedure described in sec. 3.3.3. In fig. 5.5a, a lateral cross section showing the 1 μm bead in agarose used for sharpness curves is shown. The cross section in fig. 5.5a has been acquired 7 μm before the best focal position in the central plane. In fig. 5.5b the sharpness curves corresponding to the bead in fig. 5.5a are presented. As desired, the sharpness curves profiles appear smooth. This is due to the high SNR and SBR associated with the bead used to build them (fig. 5.5a), when in focus in the central plane (41.5 and 46.5, respectively via eq. 4.3 and 4.5). Due to the size of the out of focus PSF (fig. 5.5a), it has been necessary to use a sharpness box of 150 pix to determine the sharpness curves. In fig. 5.5c the calculated against nominal axial position curve, evaluated for the calibration bead in fig. 5.5a is shown. The error bars are the standard deviations calculated at every axial position. The curve and the error bars in fig. 5.5c have been calculated by using the independent method (sec. 2.5.3) following the procedure explained in sec. 4.4.2. The axial range associated to the curve in fig. 5.5c is equal to (8.00 ± 0.23) μm and has been calculated as the range over which it was possible to calculate the axial positions with at least 100 nm accuracy. Fig. 5.5d shows the standard deviations associated with the error bars in fig. 5.5c plotted against the

nominal axial positions. The axial precision within the axial range is equal to (48.7 ± 13.2) nm. The lateral precision (fig. 5.5e) was obtained using the same procedure as for fig. 5.5d, but, with the lateral x and y positions obtained through the centre of mass (CoM) algorithm inserted in the MUM plugin in place of the axial values (sec. 2.5.3). The average x and y lateral precisions within the axial range are, respectively, (22.1 ± 5.2) nm and (79.8 ± 8.8) nm. The precision over the y direction is worse than that over the x one probably due to some non-optimal calibration sample positioning on the sample holder.

As said above, the bead flows have been acquired by using a confocal microscope and the multifocal setup. The confocal microscope (Leica, TCS SP8) was equipped with a supercontinuum laser source (NKT, SuperK Evo), an oil immersion 100x 1.4 NA objective lens (Leica, 15506372) and a hybrid detector (Leica, HyD). The excitation wavelength has been set on 488 nm, with a power at sample of 28 µW. The detector has been set to detect the wavelength in the range 500 nm - 550 nm, with a gain of 100. The image size was fixed to 25.81x51.67 µm with 512x1,024 points per acquired image, so to have a FOV comparable to that used with MUM and keep the resolution high. By setting the acquisition speed on the maximum one (2 kHz), each frame could be acquired in 261 ms. To acquire the bead flows with the confocal microscope over a 3D volume, the imaging plane has been moved by steps of 1 µm, from the axial position 0 µm (where the PPFC coverslip is positioned and the beads were stuck during the fluid motion [13]) to the axial position 20 µm, thus acquiring 21 planes. Each plane has been imaged for 2 min. All acquired planes have then be collated to create the final 3D map. Regarding the flow acquisition via the multiplane setup, given the axial range of 8 µm (fig. 5.5c), it has been necessary to make three acquisitions of 2 min each and with the central plane positioned at different distances from the coverslip of the PPFC to observe the first 20 µm. This has been achieved by placing the central plane at 3 µm, 10 µm and 17 µm from the coverslip. In terms of imaging conditions, with respect to the parameters used for the calibration sample it was necessary to reduce the laser power at sample to 3.56 µW to avoid the saturation of the camera. This could be due to the fact that dextran solutions absorb less light than agarose gels in the visible range or has a smaller fluorescence quenching effect. However, no data to confirm this have been found in the literature. Both frame acquisition times used with the two microscopes (100 ms and 261 ms, respectively for multifocal and confocal microscopes) resulted acceptable to have a high enough

temporal sampling of the bead flows at all axial positions, since no motion blur [66] was observable.

Figure 5.6 shows two selected frames of the bead flows acquired with the confocal and the multifocal microscopes. For both images the fluid flows from left to right and V_f is equal to 1.0 µl/min. The image in fig. 5.6a has been acquired with the

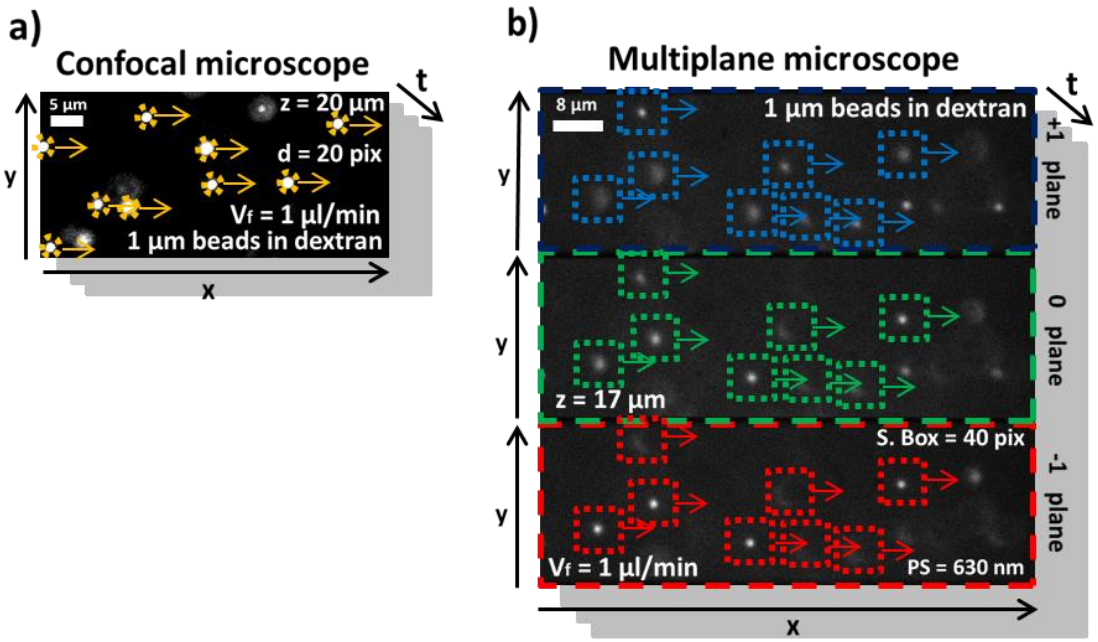

Figure 5.6 Frames extracted from the temporal series acquired to reconstruct the velocity profile inside the PPFC and showing 1 µm beads in dextran. The frame in **a** (positioned 20 µm above the PPFC bottom polymer) has been acquired by using the confocal microscope described in sec. 5.3 and the beads have been localised by using a localisation circle of diameter (d) of 20 pix with the software HuygensPro (Laser power at sample = 28 µW at λ = 488 nm, gain = 100, frame acquisition time = 261 ms, V_f = 1.0 µl/min). The frame in **b** (the central plane is 17 µm above the PPFC bottom polymer), has been acquired by using the multiplane microscope under study and the beads have been localised by using a sharpness box of 40 pix (Laser power at sample = 3.56 µW at λ = 488 nm, em gain = 2,000, ET = 100 ms, PS = 630 nm, V_f = 1.0 µl/min). The fluid flows from left to right.

confocal microscope and is positioned at 20 µm from the PPFC coverslip. The beads acquired with the confocal microscope have been tracked by using the software HuygensPro. Since the software had to discriminate the beads in focus in each acquired plane from those out of focus that belonged to other planes, it has been decided to discard all the PSFs whose diameters were larger than 20 pix. This value has been

selected by taking into account the used magnification, bead and pixel (5.1 μm) sizes. Once all the selected beads have been tracked, the software has calculated the average velocity in the flow direction (V_x) per each plane position and the corresponding standard deviations. The image in fig. 5.6b has been acquired with the MUM setup. The central plane is positioned at 17 μm from the PPFC coverslip. As observable, the beads in fig. 5.6b are densely packed. This was not avoidable, since, in situations where a live cell is present, it is necessary to quickly acquire a high density of beads homogeneously distributed over the FOV, in order to keep high both spatial and temporal sampling for the shear stress maps. As a consequence, to avoid the overlap between sharpness boxes and the calculation of wrong axial localisations, it has not been possible to keep the same sharpness box size used with the calibration sample (150 pix), but this had to be reduced to 40 pix. To understand the effect of this change in sharpness box on axial range and precision, these have been recalculated. Fig. 5.7a shows the axial range curve in case the sharpness box is reduced for the axial localisation. The error bars are associated to the axial precision. The impact is massive. Even if the sharpness curves to calculate them have not been changed (fig. 5.5b), the change of the sharpness box for the axial localisation has strongly reduced the axial range, which has become equal to (0.27 ± 0.06) μm, i.e. it is shorter than the axial distance between $\pm 1^{st}$ planes. This is more easily visible in fig. 5.7b, where the plot in fig. 5.7a has been zoomed in the axial range region. This reduction in axial range is mainly due to two reasons:

- Different sharpness box sizes include different total amounts of background and this has an influence on the sharpness values.
- As the PSF becomes larger than the sharpness box used and is cropped, some information is lost, leading to false axial localisations and, thus, reduced axial range.

Therefore, in this situation the axial range could be increased by removing the background before the calculation of the sharpness curves and of the axial localisation. However, as explained in previous chapter (sec. 4.2.1), the background subtraction operation could risk to remove also some desired pieces of information, considering the background is not always homogeneous and static. To try to minimise this problem it has been decided to use the ratiometric sharpness algorithm presented in sec. 2.5.3, rather than the independent method (sec. 2.5.3). This has been done since with the ratiometric method the background subtraction is embedded in the algorithm (sec. 2.5.3), considering the sharpness associated to the background is automatically subtracted from every calculated sharpness value. Obviously, also with this algorithm

the background should be evenly distributed and as more as possible static, in order to reduce the variations of the background sharpness in space and time. However, in

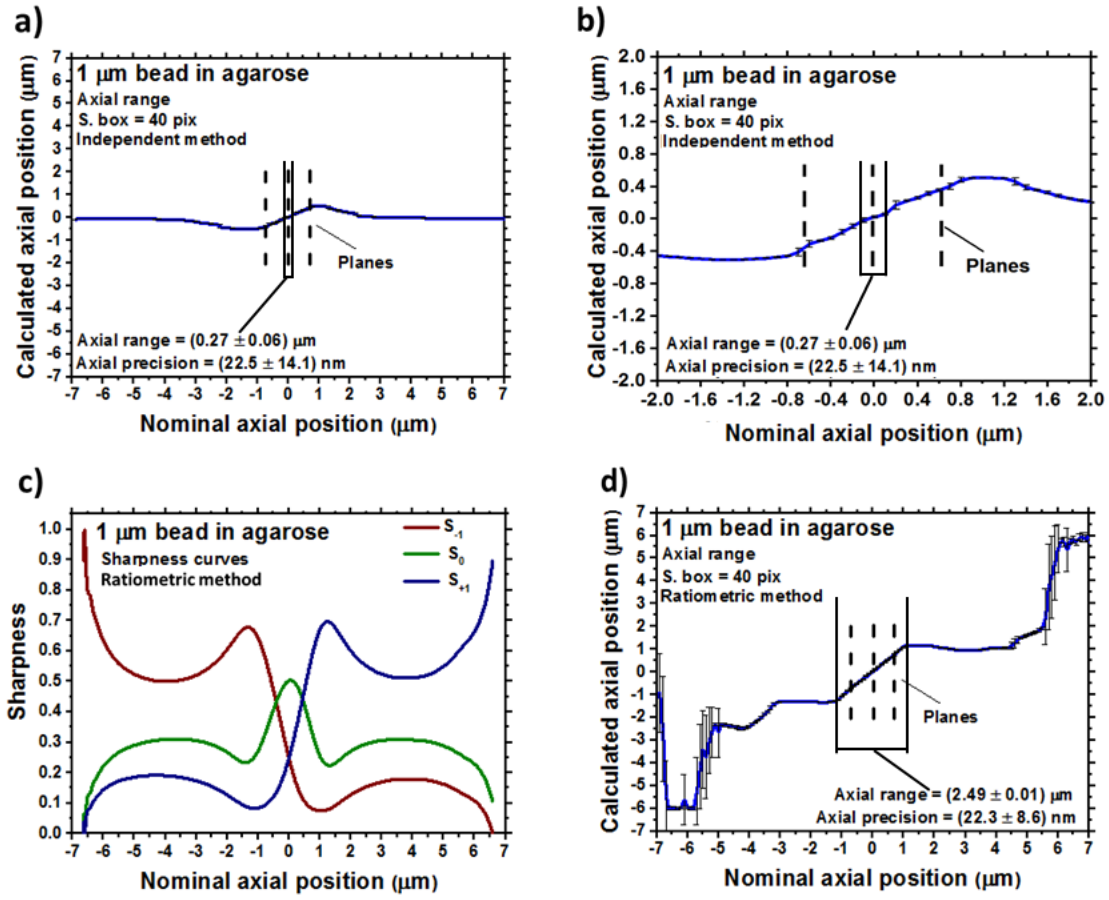

Figure 5.7 a) Calculated against nominal axial position curve, calculated as explained in sec. 4.4.2 and by using the sharpness curves in fig. 5.5b and the independent method (sec. 2.5.3), with a sharpness box of 40 pix. The error bars represent the axial precisions calculated at all acquired axial positions. The axial range is shown on the plot. **b)** Same plot as in **a**, but zoomed in the axial range region. **c)** Ratiometric sharpness curves calculated from the curves in fig. 5.5b (as explained in sec. 2.5.3) to reconstruct the flow velocity profile described in sec. 5.3 and observed through the multiplane microscope. **d)** Calculated against nominal axial position curve as explained in sec. 4.4.2 and by using the ratiometric sharpness curves in **c** and the ratiometric method (sec. 2.5.3), with a sharpness box of 40 pix. The error bars represent the axial precisions calculated at all acquired axial positions. The axial range is shown on the plot. Laser power at sample = 87.18 µW at λ = 488 nm, em gain = 2,000, ET = 100 ms, PS = 630 nm (shown in **a**, **b** and **d**).

situations where the background removal operation might be necessary, the ratiometric algorithm avoids the manual background subtraction, which could increase the bias in

the data. By using the sharpness curves in fig. 5.5b and the formula in eq. 2.4.3, the ratiometric sharpness curves associated to the curves in fig. 5.5b can be calculated. These are shown in fig. 5.7c. The ratiometric sharpness curves are automatically calculated by the MUM plugin when the ratiometric method is selected for the axial localisation (sec. 2.5.3). Fig. 5.7d shows the axial range curve obtained by using the ratiometric method. Also in this case the error bars are calculated from the axial precision values. Clearly, the axial range in fig. 5.7d has grown in comparison to that in fig. 5.7a and 5.7b, reaching a value of (2.49 ± 0.01) μm. As explained above, this is due to the fact that with the ratiometric sharpness algorithm the weight of the background is reduced in comparison to the independent one. With respect to the result in fig. 5.5c, the major factor limiting the axial range in fig. 5.7d is the fact that, over certain axial positions, the PSF becomes larger than the used sharpness box and is cropped, reducing the axial localisation ability. Indeed, the PSF in fig. 5.5a is confinable within a sharpness box of 40 pix in all the three planes in a range of around ±1.4 μm from the central plane. Regarding the axial precision, in both cases the sharpness box has been reduced to 40 pix (fig. 5.7a, 5.7b and 5.7d), this has improved in comparison to the 150 pix box case (fig. 5.5d). In particular, the axial precision has become equal to (22.5 ± 14.1) nm and to (22.3 ± 8.6) nm, respectively by using the independent (fig. 5.7a and 5.7b) and the ratiometric (5.7d) methods. This is due to the reduced amount of background included in the sharpness box.

The axial range achieved with the ratiometric method and the 40 pix box is still very limited in comparison to the 8 μm one obtained with the 150 pix box in fig. 5.5c, since the defocused PSF size exceeds the box one. However, by observing the image in fig. 5.6b, the PSFs are always confined within the 40 pix boxes and this has generally been observed in all acquired frames. This effect could be due to the refractive index mismatch between the dextran solution and the immersion oil. It is certainly not due to the mismatch between PPFC coverslip and immersion oil, since they share the same refractive index. However, the PPFC coverslip glass is reported to be 180 μm thick, while the used objective lens has been designed to work with 170 μm thick coverslips. This could introduce some additional spherical aberration and distort the PSFs from those observed in previous chapters (chap. 3 and 4). However, the coverslip glass thicknesses has not been measured and this cannot be verified. Therefore, this fact, combined with the result in fig. 5.7d, has led to the decision of preferring the ratiometric algorithm to the independent one to reconstruct the flow velocity profiles. However, due to the change in sharpness box size between calibration and sample data, some false

axial localisations might still be introduced. To reduce these, all localisations of bead clusters or where the sharpness boxes were overlapping or not fully containing the PSFs have been manually discarded. This process will be automatised in future works.

Once all the axial positions have been found, the tracks have been created by using the tracking function of the MUM plugin (sec. 2.5.3), in particular the Kalman filter and global nearest neighbour algorithm [67, 68] (Kalman + GNN). In fig. 5.8a three examples of tracks obtained from the MUM setup and with V_f = 1.0 µl/min are presented. The axial against lateral (along the flow direction) position curves of the tracks are linear as expected, since the laminar flow is unperturbed. However, it can be noticed that some localisations behave as outliers and deviate from the main tracks, where the majority of the other points are located. In general, this behaviour has been observed with several tracks. The average axial positions of tracks 1, 2 and 3 are, respectively, (2.13 ± 0.04) µm, (11.38 ± 0.19) µm and (16.73 ± 0.06) µm not including the outliers. The corresponding axial positions of the outliers are, instead, (1.04 ± 0.24) µm, (13.81 ± 0.30) µm and (12.39 ± 0.15) µm. To evaluate which axial positions are more correct, the velocities associated to these tracks need to be compared to the expected laminar velocities calculable via eq. 5.4. The local velocities of the tracks have been calculated by using the function "slope" of the software Excel [69] on the lateral x positions and the time points. This function, essentially, generates a linear fit over a group selected points and provides the associated slope, which in this case indicates the local speed of the tracks. The function slope has been applied by moving it across the points of the tracks, in order to obtain the local average velocities. The slope has been calculated every seven cells, to avoid the observation of the small deviations from the average velocities due to the noise in the localisations. This value has been selected empirically. The velocity profiles and the average velocities associated to the tracks in fig. 5.8a are shown in fig. 5.8b. These have been plotted together with the expected speeds calculated via eq. 5.4 for the corresponding axial positions of the main (solid lines) and outlier (solid-dashed lines) parts of the tracks in fig. 5.8a. The first and last three points of the velocity tracks have been removed, since these could not be averaged over seven points. As observable, in all three cases the track speeds deviate

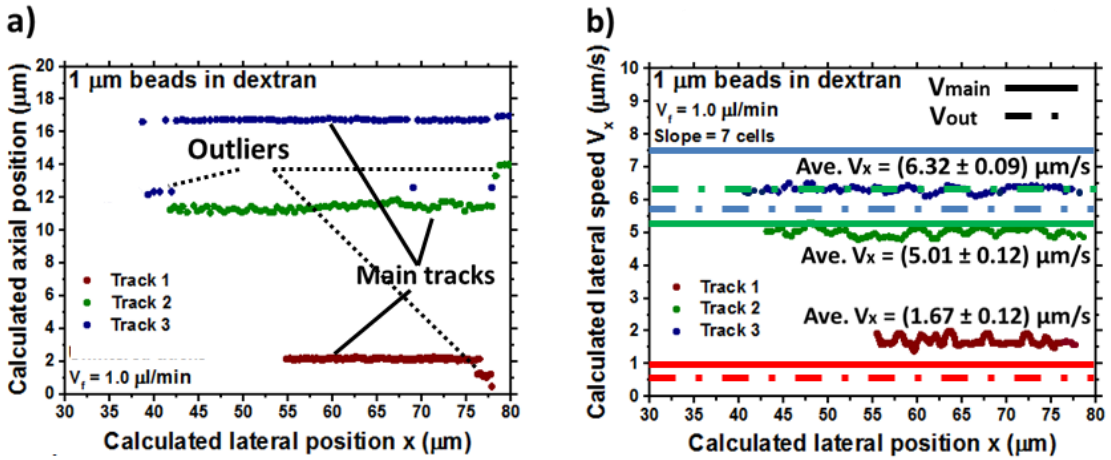

Figure 5.8 a) Three example tracks from the bead flow acquired with the multiplane microscope. These tracks have been extracted from the track list generated by the MUM plugin (sec. 2.5.3). Main tracks and outlier have been identified by following the criteria indicated in sec. 5.3. **b)** Velocities along the flow direction (V_x) associated to the three tracks shown in **a**. The average velocities are shown. Solid and solid-dashed lines indicate, respectively, the expected velocities associated to the main track and outlier axial positions highlighted in **a** and calculated with eq. 5.4. Laser power at sample = 3.56 µW at λ = 488 nm, em gain = 2,000, ET = 100 ms, PS = 630 nm, V_f = 1.0 µl/min. The fluid flows from left to right.

from those expected from theory (eq. 5.4) for both main and outlier positions. The percentage differences V_{dif} between the track speeds V_x and the theoretical velocities V_{th} (eq. 5.4) calculated for both the main and outlier positions for the three tracks in fig. 5.8a can be expressed as $100 \cdot |V_{th} - V_x|/V_{th}$. These have been summarised in table 5.2:

	Average axial position (µm)		**V_x (µm/s)**	**V_{th} (µm/s)**		**V_{dif} (%)**	
	Main	**Outlier**		**Main**	**Outlier**	**Main**	**Outlier**
Track 1	2.13 ± 0.04	1.04 ± 0.24	1.67 ± 0.12	1.05	0.52	59	221
Track 2	11.38 ± 0.19	13.81 ± 0.30	5.01 ± 0.12	5.37	6.43	7	22
Track 3	16.73 ± 0.06	12.39 ± 0.15	6.32 ± 0.09	7.67	5.81	18	9

Table 5.2 Average axial positions and theoretical velocities (V_{th}) associated to the main and outlier axial positions of the tracks in fig. 5.8a. The average measured velocities (V_x) and the percentage difference (V_{dif}) between these and V_{th} are also shown. Laser power at sample = 3.56 µW at λ = 488 nm, em gain = 2,000, ET = 100 ms, PS = 630 nm, V_f = 1.0 µl/min.

V_{dif} shows that the velocities measured for tracks 1 and 2 (V_x) are closer to the theoretical velocities (V_{th}) associated to the main axial positions than to those associated to the outlier positions by roughly 3-4 times. The contrary happens for track 3, where V_x results two times more compatible to the speed calculated for the outlier position. This indicates that the accuracy on the axial positions is lower than the 100 nm set to build the axial range curve in fig. 5.5c and that for some tracks the outliers might have a higher degree of agreement with the theory. These deviations between measured and theoretical velocities might have several sources. They can be caused by the difference in refractive index between the agarose calibration sample and the dextran solution, by the fact that the sharpness box had to be modified for the sample data, by the spherical aberration arising from the dextran solution – immersion oil refractive index mismatch, by the level of the signal, by the non-perfect identification of the position of the PPFC coverslip, etc.

To better understand the causes of these deviations, the SNR and SBR associated to the tracks in fig. 5.8 and observed in the central plane have been calculated as explained in sec. 4.2.1 (eq. 4.2 and 4.4, respectively). In fig. 5.9a, 5.9c and 5.9e the tracks in fig. 5.8 have been plotted with the corresponding SNR values colour encoded, while in fig. 5.9b, 5.9d and 5.9f the SNR and SBR data for these tracks are shown against the corresponding calculated lateral positions x. Fig. 5.9a, 5.9c and 5.9e show also the associated sharpness values in the three planes. Starting from tracks 1 and 2 (fig. 5.9a and 5.9c), in both cases it is possible to see that the outliers arise toward the end of them, as the SNR approaches values below 9-15 and the SBR below 2.5 (fig. 5.9b and 5.9d). Consequently, the reduction in signal level can be considered the cause for the appearance of the outliers in these tracks. In track 2, however, this is also due to the fact that the images of the bead starts to be partially cropped as the latter approaches the end of the FOV. This is visible in the associated sharpness profiles (fig. 5.9c) that rapidly rise near the end of the track. Another aspect to notice is that the SNR and SBR values calculated for track 1 are higher than those for track 2, but the speed measured for the latter is closer to the theoretical expected value (Table 5.2). This indicates that the signal is not the only factor that can influence the observed deviations as hypothesised. Regarding track 3 (fig. 5.9e), this also presents a couple of outliers as the signal reaches values comparable to those seen for the outliers in tracks 1 and 2. However, in this case the majority of outliers are at the beginning of the track, where the signal level is high. In addition, the axial position of the main part of the track is less

accurate than that associated to the outliers (fig. 5.8b and table 5.2). Consequently, the deviations of track 3 cannot be attributed to low signal problems. By taking into account the measured speed of track 3 and according to eq. 5.4, the corresponding bead should be positioned at around 13 µm – 14 µm from the coverslip. At this axial position, the spherical aberration introduced by the dextran solution – immersion oil refractive index mismatch could have the effect of reducing the localisation accuracy due to the distortion imposed on the PSF (fig. 3.5). However, this has not been verified. Regarding the sharpness profiles (fig. 5.9a, 5.9c and 5.9e), these present fluctuations that tend to increase moving toward the end of the tracks. These are caused by the fact that also the level of the signal fluctuates in a similar way (fig. 5.9b, 5.9d, 5.9f and sec. 4.4.1), but their origin is not clear. It cannot be due to fluctuations in the laser source, since it has not been observed in fig. 4.4b, where the SNR has been plotted against the axial positions of a bead in agarose. It might be caused by hypothetical variations in the flow velocity (V_f) imposed by the syringe pump, which in turn generate the small fluctuations visible in the axial profiles of the tracks. However, the latter is too small and could just originate from the fact that the localisation precision is not enough high. In addition, this would not explain why these fluctuations vary as the tracks move toward the end of the FOV and should have generated higher standard deviations on the measured velocities in comparisons to those obtained (table 5.2). The SNR and SBR profiles (fig. 5.9b, 5.9d, 5.9f) show also a decreasing behaviour along the flow direction. This could be due to the photobleaching of the beads during the track acquisitions and/or to a non-perfect alignment of the illumination FOV with the imaged FOV.

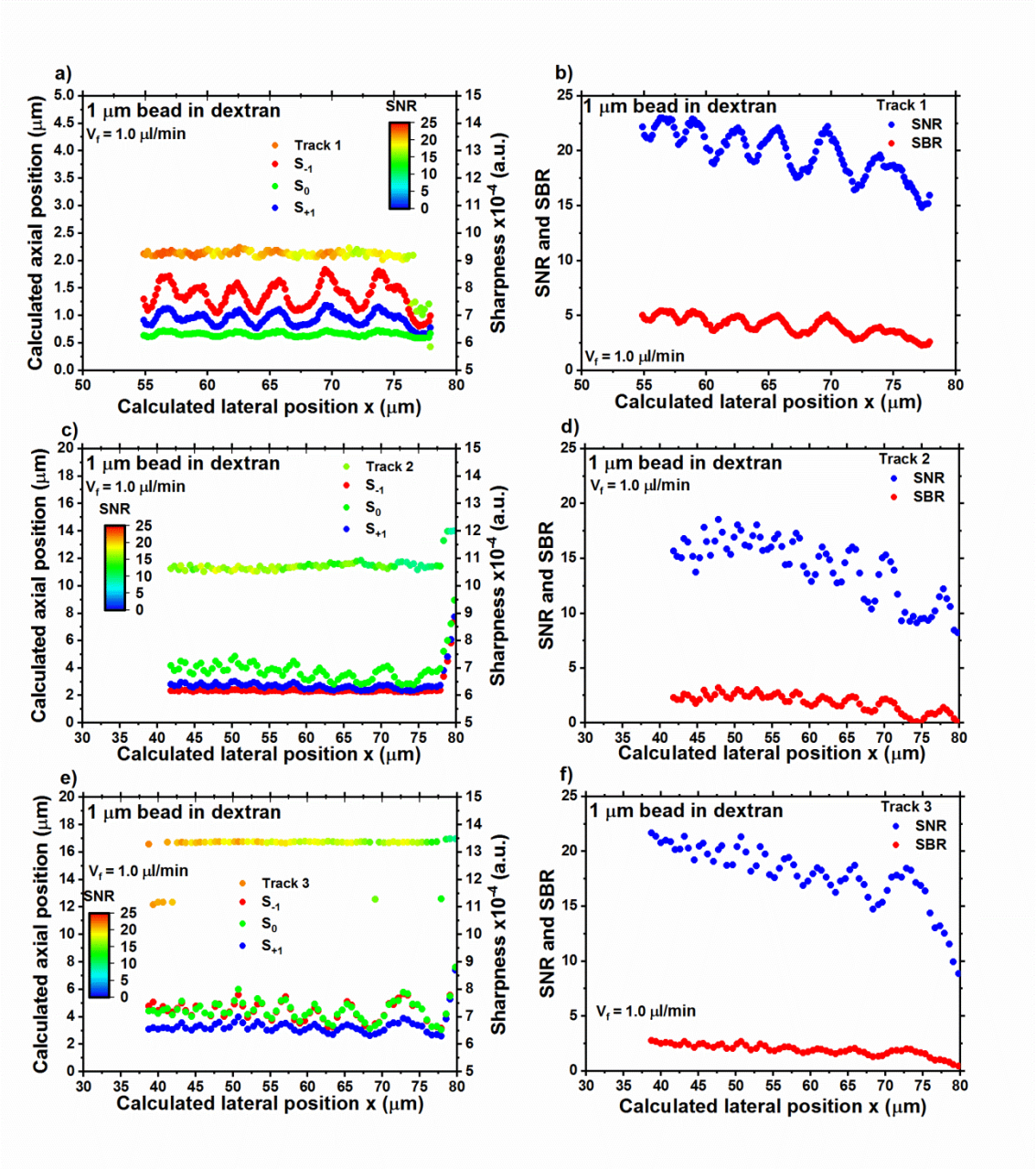

Figure 5.9 a, **c** and **e** show the tracks in fig. 5.8a and the associated sharpness values calculated in the three planes, with the corresponding SNR data colour encoded in the tracks. **b**, **d** and **f**, instead, present the SNR and SBR calculated for the same tracks. Laser power at sample = 3.56 µW at λ = 488 nm, em gain = 2,000, ET = 100 ms, PS = 630 nm, V_f = 1.0 µl/min. The fluid flows from left to right.

To reduce the impact of false localisations on the flow velocity profiles to reconstruct, it has been decided to filter out from the tracks all the outliers. This should exclude all outliers due to signal/image cropping problems, as those seen in fig. 5.9a and 5.9c. However, it will not be able to remove those tracks that have not been accurately localised due to other possible reasons and this could still introduce some

deviations from the expected behaviours. This has been done by using a code written in Mathematica that was:

- Discarding all points whose axial positions are outside the planned axial range.
- Discarding all points whose axial positions are more than 1 μm different from those of the surrounding points.

The first step has been performed to remove all those points localised before or after the axial range boundary. For example, when central plane has been positioned at 17 μm from the coverslip (fig. 5.6b), considering an axial range of 8 μm (fig. 5.5c), all axial positions below 13 μm or above 21 μm cannot be considered accurate. This step is based on the assumption that, thanks to the ratiometric algorithm and to the confinement of the beads within the sharpness boxes (fig. 5.6b and 5.7c), the axial range has remained on average the same shown in fig. 5.5c. Unfortunately, it is not possible to know the exact axial range. The second step is based on the assumption that the beads are not expected to massively vary their axial positions over very short periods of time (100 ms in this case), since the flow is laminar. Therefore, apart from the first point of every track, all the other points have been compared to the previous and following ones and, if in at least one of the two cases the absolute value of the difference in axial position was greater than 1 μm, the point was discarded. After discarding a point, the process was continuing among the remaining points, till the end of the track. This step has some drawbacks. One is that, if the initial points are outliers, the desired part of the track is discarded and the outliers preserved. Another one is that, if the outliers are grouped over extended distances, rather than being isolated points or short groups, a jump of 1 μm could be right and correct points might be removed. This could happen in presence of cells for example, but it also depends on the speed of the bead associated to the track. In total, around the 20% of the localisations has been removed by the code. More than 100,000 points per flow velocity acquisition (both 0.5 μl/min and 1.0 μl/min) have been obtained. To improve the comparison with the velocity profiles calculated for the confocal microscope and with the theoretical ones, the number of velocity data points has been reduced by calculating the average axial position and velocity of every track. This has been done by using another code written in Mathematica, which was, first, removing the first and last three points of every track and, then, calculating the average axial position and velocity of the tracks, including the associated standard deviations. This has produced a single point per track. The results for the 0.5 μl/min and 1.0 μl/min flow velocities are shown in fig. 5.10a. As noticeable, for both curves the velocities grow with the axial positions and the curve associated to the 1.0 μl/min flow

velocity increases faster than the 0.5 µl/min one, as expected. However, it can also be observed that the points do not exactly have a smooth profile as that shown by the theoretical curve in fig. 5.3, but they are spread. Some regions of the two curves in fig. 5.10a have more points than others. This could be due to the fact that some tracks have been localised at the wrong axial positions, that the beads were not homogenously distributed in the dextran solution and that more clusters and overlapping localisations have been removed from some axial positions than from others. In addition, it is also possible to see points with different velocities sharing the same axial position, a clear indication of the fact that some beads have been localised at the wrong axial position and that the filtering process could not remove all outliers. To increase the visualisation of the behaviours of the velocity profiles in fig. 5.10a, it has been decided to further group them. This has been done by averaging all the velocities associated to points in a range of ±0.50 µm from each integer axial position and positioning them on the integer positions themself. This allows to get one point per integer axial position, as for the profiles obtained with the confocal microscope. The results of this further filtering are in fig. 5.10b and the error bars are the standard deviations on the average velocities. The growing behaviour of the curves in fig. 5.10b and the distinction between the two flow velocities is now more evident than in fig. 5.10a, but it is still possible to see some

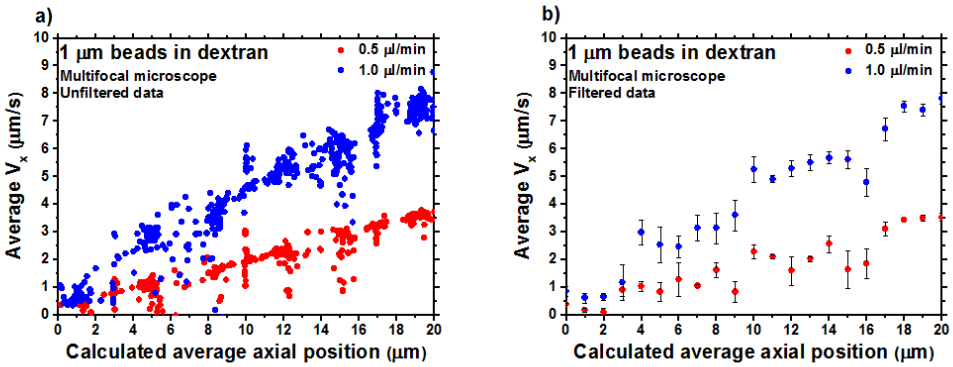

Figure 5.10 a) Average V_x values against average axial positions calculated for all tracks extracted from the bead flow acquired with the multiplane microscope and the V_f values of 0.5 µl/min and 1.0 µl/min. **b)** V_x against axial position curves obtained from the bead flow acquired with the multiplane microscope and the V_f values of 0.5 µl/min and 1.0 µl/min. These curves have been obtained by grouping the points in **a**, following the criteria explained in sec. 5.2.1. Laser power at sample = 3.56 µW at λ = 488 nm, em gain = 2,000, ET = 100 ms, PS = 630 nm.

fluctuations in the curves due to the high variations in the data they originate from (fig. 5.10a).

Finally, the curves shown in fig. 5.10b have been compared to the corresponding curves obtained with the confocal microscope and from the theory (eq. 5.4). This is shown in fig. 5.11a and 5.11b, respectively for the flow velocities of 0.5 µl/min and 1.0 µl/min. As it can be seen, in general with both flow velocities the curves associated to the confocal and the multifocal microscopes tend to follow the theoretical curves. However, it is also clear that the confocal curves are more accurate than those obtained with the multifocal system, especially at higher axial positions. At 0.5 µl/min (fig. 5.11a), the confocal velocity profile slightly overestimates the theoretical curve all over the studied range, while MUM, apart from the initial 4 µm - 6 µm, significantly underestimates it. At 1 µl/min, instead (fig. 5.11b), both confocal and MUM profiles seem in good agreement with the theoretical one up to axial positions around 12 µm - 14 µm. Then, the confocal profile overestimates the theoretical behaviour, while MUM underestimates it. MUM is more accurate at lower positions due to the fact that the filtering algorithm as been able to remove those outlier caused by signal/image cropping

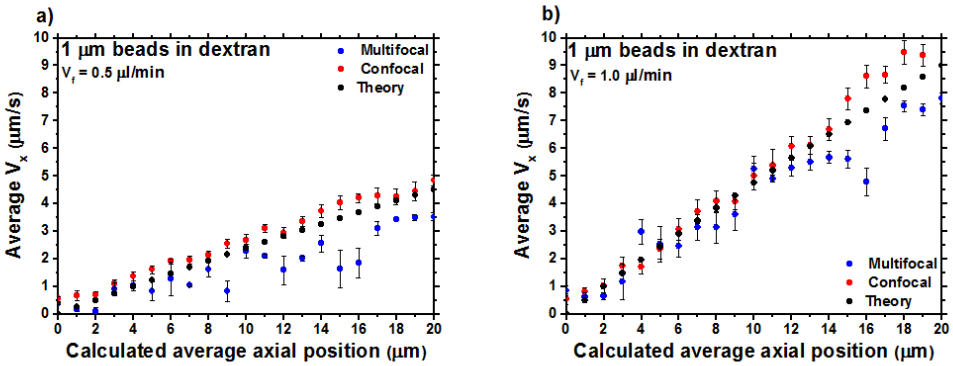

Figure 5.11 Theoretical V_x against axial position curves (black curves), compared to the experimental curves calculated from the bead flows acquired by using the confocal (red curves) and the multifocal (blue curves) microscopes. The multiplane curves are those presented in fig. 5.9b, while the confocal ones have been calculated as explained in sec. 5.3. The theoretical curves have been obtained by using eq. 5.4 and the dimensions of the used PPFC. **a)** V_f = 0.5 µl/min. **b)** V_f = 1.0 µl/min. For the MUM curves: Laser power at sample = 3.56 µW at λ = 488 nm, em gain = 2,000, ET = 100 ms, PS = 630 nm. For the confocal curves: Laser power at sample = 28 µW at λ = 488 nm, gain = 100, frame acquisition time = 261 ms. For the theoretical curves: h = 200 µm, w = 5 mm.

issues (fig. 5.9a and 5.9c). At higher axial positions, instead (fig. 5.9e), it is more likely that other problems as the mismatch-induced spherical aberration between dextran solution and immersion oil (fig. 3.5) do not allow to obtain the correct axial localisations. Obviously, this mismatch-induced spherical aberration problem is valid also for the confocal microscope, which is more in agreement with the theory at lower than at higher axial positions. In terms of signal levels, the confocal microscope can offer a higher SBR in comparison to MUM, since it is able to discard much of the background light. This, in turn, can help to improve its accuracy (fig. 4.40). For example, the SBR calculated (eq. 4.5) for a bead acquired with the multiplane system and in focus in the central plane at 17 µm from the coverslip is 2.6, while it is 210 for an equivalent bead acquired with the confocal microscope in focus in a plane at the same distance from the coverslip. The accuracies on the calculated velocities can be estimated as the absolute values of the differences between calculated and theoretical values. On average, these are equal to (0.42 ± 0.32) µm/s and to (0.30 ± 0.13) µm/s in the first 10 µm (i.e. from position 0 µm to 10 µm), respectively for the multifocal and the confocal microscope. So a slightly improved accuracy can be achieved with the confocal microscope within 10 µm from the coverslip. Moving to the following 10 µm (i.e. from position 10 µm to 20 µm), the corresponding accuracies become (0.95 ± 0.56) µm/s and (0.51 ± 0.38) µm/s and indicate that in this axial range the confocal microscope performs significantly better than MUM. Regarding the precisions on the velocities (i.e. the error bars in fig. 5.11), on average these are similar and equal to (0.30 ± 0.19) µm/s and to (0.27 ± 0.12) µm/s all over the investigated range (i.e. from position 0 µm to 20 µm), respectively for the multifocal and the confocal microscope. These data have been summarised in table 5.3:

	Average accuracy on velocity from 0 µm to 10 µm (µm/s)	**Average accuracy on velocity from 10 µm to 20 µm (µm/s)**	**Average precision on velocity from 0 µm to 20 µm (µm/s)**
MUM	0.42 ± 0.32	0.95 ± 0.56	0.30 ± 0.19
Confocal microscope	0.30 ± 0.13	0.51 ± 0.38	0.27 ± 0.12

Table 5.3 Average accuracies and precisions on the MUM and confocal velocity profiles shown in fig. 5.11. The accuracy in the first and last 10 µm of the studied axial range are shown separately. V_f = 0.5 µl/min and 1.0 µl/min. With MUM: Laser power at sample = 3.56 µW at λ = 488 nm, em gain = 2,000, ET = 100 ms, PS = 630 nm. With the confocal microscope: Laser power at sample = 28 µW at λ = 488 nm, gain = 100, frame acquisition time = 261 ms.

However, despite the fact confocal microscopy is able to provide better results in terms of accuracy/precision on the measured velocity in comparison to MUM, the latter is capable to provide competitive results with respect to those reported in table 5.1 for other 4D imaging techniques.

Concerning the fact that both MUM and confocal profiles seem to adhere more to the theoretical curve at 1.0 µl/min (fig. 5.11b) than at 0.5 µl/min (fig. 5.11a), it is not clear what is causing this behaviour. It might be due to some limits of the syringe pump to accurately deliver the required flow velocity V_f when this is below a certain value, but this has not been verified. Another factor to consider is the time needed to image a 3D volume. Each confocal image contains 1024x512 points and has been acquired in 261 ms. By using a proportion, if the number of points is reduced to the number of pixels in each multifocal channel (roughly 512x512/3 pix^2), the same frame could be acquired in around 44 ms. However, this is the time to acquire an image in a single plane. To have a an image every 100 nm (as the accuracy set for the multifocal system) and over a range of 8 µm, more than 3.5 s would be needed, since the planes cannot be imaged simultaneously. MUM, instead, can image the same volume in a single camera acquisition. Consequently, in comparison to confocal microscopy, multiplane microscopy offers a huge advantage to µPIV in terms of temporal resolution and the same is true with respect to single plane widefield microscopy as well.

In conclusion, it can be said that multifocal microscopy, at least within 10 µm from the coverslip, could be a valid method to perform µPIV. However, it is also clear the this technique is less accurate than confocal microscopy, which is commonly used for µPIV. This is especially true for deeper axial positions, where confocal microscopy

adheres to the theoretical behaviour much better than MUM. Confocal microscopy takes advantage from the higher SBR values achievable. Therefore, an increase in signal level could help to improve MUM performances. However, MUM offers the important advantage of fast 3D volume imaging, thanks to the simultaneous multiplane acquisition. This is very convenient with dynamic systems (e.g. cells adapting their morphology to the shear stress), where it might be needed to quickly track the variations in the behaviour of the flow to, in turn, follow the stresses applied by the latter and connect them to the responses of the systems under study.

5.4 Calculation of velocity and shear stress maps around a fixed HeLa cell

Once the Dalgarno multiplane system has been validated for µPIV (sec. 5.3), it has been decided to test it to reconstruct the velocity and shear maps generated by a fluid flowing around a cell. As explained in sec. 5.2, cells react to mechanical stimuli via morphological and biochemical responses [22]. Therefore, in order to better understand the latter and their mechanisms [27], it is important the evaluate the forces around the cells at subcellular level.

To perform this test, Henrietta Lacks (HeLa) cells [2] have been used. HeLa cells are cervical cancer cells, widely used in research due to their rapid growth to test vaccines, toxins, anti-tumour medicines, etc. Around of $3.6 \cdot 10^4$ HeLa cells (ATTC, CCL-2) have been seeded by Ms Sarah Gratton at the Research Complex at Harwell (RCaH) into a PPFC similar to that described above (sec. 5.2.1), but with a smaller height of 100 µm (Ibidi, µ-Slide I $^{0.1}$ Luer), to increase the shear stress around the cell (eq. 5.9, 5.10 and 5.11). To seed the cells, the following procedure has been followed:

- The cells were originally in a T75 flask (Thermo Fisher Scientific, 156499) at 37°C (with 5% CO_2 and 95% humidity) in an incubator (Thermo Fisher Scientific, Heracell VIOS CO2). The culture media has, first, been disposed of and the cells have, then, been washed with 20 ml DPBS (pre-heated to 37°C).
- To detach the cells from the flask, 1 ml of Trypsin 1x (pre-heated to 37°C, Sigma-Aldrich, 59429C-100ML) has been added and then the flask has been incubated at 37°C for 5 min.
- The solution of cells and trypsin has been transferred to an Eppendorf tube and centrifuged (Eppendorf, 5415 R) at 1,200 rpm for 6 min to separate the cells from the trypsin.
- After the centrifugation the supernatant has been removed and the cells have been resuspended into 100 µl of culture media (pre-heated to 37°C). The culture

media was composed by 88% minimum essential media (Thermo Fisher Scientific, 51200-038), 1% L-glutamine (Thermo Fisher Scientific, 25030081), 1% penicillin streptomycin (Thermo Fisher Scientific, 15140122) and 10% fetal bovine serum (Thermo Fisher Scientific, 26140079).

- 10 µl of the cell solution have been mixed with 10 µl of trypan blue (Thermo Fisher Scientific, 15250061) and the number of alive cells has been counted with a cell counter (Bio-Rad, TC20). A concentration of $4 \cdot 10^5$ cell/ml has been found.
- Finally, the remaining cell solution has been further diluted by adding 160 µl of culture media to reach 250 µl (the volume of the PPFC) and transferred to the PPFC, which has subsequently been moved to the incubator at 37°C. The cells have been injected very slowly into the PPFC to avoid the formation of bubbles.

After the seeding of the HeLa cells into the PPFC, the cells have been stained by using DiD (Thermo Fisher Scientific, V22887), a cell membrane label. This was needed to allow the visualisation of the cell profiles in fluorescence and observe some of their features. The cell staining has been done by Ms Sarah Gratton with the following steps:

- A solution of 5 µl of DiD stock solution and 1 ml of DPBS (pre-heated to 37°C) has been made.
- The culture media has been removed from the cell seeded PPFC and the latter has then been gently washed with 1 ml of DPBS (pre-heated to 37°C).
- 250 µl of diluted DiD solution have been added to the PPFC and the latter has then been incubated at 37°C for 8 min.
- Finally, the DiD solution has been removed, the PPFC has been rewashed with 1 ml of DPBS and then other 250 µl of culture media have been readded before reincubating the PPFC at 37°C.

In order to avoid a change in morphology of the cells in response to the flow, cell fixation has been done by Ms Sarah Gratton by following the following steps:

- The culture media has been removed from the cell seeded PPFC and the latter has then been gently washed with 1 ml of DPBS (pre-heated to 37°C).
- 250 µl of 4% paraformaldehyde solution (Thermo Fisher Scientific, MFCD00133991) have been injected into the PPFC and then left for 20 min.
- The paraformaldehyde solution has been removed, the PPFC washed with 1 ml DPBS and finally 250 µl of DPBS have been left into the PPFC.

To image the flow in the PPFC containing the cells, the same perfusion medium described in sec. 5.3 has been used. Therefore, the imaging parameters and the optical setup have not been modified from those used to acquire the bead flow. To image the

cell the diffraction grating and filter have been removed from the multiplane relay and a laser power at sample of 0.96 µW at λ = 561 nm (Cobolt, 04-01) has been used.

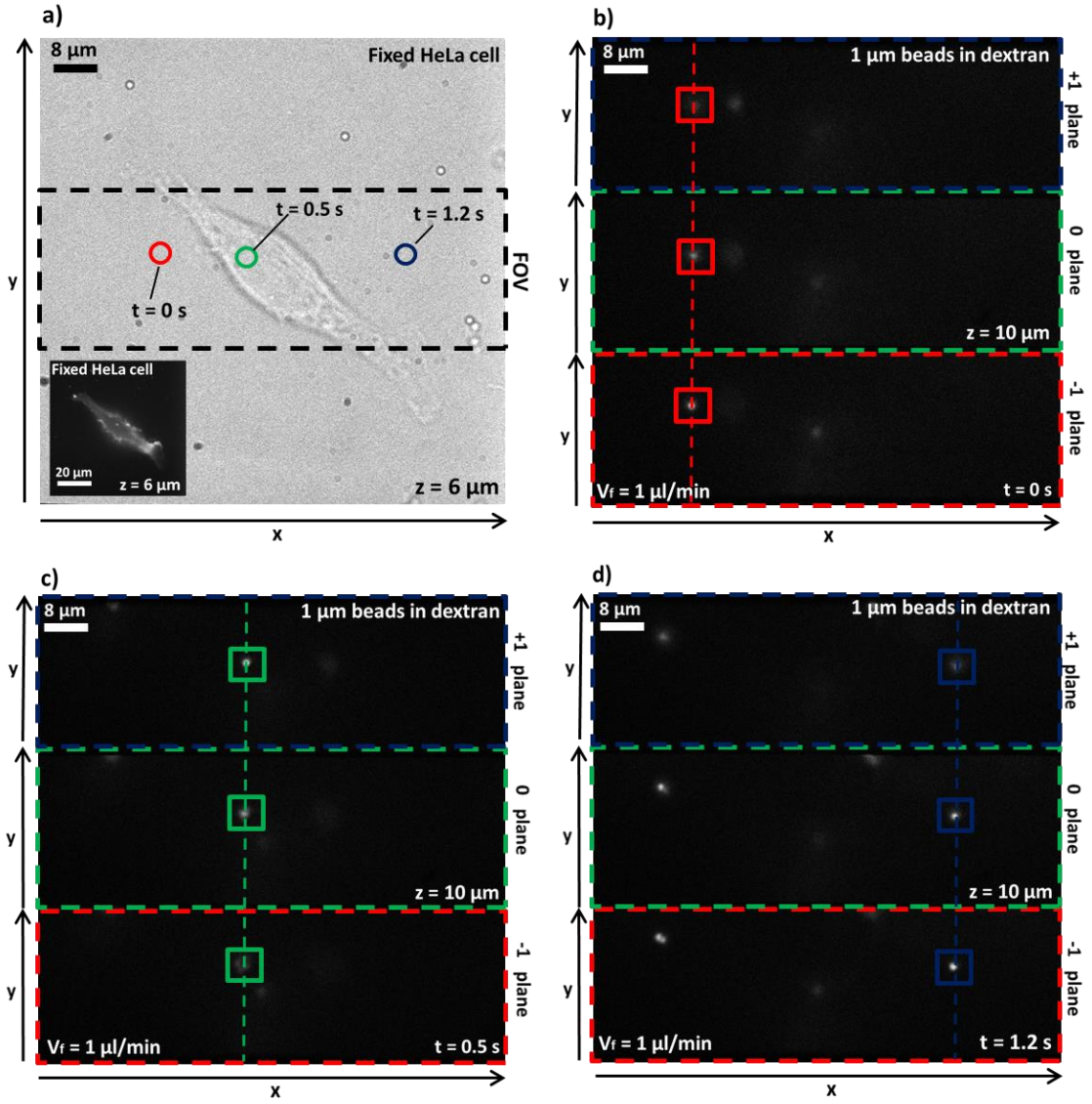

Figure 5.12 a) Transmission image of the fixed HeLa cell seeded in the PPFC and used to reconstruct the induced shear stress map. The highlighted rectangle represents the FOV imaged with the MUM. The inset shows the same cell image acquired in fluorescence. Both images are located at 6 µm from the coverslip. em gain = 2,000, ET = 100 ms. For the inset: Laser power at sample = 0.96 µW at λ = 561 nm. In **b**, **c** and **d** a 1 µm bead in dextran, flowing on top of the cell in **a** is evidenced. Setting the time as t = 0 s for the frame in **a**, the frame in **b** is at t = 0.5 s and that in **c** at t = 1.2 s. The central plane is at 10 µm from the coverslip. The positions of the bead in the different temporal frame are also shown in **a**. The fluid flows from left to right. Laser power at sample = 3.56 µW at λ = 488 nm, em gain = 2,000, ET = 100 ms, PS = 630 nm, V_f = 1.0 µl/min.

Regarding the perfusion parameters, a V_f of 1.0 µl/min has been chosen, so to achieve a wall shear stress of around 1 Pa (eq. 5.6). Since the h of the PPFC has changed to 100 µm, the L_e has been reduced to 0.029 nm (eq. 5.3), which, as mentioned in sec. 5.3, does not compromise the observation of the flow in laminar regime with the objective lens positioned at the centre of the channel.

In fig. 5.12a the brightfield transmission image of the chosen fixed HeLa cell is shown, together with an inset showing the same cell illuminated with the laser with λ = 561 nm. Both images in fig. 5.12a are positioned 6 µm above the PPFC coverslip and the FOV observed with the MUM is highlighted on the transmission image. Fig. 5.12b, 5.12c and 5.12d, instead, show three temporal frames extracted from the acquired bead flow. The flow has been imaged over a total time of 28 min 20 s. The central plane has been positioned at 10 µm from the PPFC coverslip, since at that axial position it was

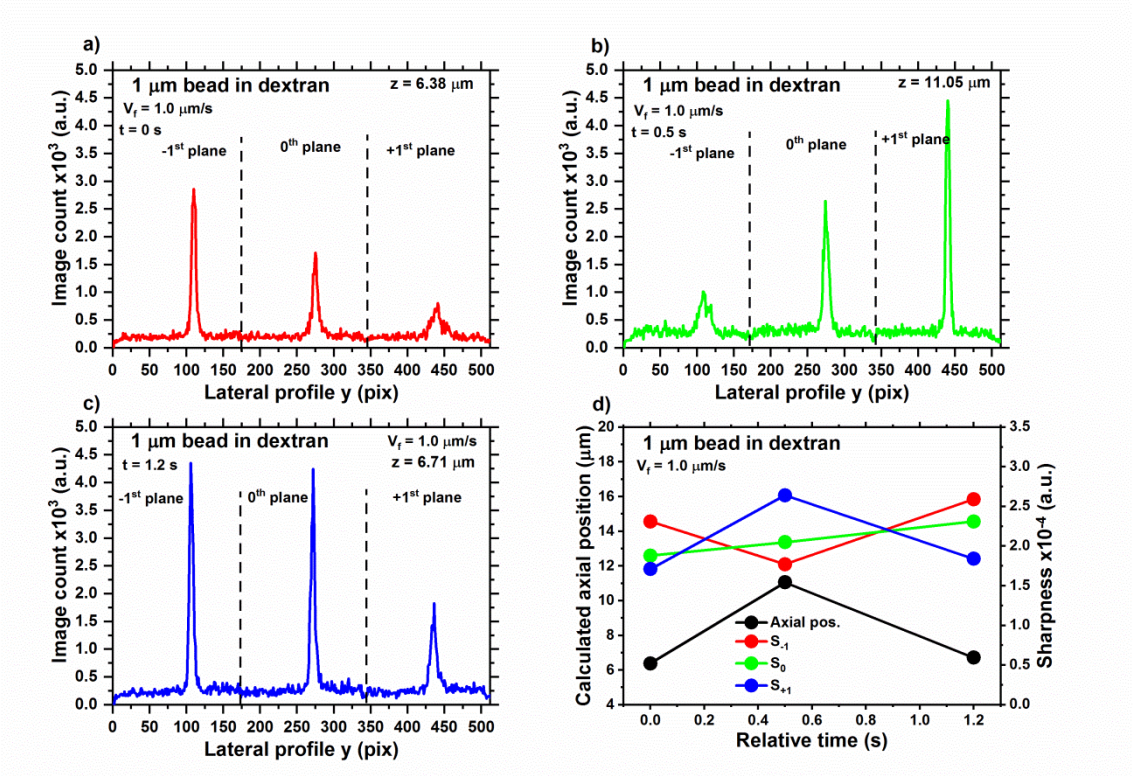

Figure 5.13 Lateral profiles traced along the dashed vertical lines in fig. 5.12a, 5.12b and 5.12c and showing the variation in image counts of the bead in the three planes in fig. 5.12 while flowing over the cell in fig. 5.12a. **a)** t = 0 s, **b)** t = 0.5 s and **c)** t = 1.2 s. The associated sharpness values and the recovered axial positions are shown in **d** with respect to the relative time points. Laser power at sample = 3.56 µW at λ = 488 nm, em gain = 2,000, ET = 100 ms, PS = 630 nm, V_f = 1.0 µl/min.

still possible to observe the top of the cell in focus in the fluorescence image and it was desired to visualise the flow around the top of the cell. In fig. 5.12b, 5.12c and 5.12d the same bead has been highlighted. Setting as t = 0 s the frame in fig. 5.12b, those in fig. 5.12c and 5.121d have been acquired at t = 0.5 s and t = 1.2 s, respectively. The lateral positions of the selected bead have also been identified on the transmission image in fig. 5.12a. As it can be observed, the highlighted bead is more in focus in the -1^{st} plane in fig. 5.12b, i.e. before it reaches the cell position (fig. 5.12a). After 0.5 s the same bead has reached the cell position (fig. 5.12a) and is more focused in the $+1^{st}$ plane (fig. 5.12c), since its axial position has increased. Finally, after other 0.7 s the bead has moved away from the cell (fig. 5.12a) and is again more focused in the -1^{st} plane (fig. 5.12d), due to the reduction in axial position. This can also be visualised by observing the lateral profiles of the bead and the associated axial positions and sharpness values (fig. 5.13). Fig. 5.13 shows the lateral profiles of the selected bead traced through the vertical lines in fig. 5.12b, 5.12c and 5.12d. At t = 0 s (fig. 5.13a) the profile peaks in the -1^{st} plane, where the highest sharpness value is (fig. 5.13d). At t = 0.5 s (fig. 5.13b), instead, the profile peak and the highest sharpness value have moved to the $+1^{st}$ plane (fig. 5.13d). Once the bead has moved away from the cell (fig. 5.13c), the profile peak and the highest sharpness value are again in the -1^{st} plane (fig. 5.13d). In terms of calculated axial positions (fig. 5.13d, done by using the ratiometric algorithm, as in sec. 5.3, and the sharpness curves in fig. 5.5b), the bead moves from z = 6.38 μm at t = 0 s to z = 11.05 μm at t = 0.5 s and to z = 6.71 μm at t = 1.2 s, confirming the change in axial position of the bead while crossing the cell.

Once all the beads have been 3D localised and the tracks have been reconstructed by using the tracking tool of the MUM plugin (sec. 2.5.3), the outliers have been removed by using the same Mathematica code described in sec. 5.3. In fig. 5.14 four selected tracks of beads flowing over the cell are presented. Fig. 5.14a shows the tracks flowing in the x-y plane with the axial positions colour encoded, while fig. 5.14b shows the same tracks in the x-z plane. The beads flow from left to right over the x axis. In general, all tracks in fig. 5.14 seem to follow the cell profile. However, by comparing the tracks in the x-y plane to those in the x-z one, it is clear that the fluctuations in the axial localisations are larger than those in the lateral ones. Track 1 flows near the bottom tail of the cell, around y = 2 μm and just above z = 6 μm. As this track approaches the cell around x = 35 μm, its trajectory in the x-y plane (fig. 5.14a) start to be deflected from the initial one, toward y positions smaller than 2 μm. Simultaneously, at the same x position, the axial position (fig. 5.14b) first increases to

around z = 6.7 µm and then goes again back to 6 µm. After x = 50 µm, x and z positions are slightly modified till around position x = 67 µm, where z increases to above 7 µm, due to what could be the primary cilium of the cell [70] (fig. 5.14a). Track 2 does not change much its lateral position y from around 7 µm - 8 µm (fig. 5.14a). Regarding its axial positions, instead, these initially fluctuate around z = 11 µm (fig. 5.14b). Then, as the track reaches what is probably a cilium of the cell around x = 33 µm, the axial position grows to around 14 µm, to then decrease and increase again to z = 13.6 µm at x around 52 µm, where an unidentified feature of the cell seem to be present. After that, the axial position of this track decreases and starts increasing again, possibly due to the

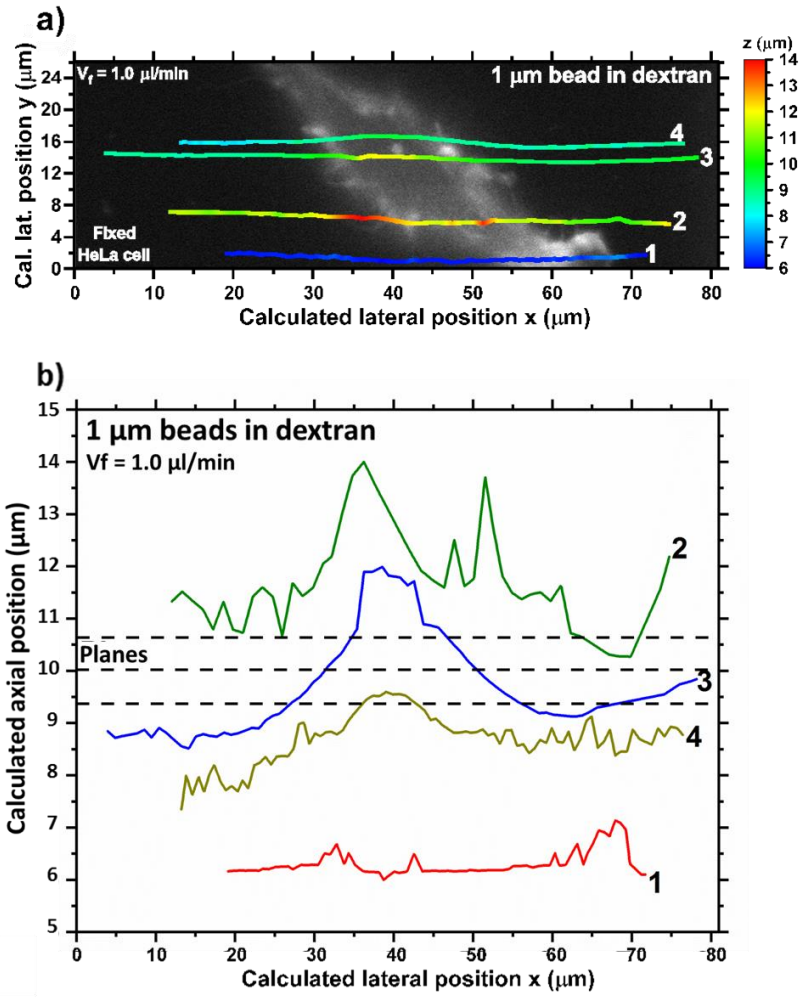

Figure 5.14 a) Four selected 1 µm beads in dextran flowing over the fixed HeLa. The tracks are projected in the x–y plane and their axial positions are colour encoded. **b)** Same beads in **a**, with the tracks projected in the x–z plane. The plane positions are shown. Laser power at sample for the beads = 3.56 µW at λ = 488 nm, laser power at sample for the cell = 0.96 µW at λ = 561 nm, em gain = 2,000, ET = 100 ms, PS = 630 nm, V_f = 1.0 µl/min.

presence of another cell outside the FOV that perturbs the flow, but this has not been verified. Track 3, as the previous one, does not change its lateral y positions much from around 14 μm (fig. 5.14a). In terms of axial positions (fig. 5.14b), these start rising at around x = 25 μm, close to the position of the cell. Between x = 36 μm and x = 42 μm, this track stays on axial positions between 11.5 μm and 12 μm, nearby a feature visible in fig. 5.14a at x = 41 μm. As the track moves away from the cell, its axial positions decrease and tend to increase again, as track 2. Finally, track 4 does not vary its lateral y position from around 16 μm until it approaches the cell at x = 29 μm (fig. 5.14a). Concerning its axial positions (fig. 5.14b), it is initially located between 7.5 μm and 8 μm. After x = 22 μm, the axial positions start to increase up to around 9.6 μm, to then decrease again to a value around 8.5 μm after x = 50 μm, when the track has passed the cell. So, as clearly visible from the tracks in fig. 5.14, the cell perturbs the laminar flow, since the tracks modify their lateral and axial directions, while this has not been observed on the tracks acquired in absence of cells (fig. 5.8). However, differently from the tracks in fig. 5.8, those in fig. 5.14 clearly show more fluctuations. This is due to the increase in autofluorescence (sec. 1.3.2), i.e. background, caused by the paraformaldehyde used to fix the cells [71]. For example, the average background per pixel could be around (189 ± 38) a.u. in an area (40x40 pix^2) where the cell is not present and could rise to (323 ± 67) a.u. in correspondence of the cell position. This raises the average background and its variability in the FOV, in turn disturbing the correct axial localisation (sec. 4.2).

As said above, the Mathematica code described in sec. 5.3 to discard the outliers has been applied. Together with the outliers, all axial positions smaller than 6 μm and bigger than 14 μm have been discarded too, since, as done in sec. 5.3, the axial range has been assumed to be equal to 8 μm (fig. 5.5c) and centred at 10 μm. This has produced almost 22,000 localisation points, three-dimensionally distributed in space. These localisations are all shown in the 3D plot of fig. 5.15a, with the axial positions colour encoded. As it can be seen, the flow appears perturbed around the centre of the plot, where the cell is positioned. As the beads flow over the cell, their axial positions tend to increase and subsequently decrease. The perturbation on the flow profile appears also tilted with respect to the x and y axes, just as the position of cell in fig. 5.14a. Once all the bead positions have been obtained, in order to build the 3D velocity and shear stress fields around the cell it has been necessary to calculate the local velocities of the tracks as done in sec. 5.3. Since the cell perturbs the flow three-dimensionally (fig. 5.14 and 5.15a), it is needed to calculate the components of the velocity along the directions

perpendicular to the flow one too, i.e. V_y and V_z. As in sec. 5.3, the local velocities have been calculated by using the slope function of the software Excel. The moving slope has

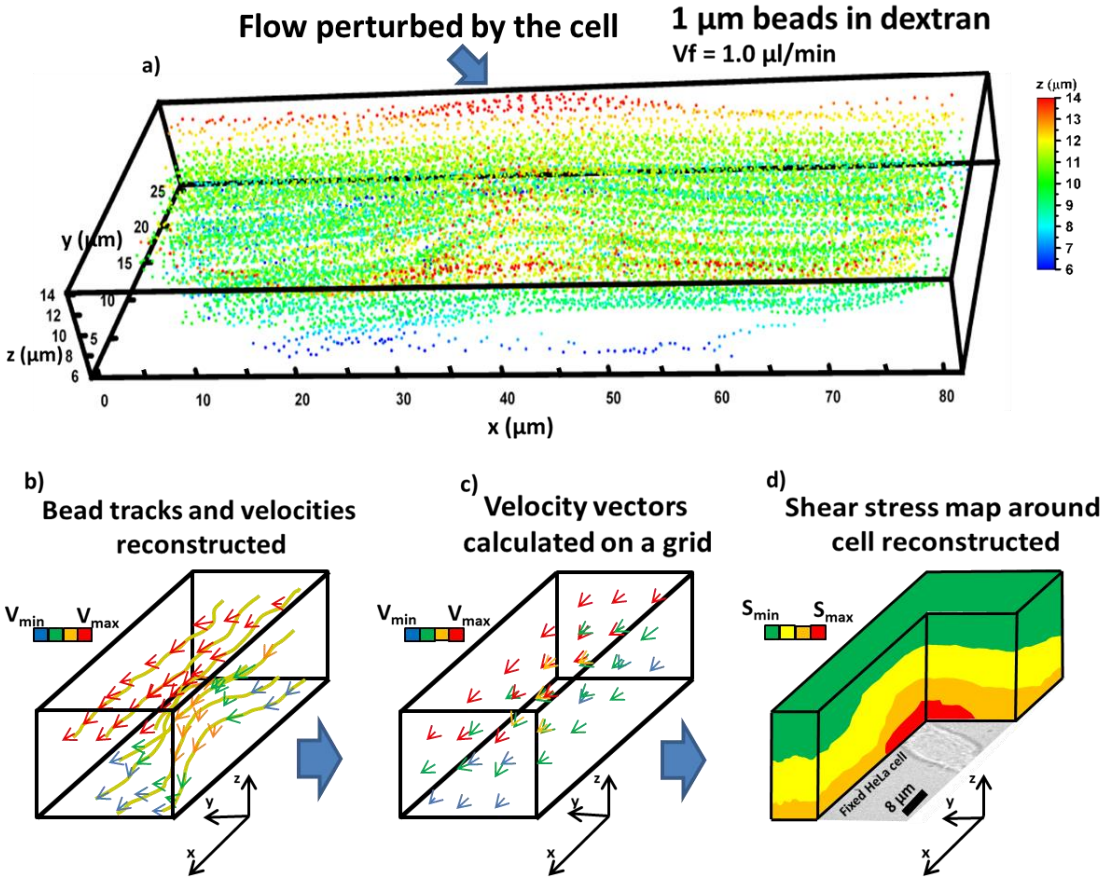

Figure 5.15 a) 3D plot showing all the 1 µm beads in dextran localised while flowing over the HeLa cell in fig. 5.12a. The perturbation to the flow generated by the cell is indicated. The axial positions are colour encoded in the plot. The central plane is at z = 10 µm. Laser power at sample = 3.56 µW at λ = 488 nm, em gain = 2,000, ET = 100 ms, PS = 630 nm, V_f = 1.0 µl/min, total acquisition time = 28 min 20 s. In **b**, **c** and **d** the process to obtain the shear stress map around the cell from the bead tracks is shown. The points constituting the tracks in **b** are used to calculate the local 3D velocities of the tracks. The velocities in **b** are then used to calculate a 3D distribution of velocities over the nodes of a periodic 3D grid and obtain an homogeneous distribution in space of velocity vectors (**c**). The components of the velocity vectors in **c** are finally used to generate the shear stress maps around the cell (eq. 5.9, 5.10 and 5.11) among the different planes (**d**).

been calculated among three adjacent cells rather than seven as in sec. 5.3, so to still remove some noise introduced by the calculations, but at the same time avoid to cancel out the variations due to the features of the cell. Therefore, only the first and last points

of every velocity track have been removed. All the velocities (V_x, V_y and V_z) obtained in this way represent the components of the vectors of the flow, which indicate its local velocities and directions (fig. 5.15b). However, these vectors are not homogeneously distributed over the 3D space and cannot allow the generation of homogeneous shear stress maps around the cell. To avoid this, Dr Kamel Madi has written a Matlab code that fits all the unevenly distributed V_x, V_y and V_z components (fig. 5.15b) into the nodes of a regular grid, which is extended over the 3D FOV acquired with the multiplane system (26x81x8 µm, fig. 5.15a) and has the nodes spaced 1 µm along x, y and z directions. By combining the homogeneous V_x, V_y and V_z fields obtained in this way, it is possible to achieve a 3D map of the velocity vectors evenly distributed around the cell (fig. 5.15c) and, by applying the differentiations in eq. 5.9, 5.10 and 5.11, the shear stress fields among the different planes (i.e. S_{xy}, S_{xz} and S_{yz}, fig. 5.15d).

Once the homogeneously distributed velocity components have been obtained with the Matlab code, velocity and vector fields around the cell have been 3D plotted by using the software Avizo [72]. Since the density of localised points is lower around the borders of the 3D FOV (fig. 5.15a), it has been necessary to crop the velocity fields in order to avoid the visualisation of the interpolation errors generated by the lack of points. The 3D FOV has been reduced from 26x81x8 μm^3 (fig. 5.15a) to 21.1x53.9x6.6 μm^3 (fig. 5.16, 5.17 and 5.18). In Avizo the velocity component fields have been filtered by using a moving 3D Gaussian filter to reduce the fluctuations amplified by the calculations of the velocities. In addition, the velocities calculated at the nodes of the regular grid (with the Matlab code) have also been linearly interpolated to have continuous velocity maps. By using eq. 5.8 the velocity maps can be combined to obtained the magnitude of the total velocity (V_{mag}) and the vector map. The latter is presented in fig. 5.16 in three different orientations, with V_{mag} encoded in the colour and in the vector lengths. The fluid flows along the x direction, from right to left. As observable in the top view of fig. 5.16a, the vectors are strongly deviated from the flow direction (x) around the position of the cell. This is because the cell behaves as an obstacle that perturbs the flow. In particular, the flow is almost completely deviated

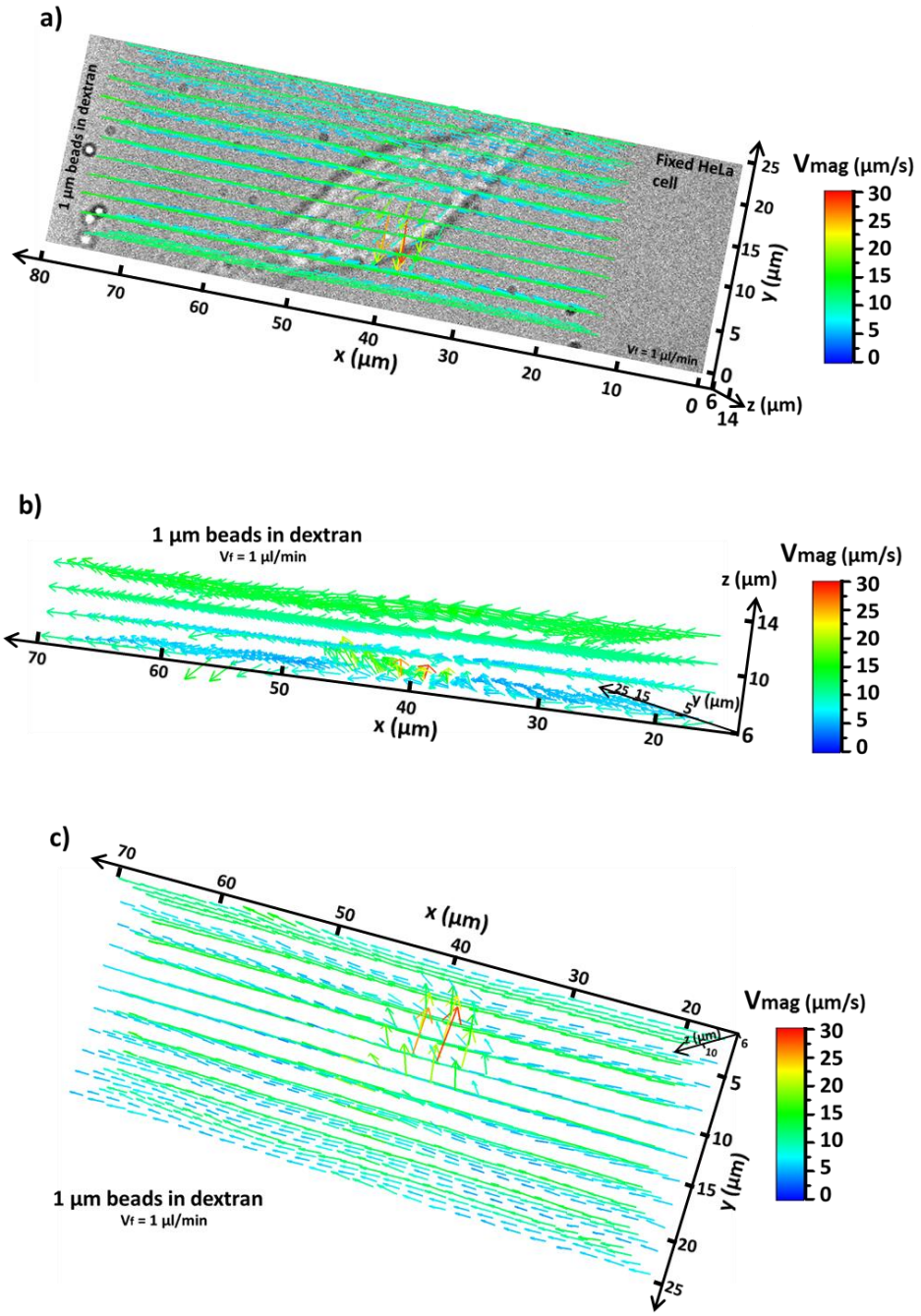

Figure 5.16 3D plots showing the velocity vectors around the selected fixed HeLa cell through different orientations. The magnitude velocities are colour encoded in the vectors. **a)** Top view, **b)** side view and **c)** bottom view. The fluid of 1 µm beads in dextran flows from right to left along the x axis. The central plane is at z = 10 µm. Laser power at sample = 3.56 µW at λ = 488 nm, em gain = 2,000, ET = 100 ms, PS = 630 nm, V_f = 1.0 µl/min.

toward the y direction, perpendicularly to the flow one. However, this perturbation does not happen everywhere on the cell position. It seems to be localised in a region of interest (ROI) that goes from around 5 µm to 15 µm along the y direction and from

35 µm to 45 µm along the x one, i.e. a ROI of around 10x10 µm in the x-y plane. This is probably the region where the cell has its most prominent features. In fig. 5.14 track 2 and track 3 flow over this region and effectively are those with the largest axial values in the selected track set. By observing the side view of the vector field in fig. 5.16b, it is possible to see that the perturbation to the flow occurs predominantly in the above identified ROI between the axial positions of around 6 µm and 10 µm. The latter (10 µm) is the position where the top of the cell has been identified and the central plane has been positioned. The axial perturbation to the vector field tends to reduce above 10 µm. The side view in fig. 5.16b shows also the increase in speed in the flow direction at higher axial positions, due to the laminar regime of the flow [13]. The bottom view in fig. 5.16c confirms the perturbation of the flow in the above identified ROI.

To have a more detailed view of the behaviour of the flow around the cell, the magnitude of the velocity components (V_x, V_y and V_z) and the total velocity magnitude (V_{mag}) are presented separately in fig. 5.17, together with some selected vector planes. The 3D maps have been cropped in order to show their profiles around the centre of the cell. Starting from V_y, i.e. the velocity along the x direction, its magnitude is shown in fig. 5.17a (side view) and 5.17b (bottom view). As noticeable, V_y, which in absence of obstacles should be around 0 µm/s, has its largest value (27.3 µm/s) around the centre of the cell, within the ROI identified in fig. 5.16, where the vectors were clearly deviated toward the y direction. In fig. 5.17b it can be observed that the area where V_y assumes values well above the minimum one calculated far from the cell place ($1.7 \cdot 10^{-4}$ µm/s) does not cover the full surface of the cell, as the ROI in fig. 5.16. In addition, the perturbation on V_y around the tails of the cell appears negligible. This can be explained by considering that the axial range has been observed between the axial positions 6 µm and 14 µm, but the perturbations to the flow caused by the tails of the cell might occur well below z = 6 µm. However, this has not been verified. Axially, the perturbation to V_y appears curved, as probably the shape of the cell is. In the ROI indicated in fig. 5.16, around z = 8 µm, V_y can assume values around 7 µm/s. Moving to V_x, i.e. the component of the velocity along the flow direction, the magnitude of its field is presented in fig. 5.17c and 5.17d. The side view in fig. 5.17c indicates how V_x increases moving toward larger z values, as expected from a laminar flow. However, it also shows how the V_x component gets reduced in intensity in the region where, conversely, V_y has its maximum. In that region V_x is at its minimum ($\approx$ 0.01 µm/s), since the flow is completely deviated toward the x direction. In the bottom view plot of fig. 5.17d another region of interest beside the previous one can be identified. This region lies

between x equal to 35 µm and 50 µm and y equal to 13 µm and 21 µm and shows a V_x higher (≈ 12.5 µm/s) than in the surrounding regions (around 5 µm/s - 7 µm/s) when z is between 6 µm and 7.5 µm. The increase in V_x visible in this region corresponds to a change in direction of the flow toward z, as visible in the vectors in fig. 5.17b. In this region the overall magnitude of the vectors increases. This could be due to some protuberance of the cell, which accelerates the flow toward x and z directions. Unfortunately, this cannot be understood by the mere analysis of the velocities. Regarding the V_x velocities at positions far from those of the cell, these appear lower

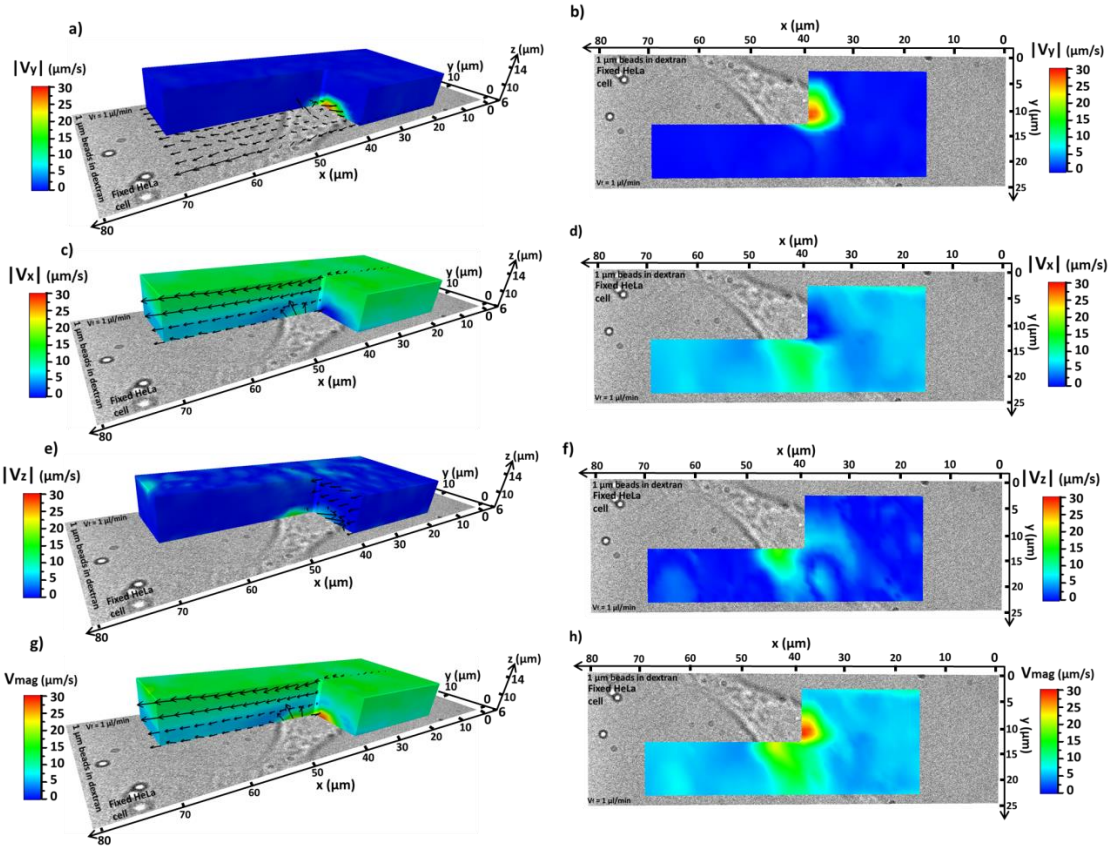

Figure 5.17 3D maps of the absolute values of the velocity components and magnitude velocity associated to the fluid of 1 µm beads in dextran flowing around the chosen fixed HeLa cell. The fluid flows from right to left along the x axis. The images in **a**, **c**, **e** and **g** show the side view, while those in **b**, **d**, **f** and **h** the bottom view. V_y is shown in **a** and **b**, V_x in **c** and **d**, V_z in **e** and **f** and V_{mag} in **g** and **h**. The vectors have been extracted from the 3D vector map. The maps have been generated by using the software Avizo. The central plane is at z = 10 µm. Laser power at sample = 3.56 µW at λ = 488 nm, em gain = 2,000, ET = 100 ms, PS = 630 nm, V_f = 1.0 µl/min.

than those of a laminar flow in absence of cells. In particular, at the z positions of 6 µm and 12.6 µm (i.e. the axial extremes of the field plots) V_x is equal to, respectively,

around 6.7 µm/s and 16 µm/s, while, following the theoretical equation (eq. 5.4), it should have been equal to, respectively, 11.3 µm/s and 22 µm/s. This is not surprising, since it has already been observed how the measured flow velocities become lower than the theoretical ones when perturbed by the presence of cells and tend to decrease as the cell density grows [31]. However, the reduction in accuracy on the measured axial positions and velocities caused by the presence of the cells, which raise the average background and its variability in the FOV might also play a role. Regarding the intensity of the V_z component, this is presented in fig. 5.17e and 5.17f. As the other two components, also this one shows a strong deviation around the position of the cell. As V_y, also V_z is expected to be negligible in a laminar flow flowing along the x direction. Indeed, far from the cell its value is around $5.3 \cdot 10^{-5}$ µm/s, but within the same ROI identified in fig. 5.17d, where the magnitude of V_x increases, V_z grows too and goes up to around 17 µm/s, since the flow is deviated toward the z direction by the cell. V_z tends to increase also in the ROI where V_y is maximised (fig. 5.17b), reaching a value around 7.3 µm/s. Another aspect to notice in fig. 5.17e is the presence of randomly distributed relative maxima on top of the 3D plot, i.e. around z = 12.6 µm. Considering that the top of the cell is located around z = 10 µm, there should be nothing strongly perturbing the flow at that axial position and not directly above the cell. Therefore, some of those relative maxima are probably just caused by the false axial localisation of some tracks at larger axial positions. Indeed, as seen in fig. 5.11, above roughly z = 10 µm the localisation accuracy tends to be significantly reduced. Finally, in fig. 5.17g and 5.17h the velocity magnitude V_{mag} (eq. 5.8) is shown. As expected, V_{mag} presents all the characteristics of the three velocity components just described, since it represents the intensity of the vector field and the overall behaviour of the flow (fig. 5.16). In those regions far from the cell position, where V_y and V_z are negligible, V_{mag} behaves as a laminar flow and has the same characteristics of V_x (fig. 5.17c). Around the cell position, instead, V_{mag} is maximised (28.6 µm/s) and shows the same ROIs observable in fig. 5.17b, 5.17d and 5.17f, due to the variation of V_x, V_y and V_z around the cell.

5.4.1 *Evaluation of the shear stress around the cell*

As described above and observable in fig. 5.17, the cell perturbs the laminar flow and allows the introduction of non-zero velocity components along the y and z directions. This, in turn, generates shear stress in the x-y, y-z and x-z planes, since the flow is deviated and stresses the cell along multiple planes in space. By using the velocity component fields in fig. 5.17 and the shear stress equations (eq. 5.9, 5.10 and 5.11), the

shear stress among the three planes mentioned above, i.e. S_{xy}, S_{yz} and S_{xz}, can be calculated. This has been done by using the software Avizo and applying the same Gaussian filter and interpolation used for the velocity components. In fig. 5.18 the magnitudes of the shear stress fields around the cell are presented. As expected, in all the three planes the shear stress results maximised around the cell, since that is the area where the wall shear stress is generated. Starting from S_{xy}, i.e. the shear stress among x-y planes (fig. 5.18a and 5.18b, eq. 5.9), its magnitude is maximised in a region around x = 40 µm and y = 12 µm (≈ 2.5 Pa), which is within the ROIs identified in fig. 5.17b and 5.17d, where, respectively, V_y and V_x have their peaks. Moving to S_{yz},

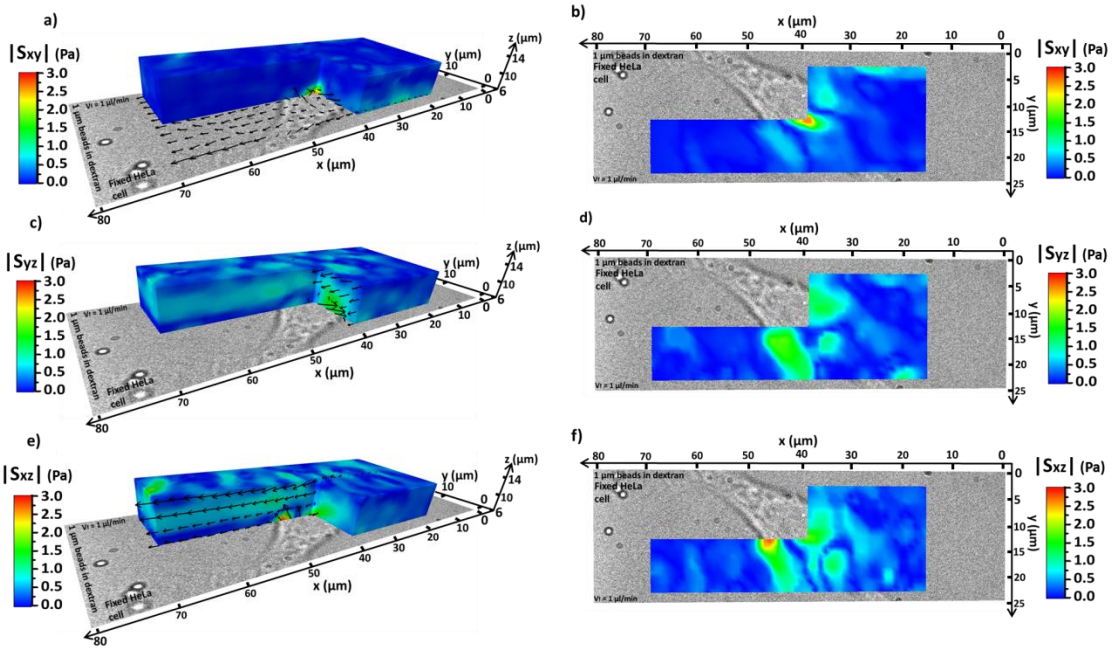

Figure 5.18 3D maps of the absolute values of the shear stress among different planes generated by the fluid of 1 µm beads in dextran flowing around the used fixed HeLa cell. The fluid flows from right to left along the x axis. The images in **a**, **c**, **e** and **g** show the side view, while those in **b**, **d**, **f** and **h** the bottom view. S_{xy} is shown in **a** and **b**, S_{yz} in **c** and **d** and S_{xz} in **e** and **f**. The vectors have been extracted from the 3D vector map. The maps have been generated by using the software Avizo. The central plane is at z = 10 µm. Laser power at sample = 3.56 µW at λ = 488 nm, em gain = 2,000, ET = 100 ms, PS = 630 nm, V_f = 1.0 µl/min.

i.e. the shear stress among y-z planes (fig. 5.18c and 5.18d, eq. 5.11), also in this case its magnitude is maximised around the ROIs where V_y and V_z are higher (fig. 5.17b and 5.17f). This can also be visualised by observing the vectors in fig. 5.18c and 5.18e, which, respectively, show a strong deviations toward y and z directions in the regions

where S_{yz} is higher in fig. 5.18d. In particular, S_{yz} reaches a value of around 1.7 Pa in the region where V_x is maximised in fig. 5.17d, while it goes up to a value of 1.5 Pa where V_y and V_z are maximised in fig. 5.17b and 5.17f. Another aspect to notice in fig. 5.18c is the presence of a local high S_{yz} band (≈ 0.7 Pa), localised around the middle of the observed axial range. Some simulations in the literature [3], even if based on different systems, have shown that obstacles in the flow can introduce similar high velocity and shear stress bands. The latter is generated by the shear between the fluid layers in the y-z planes due to the fluid first climbing and then climbing down the cell, as observable on the vectors in fig. 5.17c, 5.17g and 5.18e. Finally, the magnitude of S_{xz}, i.e. the shear stress among x-z planes (fig. 5.18e and 5.18f, eq. 5.10) shows its maximum value (≈ 2.7 Pa) in the same region where V_x and V_z are both maximised (fig. 5.17d and 5.17f, respectively). In the region where V_x assumes its minimum value (fig. 5.17d), S_{xz} is reduced too (≈ 1.6 Pa), since in that case only V_z contributes to S_{xz}. In fig. 5.18e it can be noticed the presence of another relatively high shear stress band in the middle of the axial range (≈ 0.9 Pa), which is similar to that in fig. 5.18c and probably generated in the same way, but this time due to the shear stress between x-z planes. This shear stress middle band is not present in the S_{xy} plot (fig. 5.18a), while it is observable only in the shear fields that have an axial velocity V_z component (fig. 5.18c and 5.18e). Therefore, V_z must be directly responsible for it. In all the 3D shear stress fields in fig. 5.18 it is clearly visible how the shear stress rises around the cell position. Far from the cell, instead, it can assume values near 0 Pa, but there are also some local maxima randomly distributed around the cell. These are mostly present in the S_{yz} and S_{xz} plots (fig. 5.18c and 5.18e) and derive from the false axial localisations in the V_z plot (fig. 5.17e).

In conclusion, this section has shown that multifocal microscopy can be used as a tool to reconstruct velocity and shear stress fields around the cell and perform μPIV. MUM has been able to observe the perturbations to the flow caused by the cell and how different areas of the latter influence the flow differently (fig. 5.16, 5.17 and 5.18). Therefore, MUM has allowed the reconstruction of the shear stress at subcellular level. Concerning the velocities calculated along the flow direction (V_x), these have effectively been measured as lower than the theoretical ones (fig. 5.17c, eq. 5.4). However, the latter has also been found in other studies in presence of cells [31], thus it can be considered as widely expected. In addition, it has not been noticed in absence of cells (fig. 5.11). Regarding the reconstructed shear stress maps, these present characteristics similar to those observed in the literature [3, 4] (e.g. shear stress maxima

around the cells and shear stress bands, fig. 5.18). However, the fluctuations in the tracks (fig. 5.14), due to the increase in average background caused by the presence of the cell, have, in turn, introduced some fluctuations in the shear stress maps (fig. 5.18), thus reducing the overall accuracy. A simulation of the flow around a geometrical shape equivalent to that of the studied cell could be taken into consideration to further strengthen the results [30, 31]. This could be done by acquiring a 3D image of the cell before the shear stress experiment, to then reconstruct its 3D shape and perform a computational fluid dynamics simulation [73] under the same experimental conditions.

5.5 Summary and considerations

This chapter has studied the application of MUM as a tool to perform µPIV and evaluate, for the first time, velocity and shear stress fields around a cell. To this purpose, MUM has been first validated against the theoretical expected behaviour (eq. 5.4) and confocal microscopy by reconstructing the flow velocity profile inside a PPFC (sec. 5.3). This has shown that MUM, within 10 µm from the coverslip, can achieve average accuracies on the calculated velocities that are slightly worse than the corresponding results obtainable with confocal microscopy (table 5.3, fig. 5.10). However, at larger axial distances from the coverslip, MUM becomes considerably inferior to confocal in terms of accuracy. Despite this, MUM has been capable of producing better results with respect to the values reported in the literature (table 5.1) for other 4D techniques.

After the validation step, MUM has been tested to reconstruct the velocity and shear stress profiles (eq. 5.8, 5.9, 5.10 and 5.11) around a fixed HeLa cell. This has clearly shown the perturbation to the flow caused by the cell (fig. 5.15a), which has generated the velocity components (V_y and V_z) y and z direction (fig. 5.16 and 5.17). Around the cell, V_y and V_z have reached maximum values of 27.3 µm/s and 17 µm/s, respectively. The interaction between the cell and the flow has, in turn, caused shear stress among the x-y, y-z and x-z planes (fig. 5.18, eq. 5.9, 5.10 and 5.11). Near the cell position, the wall shear stress has reached values roughly between 1 Pa and 3 Pa. In general, the behaviour of the velocity and shear stress fields around the cell are compatible with what has been observed in other studies [3, 4]. However, it is also important to notice the presence of fluctuations in the calculated fields that are not caused by the cell (fig. 5.17 and 5.18) and are due to false axial localisations that reduce the accuracy.

The point of strength of MUM is the acquisition speed, since this technique, differently from other optical microscopies, can acquire 3D FOVs simultaneously [65]. This is a very important characteristic in situations where the biological systems under study evolve quickly and it is necessary monitoring in real time entire volumes to correlate the sample responses to the forces generated by the flow. Consequently, MUM could help to clarify some of the mechanisms through which organisms develop, grow and adapt while undergoing fluid shear stress. However, due to the observed reduction in accuracy caused by the presence of incorrect localisations (fig. 5.17 and 5.18), further tests on real and simulated data should be performed to improve and strongly validate the application of MUM to µPIV.

5.6 References

[1] R. Lindken, M. Rossi, S. Große and J. Westerweel, "Micro-Particle Image Velocimetry (uPIV): Recent developments applications, and guidelines," Lab on a Chip, vol. 9, no. 17, pp. 2551-2567, 2009.

[2] R. Rahbari, T. Sheahan, V. Modes, P. Collier, C. Macfarlane and R. M. Badge, "A novel L1 retrotransposon marker for HeLa cell line identification," Biotechniques, vol. 46, no. 4, pp. 277-+, 2009.

[3] U. M. Balaguru, L. Sundaresan, J. Manivannan, R. Majunathan, K. Mani, A. Swaminathan and S. Venkatesan, "Disturbed flow mediated modulation of shear forces on endothelial plane: A proposed model for studying endothelium around atherosclerotic plaques," Scientific Reports, vol. 6, 2016.

[4] P. Eshtehardi, M. C. McDaniel, J. Suo, S. S. Dhawan, L. H. Timmins, J. N. G. Binongo, L. J. Golub, M. T. Corban, A. V. Finn, J. N. Oshinsk, A. A. Quyyumi, D. P. Giddens and H. Samady, "Association of coronary wall shear stress with atherosclerotic plaque burden, composition, and distribution in patients with coronary artery disease," Journal of the American Heart Association, p. 1:e002543, 2012.

[5] G. S. Kassab and D. Lu, "Role of shear stress and stretch in vascular mechanobiology," Journal of the Royal Society Interface, vol. 8, no. 63, pp. 1379-1385, 2011.

[6] J. A. Kornuta, Z. Nepiyushchikh, O. Y. Gasheva, A. Mukherjee, D. C. Zawieja and J. B. Dixon, "Effects of dynamic shear and transmural pressure on wall shear stress

sensitivity in collecting lymphatic vessels," American Journal of Physiology - Regulatory Integrative and Comparative Physiology, vol. 309, no. 9, pp. R1122-R1134, 2015.

[7] J. B. Dixon, S. T. Greiner, A. A. Gashev, G. L. Cote, J. E. Moore and D. C. Zawieja, "Lymph flow, shear stress, and lymphocyte velocity in rat mesenteric prenodal lymphatics," Microcirculation, vol. 13, no. 7, pp. 597-610, 2006.

[8] W. E. Thomas, E. E. Trintchina, M. Forero, V. Vogel and E. V. Sokurenko, "Bacterial adhesion to target cells enhanced by shear force," Cell, vol. 109, no. 7, pp. 913-923, 2002.

[9] J. P. Fisher and A. B. Yeatts, "Bone tissue engineering bioreactors: Dynamic culture and the influence of shear stress," Bone, vol. 48, no. 2, pp. 171-181, 2011.

[10] M. Hosseini and M. Julaey, "Stem cells culture bioreactor fluid flow, shear stress and microcarriers dispersion analysis using computational fluid dynamics," Journal of Applied Biotechnology Reports, vol. 3, no. 2, pp. 425-431, 2016.

[11] A. Horikawa, K. Okada, K. Sato and M. Sato, "Morphological changes in osteoblastic cells (MC3T3-E1) due to fluid shear stress: cellular damage by prolonged application of fluid shear stress," Tohoku Journal of Experimental Medicine, vol. 191, no. 3, pp. 127-137, 2000.

[12] J. Kiusalaas and A. Pytel, "Shear stress," in Mechanics of materials, Cengage learning, 2001, pp. 18-19.

[13] R. F. Boucher and Y. Nakayama, "Flow between parallel plates," in Introduction to fluid mechanics, Butterworth-Heinemann, 2000, pp. 87-94.

[14] S. Chien, "Mechanotransduction and endothelial cell homeostasis: the wisdom of the cell," American Journal of Physiology - Heart and Circulatory Physiology, vol. 292, no. 3, pp. H1209-H1224, 2007.

[15] R. Ogawa and C. Y. Huang, "Mechanotransduction in bone repair and regeneration," FASEB Journal, vol. 24, no. 10, pp. 3625-3632, 2010.

[16] S. Chien and J. J. Chiu, "Effects of disturbed flow on vascular endothelium: pathophysiological basis and clinical perspectives," Physiological Reviews, vol. 91, no. 1, pp. 327-387, 2011.

[17] P. F. Davies, "Hemodynamic shear stress and the endothelium in cardiovascular pathophysiology," Nature Clinical Practice Cardiovascular Medicine, vol. 6, no. 1, pp. 16-26, 2009.

[18] G. D. a. M. Soyer, "Introducing shear stress in the study of bacterial adhesion," Journal of Visualized Experiments, no. 55, 2011.

[19] R. Balint, N. J. Cassidy and S. H. Cartmell, "Electrical stimulation: A novel tool for tissue engineering," Tissue Engineering Part B - Reviews, vol. 19, no. 1, pp. 48-57, 2013.

[20] A. S. French, "Mechanotransduction," Annual Review of Physiology, vol. 54, pp. 135-152, 1992.

[21] M. L. Tate, J. R. Adamson, A. E. Tami and T. Bauer, "The osteocyte," The International Journal of Biochemistry and Cell Biology, vol. 36, no. 1, pp. 1-8, 2004.

[22] R. J. Bacabac and J. Klein-Nulend, "Mechanical loading and how it affects bone cells: the role of the osteocyte cytoskeleton in maintaining our skeleton," European Cells and Materials, vol. 24, pp. 278-291, 2012.

[23] A. Liedert, D. Kaspar, R. Blakytny, L. Claes and A. Ignatius, "Signal transduction pathways involved in mechanotransduction in bone cells," Biochemical and Biophysical Research Communications, vol. 349, no. 1, pp. 1-5, 2006.

[24] C. T. Hung, F. D. Allen, S. R. Pollack and C. T. Brighton, "Intracellular Ca^{2+} stores and extracellular Ca^{2+} are required in the real-time Ca^{2+} response of bone cells experiencing fluid flow," Journal of Biomechanics, vol. 29, no. 11, pp. 1411-1417, 1996.

[25] H. Kodama, Y. Amagai, H. Sudo, S. Kasai and S. Yamamoto, "Establishment of a clonal osteogenic cell line from newborn mouse calvaria," Japanese Journal of Oral Biology, vol. 23, no. 4, pp. 899-901, 1981.

[26] X. Liu, X. Zhang and I. Lee, "A quantitative study on morphological responses of osteoblastic cells to fluid shear stress," Acta Biochimica et Biophysica Sinica, vol. 42, no. 3, pp. 195-201, 2010.

[27] R. P. Martins, J. D. Finan, F. Guilak and D. A. Lee, "Mechanical regulation of nuclear structure and function," Annual Review of Biomedical Engineering, vol. 14, pp. 431-455, 2012.

[28] C. M. Brown and D. J. Webb, "Epi-fluorescence microscopy," Methods in Molecular Biology, vol. 931, pp. 29-59, 2013.

[29] J. B. Pawley, Handbook of biological confocal microscopy, Springer, 2006.

[30] E. J. Anderson, T. D. Falls, A. M. Sorkin and M. L. K. Tate, "The imperative for

controlled mechanical stresses in unraveling cellular mechanisms of mechanotransduction," Biomedical Engineering Online, vol. 5, no. 27, 2006.

[31] M. J. Song, D. Dean and M. L. K. Tate, "In situ spatiotemporal mapping of flow fields around seeded stem cells at the subcellular length scale," Plos One, vol. 5, no. 9, 2010.

[32] S. Fu, P. H. Biwolé and C. Mathis, "A Comparative Study of Particle Image Velocimetry (PIV) and Particle Tracking Velocimetry (PTV) for airflow measurement," International Journal of Mechanical, Aerospace, Industrial, Mechatronic and Manufacturing Engineering, vol. 9, no. 1, pp. 40-45, 2015.

[33] S. J. Williams, C. Park and S. T. Wereley, "Advances and applications on microfluidic velocimetry techniques," Microfluidics And Nanofluidics, vol. 8, no. 6, pp. 709-726, 2010.

[34] C. Cierpka and C. J. Kaehler, "Particle imaging techniques for volumetric three-component (3D3C) velocity measurements in microfluidics," Journal of Visualization, vol. 15, no. 1, pp. 1-31, 2012.

[35] P. Zammit, G., Carles and A. R. Harvey, "3D imaging and ranging in a snapshot," Optical Systems Design 2015: Computational Optics, vol. 9630, no. 963004, 2015.

[36] Y. Zhou, P. Zammit and A. R. Harvey, "3D microfluidic particle image velocimetry with extended depth-of-field and a single camera," Digital Holography and Three-Dimensional Imaging, 2016.

[37] Y. Zhou, P. Zammit, V. Zickus, G. Carles, J. Taylor and A. R. Harvey, "Video-rate 3D particle tracking with extended depth-of-field in thick biological samples," Computational Optical Sensing and Imaging, 2017.

[38] Y. Zhou, P. Zammit, G. Carles and A. R. Harvey, "Computational localization microscopy with extended axial range," Optics Express, vol. 26, no. 6, pp. 7563-7577, 2018.

[39] P. Cavadini, H. Weinhold, M. Tönsmann, S. Chilingaryan, A. Kopmann, A. Lewkowicz, C. Miao, P. Scharfer and W. Schabel, "Investigation of the flow structure in thin polymer films using 3D µPTV enhanced by GPU," Experiments In Fluids, vol. 59, no. 4, 2018.

[40] M. Tonsmann, F. Krohl, P. Cavadini, P. Scharfer and W. Schabel, "Calibration Routine for Quantitative Three-Dimensional Flow Field Measurements in Drying Polymer Solutions Subject to Marangoni Convection," Colloids and Interfaces, vol.

3, no. 1, 2019.

[41] C. Cierpka, M. Rossi, F. M. R. Segura.1 and C. J. Kähler, "Comparative study of the uncertainty of stereoscopic micro-PIV, wavefront-deformation micro-PTV, and standard micro-PIV," 15th International Symposium on Applications of Laser Techniques to Fluid Mechanics, 2010.

[42] C. Cierpka, M. Rossi, R. Segura, F. Mastrangelo and C. J. Kahler, "A comparative analysis of the uncertainty of astigmatism-micro-PTV, stereo-micro-PIV, and micro-PIV," Experiments in Fluids, vol. 52, no. 3, pp. 605-615, 2012.

[43] D. B. Murphy, "Diffraction and spatial resolution," in Fundamentals of light microscopy and electronic imaging, Wiley - Liss, 2001, pp. 85-96.

[44] J. M. Geary, "Field curvature and distortion," in Introduction to lens design, Willmann-Bell, Inc., 2002, pp. 75-77.

[45] G. Elsinga, F. Scarano, B. Wieneke and B. W. v. Oudheusden, "Tomographic particle image velocimetry," Experiments in Fluids, vol. 41, no. 6, pp. 933-947, 2006.

[46] S. I. Kabanikhin, Inverse and ill-posed problems: Theory and applications, De Gruyter, 2012.

[47] K. D. Hinsch, "Holographic particle image velocimetry," Measurement Science and Technology, vol. 13, no. 7, pp. R61-R72, 2002.

[48] S. Chen, N. Angarita-Jaimes, D. Angarita-Jaimes, B. Pelc, A. H. Greenaway, C. E. Towers, D. Lin and D. P. Towers, "Wavefront sensing for three-component three-dimensional flow velocimetry in microfluidics," Experiments in Fluids, vol. 47, no. 4-5, pp. 849-863, Experiments in Fluids, 2009.

[49] C. Cierpka, R. Segura, R. Hain and C. J. Kahler, "A simple single camera 3C3D velocity measurement technique without errors due to depth of correlation and spatial averaging for microfluidics," Measurement Science and Technology, vol. 21, no. 4, 2010.

[50] B. Huang, W. Wang, M. Bates and X. Zhuang, "Three-dimensional super-resolution imaging by stochastic optical reconstruction microscopy," Science, vol. 319, no. 5864, pp. 810-813, 2008.

[51] S. Y. Yoon and K. C. Kim, "3D particle position and 3D velocity field measurement in a microvolume via the defocusing concept," Measurement Science and Technology, vol. 17, no. 11, pp. 2897-2905, 2006.

[52] M. G. Olsen and R. J. Adrian, "Out-of-focus effects on particle image visibility and correlation in microscopic particle image velocimetry," Experiments in Fluids, vol. 29, pp. S166-S174, 2000.

[53] J. S. Park and K. D. Kihm, "Three-dimensional micro-PTV using deconvolution microscopy," Experiments in Fluids, vol. 4, no. 3, pp. 491-499, 2006.

[54] S. D. Peterson, H. S. Chuang and S. T. Wereley, "Three-dimensional particle tracking using micro-particle image velocimetry hardware," Measurement Science and Technology, vol. 19, no. 11, p. 115406, 2008.

[55] A. Tahmasbi, S. Ram, J. Chao, A. V. Abraham, F. W. Tang, E. S. Ward and R. Ober, "Designing the focal plane spacing for multifocal plane microscopy," Optics Express, vol. 2, no. 14, pp. 16706-16721, 2014.

[56] A. Tahmasbi, S. Ram, J. Chao, A. V. Abraham, E. S. Ward and R. Ober, "An information-theoretic approach to designing the plane spacing for multifocal plane microscopy," Three-Dimensional and Multidimensional Microscopy: Image Acquisition and Processing XXII, vol. 9330, no. 933011, 2015.

[57] E. R. Dowski and W. T. Cathey, "Extended depth of field through wave-front coding," Applied Optics, vol. 34, no. 11, pp. 1859-1866, 1995.

[58] R. Dahm, "The zebrafish exposed," American Scientist, vol. 94, no. 5, pp. 446-453, 2006.

[59] Y. S. Choi and S. J. Lee, "Three-dimensional volumetric measurement of red blood cell motion using digital holographic microscopy," Applied Optics, vol. 48, no. 16, pp. 2983-2990, 2009.

[60] R. F. Boucher and Y. Nakayama, "Reynolds number," in Introduction to fluid mechanics, Butterworth-Heinemann, 2000, p. 46.

[61] W. O. Lane, A. E. Jantzen, T. A. Carlon, R. M. Jamiolkowski, J. E. Grenet, M. M. Ley, J. M. Haseltine, L. J. Galinat, F. H. Lin, J. D. Allen, G. A. Truskey and H. E. Achneck, "Parallel-plate flow chamber and continuous flow circuit to evaluate endothelial progenitor cells under laminar flow shear stress," Journal of Visualized Experiments, vol. 59, 2012.

[62] A. K. Wong, P. LLanos, N. Boroda, S. R. Rosenberg and S. Y. Rabbany, "A parallel-plate flow chamber for mechanical characterization of endothelial cells exposed to laminar shear stress," Cellular and Molecular Bioengineering, vol. 9, no. 1, p. 127–138, 2016.

[63] D. R. Sandison and W. W. Webb, "Background rejection and signal-to-noise optimization in confocal and alternative fluorescence microscopes," Applied Optics, vol. 33, no. 4, pp. 603-615, 1994.

[64] C. F. Snyder, H. S. Isbell, M. R. Dryden and N. B. Holt, "Optical rotations, refractive indices, and densities of dextran solutions," Journal of Research of the National Bureau of Standards, vol. 53, no. 3, pp. 131-137, 1954.

[65] P. A. Dalgarno, H. I. Dalgarno, A. Putoud, R. Lambert, L. Paterson, D. C. Logan, D. P. Towers, R. J. Warburton and A. H. Greenaway, "Multiplane imaging and three dimensional nanoscale particle tracking in biological microscopy," Optics express, vol. 18, no. 2, pp. 877-884, 2010.

[66] B. Jähne, "Velocity Smearing," in Practical handbook on image processing for scientific and technical applications, 2nd ed., CRC PRESS, 2004, p. 297.

[67] R. E. Kalman, "A new approach to linear filtering and prediction problems," Transactions of the ASME – Journal of Basic Engineering, vol. 82, pp. 35-45, 1960.

[68] K. Fukunaga, "An optimal global nearest neighbor metric," IEEE Transactions on Pattern Analysis and Machine Intelligence, vol. PAMI-6, no. 3, pp. 314-318, 1984.

[69] "Microsoft Excel," [Online]. Available: https://products.office.com/en-gb/excel. [Accessed September 2018].

[70] M. M. Falk and T. J. Kowal, "Primary cilia found on HeLa and other cancer cells," Cell Biology International, vol. 39, no. 11, pp. 1341-7, 2015.

[71] Y. Williams, S. Byrne, M. Bashir, A. Davies, A. Whelan, Y. Gun'ko, D. Kelleher and Y. Volkov, "Comparison of three cell fixation methods for high content analysis," Journal of Microscopy, vol. 232, p. 91–98, 2008.

[72] "Avizo," [Online]. Available: https://www.fei.com/software/amira-avizo/. [Accessed September 2018].

[73] H. Versteeg and W. Malalasekera, An introduction to computational fluid dynamics: The finite volume method, 2nd ed., Pearson Education, 2007.

Chapter 6
Conclusions

This thesis has investigated the impact of different levels of spherical aberration [1] (chap. 3) and signal (chap. 4) on multifocal microscopy (MUM) systems and has tested this latter as tool to perform micro-particle image velocimetry [2] (μPIV, chap. 5). MUM is a widefield microscopy able to image several planes at sample level simultaneously, thus allowing for full and axially extended 4D imaging [3] (sec. 1.3.9 and 2.2). For this study, the Dalgarno diffraction relay [4] has been selected. This, in comparison to the non-diffractive systems present in the literature (sec. 2.3), offers the advantage of being telecentric from the object side [5] (sec. 2.4.2) and makes use of a single camera, thus avoiding problems as different magnifications among imaged planes and camera synchronisation [6]. With respect to the Abrahamsson [7] and the grism based [8] relays (sec. 2.4.4 and 2.4.5), instead, Dalgarno relay is more versatile, since it is not tailored for a specific objective lens, it is easier to design, build and align and can access more practical plane spacing. However, it is not corrected for the spherical aberration induced by the use of the objective lens at non-design planes [9] and for the grating-induced lateral and axial chromatic aberration [10]. Consequently, it might require the use of a narrow bandwidth filter that discards the majority of the photons and limits the applicability of this system to single molecule investigations in cells (sec. 2.4.3). In addition, the size of the acquirable field of view (FOV) decreases as the number of the imaged planes increases, due to the use of a single camera. To evaluate the performance of Dalgarno relay, the sharpness algorithm has been chosen, since it does not require the modelling of the system point spread function (PSF) and to axially align the imaged planes as in PSF fitting methods (sec. 2.5.1) and it is easy to implement and use with more than two planes. The sharpness algorithm has been used via the MUM plugin for ImageJ [11] designed by Dr Eric Pitkeathly.

In chap. 3 it has been shown how the spherical aberration induced by the mismatch between sample and immersion medium refractive indices influences the plane spacing of multiplane systems (fig. 3.10). In particular, this latter shows a clear increase with the refractive index mismatch and the depth of the emitting source within the sample, since this raises the spherical aberration level [1] (fig. 3.1). This behaviour has been observed via both the sharpness [12] and the centre of mass [13] (CoM) algorithms, which are generally in agreement (fig. 3.12 and 3.13). The impact of the spherical aberration on the PSFs has also been quantified via the influence on the shapes

of the sharpness curves (sec. 3.6). This latter has shown a general increase in full width half maximum (FWHM), again, with the refractive index mismatch and the source depth (fig. 3.16) and this is not due to variations in the level of the signal. In addition, the sharpness curve peaks and FWHMs have indicated they could be linked via a simile-hyperbolic relation (eq. 3.12 and fig. 3.19), since the former tend to decrease as the latter increases and vice versa. This could be used to quantify the rate of change in the shape of the PSF with the level of spherical aberration. However, further studies are needed in this sense to verify this hypothesis. The influence of spherical aberration on sharpness curves could be potentially exploited to derive the associated correction factors and take to a more accurate evaluation of the axial positions.

In chap. 4 the impact of the levels of signal to noise ratio (SNR), signal to background ratio (SBR) and of the plane spacing on sharpness curves and on the performances of MUM systems has been investigated. In general, the sharpness peaks tend to grow with the signal, the axial range has shown a linear improvement as the signal level increases, while the behaviour of the axial precision can be described by an exponential profile (eq. 4.8) with characteristic decay constant τ of 0.51 ± 0.10 per SNR unit (fig. 4.40). The speed at which the axial range grows with the signal can be raised by increasing the plane spacing (fig. 4.41). This allows to extend the axial range without increasing laser power and/or camera exposure time, which would worsen the photobleaching problem and reduce the temporal resolution. However, the plane spacing value should always allow the observation of the emitters through multiple planes simultaneously to avoid the loss of the multiplane abilities. Below a SNR_0 threshold of around 1.23 ± 0.71 the axial range collapses to 0 µm when an accuracy on the axial localisation of 100 nm is required. The investigation presented in chapter 4 has allowed to formulate two equations to quickly evaluate the performance of the studied multiplane system in terms of axial range (eq. 4.14) and precision (eq. 4.8), given the required parameters are known. The study of the impact of the signal level has taken to the conclusion that Dalgarno relay could hardly be used to investigate single molecules in cells, due to the limits to the photon flux imposed by the narrow bandwidth filter (sec. 4.4.3). By increasing the allowed bandwidth the signal level can be raised (fig. 4.22) and this could improve the axial localisation performances of the system (fig. 4.26). However, this would reduce the lateral localisation accuracy due to the chromatic smearing introduced (fig. 4.27), remove the intensity balance among the different orders, since the grating is not balanced for multiple wavelengths (fig. 2.3), and introduce axial chromatic smearing in the non-zeroth planes (eq. 2.30). Another

way to improve the signal level can be by designing the distorted diffraction grating (DDG) to have multiple etching levels rather than being a binary one, since this has been proved to be beneficial to the grating transmission efficiency [14]. However, this would unavoidably raise the grating manufacturing costs. A different solution to improve the signal transmission in Dalgarno relay could be the substitution of the DDG with custom made lenses, whose focal lengths are equal to those provided by the DDG element itself (eq. 2.15). This would require the use of multiple relays coupled by mirrors and beam splitters, each one connected to its own dedicated camera and used to image a single plane. Obviously, this solution would need the synchronisation among the different cameras and a more difficult alignment of the different components. However, this non-diffractive relay would not be affected by the grating-induced lateral and axial chromatic smearing, there would not be loss of photons into higher orders, it would be telecentric and the FOV could be increased to match the entire chip size. The results shown in chap. 4 in terms of axial range and precision can be used to provide a general reference to evaluate the performances of used multifocal system with the level of the signal.

In chap. 5 MUM has been applied to reconstruct the velocity profile of a fluid flow inside a parallel plate flow chamber (PPFC) and, for the first time, around a fixed HeLa cell, to evaluate the generated fluid shear stress. In general, MUM, despite the advantage of being several time faster, is not able to provide the same accuracy on the calculated velocities that confocal microscopy can achieve (fig. 5.11 and table 5.3), even though it has shown better performances than those reported in the literature for other 4D imaging techniques (table 5.1 [15, 16, 17, 18, 19, 20]). At axial positions within 10 μm from the coverslip glass MUM reaches an average accuracy slightly worse than that obtained with the confocal microscope, while above 10 μm MUM is considerably inferior. However, the calculated accuracy is poorer with both MUM and confocal microscopes at axial positions over 10 μm. This suggests that problems as the increased spherical aberration at deeper axial positions into the sample (sec. 3.4) could significantly reduce the accuracy on axial localisation. This could be verified by extending the study in chap. 3 to include the effect of the level of spherical aberration on axial range and precision. Considering the refractive index of the perfusion medium (i.e. the dextran solution) was around 1.37 (sec. 5.3), the use of a water immersion objective lens could help to mitigate the refractive index mismatch-induced spherical aberration [21], even though this would come at the expenses of the resolution (sec. 1.3.4). The impact of spherical aberration could also be reduced by exploiting adaptive

optics [22] to correct for the wavefront errors introduced (sec. 1.5). The reconstruction of the flow velocity profiles around the cell (fig. 5.16 and 5.17) has allowed to calculate the generated shear stress fields (fig. 5.18). This latter presents characteristics similar to those observed in the literature [23, 24]. However, it also shows unexpected features due to the presence of false localisations that reduce the overall accuracy on the calculations. To strengthen the obtained results, the study presented in chap. 5 could be expanded and compared to a computational fluid dynamic simulation [25] of the flow around a geometrical model of the observed cell. This would require the pre-acquisition of a z-stack to three-dimensionally reconstruct the cell, which, for example, could be deconvolved to reduce the impact of the background [26] (sec. 1.3.5). Alternatively, the z-stack could be acquired by exploiting a commercial kit to transform epifluorescence microscopes into confocal ones [27]. This would also allow to image the flow by using confocal microscopy and further validate the results. These tests, together with the evaluation of the shear stress fields around several other biological samples could help to improve the use of MUM for µPIV and fully exploit its high speed and axially extended volumetric imaging abilities.

6.1 References

[1] S. F. Gibson and F. Lanni, "Experimental test of an analytical model of aberration in an oil-immersion objective lens used in 3-dimensional light-microscopy," Journal of the Optical Society of America A - Optics Image Science and Vision, vol. 8, no. 10, pp. 1601-1613, 1991.

[2] R. Lindken, M. Rossi, S. Große and J. Westerweel, "Micro-Particle Imaging Velocimetry (uPIV): Recent developments applications, and guidelines," Lab on a Chip, vol. 9, no. 17, pp. 2551-2567, 2009.

[3] S. Ram, D. Kim, R. J. Ober and E. S. Ward, "3D single molecule tracking with multifocal plane microscopy reveals rapid intercellular transferrin transport at epithelial cell barriers," Biophysical Journal, vol. 103, no. 7, pp. 1594-1603, 2012.

[4] P. A. Dalgarno, H. I. Dalgarno, A. Putoud, R. Lambert, L. Paterson, D. C. Logan, D. P. Towers, R. J. Warburton and A. H. Greenaway, "Multiplane imaging and three dimensional nanoscale particle tracking in biological microscopy," Optics express, vol. 18, no. 2, pp. 877-884, 2010.

[5] S. Djidel, K. J. Gansel, I. H. Campbell and H. A. Greenaway, "High-speed, 3-

dimensional, telecentric imaging," Optics Express, vol. 14, no. 18, pp. 8269-8277, 2006.

[6] A. D. Edelstein, M. A. Tsuchida, N. Amodaj, H. Pinkard, R. D. Vale and N. Stuurman, "Advanced methods of microscope control using μManager software," Journal of biological methods, vol. 1, no. 2, p. e10, 2014.

[7] S. Abrahamsson, J. J. Chen, B. Hajj, S. Stallinga, A. Y. Katsov, J. Wisniewski, G. Mizuguchi, P. Soule, F. Mueller, C. D. Darzacq, X. Darzacq, C. Wu, C. I. Bargmann, D. A. Agard, M. Dahan and M. G. L. Gustafsson, "Fast multicolor 3D imaging using aberration-corrected multifocus microscopy," Nature Methods, vol. 10, no. 1, pp. 60-U80, 2013.

[8] Y. Feng, P. A. Dalgarno, Y. Y. D. Lee, R. R. Thomson and A. H. Greenaway, "Chromatically-corrected, high-efficiency, multi-colour, multi-plane 3D imaging," Optics Express, vol. 20, no. 18, pp. 20705-20714, 2012.

[9] E. J. Botcherby, R. Juškaitis, M. J. Booth and T. Wilson, "Aberration-free optical refocusing in high numerical aperture microscopy," Optics Letters, vol. 32, no. 14, pp. 2007-2009, 2007.

[10] E. Hecht, "The Diffraction grating," in Optics, 4th ed., Addison Wesley, 2002, pp. 476-485.

[11] ImageJ, [Online]. Available: https://imagej.nih.gov/ij/index.html. [Accessed September 2018].

[12] H. I. C. Dalgarno, P. A. Dalgarno, A. C. Dada, C. E. Towers, G. J. Gibson, R. M. Parton, I. Davis, R. J. Warburton and A. H. Greenaway, "Nanometric depth resolution from multi-focal images in microscopy," Journal of the Royal Society Interface, vol. 8, no. 60, pp. 942-951, 2011.

[13] H. R. Harrison and T. Nettleton, "Centre of mass," in Principle of engineering mechanics, 2nd ed., Edward Arnold, 1994, pp. 25-26.

[14] S. Abrahamsson, R. Ilic, J. Wisniewski, B. Mehl, L. Yu, L. Chen, M. Davanco, L. Oudjedi, J. B. Fiche, B. Hajj, X. Jin, J. Pulupa, C. Cho, M. Mir, M. E. Beheiry, X. Darzacq, M. Nollmann, M. Dahan, C. Wu, T. Lionnet, J. A. Liddle and C. Bargmann, "Multifocus microscopy with precise color multi-phase diffractive optics applied in functional neuronal imaging," Biomedical Optics Express, vol. 7, no. 3, pp. 855-869, 2013.

[15] C. Cierpka and C. J. Kaehler, "Particle imaging techniques for volumetric three-

component (3D3C) velocity measurements in microfluidics," Journal of Visualization, vol. 15, no. 1, pp. 1-31, 2012.

[16] C. Cierpka, M. Rossi, F. M. R. Segura.1 and C. J. Kähler, "Comparative study of the uncertainty of stereoscopic micro-PIV, wavefront-deformation micro-PTV, and standard micro-PIV," 15th International Symposium on Applications of Laser Techniques to Fluid Mechanics, 2010.

[17] G. Elsinga, F. Scarano, B. Wieneke and B. W. v. Oudheusden, "Tomographic particle image velocimetry," Experiments in Fluids, vol. 41, no. 6, pp. 933-947, 2006.

[18] S. Chen, N. Angarita-Jaimes, D. Angarita-Jaimes, B. Pelc, A. H. Greenaway, C. E. Towers, D. Lin and D. P. Towers, "Wavefront sensing for three-component three-dimensional flow velocimetry in microfluidics," Experiments in Fluids, vol. 47, no. 4-5, p. Experiments In Fluids, 2009.

[19] J. S. Park and K. D. Kihm, "Three-dimensional micro-PTV using deconvolution microscopy," Experiments in Fluids, vol. 4, no. 3, pp. 491-499, 2006.

[20] Y. S. Choi and S. J. Lee, "Three-dimensional volumetric measurement of red blood cell motion using digital holographic microscopy," Applied Optics, vol. 48, no. 16, pp. 2983-2990, 2009.

[21] M. Abramowitz, K. R. Spring, H. E. Keller and M. W. Davidson, "Basic principles of microscope objectives," Biotechniques, vol. 33, no. 4, pp. 772-+, 2002.

[22] N. Ji, "Adaptive optical fluorescence microscopy," Nature methods, vol. 14, no. 4, pp. 374-380, 2017.

[23] U. M. Balaguru, L. Sundaresan, J. Manivannan, R. Majunathan, K. Mani, A. Swaminathan and S. Venkatesan, "Disturbed flow mediated modulation of shear forces on endothelial plane: A proposed model for studying endothelium around atherosclerotic plaques," Scientific Reports, vol. 6, 2006.

[24] P. Eshtehardi, M. C. McDaniel, J. Suo, S. S. Dhawan, L. H. Timmins, J. N. G. Binongo, L. J. Golub, M. T. Corban, A. V. Finn, J. N. Oshinsk, A. A. Quyyumi, D. P. Giddens and H. Samady, "Association of coronary wall shear stress with atherosclerotic plaque burden, composition, and distribution in patients with coronary artery disease," Journal of the American Heart Association, p. 1:e002543, 2012.

[25] H. V. a. W. Malalasekera, An Introduction to Computational Fluid Dynamics: The

finite volume method, 2nd ed., Pearson Education, 2007.

[26] D. S. C. Biggs, "3D deconvolution microscopy," Current Protocols in Cytometry, vol. 52, no. 1, pp. 12.19.1-12.19.20, 2010.

[27] "Thorlabs," [Online]. Available: https://www.thorlabs.com/newgrouppage9.cfm?objectgroup_id=5696#ad-image-0. [Accessed September 2018].